A SINGLE-CELL ANALYSIS APPROACH

TO UNDERSTANDING

MOLECULAR ORGANIZATION AND PLASTICITY IN THE BRAIN

by

James Hyun-Woo Park

A dissertation submitted to the Faculty of the University of Delaware in partial fulfillment of the requirements for the degree of Doctor of Philosophy in Chemical Engineering

Fall 2016

A SINGLE-CELL ANALYSIS APPROACH

TO UNDERSTANDING

MOLECULAR ORGANIZATION AND PLASTICITY IN THE BRAIN

by

James Hyun-Woo Park

Approved: _____

Abraham M. Lenhoff, Ph.D.
Chair of the Department of Chemical and Biomolecular Engineering

Approved: _____

Babatunde A. Ogunnaike, Ph.D.
Dean of the College of Engineering

Approved: _____

Ann L. Ardis, Ph.D.
Senior Vice Provost for Graduate and Professional Education

I certify that I have read this dissertation and that in my opinion it meets the academic and professional standard required by the University as a dissertation for the degree of Doctor of Philosophy.

Signed: _____

Babatunde A. Ogunnaike, Ph.D.
Professor in charge of dissertation

I certify that I have read this dissertation and that in my opinion it meets the academic and professional standard required by the University as a dissertation for the degree of Doctor of Philosophy.

Signed: _____

James S. Schwaber, Ph.D.
Professor in charge of dissertation

I certify that I have read this dissertation and that in my opinion it meets the academic and professional standard required by the University as a dissertation for the degree of Doctor of Philosophy.

Signed: _____

Rajanikanth Vadigepalli, Ph.D.
Professor in charge of dissertation

I certify that I have read this dissertation and that in my opinion it meets the academic and professional standard required by the University as a dissertation for the degree of Doctor of Philosophy.

Signed: _____

Prasad S. Dhurjati, Ph.D.
Member of dissertation committee

I certify that I have read this dissertation and that in my opinion it meets the academic and professional standard required by the University as a dissertation for the degree of Doctor of Philosophy.

Signed: _____

David W. Colby, Ph.D.
Member of dissertation committee

I certify that I have read this dissertation and that in my opinion it meets the academic and professional standard required by the University as a dissertation for the degree of Doctor of Philosophy.

Signed: _____

Abhyudai Singh, Ph.D.
Member of dissertation committee

ACKNOWLEDGMENTS

First and foremost I thank God for blessing me with the desire, abilities, and opportunities to learn about and experience this beautifully complex and intricate world.

I am blessed to have been admitted into a top-tier Chemical & Biomolecular Engineering program and given the opportunity to work alongside remarkable individuals who have pushed me to become the best engineer and scientist that I can be. I have come to think of the scientific training I have received as somewhat analogous to the training athletes endure in their journey to reach their maximum potential. Consequently, I found it fortuitous that the writing of this dissertation aligned with the Summer Games of the XXXI Olympiad in Rio de Janeiro, Brazil. The physical feats and mental fortitude displayed by these Olympians were simply awe-inspiring and provided the motivation I desperately needed to complete this dissertation. While I am no Olympian by any stretch of the imagination, I believe that Olympic spirit, exemplified by these Olympians and best expressed by the Olympic creed, aptly describes my feelings towards my experiences here at the University of Delaware (UD) and Thomas Jefferson University (TJU).

> The most important thing … is not to win, but *to take part*, just as the most important thing in life is not the triumph, but *the struggle*. The essential thing is not to have conquered but *to have fought well*.

Training to become an independent researcher has been a tremendous struggle, but I believe that I am now a better person, certainly a better scientist and engineer, for having engaged in this struggle. The challenges faced during my graduate studies would have certainly been unbearable had it not been for the help of so many people here at UD and TJU. There are far too many people that deserve acknowledgement for their support, but I want to acknowledge a few whose guidance and support have been exceptional.

To my advisors, it has been an honor and privilege learning from and working with you all. I am grateful for all that you have done for me, for the things said and the deeds left unsaid. Thank you all for taking me on as a graduate student, for training me to be a better scientist, and for providing an example of what it takes to conduct research at the highest level. While the following thoughts apply to all three of you, I want to acknowledge specific ideals that I have learned from each one of you, ideals which I will carry with me henceforth.

To my advisor, Babatunde Ogunnaike, thank you for this opportunity and for making it as rich and fulfilling as it has been. You have been and will continue to be a role model for me, as a scientist, engineer, educator, and above all else, a man of character. You have set a high bar, something that I will continually strive for throughout the rest of my career and life.

To my advisor, James Schwaber, thank you for sharing your rich insight and experiences with me. You have shown me the value of thinking BIG and being courageous in pushing forward ones' scientific ideas. Your vision of a truly

collaborative research environment has been an eye-opening experience and I hope to carry that truly collaborative vision forward in my own career. Despite my stubbornness and self-doubt, you continued to be patient with me and encouraged me as best as you could – thank you.

To my advisor, Rajanikanth Vadigepalli, thank you for showing me what it means to "hustle." You have redefined that word for me and have provided an example for me to work towards. Thank you for guiding me and for pushing me to see the opportunities that lay hidden not just in the sea of noise that is high-throughput data, but in my work and future career. Your scientific vision is truly awesome and I hope to carry the lessons you have imparted upon me, particularly that of not being afraid to fail, for the rest of my days.

To my thesis committee members, thank you for keeping me on track. Thank you for your scientific insight and for sharing your own career and life experiences so that I may make my own that much more fulfilling.

To my committee member, Prasad Dhurjati, thank you for your perspective and your insight. I've enjoyed our discussions about science, research, and life. I've always appreciated your willingness to talk and to help me think about situations from a broader perspective.

To my committee member, David Colby, thank you for your support throughout this entire process. Your concern for my training and education has been incredibly encouraging and has motivated me to think about future objectives I should incorporate into my plans to become a better scientist.

To my committee member, Abhyudai Singh, thank you for your insight and support throughout my research training. It has been a pleasure working with you and learning from you. Your enthusiasm for science is inspiring. I can only hope to express similar enthusiasm in whatever I do next.

To Daniel Lees, thank you for your time and input in the manuscripts we have been fortunate enough to have published. Your insight and feedback have dramatically improved my writing and have helped me to discover a writing style all my own, one far superior than what I could have ever hoped to have found by myself.

To Abraham Lenhoff and Eric Furst, thank you for taking me on as a Teaching Fellow for ChEG 401. I learned a tremendous amount not only about process dynamics and control, but also about how to manage a course and how to simulate and motivate young minds. The experience, knowledge, and energy you both brought to each lecture is something that I hope to emulate in my future endeavors. Thank you for showing me what it takes to be an excellent teacher.

To my former and current colleagues at the Daniel Baugh Institute for Functional Genomics and Computational Biology at TJU – Dr. Warren Anderson, Dr. Anthony Brureau, Dr. Danielle DeCicco, Dr. Kate Kernan, Dr. Lakshmi Kuttippurathu, Dr. Carmen Nichols, Dr. Jessica Schwaber, Dr. Haisun Zhu, Sirisha Achanta, Jon Gorky, Hiren Makadia, Sean O'Sullivan, Austin Parrish, and Aalap Verma – I have gained a tremendous amount from working with each and every one of you. Your patience and support in helping me to understand the intricacies of molecular biology, animal handling, neuroscience, cellular biology, medicine, health,

mathematical modeling, coding, education, and the many other aspects of life we've discussed have been invaluable to my development as a scientist and as an individual.

To my former and current colleagues in the Ogunnaike research group – Dr. Seung-Wook Chung, Dr. Qian Gou, Dr. Robert Lovelett, Dr. Jake McGill, Dr. Melissa St. Amand, Dr. Mary McDonald Staehle, Dr. Chia-Hung Tsai, Dr. Zack Whiteman, and Devesh Radhakrishnan – your continual support throughout this journey has been essential to my graduate training. It was only because of your help in refining my writing, presentations, and mindset was I able to come off as a semi-literate engineer/scientist, pass Qualifiers, and maintain my general sanity throughout this journey. You all have provided me with many examples of what it takes to excel as engineers/scientists and more importantly what it takes to be a person of character. And a special thank you goes to my UD/TJU partner in crime, Dan Cook. You were always willing to lend an ear, a helping hand, or provide an objective viewpoint on all things whenever I needed it. I would not be where I am nor would have been able to accomplish the things I have been able to had it not been for your support. Thank you many times over. I think we've just taken one step up in that layer cake. To these remarkable people at UD and TJU, thank you for your scholarship, fellowship, and above all, your friendship.

To the friends I have been fortunate enough to make in the broader UD and TJU community, I know my time here would have been much more difficult and much more challenging without your company. Thank you for understanding the challenges I faced as a graduate student and for being great people.

To my friends from NOVA and NYC – I cannot thank you enough for your love and support, for the dinners, drinks, trips, and good times we've shared. I am truly fortunate to know you all and I look forward to the many more good times that await us.

To my family – none of this would have been possible had it not been for your love and support. I am who I am because of everything you have done for me. Mom and Dad, I don't think I'll ever truly understand what you have sacrificed to put me in a position to succeed at all stages of my life. I simply hope that you know that I love you and that I am forever grateful for all that you have done. This dissertation is a result of all that you have raised me to be and I hope that this makes you proud. To my older brother John, what can I say? You've always supported me in everything that I have done. You've supported me through the difficult times and helped me celebrate the good times as well. You have always been there for me and I can never repay in full what you have done for me. Thank you for being my brother and my friend.

And finally, to the U.S. taxpayers, the National Institutes of Health, the National Institute of Alcohol Abuse and Addiction, the Department of Chemical and Biomolecular Engineering at the University of Delaware, and the Daniel Baugh Institute for Functional Genomics and Computational Biology at Thomas Jefferson University, thank you for funding me and the work that I've done. I hope that this work is worthy of the financial investment you have placed in me.

TABLE OF CONTENTS

LIST OF TABLES

LIST OF FIGURES

ABSTRACT

Single-cell transcriptional heterogeneity pervades the fully differentiated brain. This heterogeneity is particularly prevalent in brain nuclei involved in the autonomic regulation of physiological functions such as cardiovascular homeostasis. Because neuronal function largely depends on its transcriptome, such heterogeneity confounds our understanding of how heterogeneous neurons contribute to their broader phenotypic function. In addition to the transcriptome, functional connectivity and *in vivo* anatomical environment are additional factors central to defining a neuron's functional state. Given their importance, these factors may provide the added context necessary to understand how a distribution of heterogeneous neurons contributes to phenotypic function. Consequently, *the overall goal of this work is to establish an organizational framework that characterizes single-neuron heterogeneity within a brain nucleus and elucidates its functional relevance.*

Towards this goal, we have taken a combined experimental and computational approach to determine the organizing principles driving complex interaction networks within and among transcriptionally diverse neurons within a brain nucleus. First, we generated a large-scale gene expression dataset from several hundred neurons, selected on the basis of their synaptic input types, taken from the nucleus tractus solitarius (NTS), a brainstem nucleus involved in the central regulation of blood pressure. Our

analysis of these neurons revealed an organizational structure in which transcriptional variability aligns with synaptic input type along a continuum of graded gene expression. This continuum is populated by distinct neuronal subtypes characterized by gene groups exhibiting correlated expression.

In order to identify the molecular mechanisms driving this correlated behavior, we next developed a fuzzy logic modeling-based methodology to model quantitatively causal gene interaction networks from single-cell transcriptomic data. Our modeling results suggest that distinct input stimuli operating on distinct network structures corresponding to these subtypes can drive neurons through various transcriptional states. These results suggest that transcriptional heterogeneity represents a neuron's adaptive response to various inputs. Based on these results, we propose that neuronal adaptation may be a mechanism through which the NTS robustly regulates blood pressure and cardiovascular homeostasis.

To test this proposal, we examined what impact adaptation to neuronal subtypes in the NTS and brainstem would have on the short-term autonomic regulation of cardiovascular homeostasis under the simulated disease state of systolic heart failure via mathematical modeling. We developed a closed-loop control model characterizing neuronal regulation of the cardiovascular system by integrating previous quantitative models that simulated various aspects of the cardiovascular system. Because the goal of this study was to investigate the effects of neuronal subtype adaptation, we incorporated brainstem neuronal subtypes, such as those identified in our analysis of the NTS. Modeling simulation results suggest that

adaptation of these neuronal components can compensate for an impaired cardiovascular state due to systolic heart failure by decreasing neuronal inhibition (i.e. parasympathetic tone) of cardiac contractility.

Finally, we tested the utility of a single-cell analysis approach to interpret single-cell heterogeneity throughout the brain by identifying a cellular network organization in a distinct brain nucleus – the suprachiasmatic nucleus (SCN), which regulates circadian rhythms in mammals. Similar to our analysis of the NTS, we generated and analyzed a high-dimensional gene expression dataset consisting of hundreds of transcriptionally heterogeneous SCN neurons. Our multivariate analysis of these neurons revealed both known and previously undescribed SCN neuron-types, which organize into a neuronal interaction network via known paracrine signaling mechanisms underlying the synchronizing functions of the SCN.

Based on the analysis of heterogeneous single neurons, we have identified an organizational framework with which we can now interpret single-cell heterogeneity; a heterogeneous neuronal population comprises a mixture of distinct neuronal subtypes whose adaptive response to inputs is driven by distinct regulatory networks. Such adaptation provides a mechanism in which the brain is able to regulate robustly physiological functions by providing compensatory effects under perturbed or challenged states.

Chapter 1

INTRODUCTION

"The brain seems to be made up of a bewildering complexity of parts, and the cells within the parts seem to be characterized by an inscrutable complexity of form, extent, and relationships with each other."

Gordon M. Shepherd, in *The Synaptic Organization of the Brain* [1]

"The brain is a wonderful organ, it starts working the moment you get up in the morning and does not stop until you get into the office."

Robert Frost (1874 – 1963)

1.1 Motivation: Cell-Type and the Brain

The human brain, highly differentiated and sophisticated, is the most complex organ of the body. During development, its neural components organize themselves into a rich and complex array of neuroanatomical structures that provide the biological foundation underlying not only the brain's ability to regulate and coordinate physiological function, but also its emergent properties of cognition, memory, and intelligence [2–4]. While other mammals, such as rats and mice have similar neuroanatomical structures, what distinguishes our unique cognitive capabilities from our mammalian counterparts is the presence of an immense diversity of cell types and

the associated various complex cellular networks that maintain patterns of activity in the human brain. This diversity arises from the billions of neurons and trillions of synaptic connections between neurons in the human brain and underlies the emergent properties that enable it to generate and regulate physiological responses and behavior in order to predict, interpret, and respond to the external world. Consequently, dysfunction in these networks contribute to or cause maladaptive behavior and dysregulation associated with diseases [5–9]. Understanding how these networks organize, change, and adapt over time in the brain would bring insights into the neural mechanisms associated with healthy and disease states. Towards this goal, we first require an understanding of their constituent components i.e. the individual neuron and neuron types within the brain. .

The investigation of neurons and their interactions with one another and other cellular components in the brain is one primary goal of Neuroscience. From the seminal work of Ramon y Cajol, which classified neurons based on their microscopic structures via golgi staining [10], dedicated efforts in the field have revealed a substantial amount of diversity in neuron types, based on connective, morphological, and histochemical properties of neuronal populations. With continual improvements being made to the resolution with which one can analyze a cell, these efforts have shifted to include the molecular properties and characteristics of neurons. For example, recent investigations have examined the developmental processes that drive a nascent cell into the various differentiated neurons types in the brain and nervous system by studying the molecular-scale characteristics such as the expression of a

single gene or a subset of them [11–13]. In addition to revealing the molecular programs central to the differentiation process, molecular-scale studies have been used to define disease phenotypes in the brain For example, variations in gene sequence or level of gene expression are associated with or cause Fragile X syndrome and Huntington's disease [14–16]. Similar approaches focusing on a candidate gene or a small subset of genes, (i.e. one or few of the approximate 30,000 genes that comprise the genome within a neuron), continue to make up much of the basic and translational neuroscience research [4]. While these focused studies are critical to expanding our knowledge base, they do not fully account for the complexities involved in the regulation of gene expression. Within the sum total of a cell's expressed genes, the cell's *transcriptome*, genes interact with and are regulated by one another resulting in complex non-linear behaviors [17–20]. Because the transcriptome is a manifestation of the active genetic programing contributing to cellular function, the transcriptome and its associated processes are a major focus of investigation towards understanding the molecular mechanisms driving cellular function [21–27]. In this context it has been a major aspiration to connect cellular phenotype to genotype.

The mapping of the human genome [28] and the recent initiation and progress of the Encyclopedia of DNA Elements (ENCODE) research project has provided an unprecedented perspective on the genome, including its transcriptional regions [29]. Coincident with these projects, recent technological advances in the precision of experimental techniques and high-throughput technologies have provided capabilities to enable sizeable amounts of data to be generated at faster and cheaper rates. Lately,

studies have begun to capitalize on these technological advances by characterizing the transcriptional programs and molecular landscape driving organ and brain development [26,30–32]. Techniques such as laser capture microdissection [33], lentiviral vector, and pseudorabies virus labeling [34–38] have enabled the Neuroscicence and broader research community to examine and manipulate targeted cell populations and even individual cells. The convergence of this comprehensive knowledge of the genome and the experimental and technological advances being achieved has created an environment in which the scientific community is on the verge of advancing tremendously our understanding of the brain, its constituent neuronal components, and the regulatory and integrative role in health and disease.

1.1.1 The significance of cell-type in the BRAIN

A recognition of the significance of cell-type, shared by researchers and non-researchers alike, is evidenced strongly by the recent formation of Presidential initiative for Brain Research through Advancing Innovative Neurotechnologies (BRAIN initiative) [39]. The purpose of this initiative is to "accelerate the development and application of new technologies, theories, and analytical approaches to understand how individual brain cells and complex neural circuits interact at the speed of thought." [39]. This initiative consists of a $100 million, 12 year commitment that spans multiple federal government funding agencies including the National Institute of Health (NIH), the Defense Advanced Research Projects Agency (DARPA), the National Science Foundation (NSF), and the Food and Drug

Administration (FDA). The shared understanding across these agencies emphasizes the magnitude of opportunities now within scientific reach, as plainly stated by this initiative [40]:

> The time is right to… undertake the most groundbreaking and integrated approach ever contemplated to understanding how the brain works in health and disease. This is a moment when our knowledge base, our new technological capabilities, and our dedicated and coordinated efforts can generate great leaps forward… the public health need and scientific opportunity are so great that there has never been a better time to undertake this challenge.

Towards this effort, seven major research priorities were identified that drive and will continue to drive research efforts, supplementing rather than replacing current efforts in basic, translational, and clinical neuroscience.

Because the cell can be considered as the fundamental biological unit, and thus neurons as a core component of the brain [2], the first major research priority of the BRAIN initiative focuses on "*Cell Type*." Specifically, this priority aims to define the cellular components of complex cellular networks in the brain. Classifying neurons and identifying the appropriate classifiers with which to classify them is central for understanding what neuron types are present and how these neuronal components are organized to drive the multicellular, networked behavior in the brain and in healthy and diseased states. Reaching a consensus regarding neuron-types, identifying the "parts-list" of the brain's neuronal components of the brain will provide a foundation that will support future efforts in unraveling the mysteries of the brain.

The work presented in this dissertation takes place within the broad context described above. Here, this work seeks to develop and apply methodologies towards understanding the organizational principles of the brain's neuronal components and how these principles define neuronal phenotypes and their functional role in regulating physiology. This work takes place against the backdrop of rapid innovation in -omics scale technologies and advances in experimental precision and accuracy that enable molecular-level examination of the brain at the single-neuron scale. Because characterization and classification of neurons should ". . . consist of the molecular, cellular, and structural properties of these components, which are major determinants of system-wide activity in the brain," [39] this work capitalizes on these technological capabilities to identify molecular mechanisms underlying organizational and functional principles of neuron types and how such mechanisms apply towards their function. Before proceeding further, a brief introduction to the neuron's structure, anatomical organization, and its relationship to the nervous system is given in the following section to provide some additional context.

1.2 Neuron Structure and Anatomical Organization

1.2.1 Structural organization of neurons

Neurons, a principal cellular component of the brain, process and convey information through electrical and chemical signaling mechanisms. Generally, electrical signals are used to convey information from on part of the neuron to another.

Consequently neurons contain specialized regions for integrating, conducting, and transmitting information. All neurons include *i)* a *soma* or *perikaryon* – the cell body, which supports the metabolic and synthesis functions of the neuron, while most neurons also have *ii) dendrites* – a series of branching, tapering projections that receive stimuli or inputs relaying information from other neurons via *iii) synapses* (synaptic contacts), and *iv) axons* – long cylindrical structure, i.e. process (nerve fiber), that carries information from the soma and from terminal branches arise that synapse onto other neurons. Neurons can differ dramatically from one another based on their somatic, dendritic, and axonal morphology, thereby contributing to their functional diversity. In addition to underlying functional aspects of an individual neuron, these structural components contribute to the anatomical organization of neurons in the brain and nervous system.

1.2.2 Anatomical organization of neurons

Mature, fully differentiated, or *post-mitotic*, neurons within the fully developed brain are anatomically organized into densely packed cell bodies known as *nuclei* (not to be confused with the chromosome-containing organelle of a cell). Nuclei are one of two principal forms of anatomical organization of neurons found in the brain, the other being layered structures, observed in areas such as the cerebral cortex or cerebellum [2]. Individual neurons within a nucleus are traditionally understood to share similarities in their function and connectivity to other brain structures, though a nucleus may consist of complex internal structures, containing distinct region-specific

neuron-types. Brain nuclei connect to other nuclei by *tracts*, bundles of axons extending from the cell bodies and forming the basis of many major neuroanatomical structures in the brain. Brain nuclei and the individual neurons within them are traditionally understood to perform integrative and regulatory functions, receiving and responding to continual signals and synaptic inputs from other brain regions and various parts of the body in order to regulate critical physiological functions in the broader context of the nervous system.

1.2.3 Organization of the nervous system

The nervous system is composed of two main parts, the *central nervous system* (CNS) and the *peripheral nervous system* (PNS), the former consisting of the brain, its nuclei, and the spinal cord, the latter consisting mainly of *sensory* neurons, nerve cells that transduce external stimuli into internal electrical signals that are sent to the CNS. Thus the PNS connects the CNS to the limbs and organs of the body. These signals carry information regarding the external stimuli along *afferent* nerve fibers *to* the CNS. These primary afferents terminally connect to specific brain nuclei that integrate, process, and generate signals. Neurons receiving afferent inputs via direct synaptic connection, aptly named *second-order* neurons, serve as the second link in the signaling chain. In-turn these neurons connect to *third-order* neurons, which carry information to higher brain regions such as the cerebral cortex. Signals generated by various nuclei and networks of interconnected nuclei ultimately result in motor outflow signals sent *from* the CNS along a system of two neurons sets. The first of

these, called *preganglionic* neurons, serially connect to the second set of neurons known as *postganglionic* neurons. Signals are sent along the postganglionic axons (i.e. *efferent* fibers) that connect to and modulate the functional states of tissues and organs.

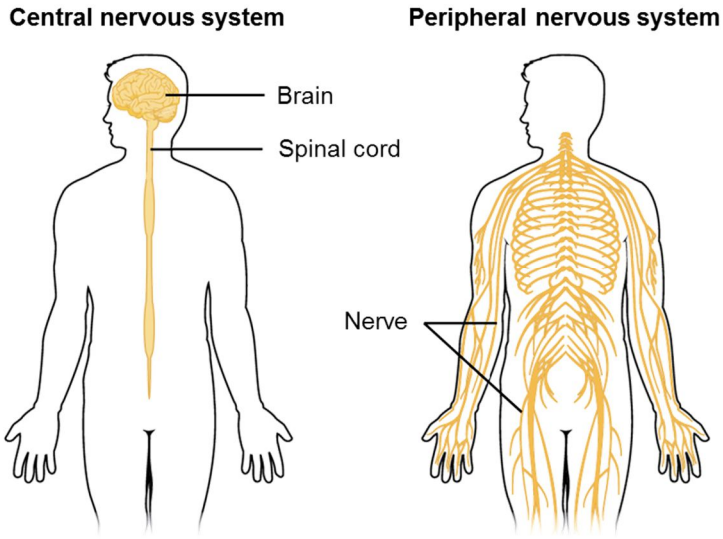

Figure 1.1 The nervous system. A breakdown of the nervous system into the central and peripheral nervous systems is shown. Image has been modified from [41].

It is through these connections that the brain interacts with and regulates voluntary (conscious) and involuntary (unconscious) physiological actions and process throughout the body. In the context of regulating involuntary physiological functions critical to survival, such as heart rate and respiration, the brain controls a subdivision of the PNS known as the *autonomic nervous system* (ANS). The ANS consists of two arms or branches known as the *sympathetic nervous system* and *parasympathetic*

nervous system. The sympathetic nervous system is traditionally understood to regulate physiological responses associated with the "fight or flight" responses including increased heart rate, constriction of blood vessels, and dilation of lung airways. Sympathetic signals are transmitted through the splanchnic nerves, which carry nerve fibers that innervate almost every organ in the body. Conversely, the parasympathetic system is associated with "rest and digest" responses of the body including decreased heart rate, dilation of blood vessels, and constriction of airways in the respiratory tract (*bronchi*). Parasympathetic signals are transmitted to and from the brain primarily along the glossopharyngeal and vagus nerve. The sympathetic and parasympathetic branches act as modalities through which the brain modulates physiological responses of specific tissue and organ systems in order to maintain internal conditions in a stable steady state or *homeostasis* amid constantly changing internal and external bodily conditions and environments.

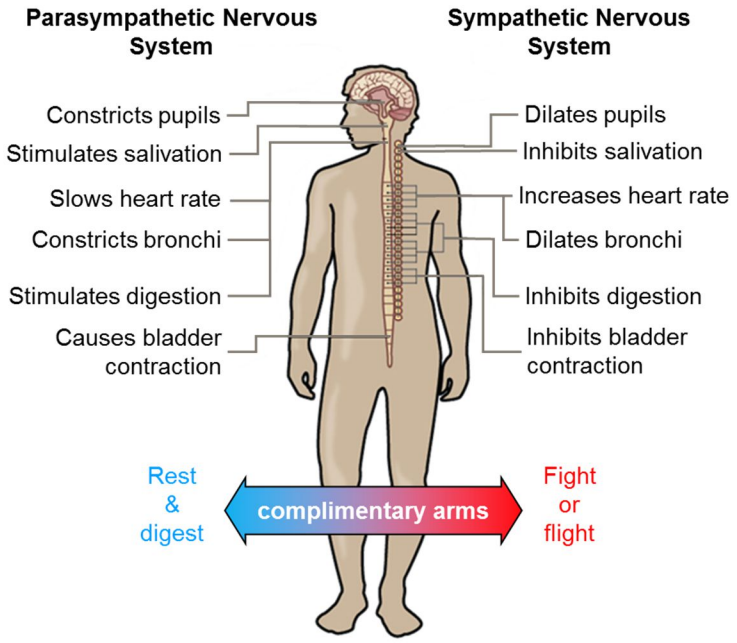

Figure 1.2 Autonomic nervous system. The diagram above lists some of the varying effects that each branch of the autonomic nervous system has on physiological functions. Both branches of the autonomic nervous system work in tandem to maintain homeostasis throughout the body. Image has been modified from [41].

To maintain this stable, dynamic constancy, brain nuclei and the individual neurons within them receive and integrate continual synaptic inputs from a multitude of sources, examples of which include, but not restricted to *i)* afferent fibers relaying information about the state of the peripheral state, *ii)* neighboring neurons within the microenvironment of the nucleus, as well as *iii)* neurons from other nuclei to which it they are connected. Furthermore, these synaptic inputs change continually, reflecting the dynamic nature of the internal and external environment. In this context, the function and state of an individual post-mitotic neuron is dependent upon its local anatomical environment and connectivity.

In connection with such structural and anatomical characteristics, molecular processes such as neuropeptide/neurotransmitter production, metabolism, and gene expression, play a central role in defining and distinguishing neuron-types and their functional states [24,42–45]. Each of these molecular processes and associated components has invited and continue to drive extensive research activity on their own behalf. Consequently, functionally defining neuron-types based on the totality of their underlying molecular processes is beyond the scope of this work. Rather, the present focus is on the analysis and identification of neuronal phenotypes by analyzing and developing methodologies to characterize the transcriptional state of individual neurons in a functional neuroanatomical context. In addition to the motivation provided in §1.1, experimental and theoretical evidence is described in the following section to motivate the utility of examining the transcriptome as it relates to the functional state of a cell.

1.3 Cellular State and the Transcriptome

Although every neuron in the brain contains the same genome, the combinations, dynamics, and interactions involved in a genome's expression in a central manner distinguish these neurons and the developmental trajectory they take [26,46]. From the moment pluripotent stem cells are generated, they differentiate along developmental trajectories that enable these progenitor cells to mature into distinct cellular groups that share similar biochemical, morphological, and anatomical characteristics, or *phenotypes*. Experimental evidence has shown this differentiation is

largely a result of dynamic gene expression (transcriptional) programs. The differentiation and maintenance of a differentiated cell state depends on underlying transcriptional programs involving key molecular regulators and the modulation of multiple molecular pathways. Moreover, the sequence in which these programs occur also plays a factor in the differentiation process [47–50]. Examples of transcriptional programs influencing cellular differentiation have been identified in spinal neuron development [11–13] as well as other cell-types and tissues [26,30,51–53].

This developmental process has been analogously described as one where an object traverses a topographical landscape, following various paths along this landscape into distinct wells or valleys representing differentiated cell-states, as illustrated in Figure 1.3.

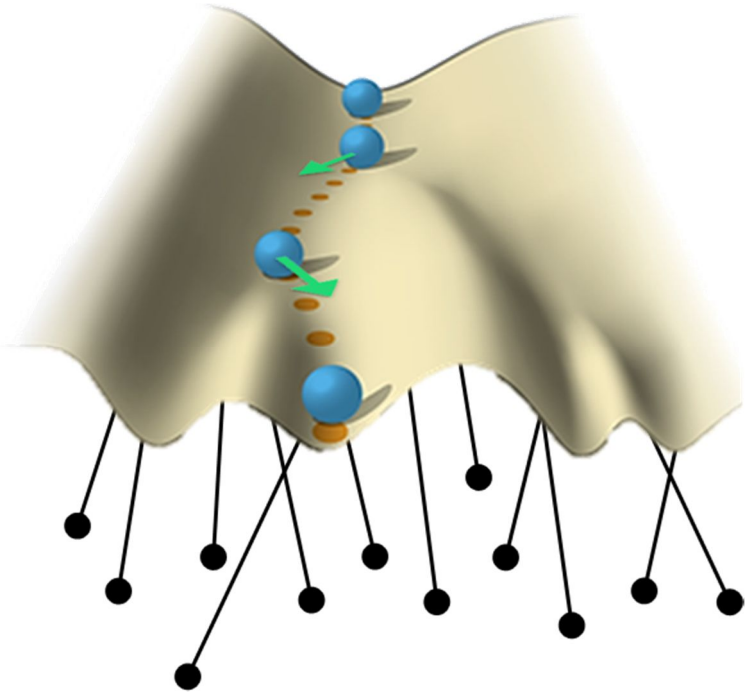

Figure 1.3 Waddington's "canalization." A depiction of the classical Waddington representation of canalization where a ball rolling down the hill is directed into one of several different valleys, each representing some differentiated cell state. The ball represents some progenitor cell and its trajectory represents its development. The topology of the landscape, is effected by genes, which are represented by the black circles. Mutations in these genes can cause the shifts in the position of the black circles and can alter the landscape, affecting a cell's developmental trajectory. Figure has been modified from [54,55].

The wells and canalized paths are shaped by pegs and stabilizing ropes representing the static influence genes have on the landscape through genetic mutations that affect the landscape over generations. This "canalization" process, a coinage of the developmental biologist C.H. Waddington [54,56,57], provides a conceptualization of cellular development that helps organize and relate the various cell types emerging from this process. The concept has been further modified to

include multiple molecular mechanisms such as changes in chromatin structure, extracellular signaling cues, and the random nature of gene expression that have more immediate effects on the developmental topology [26,55,58].

Not only do the transcriptome and transcriptomic programs play a central role in phenotypic development, recent experiments have demonstrated the transformative impact the transcriptome plays in *maintaining* cellular phenotype, or *cell-type competence* [21]. A prominent example of the relationship between transcriptome and cellular phenotype was demonstrated elegantly by the induction of pluripotent cells from adult fibroblasts, a type of cell that synthesizes extracellular matrix and collagen and provides the structural framework of animal tissue [59]. This phenotypic change was stimulated by introducing a defined set of four transcription factors (*Oct3/4*, *Sox2*, *c-Myc*, and *Klf4*) into fibroblasts by retroviral transduction. These transduced cells exhibited morphology, growth properties, and biological markers associated with embryonic stem cells. Such results highlight the fact that perturbations to the transcriptomic state of a cell can trigger a cascade of molecular events that lead to phenotypic change and further support the idea that a differentiated cell-state is not immutable.

Similarly, another experimental technique, aptly named transcriptome-induced phenotype remodeling (TIPeR) [60], illustrates the importance of the transcriptome in defining cellular phenotype. In this technique, the entire transcriptome of one cell-type is transfected into a host cell, allowing one to "directly point the transcriptome towards the target state by introducing the target transcriptome itself" [60]. Sul et al.

used TIPeR to convert mature, post-mitotic differentiated neurons into astrocyte-like cells by introducing into the host neuron astrocytic RNA components, including messenger RNA (mRNA), microRNA (miRNA), and long noncoding RNA (lncRNA) with ~40% efficiency. Additional experiments have also correlated the transcriptional states of neurons in the rat neocortex to their electrophysiological properties, a central phenotypic-defining characteristic used to define neuron types [61]. Examination of the transcript levels of 26 ion channels that regulate action potential and electrical activity of a neuron and electrical firing characteristics of such neurons to a particular type of electrical stimulation (including for example electrical spike frequency, action potential amplitude, and amplitude duration) showed that a positive correlation exists between expression of these ion channels and the distinct firing characteristics of unique neuron groups.

Taken together, these results indicate the critical role the transcriptome fulfills in the development *and* maintenance of cellular phenotype. The transcriptome can be viewed as a molecular read-out, a ”snap-shot”, of a neuron’s functional state and more generally that of a cell [21,46,62,63]. Thus analyzing the transcriptome of individual neurons would elucidate the molecular mechanisms driving neuronal state and function and further elucidate what neuron-types exist in the brain.

1.4 Transcriptional Variability

Recent work examining the transcriptome at the single-cell scale, however, has revealed repeatedly significant variability in transcriptional state of individual cells

within functionally homogeneous populations [27,63], a phenomenon that has also been observed among clonal cell populations and *in vitro* cultures [64–69]. The phenomenon of single-cell transcriptional heterogeneity has been observed throughout the body, including the immune system [52,70–72], lungs [32], and heart [73]. This transcriptional heterogeneity complicates our understanding of how the transcriptional state of a cell relates to its phenotype function [22,25,27,74]. As high-throughput data acquisition methods have now become highly precise [70,75–78], we see that the variability observed in the results is not a mere distribution around a mean, but a reflection of true heterogeneity. Thus, individual cells appear to exist in a range of distinct states. Given that this single-cell transcriptional heterogeneity exists, several questions arise including *i)* what are the sources of this heterogeneity?, and *ii)* how do we integrate this variable transcriptomic behavior in defining cell-type? The following summaries of some experimental and computational efforts provide partial answers to these questions.

1.4.1 Intrinsic sources of variability

Two distinct causes of transcriptional heterogeneity may be classified as intrinsic or extrinsic. *Intrinsic* sources of variability refer to the random or stochastic nature of the multiple biochemical reactions that drive gene expression, or transcription, in cells. From a basic perspective, a gene can be divided into two parts, *i)* a promoter region and *ii)* a messenger RNA (mRNA) coding region. The promoter region, located upstream from the mRNA coding region, based on its interactions with

nuclear proteins in the cell nucleus (distinct from a brain nucleus), determines the conditions in which the gene's coding region will be transcribed. Nuclear proteins that bind themselves to the promoter region include proteins known as transcription factors (TFs) that bind to a short DNA segment. These segments, known as the transcription regulatory element (TRE), are 8-24 base-pair sequences in length and lie within the promoter region. The TFs typically includes two functional domains: a DNA binding region that has a high affinity for the TRE and a protein interaction region that binds with a separate biological complex, consisting of RNA polymerase II (Pol II) and other factors [79–81]. Once bound, the Pol II complex, begins the elongation step, where it traverse the template DNA strand and begins to form an RNA copy, based on base pairing complementarity. Termination of elongation can occur through multiple mechanisms including the use of a termination factor or termination complex that binds to the polymerase [82]. This results in cleavage of the mRNA product, which is followed by the subsequent addition of a polyadenylated (poly-A) tail.

The transcription process has been shown experimentally to occur in short "bursts" at a high frequency, followed by quiescent periods. The discrete, burst-like nature of transcription highlights the inherent or *intrinsic* nature of transcriptional variability. A landmark paper by McAdams and Arkin [83], demonstrates via mathematical modeling how intrinsic variability in transcription can lead to cell-type variability. Subsequent work and reviews have examined how variability in these processing steps affects gene expression and contributes ultimately to phenotypic variability [17,84–86].

1.4.2 Extrinsic sources of variability

Global sources of variation that affect expression of all genes within a cell are extrinsic sources. For instance, both the total amount or concentration of transcriptional activators or cell size affect transcriptional variability (upstream of transcriptional process or transcriptional cascades), greatly increasing variability in certain cases [86]. Cellular population growth dynamics examined experimentally in model systems such as E. coli indicates that cell division contributes to extrinsic variation. Computational models have also been developed that study these effects in yeast. In certain cases, population dynamics accounts for a portion of the extrinsic variability observed in GAL1 expression [87]. Mathematical models of gene expression variability that account for cell-cycle dependent changes in single-cell gene expression are still unable to account for expression variation observed experimentally [88].

More recent studies have examined gene expression variability at a genome-wide scale. Studies in yeast suggest that certain essential proteins involved in specific functions are associated with minimal variation. Another investigation in yeast examined the expression levels of multiple genes that were grouped together based on their co-expression behavior [89]. These groups of co-expressed genes, or *transcription modules*, exhibited distinct differences in expression variability, which suggests underlying gene interactions and regulatory relationships exist among these co-expressed genes and affect gene expression variation.

1.4.3 Gene networks impact transcriptional variability

Genes interact with one another, often in a regulatory manner, to form gene networks that exhibit correlated expression behavior. The organization and structure of these networks result in network properties that affect expression variability. A prominent example in biological systems includes transcriptional cascades–a common gene regulatory feature or motif [90,91]. Experiments involving fluorescent protein showed that expression noise in an upstream gene can be transmitted to a subsequent downstream target gene, adding to the inherent (or intrinsic) noise of that downstream gene and amplifying the noise in that downstream gene's expression [92]. Other computational studies have shown counterintuitive examples where stochastic gene expression behavior within a gene network can lower transcriptional variability [17]. Feedback interactions within gene networks also affect expression variability. For example, a protein encoded by a gene may either negatively or positively influence that gene's expression, or that of an upstream gene. Negative feedback reduces transcriptional variability because fluctuations in expression are pushed back towards a mean or some set point value. On the other hand, positive feedback interactions can amplify expression variation. The generated protein increases gene expression, resulting in more protein production, which subsequently continues to promote its corresponding gene expression. Positive feedback interactions lead to a rapid response in gene expression, analogous to switching a gene from an OFF (unexpressed) state to an ON (expressed) state [90]. Based on such supporting evidence, we find that network structures, in addition to intrinsic and extrinsic sources of variability, should

be considered when analyzing and interpreting transcriptional heterogeneity that affects the phenotypic state of a cellular or, more specifically, a neuronal population.

1.4.4 Single-cell transcriptional heterogeneity in the brain

These concepts provide a conceptual framework within which to view transcriptional heterogeneity not only across cellular populations, but even within systems as complex and heterogeneous as that of the brain. Before considering further how these concepts may help us to interpret transcriptional heterogeneity in the brain, it is important to understand the extent to which transcriptional heterogeneity exists throughout the brain and how such heterogeneity affects our ability to define phenotype, given the pervasive variability that has been reported in individual neurons with nuclei and throughout the brain.

Eberwine and Bartfai [93] revealed transcriptional heterogeneity across individual warm sensitive neurons belong to a neuronal circuit in the Preoptic area of the hypothalamus. Despite the fact that these warm sensitive neurons are functionally similar and are claimed to be identical, based on their electrophysiological behavior and properties, Eberwine and Bartfai have shown that transcript levels of 500 neurotransmitters, hormone receptors, and ion channels vary dramatically across individual warm sensitive neurons. This transcriptional heterogeneity has been observed repeatedly in different regions of the brain as well [94–99]. This variability is not only present at an individual cell level, but extends even to the neural network

function level [100,101]. These results directly conflict with the traditional understanding of how neurons are organized and function in the brain, in which definitions of neuron-types are based upon similarities of anatomical, physiological, and biochemical features and functionality. Reconciling cell-type in the face of the high degree of heterogeneity found in the adult mammalian brain and accurately defining post-development diversity is a difficult challenge [74,102].

Cells remain plastic, able to change adaptively in response to inputs; rather than reaching a final stable state or cell fate they continue in the mature organism to acquire new response capabilities. Thus, the current state of a cell is a product of the cumulative influences or inputs received throughout its history. The transcriptome, represents an essential "snapshot state memory" of a cellular phenotype [21]. The cell's transcriptome adapts to inputs that change the cell, in effect becoming a repository of the cell's input history. In the context of mature post-mitotic neurons, recent experiments demonstrate how cellular experience influences heterogeneity through "neurotransmitter respecification" in adult rat brains, accomplished by modifying the amount of light/dark stimulus received by adult rats [103]. Another example shows *in vivo* reprogramming of circuit connectivity in mature neocortical neurons in mice [104], results that can be considered as examples of extrinsic or external sources of variability driving functional diversity. These results further emphasize the impact that inputs have in shaping functional states of an individual neuron (as described in § 1.2.1). Taken together, these results point towards the

importance of analyzing single neuron heterogeneity in the context of the neuroanatomical environment and connectivity in which individual neurons function. Doing so may help reconcile the disparity between the shared functional purpose of individual neurons within a brain nucleus or neuronal circuit and the stark transcriptional heterogeneity they exhibit.

1.5 Thesis Overview

The previous sections demonstrate that much research has been performed and is on-going towards understanding neuronal function and neuron-type in the brain. Given the importance of the transcriptome in defining cellular function and the transcriptional variability pervasive across individual neurons within a brain nucleus, it is pertinent to ask how such variability affects the regulatory functions of a brain nucleus, presumably composed of homogeneous neuronal components. Although many of the previous examples described in §1.4 analyze transcriptional heterogeneity these studies typically involve the characterization of single neurons dissociated from an in vitro culture or organo-tissue samples. Consequently, such efforts are unable to incorporate the connective and anatomical micro-environment that plays a large part in defining neuronal function and neuron-type, as described in §1.2.1. Consideration of the neuroanatomical and connectivity characteristics of individual neurons may provide functional contexts for interpreting and understanding more clearly the purpose of single-neuron transcriptional heterogeneity pervasive within a neuroanatomical phenotype. *This work focuses on this goal, to interpret single neuron*

heterogeneity in the context of the synaptic connectivity and local anatomical environment to understanding the functional relevance of neuronal heterogeneity.

This dissertation is organized into chapters that investigate the transcriptional heterogeneity of single neurons and interpret the functional relevance of such heterogeneity in the context of the regulatory function of the brain nuclei to which they belong. This is then followed by the development of a methodology that applies a systems identification approach towards identifying gene regulatory networks from single-cell transcriptional data. The functional relevance of single-cell heterogeneity is subsequently explored mathematically in a closed-loop model of the cardiovascular system. The work is concluded with an analysis of another brain nucleus, demonstrating the applicability of the single-cell analysis approach towards identifying organizing principles that reconcile single-cell heterogeneity and brain nucleus function. The chapters are described individually below:

The initial research chapter, Chapter 2 describes the experimental and computational approaches applied in this work. First, motivation and a general description of the animal models used for studying individual neurons are provided. In addition, a description of the experimental techniques applied to collect and investigate the transcriptional response of single neurons is provided. The second half of the chapter provides a detailed description of the analytical techniques used to normalize high-throughput quantitative reverse transcription-polymerase chain reaction (qRT-PCR) gene expression data, which is a core component to this work. Finally, this chapter concludes with a brief review of the multivariate analytical

techniques relevant to high-dimensional data analysis that were applied throughout the work presented here to analyze single-neuron transcriptional heterogeneity.

In Chapter 3, an analysis of the transcriptional responses of single NTS neurons is presented. Despite the high level of transcriptional heterogeneity observed, a multivariate analysis incorporating information regarding the well-established synaptic connectivity that in part defines neurons reveals a molecular organization that suggests an underlying structure to the variability observed in this brain nucleus. The work presented in this chapter has appeared in a journal article by the author [105].

Chapter 4 continues with the analysis of the molecular organization identified in Chapter 3. Because correlated gene expression behavior, identified in the analysis of single NTS neurons, suggests the presence of gene regulatory network influence, Chapter 4 focuses on the development of a methodology to identify underlying gene interaction networks from single-cell transcriptional data. The work presented here deals with the challenge of identifying causal gene interactions amidst the highly variable and continuous nature of single cell transcriptomic qRT-PCR data. Quantitative gene interaction network models from single-cell transcriptomic qRT-PCR data are presented and statistical and simulation analysis is performed to gain insight into how gene network structures contribute to single-cell heterogeneity. This work has been presented in a journal article by the author [106].

In Chapter 5, the functional significance of the results and concepts of molecular organization of single NTS neurons presented in Chapters 3 and 4 is examined using a model that describes mathematically the physiological control

system known as the baroreceptor vagal reflex. A closed-loop model is developed that examines the functional relevance a molecular organization underlying single-cell heterogeneity in the NTS provides and how the types of adaptive transcriptional responses supported by results described in Chapter 3 provide robust regulation of the baroreceptor-vagal reflex and maintenance of cardiovascular homeostasis.

In Chapter 6, the final research chapter in this dissertation, an analysis of single-neuron heterogeneity (similar to the analysis described in Chapter 3) is performed in a distinct brain nucleus, the suprachiasmatic nucleus (SCN). In addition to identifying an underlying molecular organizational framework that reconciles single neuron heterogeneity with overall brain nucleus function, this chapter presents results indicating that the organizing principles revealed from single neuron analysis are not specific to the NTS but can be applied to other regions of the brain as well.

In Chapter 7, the results from Chapters 3-6 are summarized. Potential avenues for future research based on this work are proposed and discussed.

Chapter 2

EXPERIMENTAL DESIGN AND COMPUTATIONAL APPROACHES TO ANALYZE FUNCTIONAL RELEVANCE OF SINGLE-CELL HETEROGENEITY

To gain insight into the molecular organization and functional relevance of single-cell transcriptional heterogeneity in the brain, a combined experimental and computational approach is applied. This chapter provides a rationale for examining two specific brain nuclei, the nucleus tractus solitarius and the suprachiasmatic nucleus. Details regarding the experimental approaches used to perturb the animals, isolate in vivo single neuron samples, and multivariate analytical techniques to analyze high-dimensional transcriptomic data are provided in this chapter.

2.1 Introduction

Post-mitotic neurons in the brain constantly receive and respond to various synaptic and molecular inputs. The responses and adaptations of these neurons to extracellular stimuli are driven, in part, by their morphological features, where "form underlies function" [25]. Based on the importance that a neuron's neuroanatomical environment and connectivity play in defining its functional state, as described in § 1.2.2, considering these key features when analyzing the transcriptomic state of a neuron will provide additional context that will help us connect a neuron's genotype to

its functional phenotype. Towards this goal, it is necessary to analyze neurons and their transcriptional responses *in vivo*. Despite the complexity of the brain and its sophisticated integration within the nervous system, significant advances have been made towards understanding the neural circuits and networks in which nuclei in the brain function and the physiological functions they regulate [107,108].

Using well-characterized neural systems, it is possible to trigger transcriptional responses in specific neuronal populations under controlled experimental conditions. However, due to the high-dimensional and highly variable nature of the transcriptomic state of individual neurons, as described in §1.4, it is necessary to apply both experimental and computational methodologies to manipulate, analyze, and interpret the transcriptional state of neurons in their neuroanatomical and functional context. Therefore, an integrated experimental and computational approach is employed in this dissertation to determine the functional relevance of transcriptional heterogeneity in the brain. Details regarding the experimental and computational approaches employed in this work are provided in this chapter, which is divided into four main sections:

i. Introduction and rationale for the study of two specific brain nuclei, the *nucleus tractus solitarius* (NTS) and the *suprachiasmatic nucleus* (SCN) and the challenges functional heterogeneity of individual neurons poses in understanding the functional state of a single neurons as it pertains to the larger phenotypic function of these nuclei.

ii. Overview of the animal models and physiological perturbations applied in these experimental systems to trigger nuclei-specific responses.

iii. Summary of the experimental techniques employed in this dissertation, including a review of the laser capture microdissection technology, the key experimental method utilized in this work for the analysis of single neurons in their neuroanatomical context.

iv. Review of the various analytical and multivariate analytical techniques used in the analysis of high-throughput transcriptomic data.

Finally, the chapter concludes with a brief discussion of the key points raised and how they pertain to the remaining research chapters in this dissertation.

2.2 Brain Nuclei of Interest

2.2.1 The Nucleus Tractus Solitarius

The nucleus tractus solitarius (NTS) is the principal sensory integrative center for the internal organs of the periphery, i.e. *viscera*, and regulates physiological functions to maintain cardiovascular homeostasis. Extensive characterization of its functional role [34,107,109–116] and neuroanatomical connectivity [117–125] make the NTS an ideal candidate in which to study single neurons in the context of their

functional connectivity. Consequently, investigation of NTS neurons constitutes a majority of the work presented in this dissertation.

The NTS is a brainstem nucleus located in the lower-half of the brainstem (*medulla oblongata*) and consists of the neuroanatomical phenotype defined by medium sized, fusiform neurons that form a column in the dorsal medulla. These neurons surround and are innervated by a tract, the tractus solitarius (ts), that conveys afferent inputs from two cranial nerves (CN), the glossopharyngeal (CN IX) and vagus nerve (CN X), which relay sensory information from visceral organs. Multiple afferent inputs converge onto NTS neurons and originate from multiple sensory neurons including, but not limited to *i) baroreceptors*–a type of mechano-stretch sensory neurons, located in the carotid sinus and aortic arch, that send electrical pulses (action potentials) when they sense a change (and rate of change) in arterial blood pressure, *ii) chemoreceptors*–sensory neurons also located in the carotid and aortic bodies that detect changes in oxygen, CO_2 and pH changes in the blood, *iii) cardiopulmonary receptors*–a sub-type of baroreceptors that respond to lower blood pressures and are associated with the regulation of blood volume, and *iv) lung stretch receptors*–sensory neurons that respond to changes in lung volume during the course of the inspiration-respiration cycle.

The NTS acts as a central relay where the afferent inputs from the sensory neurons related to the cardiovascular and respiratory state of the body are integrated with other viscerosensory signals. In addition, the NTS receives synaptic inputs from higher-order brain structures through reciprocal connections shared with other brain

nuclei. These connections include the paraventricular and lateral nuclei of the hypothalamus, the rostral ventrolateral medulla (RVLM), caudal raphe nuclei, and area postrema [107]. NTS neurons also project to other nuclei within the medulla including the dorsal motor nucleus of the vagus (DMV) and the nucleus ambiguus (NA), which act as the sources of parasympathetic outflow affecting cardiac functions [38,126–130]. Interconnections among the NTS, CVLM, RVLM, DMV, and NA are part of a larger neural pathway, i.e. *reflex arc*, known as the baroreceptor reflex, which provides autonomic regulation of cardiovascular parameters such as heart rate, cardiac output, arterial resistance, and blood pressure in order to maintain cardiovascular homeostasis.

2.2.1.1 The Baroreceptor Reflex

The baroreceptor reflex (i.e. baroreflex) is a physiological control system that provides negative feedback regulation of arterial blood pressure [107]. The baroreflex is primarily responsible for short-term regulation of arterial blood pressure. The synaptic inputs that terminate in the NTS, with the exception of the lung-stretch receptors, are key components of the baroreflex. Axons of baroreceptors in the aortic arch travel along the glossopharyngeal nerve while baroreceptors in the carotid sinus travel along the vagus nerve, both of which converge on the NTS. The integration of these inputs in the NTS subsequently triggers a signaling cascade that regulates the activity of the sympathetic (SNS) and parasympathetic nervous systems (PNS). Sympathetic tone is regulated via NTS excitatory projections to the CLVM, which in-

turn sends inhibitory fibers to the RVLM, which is the primary regulator of the SNS. The SNS supplies innervates cardiovascular targets such as the heart and arterioles. When blood pressure rises, synaptic inputs from the baroreceptors will activate NTS neurons, which activate CVLM neurons, which in turn inhibits the RVLM and decreases sympathetic outflow. Alternatively, some NTS neurons project excitatory fibers that innervate the DMV and NA to regulate the PNS. Like the SNS, the PNS innervates the heart and increases in PNS activity inhibits cardiac pace-making cells in the heart, reducing heart rate. When blood pressure rises, PNS activity is increased to reduce heart rate and contractile forces in the ventricles of the heart [130–132], and as a consequence, blood pressure.

Because the NTS is the primary integrative center of cardiovascular sensory signals, it has been defined as the homeostatic control center of the baroreflex, regulating sympathetic and parasympathetic tone to modulate effector functions and maintain some nominal blood pressure set point [133–135]. Experimental manipulations on the reflex support its essential role in baroreflex integrity. For example, targeted manipulations of A2 neurons, a noradrenergic cell group embedded within the NTS that produce the neurotransmitter norepinephrine, result in a shift in the blood pressure set point in a rodent animal mode [34]. Conversely, electrical or pharmaceutical stimulation of the middle (i.e. medial) region of the NTS evokes decreases in heart rate, blood pressure, and sympathetic nerve activity [136]. Stimulation of NTS neurons with angiontensin II (Ang II), a neuropeptide whose corresponding receptor angiotensin II type 1 receptor (AT1R) is expressed heavily by

NTS neurons, leads to increases in blood pressure as well [137]. Animal models of hypertension have also demonstrated shifts in the molecular characteristics of the NTS in animal models of hypertension. Increases in pro-inflammatory molecules, including Ang II, are associated with hypertension pathology in animal models [111,138,139]. Moreover, Khan et al., demonstrated that a complex and coordinated transcriptional responses occurs in the NTS in response to changes in blood pressure [140] using an established experimental protocol involving an acute hypertensive challenge on rats. These results support the role that transcriptional state and its dynamics play in driving neuronal function, specifically within the context of NTS neurons and their role in regulating blood pressure.

2.2.1.2 Functional heterogeneity in the NTS and baroreceptor reflex

NTS neurons exhibit nonlinear signal processing capabilities as part of its integrative role in regulating cardiovascular homeostasis. This nonlinear behavior is exemplified at the single-neuron level. Despite the strong pulse-rhythmic inputs that are supplied by baroreceptors, single neurons do not encode this behavior in any obvious manner. In vivo recordings of NTS neurons show neuronal activation (as indicated by the generation of action potentials) in response to direct electrical stimulation of an incoming nerve or stretch-induced activation of the baroreceptors. But rarely do individual NTS neurons exhibit bursting patterns that align with the pulse-synchronous behavior of baroreceptor neurons [141]. This behavior conflicts with the general expectation that neurons belonging to a particular phenotype, such as

cardiovascular NTS neurons, should display similar functional behavior. Reconciling this nonlinear heterogeneous behavior, in the context of the single neuronal transcriptional heterogeneity, is the subject of Chapters 3-5.

2.2.2 The Suprachiasmatic Nucleus

The principal biological clock in mammals resides in the suprachiasmatic nucleus of the hypothalamus. SCN neurons express genes and generate electrical signals in a coordinated and oscillatory manner which ultimately synchronize physiology and behavior in a daily program that allows coordinated anticipation of the 24 hr light/dark cycle. Thus, the SCN is known as the master circadian pacemaker (*circa*–about , *diem*–day). This nucleus is a paired neuronal structure that surrounds the third ventricle, a central fluid-filled cavity in the brain, just above the optic chiasm, where the optic nerves projecting from each retina cross. Within each side of this nucleus, or unilateral SCN, neurons are organized into two anatomic subdivisions: *i)* the "core"–the underside or ventral region, and *ii)* the "shell"–the upper side or dorsal region. Neurons within the core project densely to the shell while neurons in the shell project sparsely to the core [108,142]. In addition to their anatomic organization, SCN neurons are defined by their neurochemical content. Immunohistochemical studies have demonstrated that neurons in the core contain a neurotransmitter known as vasoactive intestinal polypeptide (VIP). Neurons in the shell contain another neurotransmitter known as arginine vasopression (AVP). Most SCN neurons,

regardless of their anatomic region, co-express gamma aminobutyric acid (GABA), a prominent inhibitory neurotransmitter pervasive throughout the brain [143–148].

The SCN receives synaptic inputs from the retinohypothalamic tract, which is composed of axons of photosensitive retinal ganglion cells. In response to light or photic inputs received by the retina, glutamate and pituitary adenylate cyclase-activating polypeptide (PACAP) is released at synaptic contacts in the SCN. The neuropeptide PACAP is known to have a modulatory role, enhancing the effects of glutamate, which depolarizes the neuronal membrane resulting in an influx of calcium. This influx triggers a complex signaling cascade involving kinases resulting in the phosphorylation of cAMP response element-binding protein (CREB), a transcription factor that binds to the calcium/cAMP response elements (CRE), a DNA sequence found within the promoter region of genes, and activates gene expression [149–151].

Output signals generated by the SCN coordinate and synchronize processes in other brain regions and peripheral tissues. Synchronization is achieved through diverse pathways including hormonal factors and autonomic efferent neural connections within the brain [152,153] and to the periphery, which allow for direct communication between the SCN and peripheral tissue [153]. Through sympathetic efferent connections to various hormone producing glands, such as the pineal gland, and adipose tissue, the SCN is able to control directly hormonal secretion and body temperature [108,153]. Additional sympathetic efferent outflow from the SCN target the kidney, bladder, spleen, and hormone producing glands such as the thyroid gland, located in the neck, and the adrenal gland, located above the kidneys. The SCN is also

involved in parasympathetic innervation of the liver, pancreas, and submandibular gland in the lower jaw [108,153].

While nearly all cells and organs exhibit their own periodic behavior, the central role the SCN plays in synchronizing circadian rhythms in mammals has been verified through extensive experimental studies. Lesions of the SCN result in the loss of circadian rhythmicity in behavior and endocrine production in rodents [150]. Rats that have had lesioned SCNs have had their circadian rhythms restored when fetal SCN tissue is implanted. Further, in animals genetically engineered to have abnormally short or long circadian rhythms, implanting SCN tissue modulated their circadian periods, indicating that circadian rhythms were determined by the genotype of the SCN donor, rather than the SCN-lesioned host [154].

2.2.2.1 Functional heterogeneity in the SCN

As the ability to synchronize behavior and physiological processes by the SCN is dependent on the coherent and robust signals it generates, it is surprising that individual SCN neurons exhibit autonomous circadian oscillations [142]. This is reflected not only in multi-electrode recordings of dispersed SCN neurons, but also in the period of their underlying transcriptional programs that provide the basis of their oscillatory behaviors. Despite the established neuroanatomical and biochemical organization of SCN neurons previously described, cross-species analysis and transcriptomic studies of the SCN suggest a greater complexity than supported by our current understanding. This complexity is studied through the use of an established

experimental animal model described in § 2.3.2. The analysis of the transcriptional heterogeneity of single SCN neurons is the subject of Chapter 6.

2.3 Animal Models and Experimental Perturbations

2.3.1 Acute hypertension challenge

The use of carefully selected animal models and appropriately designed experimental perturbations enables us to conduct controlled studies to investigate the transcriptional responses of individual neurons to specific, controlled, physiological perturbations. Rat models such as the Sprague Dawley rat provide an extremely useful animal model with which to study many functional aspects of the brain in health and disease. The reason for using Sprague Dawley rats in this work is five-fold:

1. The rat shares similar neural and cardiovascular structures and connectivity to those in humans.

2. The rat has been thoroughly characterized, with its genome having been sequenced completely.

3. The rat brain is large enough to enable identification and microdissection of specific brain structures of interest and has been used extensively to investigate the neurogenic aspects of blood pressure regulation and hypertension development.

4. Rat brain connectivity and function with respect to blood pressure regulation is well-characterized.

5. The Animal Facility at Thomas Jefferson University have established protocols and experience with both rats and mice for the purposes of investigating blood pressure and circadian rhythm regulation.

To investigate the transcriptional responses of individual NTS neurons within the context of their functional role and connectivity, we used the acute hypertensive model previously used by Khan et al [140], to investigate the dynamics of the transcriptional responses in NTS tissue. The following excerpt summarizes the acute hypertensive perturbation applied:

> Animals were anesthetized with isoflurane vaporized in O_2 (5% induction; 1% maintenance), and one femoral artery and vein were cannulated (PE-50 tubing) via a small medial incision for measurement of arterial pressure and infusion of [Phenylephrine] drug, respectively. The cannulas were run subcutaneously to an exit incision between the scapulas. The leg wound was sutured and topical anesthetic (lidocaine) was applied to both skin incisions.
>
> Following the surgery and 1-h recovery, characterized by stable, normal resting blood pressure and heart rate, either 1 mL/hr sailine (control) or ~200 μg/mL phenylephrine (~1 mL/hr) was infused [into the rat]. The latter was manually tittered to maintain an increase of [40] mmHg diastolic arterial pressure. [The] experimental design used a standard 60 min acute hypertension experimental treatment… [Following the 60 min treatment], rats were rapidly decapitated and brains were quickly removed…

Following rapid decapitation, brain samples were placed in ice-cold artificial cerebral spinal fluid (ACSF). Brainstem samples were then quickly isolated manually from the rest of the brains and embedded and frozen in optimal cutting temperature (OCT) compound, which provides a convenient matrix for subsequent tissue slicing. OCT-embedded brainstem samples were stored at -80˚C.

2.3.2 Circadian phase shift response

The phasic behavior of the cellular components of the SCN are due, in part, to the negative feedback transcriptional regulatory cycle that results in the oscillatory expression patterns of key circadian genes [142,149]. Previous experiments have repeatedly shown that the circadian rhythms that resides in the SCN is susceptible to a phase shift induced by light at particular times throughout the 24 hour light-dark cycle [149,155]. Moreover, prior studies have shown that coordinated gene expression behaviors, or multi-genic responses, underlie this light induced phase-shift [149]. This has been demonstrated in unbiased global microarray studies [156,157]. This is evidenced by the induction of multiple immediate early genes (IEGs) such as *Fos* and *Jun* and genes involved in the circadian oscillatory cycle including *Per1* and *Per2* [158,159]). These IEGs and circadian genes regulate directly or indirectly gene expression of downstream target genes that code for neuropeptides, membrane receptors, and signaling pathways facilitating intra- and inter-cellular communication.

We have previously used a light-induced phase shift model in mice to study the multi-genic response of SCN tissue that drives this phase shift in circadian rhythms, as described by Zhu et al. (2012)

> 4-6 week old male C57BL/6J mice were purchased from Charles River (Wilmington, Massachusetts). The animals were housed with 12-hour light, 12-hour dark cycles. During the light phase of the lighting cycle, light (150 lux) was provided by warm white fluorescent bulbs. Animals were entrained for 10 days with free access to food and water. On the day of experiment [i.e. physiological perturbation], animals were given a one-hour light exposure (150 luck of white light at ZT (Zeigtgieber) 14, which is 2 hours into their regular dark period, and sacrificed one

> hour later at ZT 15. SCN's were also collected from non-light-pulsed animals at ZT 15… Animals were euthanized by CO_2 asphyxiation in prevailing lighting condition (dim red light for ZT 15). Their brains were extracted, and the hypothalamic blocks [where the SCN exists] were dissected. Blocks were embedded in OCT compound, and frozen on dry ice.

All animals were housed, fed, and handled according to pre-approved protocols approved by the Thomas Jefferson University Institutional Animal Care and Use Committee.

These experimental approaches represent only a portion of the experimental aspects required to isolate and analyze the transcriptional state of single neurons. Multiple steps are involved in order to obtain individual neuron samples including *i)* cryosectioning, *ii)* cell-type visualization, and *iii)* single-cell isolation via laser capture microdissection. Before these experimental methodologies are discussed, however, it is necessary for one to have a basic understanding of the anatomical planes, as they apply to the rat and mouse, in order have an appropriate frame of reference to understand how neural tissue is handled for single neuron sample collection.

2.3.3 Anatomical planes and terminology

Before describing the techniques involved in collecting brainstem slices, it is pertinent to define the appropriate terminology used to describe anatomical locations and planes of the rat and mouse. This reference terminology will clarify for the reader the specific physical orientation in which brain tissue samples were cut and collected. Unlike humans, in which the brain and brainstem are oriented approximately 90

degrees from each other, these two sections lie along a single axis in the rat. The nose-end (front) of the rat is defined as the *rostral* end, while the tail-end (rear) is defined as the *caudal* end. The underside of the rat is defined as the *ventral* side while the top side of the rat is defined as the *dorsal* side. In addition, three basic reference planes are used to further describe anatomical positioning throughout the rat, which include, *coronal*, *saggital*, and *horizontal* planes. The coronal plane divides the rostral and caudal sections of the rat, the saggital plane divides the left and right sides of the rat, and the horizontal plane divides the ventral and dorsal side sections of the rat.

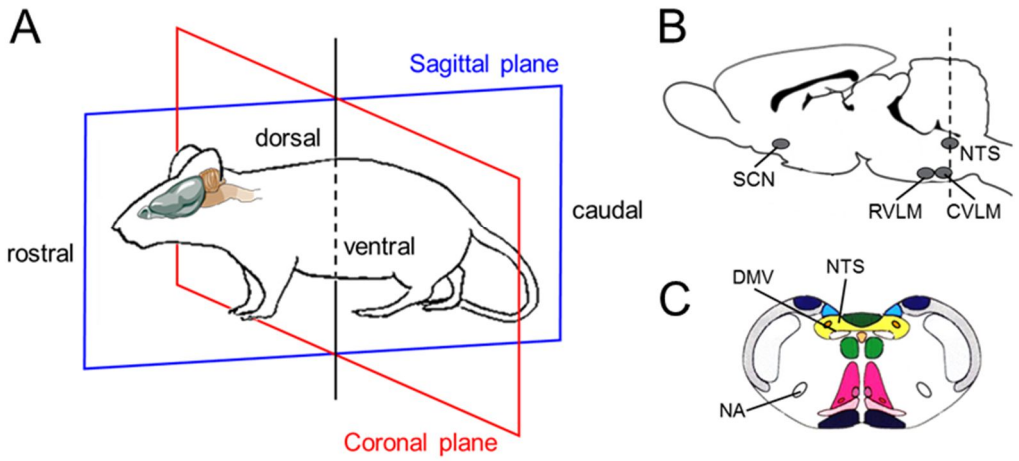

Figure 2.1 Anatomical planes of the rat. (A) Anatomical planes and terms illustrated for reference. (B) Sagittal cross-section of a rat brain, with a few brain nuclei (grey ovals) included for reference. (C) Coronal cross-section of brain stem, corresponding to the dashed-line in subpanel B. Images modified from [160,161]. Abbreviations include NTS (nucleus tractus solitarius), RVLM (rostral ventrolateral medulla), CVLM (caudal ventrolateral medulla), SCN (suprachiasmatic nucleus), NA (nucleus ambiguus), DMV (dorsal motor nucleus of the vagus).

2.4 Experimental Methods

2.4.1 Tissue cryosectioning

In order to collect sections of the brainstem, the embedded brainstem blocks were sectioned at 10μm using a cryostat (Microm Microtome Cryostat HM 505 E) and then thaw mounted onto glass slides (Fisherbrand™ Superfrost™ Plus Microscope Slides).

2.4.2 Rapid immunofluorescent staining

To preserve RNA, immunostaining is performed within 30 minutes using an accelerated protocol. This protocol is a variation of previous protocols tailored specifically for laser capture microdissection of samples. Slides are first fixed in ice-cold acetone and hydrogen peroxide (Sigma–Aldrich) solution mixture (50 ml: 50 μl) for 1 minute, then blocked and permeabilized with a blocking buffer consisting of PBS (1X) and 2% (m/v) BSA (lyophilized powder, ≥ 96%, Sigma–Aldrich) for 30 seconds. Afterwards, brain sections were incubated with an appropriate primary antibody solution (1:25 – 1:50 primary antibody:blocking buffer ratio, depending on the primary antibody) for 2 minutes at room temperature. Slides were then washed and incubated with a secondary antibody (typically at a 1:50 antibody:blocking buffer ratio) for 3 minutes at room temperature in the dark. Subsequently slides were gently rinsed with PBS followed by a series of five dehydration steps involving 30s ethanol baths of increasing concentration (70%, 75%, 95%, 100%, 100%). Finally, stained

slides were dehydrated in Xylene for 5 min. The dehydration steps are critical to ensure that any residual water or moisture within the tissue is removed or displaced as excess water and moisture within the sample can negatively affect the laser-capture process [162].

2.4.3 Laser capture microdissection

Originally developed at the National institutes of Health (NIH), laser capture microdissection (LCM) is an experimental technique designed for isolating highly pure cell populations (or individual cells) from some complex heterogeneous tissue sections. By taking advantage of the molecular profiling technologies available, LCM would enable one to characterize the molecular fingerprint of an individual tissue lesion, specific cell population, or individual cell sample, which would be beneficial for diagnosis and prognosis of disease conditions, for example.

Two main classes of LCM currently exist, which include infrared (IR) capture systems and ultraviolet (UV) cutting systems. While the laser technology distinguishes these two classes, there are three principle factors that underlie LCM technology. These components include *i)* visualization of the cell(s) of interest via microscopy, *ii)* transfer of laser energy to a thermolabile polymer leading to either the formation of a polymer-cell composite (IR-laser) or phot volatilization of cells surrounding a selected area (UV system), and *iii)* removal of the cell(s) of interest from the heterogeneous tissue section [33]. This technique is compatible with various types of samples and has been applied successfully for the molecular profiling of a wide range of tissue types

including tumors, liver, and brain sections [163]. Moreover, this technique can obtain cells with a precision of 3-5 μm. Given the single-cell focus of this work, an IR-laser LCM was used due to its precise nature and ability to capture individual cells from heterogeneous tissue sections while maintaining cellular morphology, proteins, DNA, and RNA of the collected cell(s) [33,164,165]. While the UV laser is able to microdissect thicker tissue sections up to 200 μm thick, the UV laser is currently not precise enough to cut an individual cell sample.

LCM incorporates an inverted light microscope and a near-IR laser for collecting the desired cells. After direct visualization of the sample, a laser pulse would be triggered, which would activate a thermoplastic film that expands and binds to the cell of interest and create a polymer-cell composite. This composite would then be lifted from the tissue sample, shearing the polymer-embedded cell from the tissue section.

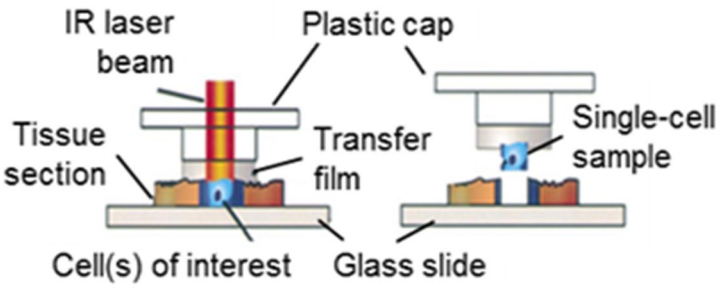

Figure 2.2 Laser capture microdissection schematic. The process to capture a single cell from a tissue sample is illustrated above. The IR laser melts the thermolabile surface of the cap, which is in contact with the tissue sample. Once the thermolabile surface bonds with the cell of interest, the cap is pulled up from the tissue and the individual cell is gentle removed from the tissue sample. Image modified from [166].

Despite its remarkable precision, issues of cross contamination of LCM samples have been raised [167], particularly due to the heterogeneous nature of tissue samples, particularly within the brain, and the micro-length scales required for acquiring individual cell samples precisely. To address these concerns, we have conducted quality control studies to quantify the amount of non-specific cell contamination may occur in LCM-acquired samples and how this may affect gene expression measures at the single-cell level. These experiments and results are described in greater detail in Chapter 3.

2.4.4 RNA extraction, reverse transcription, and pre-amplification

In order to measure gene expression from an individual cell for subsequent reverse transcription and amplification via qRT-PCR, individual cell samples were lysed directly on the cap, using a lysis buffer solution. A lysis buffer solution (0.5 μL: 5 μL

solution of Lysis Enhancer:Resuspension Buffer; Life Technologies, Grand Island, NY) is added onto the single cell on the cap, incubated to lyse the cell and release the RNA. The sample is subsequently cooled on ice before storage at −80°C for subsequent reverse transcription, which would convert the RNA into cDNA. The cDNA generated provides the template for amplification.

2.4.5 Quantitative PCR using the BioMark™ platform

To measure the transcriptomic state of a functionally relevant set of genes, we used the BioMark™ platform (Fluidigm®, South San Francisco, CA). The BioMark™ is a high-throughput quantitative PCR (qPCR) platform that enables the simultaneous measurements of 96 gene assays across 96 samples (i.e. single neurons) for a total of 9,216 simultaneous reactions. This platform has been used extensively to transcriptionally profile a wide variety of biological samples across multiple length scales [32,78,95,168–170] with minimal technical variation [105,171]. Since the two nuclei (i.e. the NTS and SCN) investigated in this work regulate distinct physiological functions, two distinct gene sets were used to assay individual NTS and SCN neurons. Using prior knowledge derived from global microarray analysis of gene expression in the NTS [140] and in the SCN [83], focused sets of genes were selected based on their functional relevance in blood pressure regulation and involvement in the transcriptional programs associated with circadian regulation. Additional details are outlined in Chapters 3 and Chapters 6, respectively. Quantitative measures of gene

expression are reported as raw C_t values, which are calculated by the Real-Time PCR Analysis Software (Fluidigm®).

2.4.6 Primer design

Oligonucleotide forward and reverse primer sequences for the respective gene sets described in the previous section were designed and corresponding probes were selected using the Roche Universal Probe Library and used for the amplification process. Intron-spanning PCR primers and probes for every assay were designed using the Universal Probe Library Assay Design Center (www.universalprobelibrary.com), provided by Roche. This tool uses the Primer3 algorithm [172] to generate the intron-spanning primer sequences. Intron-spanning primers are desirable because they distinguish between mRNA-derived cDNA and any genomic DNA, which does not reflect transcript levels of interest, present in the sample.

2.5 Computational Methods

Following sample and data acquisition, it is critical to first assess the quality of and normalize the high-dimensional transcriptional data obtained. Raw C_t values generated by the BioMark™ must be normalized to enable an appropriate comparison of expression across genes and across samples by removing any systematic differences that could affect gene expression measures. Systematic differences such as unequal sample loading, non-identical reverse transcription efficiencies, RNA quantification errors, or other unforeseen technical causes may all affect initial sample

concentrations prior to PCR amplification. In the following sections, the normalization methodologies applied in this work are described.

2.5.1 Data normalization

The importance of selecting a proper normalization technique cannot be overstated. It is critical to normalize data in a manner that does not inadvertently add additional biases to the data. The addition of additional biases would result in an incorrect analysis and interpretation of the data [173–176]. While numerous methodologies have been developed to normalize gene expression data, a comprehensive review of such strategies is beyond the scope of this work. However, a brief review of some traditional strategies involved in gene expression normalization is given to provide additional context to the data processing procedures used in this work.

Several strategies for gene normalization have been developed including data-driven techniques and baseline reference normalization techniques, each type of technique having specific advantages and limitations. A traditional, data-driven technique that is used for normalizing qRT-PCR data involves mean-centering gene expression data, which shifts the expression distribution of a particular gene, across samples, about the mean. Thus for some gene *g*, the sample mean of the expression value of gene *g*, is subtracted from each individual g_i value, where *i* represents the index of a particular sample. The result of mean-centering is the ΔC_t value (Equation

2.1). These scaled expression values can now be used for subsequent analysis such as treatment comparison, for example. Comparing ΔC_t values of samples across treatment conditions *j* and *k*, for instance, would involve the straightforward calculation of the difference between $\Delta C_t^{g_{ij}}$ (the scaled expression of gene *g* within the i^{th} sample from treatment *j*) and $\Delta C_t^{g_{ik}}$ (the scaled expression of gene *g* within the i^{th} sample from treatment *k*), which would result in the $\Delta\Delta C_t^{g_{ijk}}$ [171].

$$\Delta C_t^{g_i} = C_t^{g_i} - mean(C_t^g) \qquad 2.1$$

$$\Delta\Delta C_t^{g_{ijk}} = \Delta C_t^{g_{ij}} - \Delta C_t^{g_{ik}} \qquad 2.2$$

This technique assumes that the data being normalized can be appropriately described with a normal distribution. As the raw C_t data represents the log-transformation of the number of doublings that occurred during the amplification process, the log-transform makes the expression distribution more symmetric, and enables one to assume that the distribution of the data can be described by statistics characterizing a Gaussian distribution, which has been shown to be a fair assumption [75].

Mean-centering expression data scales the data, preventing only a few genes that are highly expressed from dominating subsequent results [176]. Because gene expression at the single-cell level has repeatedly exhibited large variation, as described in § 1.4, a median-centering approach is used in this work as it is less susceptible to

outlying gene expression values, which would have a greater effect on the mean than the median and skew the scaled data.

In addition, $\Delta C_t^{g_i}$ values are somewhat non-intuitive because a negative $\Delta C_t^{g_i}$ value indicates that the expression of gene g in sample i is greater than the mean expression level of gene g. Since C_t values represent the number of cycles required for the fluorescent detection, a large C_t value represents a low initial amount of cDNA and vice versa. Thus the C_t value is inversely related to the initial amount of cDNA in the sample and ultimately negative $\Delta C_t^{g_i}$ for sample i must be interpreted as having a higher than average expression level. To ease the interpretation of scaled gene expression data, we used Equation 2.3 to obtain median-centered expression data:

$$-\Delta C_t^{g_i} = mean\left(C_t^{g}\right) - C_t^{g_i} \qquad 2.3$$

An additional method that has been used is a geometric mean-based normalization. Similar to the median-based normalization, the geometric mean, defined by Equation 2.4 is not affected as greatly by outlying values or abundance differences between different genes.

$$\bar{x}_{geo} = \sqrt[n]{\prod_{i=1}^{n} x_i} \qquad 2.4$$

Here, n represents the number of genes used to determine the geometric mean and x_i represents the C_t value of the i^{th} gene. This method has been used to normalize microarray data as well as BioMark^{TM} data [169,177].

Alternatively, a widely-used baseline reference approach for normalizing high-throughput expression data, such as microarrays and qRT-PCR data, involves scaling gene expression data to an internal reference or "housekeeping" gene. This gene acts as an internal control that should not change, or change minimally, in response to perturbations applied to the sample. Subtracting expression levels of the housekeeping gene from expression levels of the gene of interest will scale the expression level and account for any offsets that may have occurred due to unequal loading across samples and so forth. Although the use of an internal reference gene is widely used, a major assumption made when using an internal reference is that this reference exhibits stable expression behavior. Previous work has shown that this assumption for several traditionally used housekeeping genes may vary considerably [174,178,179]. To account for such potential variability in internal reference genes, several methods have been developed, two of which will now be discussed below.

2.5.1.1 Reference gene selection methods

Given the potential variability in housekeeping gene expression behavior, it is important to determine whether or not these genes do indeed exhibit stable expression. Two methods that have been widely used, and which I have applied in this work, are

geNorm [174] and NormFinder [180]. geNorm, is a normalization approach developed originally for normalizing microarray data.

2.5.1.1.1 geNorm

Because the internal reference (housekeeping) gene approach assumes stable expression behavior of this gene, prior knowledge of another reliable measure to normalize the internal reference is required, in order to remove any nonspecific variation. Unless the same experimental conditions are conducted, allowing one to determine what gene is the most stable for those specific conditions, additional prior knowledge would be required to verify the stability of the gene that would then be used to normalize the "internal reference" gene, resulting in a circular problem. Therefore, Vandesomplete et al. developed an approach that would determine the expression stability of multiple control genes based on non-normalized expression levels. The method then identifies which combination of control genes provides the most stable normalization factor.

The underlying principle of this approach is that the expression ratio of two "ideal" internal reference genes would be identical across samples, regardless of condition or cell type. Variation in the expression ratio that may exist across conditions would therefore suggest that one or both of these reference genes are not stable. This approach can be applied across multiple pairs of potential reference genes included in the experimental design. Using this approach, Vandesompele et al. [174]

defined a gene-stability measure, *M*, that quantifies the stability of a potential control gene, as measured against the expression behavior of other possible control genes. Since geNorm was developed originally to analyze microarray fluorescence intensity data, which requires the log-transformed data, adjustments to the approach are required making this approach suitable for the normalization of raw C_t data generated by the BioMark™, as outlined below:

1. Calculate set of expression ratios A_{jk}. For all possible pairwise combinations of genes j and k, calculate expression ratios across all samples

$$A_{jk} = \{(C_{t-ij} - C_{t-ik})\}_{i=1\rightarrow m} \quad 2.5$$

   Where $j \neq k$. This will result in a vector of length m, where m is the number of samples.

2. Calculate pairwise variation value V_{jk}.

$$V_{jk} = \sigma(A_{jk}) \quad 2.6$$

3. Calculate the internal control stability measure, M_j. The stability measure is defined by Vandesompele et al. as the average of pairwise variation values V_{jk}. Because the same gene across samples were not used in the calculation of A_{jk} ($j \neq k$), a normalization factor of *n-1* was used in the calculation of M_j.

$$M_j = \frac{\sum_{k=1}^{n} V_{jk}}{n-1} \quad 2.7$$

These steps were applied to a predetermined set of potential housekeeping genes, which have exhibited stable gene expression behavior in previous work [181–

183]. This procedure, as developed originally, was performed iteratively, such that the gene with the highest M_j value (i.e. the least stable gene) was removed and the three steps were repeated. We applied this approach to our BioMark™ data exploring the expression states of single brainstem neurons from hypertensive and normotensive rats.

In addition to identifying reference genes with minimal expression variation, Vandesompele et al. proposed using multiple reference genes for expression normalization by applying the geometric mean of the genes found to be most stable (i.e. lowest M_j). Based on their analysis of RT-PCR microarray data measured from various types of human tissue, Vandesompele et al. recommend a range of 3-9 internal reference genes be used to calculate the geometric mean for subsequent gene expression normalization [174].

The use of multiple internal reference genes reduces variation in the normalization (i.e. centering) factor and therefore minimizes systemic variation in the expression data set. In the context of the C_t data generated by the BioMark™ (Fluidigm®) the arithmetic mean of the raw C_t values is used. Because C_t values represent the log-transform of the expression fluorescence intensity of the qRT-PCR reaction the geometric mean of the log-transformed microarray fluorescence data is equivalent to the arithmetic mean of the raw C_t values.

$$let\ a_{ij} = fluorescence\ intensity\ of\ RT - PCR\ reaction$$

$$\bar{a}_{geo} = \sqrt[n]{\prod_{i=1}^{n} a_{ij}} \qquad 2.8$$

$$\log(\bar{a}_{geo}) = log\left(\sqrt[n]{\prod_{i=1}^{n} a_{ij}}\right) \qquad 2.9$$

$$\log(\bar{a}_{geo}) = log\left(\prod_{i=1}^{n} a_{ij}\right)^{\frac{1}{n}} \qquad 2.10$$

$$\log(\bar{a}_{geo}) = \frac{1}{n}\sum_{i=1}^{n} \log(a_{ij}) \qquad 2.11$$

The derivation above shows that the geometric mean of the fluorescence data over *n* samples is indeed the arithmetic mean of the log-transformed data.

2.5.1.1.2 NormFinder

The second method used in this work to identify internal reference genes is NormFinder [180]. However, in addition to determining the overall expression variation of potential reference genes, Andersen et al. designed this method to determine if a gene of interest exhibits any systematic variation across sample subsets. In this approach, Andersen et al. apply a model-based approach to estimate expression variation. Here, the log-transformed measured gene expression for the gene *i* in the j^{th} sample in group g (y_{igj}) is described by the following model:

$$y_{igj} = \alpha_{ig} + \beta_{gj} + \varepsilon_{igj} \qquad 2.12$$

Where α_{ig} represents the general expression level for the i^{th} gene in the g^{th} group. The variable β_{gj} represents the amount of mRNA in the j^{th} sample in the g^{th} group and ε_{igj} represents the random variation, characterized by a normal distribution with mean zero and some variance σ_{ig}^2, due to biological and experimental factors. As part of this methodology, both the intra- and inter-group expression variation is estimated from the sample dataset. These two measures of variation are then used to define a stability score of the internal reference. This approach, (http://moma.dk/normfinder-software), was used as an alternative and independent method to verify the stability of possible internal reference genes.

2.5.2 Multivariate techniques to analyze high dimensional transcriptomic data

Concurrent to the completion of this dissertation, numerous multivariate techniques were being developed and continue to be refined to analyze the copious amounts of high-dimensional data being generated from high-throughput and –omics scale technologies. Several approaches have been applied and developed to identify underlying patterns or clusters of gene expression. These patterns of upregulated and downregulated expression behavior of genes, correlated expression patterns, and alternative organizational patterns of genes across individual cells provide insight into the transcriptional responses of cells to the inputs they receive. Because a plethora of multivariate analytical methodologies exist and continue to be developed and be

refined, a thorough review of such methods is beyond the scope of this work. However, we provide a brief review of some of the more widely used and recently developed analytical approaches designed to identify underlying patterns in transcriptomic data.

2.5.2.1 Clustering-based algorithms

Clustering-based algorithms are well-established approaches used in single-cell analysis that have been used to identify molecular phenotypes within a heterogeneous population. Clustering is iteratively performed to either agglomerate samples into a comprehensive group or divide samples into stand-alone classifying groups. Ultimately, both types of clustering algorithms partition samples into groups from the initial data set based on some measure of distance or dissimilarity between two samples, which in this case will be determined from the transcriptomic profiles of the single-cell samples collected. Euclidean, Pearson correlation, or Spearman rank correlation distances are typically used as a dissimilarity measure for clustering analyses [184].

2.5.2.2 Data dimensionality reduction techniques

Principal component analysis (PCA) is a mathematical technique that belongs to a larger group of unsupervised learning approaches and is used to identify hidden structures from unlabeled data. PCA has a wide range of applications including analysis of high-throughput qPCR and single-cell qRT-PCR data, RNA-seq data and

other high-dimensional datasets [185]. PCA reduces data dimensionality while retaining most of the variation in the data set by constructing principal components along which the variation in the data is maximal in the first principal component, with each subsequent principal component capturing the next largest amount of variation remaining in the data. These principal coordinates are constructed as a linear combination of the variables (i.e. genes) within the data set. Although gene interactions and correlations are far more complex and nonlinear in nature, this approach can be thought of as applying a linear filter to a data set with large variation and noise. Filtering out this variation has been useful in distinguishing cellular subtypes. For example, Hart et al. used PCA to not only identify potential clusters of single cells, but also to identify gene(s) that principally contribute to the variation observed [186]. PCA is one type of a data dimensionality reduction technique that enables one to identify a manageable set of genes/factors for subsequent analysis as in the characterization of neuronal subtypes [168,187].

Non-metric multidimensional scaling (MDS), another unsupervised data analysis and visualization technique, is a powerful tool used to identify relational patterns within high-dimensional data. Similar to clustering methods described earlier, MDS relies on some dissimilarity metric between samples. In order to identify underlying subtypes, all pairwise dissimilarity measures are determined. Similar to PCA, MDS reduces data dimensionality, projecting or mapping the original higher n-dimensional data points onto a new set of "configuration" points $x_i, \ldots, x_n$ in a lower k-dimensional space. The goal of MDS is to project the samples in the lower k-

dimensional space (typically 2- or 3-dimensions) such that their dissimilarities (or rank-order of dissimilarities) are well approximated by the pairwise distances of the projected samples. Applying MDS to high-dimensional transcriptomic data enables one to compare samples by visualizing the (dis)similarities among samples in an easily interpretable manner; the closer two cells are in the projected space, the more similar their transcriptional behavior are and vice versa. Because non-metric MDS focuses on maintaining the rank-order of dissimilarities between the original higher-order dimensional data and lower-order projected data, MDS is a nonlinear alternative to PCA and has been used extensively for classification in gene expression studies [188–190].

Alternatively, more recent visualization approaches, such as *t-Distributed stochastic neighbor embedding* (t-SNE), have been developed to discern multiple cell-types from transcriptomic data [191]. This technique, and variations of this method, have been useful in recapitulating known cell types and identifying rare and novel cell-types due to its ability to represent the structure of relationships among high-dimensional data in a two-dimensional (2D) representation more faithfully than methods such as PCA or MDS [191]. Unlike methods that rely on some distance metric, t-SNE represents pairwise (dis)similarity measures as a joint probability distribution in both the original high-dimensional and targeted 2-dimensional space representing the data.

The high-dimensional distance between samples x_i and x_j is represented by a Gaussian distribution while the corresponding 2D "distance" is represented by a

Student's t-distribution (with one degree of freedom [DF]). To maintain the (dis)similarities within the data, it is necessary to minimize the difference between the distributions of the two-dimensional projections and their original high-dimensional data points. The t-SNE approach involves an iterative optimization of the parameters that define the Gaussian and Student's t-test distribution. The significance of using the Student's t-test distribution (with 1DF) is that this distribution represents very small dissimilarity values with a non-negligible probability, due to the heavy-tailed nature of this distribution with 1DF. In other words, the use of the t-distribution minimizes "crowding" issues where samples with slight differences overlap with each other, which may occur when using PCA or MDS. Thus t-SNE is able to map similarities and differences in the 2D space and represent the "local" and "global" relationships among samples more faithfully [191]. This method and variations of this approach (e.g. viSNE, BH-SNE) have been used, often in combination with PCA, to identify cortical neuron types and visualize the spatial organization of gene expression in the brain [187,192,193].

2.5.2.3 Graphical analysis techniques

Minimum spanning trees (MST) is a well-established approach used in problems of combinatorial optimization. This is a graphical approach in which nodes are connected by undirected, weighted edges. In our case, nodes would represent a single neuron's multi-genic transcriptional profile. Similar to the clustering methods and several of the data-dimensionality reduction methods described earlier, the edges

connecting the nodes represent some type of dissimilarity or distance metric between pairs of nodes. The objective of the MST is to then connect all nodes in such a way that the sum of the edges is a minimum value as compared to the other possible connectivity configurations of the graph. This technique has been used effectively to identify cellular subtypes in the human cortex [97], identify continuums of single-cell molecular states in the immune system and the brain [194,195], and organize biological samples in a temporal manner [196]. In addition, MST has provided the basis of more recent techniques for single-cell analysis such as SPADE and Monocle [194,197].

Spanning-tree progression analysis of density-normalized events (SPADE) – builds upon agglomerative clustering and minimum spanning tree approaches to analyze and identify phenotypes along the continuum of phenotypic progression [194]. SPADE analyzes the high-dimensional set of characteristics describing a single-cell population to define a two-dimensional map that visualizes the potential cellular hierarchy that underlies cellular states. This approach consists of four computational modules which involve *i)* population density-dependent down-sampling to represent equally the various molecularly defined cell-types, *ii)* agglomerative clustering to group cell-types based on molecular phenotype similarity, *iii)* developing a minimum spanning tree to link clusters identified in the prior step, and *iv)* re-populating the clusters with the original samples collected.

Monocle was developed to identify a "trajectory" of a single-cell's progress along a biological process by means of sorting transcriptomic profiles of single-cells

based on their similarity relative to one another [197]. Monocle also builds upon previous minimum spanning trees applications [196]. The Monocle algorithm also involves a data dimensionality reduction step, which involves Independent Component Analysis (ICA) – a similar analytical technique to PCA, but assumes a non-Gaussian, statistical independence within the data. The dimensionality reduction step is followed by the development of a minimum spanning tree. Once the minimum spanning tree has been constructed, the longest sequence of transcriptionally similar cells is defined as the "main" transcriptional trajectory, whereas branching points are interpreted as alternative trajectories towards distinct cell fates [197], or in the case of post-mitotic neurons, distinct functional states.

Community structure detection is yet another graphical approach that can be used to identify neuronal phenotypes by identifying community structures or modules of highly interconnected nodes, which may be representative of highly similar nodes, within some network topology. Unlike spanning trees, where a minimal path that connects all nodes is optimized, this approach seeks to identify communities hidden in an existing network topology. Here, a network graph is represented as a modular matrix, which represents the difference between the actual number of edges connecting to a node and the expected number of edges connecting to a node by chance. Thus the modular matrix represents the degree to which a node belongs to a highly interconnected module. The modular matrix is then partitioned into a set of representative vectors (of node members) that make principal contributions to the modularity of the original network topology [198]. Conceptually similar to PCA,

community detection seeks to identify groups of highly interconnected nodes that principally contribute to the overall modularity of the original network graph. This technique is applied in Chapter 6 to identify modules (i.e. neuronal phenotypes) of transcriptionally similar SCN neurons.

2.5.2.4 Network-based classifiers to distinguish cellular subtypes

In § 1.4.3, the importance of network structure and organization and their impact in transcriptional variability and thus the functional state of a cell was emphasized. A multitude of computational methodologies have been developed to determine gene networks. Boolean and Bayesian networks have been used successfully to identify regulatory interactions. Although Boolean models characterize genes in a simplified binary ON-OFF state, large-scale computable network models can be generated and analyzed for insights into signaling pathways and biological function [199,200]. Bayesian network models provide a probabilistic framework that integrates gene-expression data, for example, with *a priori* knowledge of the biological system.

While Bayesian network models typically discretize expression data as well (though not necessarily in a binary manner) this approach has been successfully employed to identify gene-interaction networks associated with cell-function regulation and corresponding disease states [201–203]. Alternatively, a popular information-theoretic methodology recently developed is known as ARACNE. This approach improves over other methods such as Bayesian networks [204] by

identifying key interactions based on observed nonlinear correlations between the components. Moreover, ARACNE is well-suited to discern between direct and indirect gene interactions by employing information-theoretic approaches, which are more robust to estimation errors than Bayesian network estimation [205].

2.6 Discussion

In the current chapter, rationale for the examination of the NTS and SCN using a combined experimental and computational approach to investigate single-cell transcriptional heterogeneity was provided. Two established experimental protocols to trigger transcriptional responses in the NTS and SCN were described, specifically the acute hypertension challenge in Sprague Dawley rats and the light-induced circadian phase shift in C57BL/6J mice. In order to analyze the transcriptional states of individual neurons in the context of their local neuroanatomical context and functional connectivity, multi-genic expression measures using high-throughput real-time qPCR (BioMark^{TM}) in conjunction with laser capture microdissection technique are used throughout this work and a detailed review of these methodological approaches were provided.

A brief review of the importance of data normalization and recently developed normalization techniques was also provided. Once appropriate internal reference genes are selected and gene expression data is normalized, multiple analytical techniques can be used to analyze and identify potential meaningful organizational patterns within the data. Several multivariate techniques developed from the fields of computer science

and graph network theory have proven to be quite useful in analyzing high-dimensional datasets, such as high-dimensional multi-genic expression data that is the analyzed in this dissertation.

These algorithms can be used to identify correlated expression behavior or clusters of samples based on gene expression, i.e. molecular signatures that would provide insight into the organizational structure underlying the transcriptional state of individual neurons. A review of a sample of these multivariate algorithms was provided and lays the technical foundation from which many of the multivariate analysis performed in subsequent chapters arise. In Chapter 3 PCA, MDS, and gene correlation network analyses are applied to the single-cell transcriptomic data set obtained from the acute hypertensive challenge model to gain insights into what molecular organization may exist underlying NTS neuronal heterogeneity. Building on the insights gained from this study, a novel gene interaction network identification approach is developed in Chapter 4. In Chapter 6, which represents a departure from the NTS, similar methodologies are applied to analyze the SCN to gain insights into the complex neuronal organization underlying transcriptionally heterogeneous SCN neurons.

Chapter 3

IDENTIFYING TRANSCRIPTIONAL PHENOTYPES UNDERLYING SINGLE-NEURON HETEROGENEITY IN THE NUCLEUS TRACTUS SOLITARIUS

In vivo experimental and multivariate analytical approaches are applied to analyze and interpret the transcriptional heterogeneity across individual neurons of the nucleus tractus solitarius in this chapter. Following the experimental and computational approaches described in Chapter 2, these approaches are used to identify a molecular organizational framework in which neuronal phenotypes, defined by their transcriptional state, align with cardiovascular synaptic input-types.

3.1 Introduction

As described in § 1.2.3, the functional states of individual neurons and the interactions among them play a central role in determining brain nuclei function that regulates physiological function. Thus identifying the constituent components or cell-types that compose the tissue is central to elucidating overall brain nucleus function. Because the transcriptome plays a major role in driving cellular and neuronal phenotype, analyzing a neuron's transcriptional state with respect to its functional connectivity would connect underlying molecular mechanisms to its functional phenotype [21,60]. However, accomplishing this task has proven to be quite

challenging due to the transcriptional variation that has been observed repeatedly in individual neurons from what was expected to be a homogeneous cell populations [93]. Reconciling cell-type in the face of such transcriptional heterogeneity in the adult mammalian brain and defining accurately post-development diversity is a difficult challenge [74,102] due, in part, to the fact that **"***phenotypes based on transcriptional profiles may change as a function of developmental stage, age, cell state (e.g., cell cycle for mitotic cells), activity levels, and experience among other things"* [40].

Since neurons respond and adapt to varied and continual sensory synaptic inputs from tissues and organs in the periphery, it is plausible that the adaptive responses of neurons to inputs of this kind may cause, in part, the transcriptional variability observed in transcriptomic studies of phenotypically similar cells [62,93]. If this were the case, a phenotypic population of mature neurons, which would previously be expected to consist of transcriptionally homogenous cells, may rather consist of transcriptionally heterogeneous cells, divergent from one another due to the distinct synaptic inputs received by an individual neuron over its post-development history. Therefore, it is plausible to hypothesize that neuronal transcriptomic variability reflects the variety of synaptic inputs received by an individual neuron that belongs to a particular phenotype. Accordingly, the examination of gene expression across individual mature neurons belonging to the same neuroanatomical phenotype within the context of their functional connectivity may provide insight into this variability. In this chapter, the potential organization of expression differences in terms of neuronal input types is analyzed. If such an organization were supported by

the data, gene expression variability would be functionally meaningful, representing alternative responses of individual neurons within the phenotype.

The hypothesis that synaptic input drives transcriptional variability is investigated in this chapter by analyzing the transcriptional state of several hundred individual neurons from the nucleus tractus solitarius (NTS). As outlined in § 2.2.1, the NTS plays an integrative role in autonomic cardiovascular homeostasis, receiving synaptic inputs conveying states of the peripheral organs, posture, exercise, temperature, circadian time, pain, and mood. These inputs place various physiological demands on the body and require appropriate physiological responses to maintain homeostasis. As individual NTS neurons must integrate multiple combinations of inputs in an effort to maintain cardiovascular homeostasis, their transcriptional variability may reflect the inputs received.

We applied the pharmacologically induced acute hypertensive challenge on Sprague Dawley rats (detailed in § 2.3.1), causing a transcriptional response in NTS neurons. We subsequently examined the NTS neuronal phenotype *in vivo* by measuring the multi-genic state across several hundred NTS neurons, collected from their *in situ* tissue context, using microfluidic qRT-PCR (BioMark^{TM}) The expression of a functionally relevant set of 96 genes was derived from a previous global microarray study of the nucleus [140].

This chapter presents a detailed analysis of the transcriptional profiles of NTS neurons responding to the acute hypertensive challenge. In the first part of this chapter, specific experimental details are provided. This is then followed by a

discussion of the specific challenges associated with analyzing heterogeneous transcriptional profiles of individual neurons and the computational approaches used to deal with these challenges. The findings from the multivariate analysis performed on the high-dimensional multi-genic expression profiles of single NTS neurons, with respect to synaptic input types, are discussed. In addition, statistical analysis is performed to verify the statistical significance of the reported findings. Lastly, the results and findings generated in this study are discussed. The key results in the current chapter have appeared in a journal article co-written by the author [105].

3.1.1 Identifying synaptic input types in the NTS

Two synaptic input-types that are critical for maintaining cardiovascular homeostasis are those that relay information related to changes in blood pressure and higher-order cardiovascular demands of the body. To analyze the differences in gene expression across neurons with respect to synaptic input types, we collected individual NTS receiving either one of these two synaptic input-types.

Two intracellular markers that signify distinct inputs were used to identify NTS neurons, the immediate early gene *Fos* and tyrosine hydroxylase (*Th)*. Extensive literature demonstrates the use of *Fos* as an indicator for the subset of NTS neurons that receive second-order synaptic inputs directly from first-order sensory neurons (i.e. baroreceptors) and is responsive to acute hypertensive disturbances. Carefully conducted control studies have shown that high *Fos* levels depends on neurons being

directly influenced by the increased activity of the blood pressure baroreceptor afferent inputs [206,207]. In this context, we used *Fos* expression to identify neurons directly influenced by blood pressure-baroreceptor afferent inputs [122–125,141,208,209]. Simultaneously, the NTS population of norepinephrine cells, indicated by the expression of the gene coding for the catecholamine synthesis enzyme *Th*, receive higher-order influences through one or more additional interneurons and integrative inputs rather than direct blood pressure inputs from baroreceptors afferents [116,123–125,210]. Thus, the expression of *Fos* and *Th* and the presence of their corresponding proteins, FOS and TH, differentiate distinct NTS neuronal populations in terms of their expected inputs. Using *Fos* and *Th* as markers to distinguish expected input-types received by NTS neurons, we investigated differences in transcriptional states of individual NTS neurons with respect to these inputs.

3.2 Materials and Methods

3.2.1 Animal model

Male, Sprague-Dawley rats (270-280 g, Charles River Laboratories, Wilmington, MA) were housed two per cage in the Thomas Jefferson animal facility. Facilities were maintained at constant temperature and humidity with 12/12 hour light/dark cycles. Lights were turned on at Zeitgeber time (i.e. experimental time) 0 h. By maintaining a consistent Zeitgeber time, all rats would synchronize or entrain to the same 12/12 hour light/dark cycle, which would minimize any circadian-based gene

expression variation across animals. The TJU Institutional Animal Care and Use Committee approved all protocols.

3.2.2 Acute hypertension challenge

Each rat was placed into an induction chamber to induce anesthesia (isoflurane 5% in oxygen, Piramal, Bethlehem, PA). Once the rat was anesthetized, the rat was moved to a surgical station and remained anesthetized throughout the procedure by placing a breathing tube over the nose of the rat, which delivered an oxygen-isoflurane gas mixture (2% isoflurane in oxygen). The common iliac vein and artery were cannulated for delivery of pharmaceuticals (phenylephrine, or saline solution) and blood pressure measurement. During the drug infusion period (1 h), animal subjects received either phenylephrine, a vasoconstrictor that would cause a peripheral increase in blood pressure, or an equivalent amount of saline without phenylephrine, both of which were delivered via the venous cannula. In the phenylephrine-injected animals, hypertension was induced and maintained using a phenylephrine concentration that was determined to maintain a blood pressure level 40 mmHg above baseline levels. The infusion rate and dosage were maintained by an adjustable pump in order to maintain the 40mmHg increase in blood pressure.

3.2.3 Experimental design

Sprague-Dawley rats were divided into two experimental groups: *i)* hypertensive (n = 4 animal replicates), and *ii)* baseline normotensive (n = 2 animal

replicates). The reason for the unequal number of animal replicates between treatment groups is worth a brief discussion. Neurons responding to a change in blood pressure (FOS+) are only detectable in rats undergoing the acute hypertensive challenge. As a result, we collected both TH+ and FOS+ neurons from the hypertensive rats while we only collected TH+ neurons in the baseline normotensive rats.

3.2.4 Tissue and sample preparation

3.2.4.1 Rapid immunofluorescent staining

We visualized NTS neuronal populations defined by their synaptic input-type using the rapid immunofluorescent staining procedure (§ 2.4.2). The primary antibodies used included anti-Tyrosine Hydroxylase (TH) (Pel-Freez® Biologicals, Rogers, AR) and anti-c-Fos solution, both of which were diluted to 1:25 (antibody:blocking-buffer), The secondary antibody used was Alexa-488 anti-rabbit (Life Technologies, Grand Island, NY) (1:50, antibody:blocking-buffer). Only one secondary antibody was used since only one neuron-type (FOS+ *or* TH+ neurons) was selected from each tissue slice. Once primary and secondary antibody staining and incubation were completed, stained tissue sections were dehydrated in the series of EtOH baths and subsequent Xylene bath (§ 2.4.2), prior to sampling single neurons via laser capture microdissection.

3.2.4.2 Single neuron sampling

As part of the experimental design, 300 single neurons were lifted from the NTS of the four hypertensive and two normotensive rats, 220 of which were collected from hypertensive rats and the remaining 80 individual neurons collected from

normotensive rats. Due to the absence of a perturbation in arterial blood pressure in normotensive rats, *Fos*+ neurons responding to an acute hypertensive challenge were only collected in hypertensive rats. The anatomical distribution of collected *Fos*+ neurons within the NTS was consistent with the extensive literature characterizing *Fos* expression in the NTS [121–125,207,208,211–213].

3.2.4.3 Gene selection

Genes included in this study were chosen based on their functional relevance in the transcriptional programs underlying blood pressure regulatory functions in the NTS. Previous work in this laboratory analyzing the coordinated transcriptional responses to an acute hypertensive challenge in rats provided the foundation from which the 96 gene panel was designed [140]; Appendix A.1).

3.2.4.4 High-throughput qRT-PCR

Gene expression levels were measured across four high-throughput qPCR assay chips on the BioMark^{TM}, a highly reproducible qPCR platform. In order to characterize the technical variability inherent with the BioMark^{TM} platform, a set of serially diluted mRNA, extracted from tissue punches from the NTS of Sprague Dawley rats were assayed on each 96.96 BioMark^{TM} dynamic array (also referred to as a chip). A comparison of the same serial dilution set that was run across all four dynamic arrays, showed a tight clustering of samples along the 45 degree line, as shown in Figure 3.1. The minimal variation of dilution points from the 45 degree line,

which represents identical measures across two chips, indicates minimal technical variability from chip to chip, as shown in Figure 3.1.

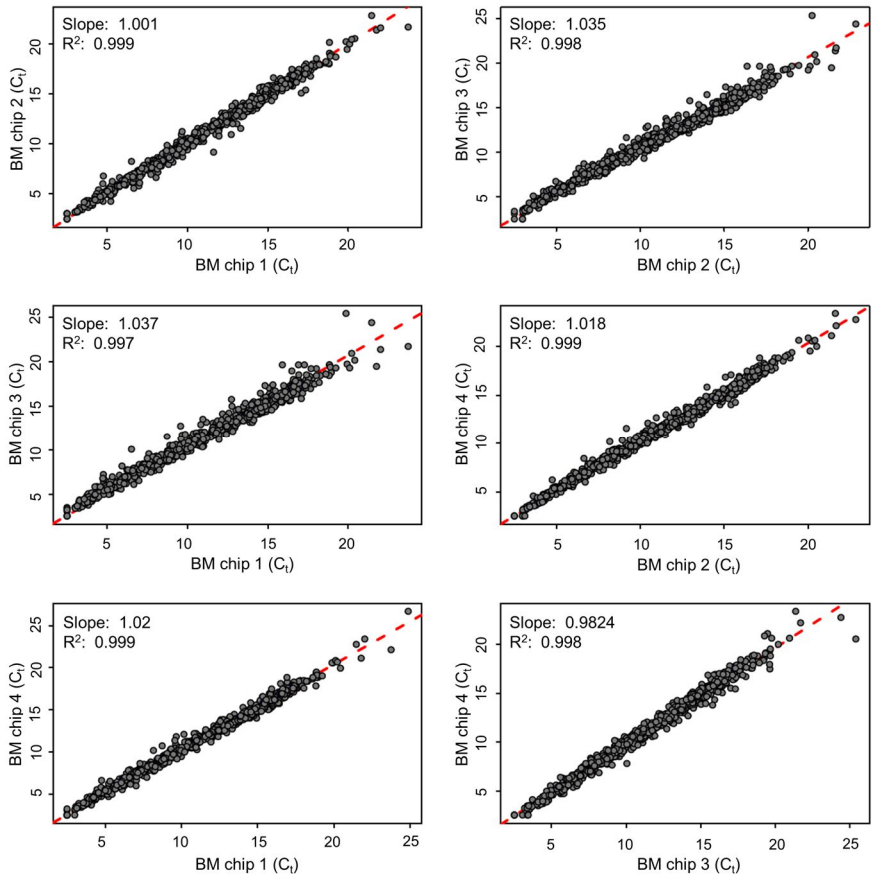

Figure 3.1 High-throughput qPCR reproducibility. A serial dilution sample set of mRNA extracted from tissue punches from the NTS of a Sprague Dawley rat was assayed on each 96.96 BioMark™ dynamic array. A pairwise comparison among all dynamic arrays shows that the measured C_t values for the serial dilution sample sets fall along the 45 degree line (red dashed line) with minimal deviation. The slope and R^2 values are nearly 1 for all graphs indicating that the arrays are capable of measuring gene expression values, over 5 orders of magnitude, consistently with minimal technical variability.

3.2.4.5 Single-cell sample quality assessment

Several concerns have been raised regarding the purity of single neuron samples obtained via laser capture microdissection (LCM) [167]. To minimize potential non-specific cross-contamination, we followed established sampling procedures [33], which involve visual inspection of the sample tissue and captured neuronal cell body. In addition, we measured the expression level of genes specific to neuron, astrocyte, microglial, and endothelial cells in a separate set of single neurons and astrocytes collected from the NTS via LCM. This sample quality assessment was performed to evaluate the extent of any potential cross-contamination from non-targeted cell types that may have affected the single cell samples. Our results showed minimal to nonexistent cross-over contamination (Figures 3.2 and 3.3), consistent with the repeated performance of LCM approach by a number of other groups as seen in [33,214–217].

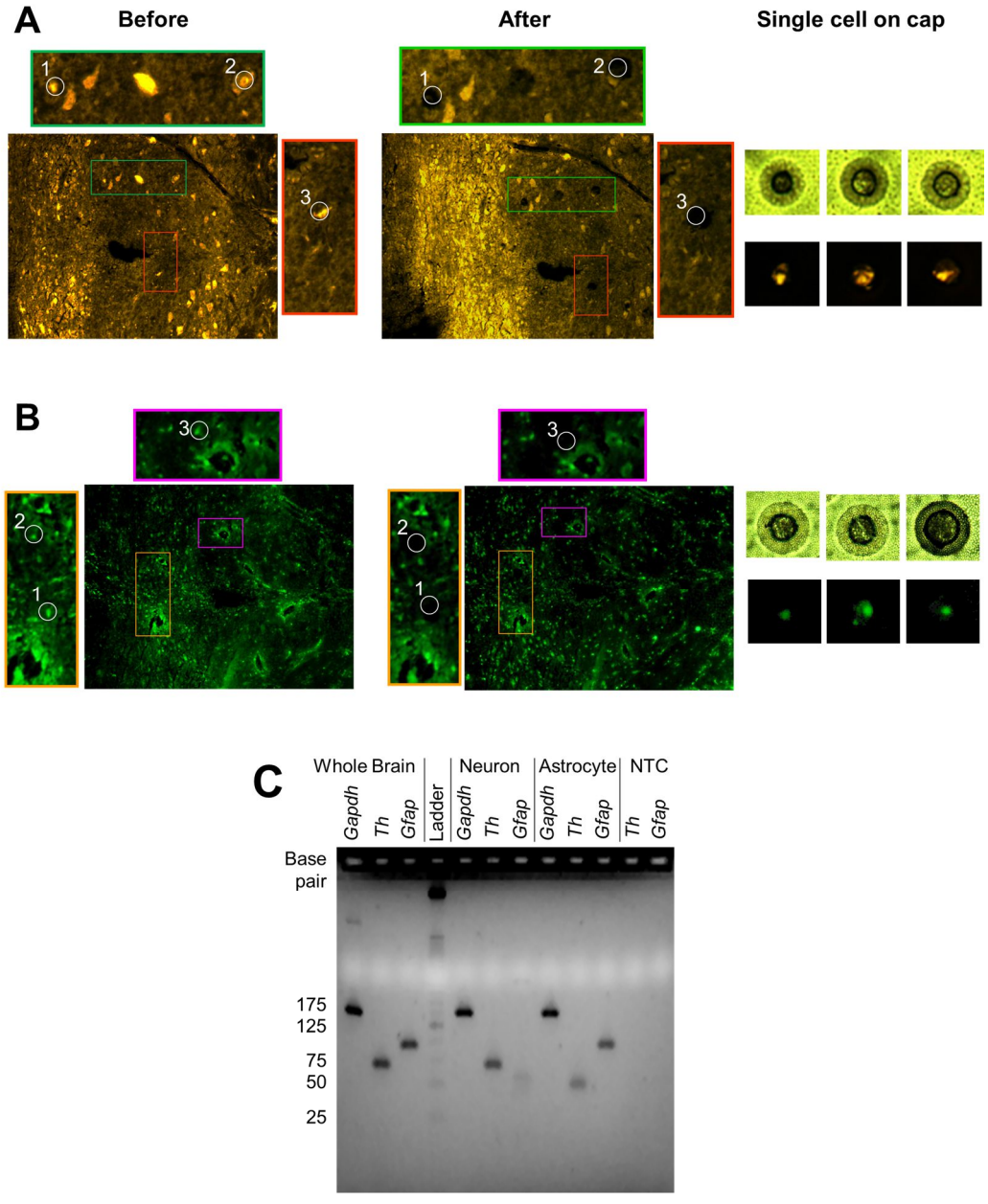
A
Before
After
Single cell on cap
B
C
Whole Brain
Neuron
Astrocyte
NTC
Gapdh
Th
Gfap
Ladder
Base pair
175
125
75
50
25

Figure 3.2 Single neuron and astrocyte laser capture microdissection. (A) Tyrosine hydroxylase (TH) immunohistochemical staining and collection of TH+ single cells from a coronal section of a normotensive rat brainstem. Colored outline images represent magnified tissue sections from which TH+ single cells were captured. (B) Glial fibrillary acidic protein (GFAP) immunohistochemical staining and collection of GFAP+ single cells from an adjacent coronal section of a normotensive rat brainstem. Colored outline images represent magnified tissue sections from which GFAP+ single cells were captured. (C) Gel electrophoresis image of reverse-transcribed cDNA from whole brain tissue (positive control; lanes 1-3), a representative single neuron sample (lanes 5-7), a representative astrocyte sample (lanes 8-10), and a no-template control (NTC; negative control, lanes 11-12). All samples underwent 22 pre-amplification cycles prior to undergoing a 40-cycle PCR. Products from the 40-cycle PCR were placed on an E-Gel® EX Agarose Gel 4% (Invitrogen™). The rat whole brain positive control shows product bands for *Gapdh* (148 bp), *Th* (68 bp), and *Gfap* (93 bp). Both single neuron and astrocyte samples show formation of *Gapdh*. However, the neuron sample does not show any *Gfap* product at the expected 93 bp size. A light band in lane 7 at < 50 bp suggests a non-specific product. Similar behavior is observed in lane 9, where the astrocyte sample shows no *Th* product at the expected 68 bp size. Only a light product band at < 50 bp is present, suggesting a non-specific product. The results indicate minimal to no crossover contamination occurring between astrocytes and neurons.

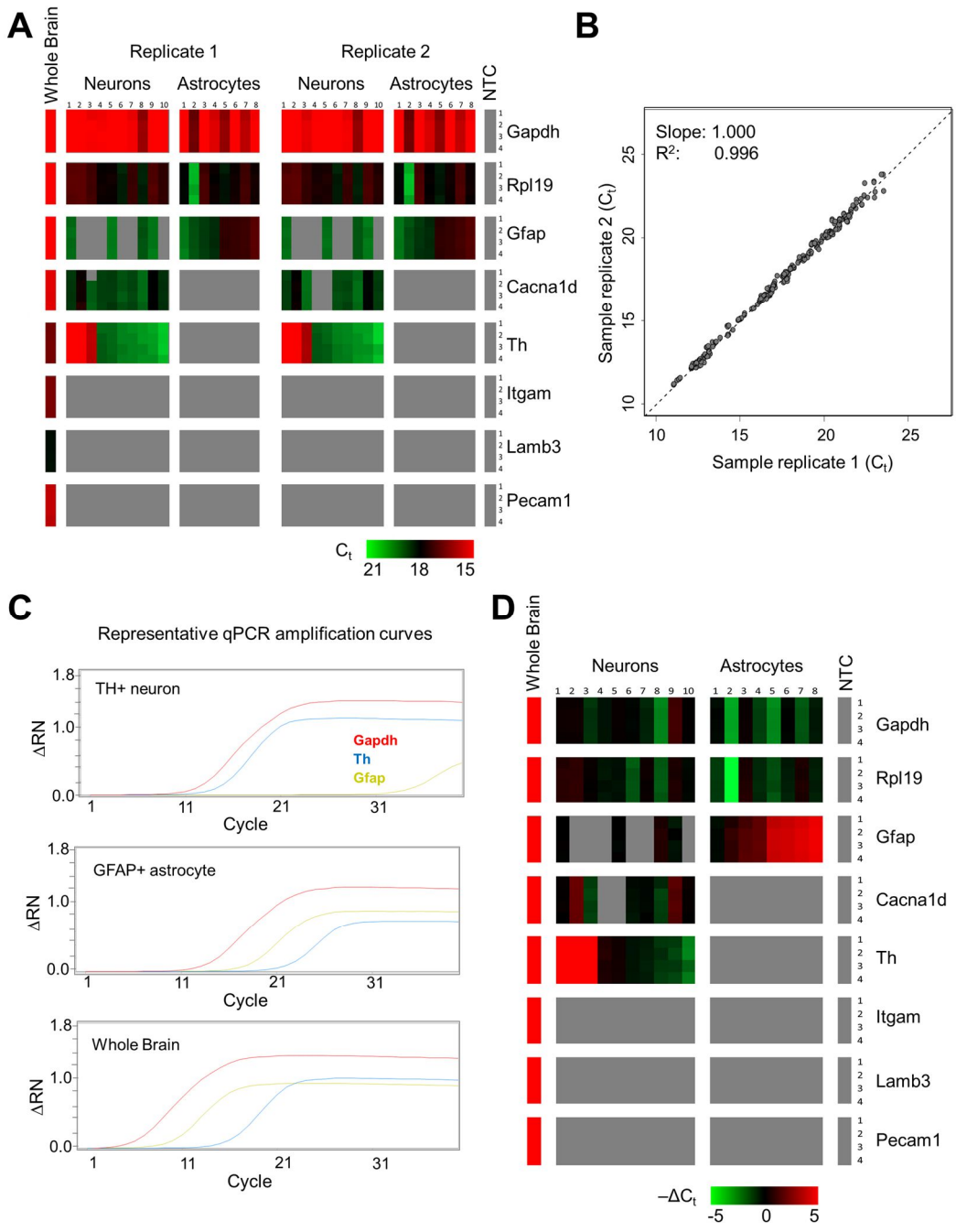
A
Whole Brain
Replicate 1
Replicate 2
Neurons
Astrocytes
Neurons
Astrocytes
NTC
Gapdh
Rpl19
Gfap
Cacna1d
Th
Itgam
Lamb3
Pecam1
Ct
21 18 15
B
Slope: 1.000
R2: 0.996
Sample replicate 2 (Ct)
Sample replicate 1 (Ct)
10 15 20 25
C
Representative qPCR amplification curves
TH+ neuron
GFAP+ astrocyte
Whole Brain
Gapdh
Th
Gfap
ΔRN
Cycle
1.8
1.0
0.0
1 11 21 31
D
Whole Brain
Neurons
Astrocytes
NTC
Gapdh
Rpl19
Gfap
Cacna1d
Th
Itgam
Lamb3
Pecam1
−ΔCt
-5 0 5

Figure 3.3 High-throughput qPCR analysis of LCM collected single neurons and astrocytes. (A) Heat map representing gene expression levels of single neuron and astrocyte samples obtained via BioMark^{TM}. Raw C_t values are visualized in the heat map. Ten single neuron and eight single astrocyte samples were collected and measured. Two sets of technical replicates across samples and four technical replicates across each assay were measured. Assays measuring the expression of housekeeping genes (*Gapdh*, *Rpl19*) and cell-type enriched genes were used. Cell-type enriched assays include an astrocyte-enriched gene (*Gfap*), neuron-enriched genes (*Cacna1d, Th*), microglia-enriched gene (*Itgam*), and endothelial-enriched genes (*Lamb3, Pecam1*). Rat whole brain RNA extract was included as a positive control while DNA suspension buffer was included as a negative control. Expression of housekeeping genes occurs in both types of single cells (neurons and astrocytes) as expected. *Gfap* expression is present in all astrocyte samples while it is either low or non-existent in single neuron samples, which suggests minimal cross-contamination of astrocytes in neuron samples. Expression of *Cacna1d* and *Th* is present in all neuron samples while it is non-existent in single astrocyte samples indicating no cross-contamination of neurons in astrocyte samples. Additionally, expression of microglia and endothelial-enriched genes is non-existent in either neuron or astrocyte samples, which indicates no cross-contamination of microglial or endothelial cell-types in either neuron or astrocyte samples collected by LCM. (B) A plot of sample (technical) replicate 1 versus sample (technical) replicate 2 shows the highly-reproducible nature of the BioMark^{TM} platform and demonstrates the low technical variability affecting gene expression measures of single cell samples. (C) Representative qPCR amplification curves from the same single cell samples used in the gel-electrophoresis run (Figure 3.2). (D) Heat map representing median centered $-\Delta C_t$ values. Raw C_t values were subtracted from the corresponding median Ct value of neuron replicate sample set 2 within each assay. Neuron samples show higher normalized expression of *Cacna1d* and *Th* (neuron-enriched assays) than astrocyte samples and minimal to no normalized expression of *Gfap* (astrocyte-enriched assay).

3.2.4.6 Quality assessment of gene expression data

Prior to data normalization of the raw C_t data, individual qRT-PCR results were examined to determine the quality of the qRT-PCR. An initial pass-fail-no call assessment was made for each reaction based on the qualitative nature of the reaction

curves obtained from the PCR. Following this initial review, both samples and gene assays having greater than 30% failed reactions were excluded from the present analysis. The "failure" criteria for a sample or gene assay was set fairly low in order to ensure that these failures would not bias the subsequent data analysis and further increase the quality and confidence in the data used for analysis. A total of 192 single cell samples (41 normotensive samples and 151 hypertensive samples) and 81 different gene assays were included in the present analysis.

3.2.5 Computational analytical techniques

3.2.5.1.1 Data normalization

Following a rigorous quality control (QC) assessment of the data, 192 single cell samples (41 normotensive samples and 151 hypertensive samples) and 81 different gene assays were included in this analysis. Raw C_t values for individual samples were normalized against an average expression level between *Actb* and *Rpl19* to obtain a $-\Delta C_t$ using Equation 3.1.

$$-\Delta C_t^{gene} = mean(C_t^{Actb}, C_t^{Rpl19}) - C_t^{gene} \qquad 3.1$$

Of the potential reference housekeeping genes included in the gene assay set, *Actb* and *Rpl19*, had the most stable behavior across the single neuron samples, per the stability measures as determined by using both the geNorm and NormFinder method [174,180] described previously in § 2.5.1.1.

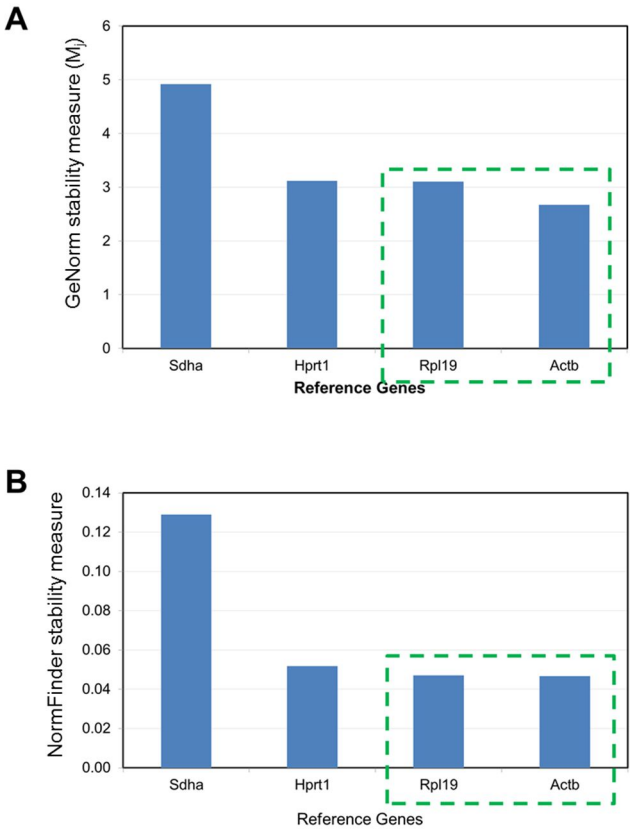

Figure 3.4 Reference gene stability. (A) Stability measures of the four potential housekeeping genes as determined by the geNorm method developed by Vandesompele et al., (2002). The variability measure indicates a gene that has lower gene expression variation across the samples and conditions measured. (B) Variability of the four potential housekeeping genes as determined by the NormFinder method developed by Andersen et al., (2004). Similarly a lower variability value indicates more stable gene expression behavior across samples and conditions measured. In both cases, *Actb* and *Rpl19* exhibited the most stable behavior.

3.2.5.2 Principal Component Analysis

The *pcaMethods* package [218] and associated functions in the R statistical software [219] were used to perform PCA. A subset of 48 genes was derived as significantly contributing to the observed variability, using the five highest and lowest

corresponding loading values along the first five principal components as a basis for gene identification.

3.2.5.3 Similarity distance and multidimensional scaling

Relative distances between single cells were determined using the Spearman rank correlations obtained for the set of hypertensive samples and subset of 48 genes identified from PCA. The following equations were used to determine distance:

$$\rho = \frac{\sum_i (x_i - \bar{x}_i)(y_i - \bar{y}_i)}{\sqrt{\sum_i (x_i - \bar{x}_i)^2 \sum_i (y_i - \bar{y}_i)^2}} \qquad 3.2$$

Where x_i and y_i correspond to gene expression rank between two single cell samples

$$d = 1 - \rho \qquad 3.3$$

Where d corresponds to the Spearman rank distance between two cells.

The pairwise relative distances between single cell samples was performed using the *stats* package provided through the R statistical software [219].

Non-metric multidimensional scaling was performed on single cells in conjunction with PCA in order to analyze single cells that lie in an *n*-dimensional space (due to the nature of the multiplex gene expression data). MDS was applied to visualize the (dis)similarities among the transcriptional states of the single cells obtained from hypertensive rats (based on $-\Delta C_t$). The *isoMDS* function provided in

the *MASS* package [220] for R platform was used to perform the MDS. Following MDS, single cell samples were annotated by their respective synaptic-input marker categorization (combinatorial expression levels of *Th* and *Fos*) overlaid on the samples. The first MDS axis discriminates samples based on the rank-ordering of expression levels of genes from transcription module 2. MDS axis 2 accounts for biological variability in both hypertensive and baseline samples (Figure 3.16) and MDS axis 3 discriminates cells based on rank expression levels of genes from transcription module 1. Both 2-dimensional and 3-dimensional plots were created via *plotrix* and *rgl* packages [221,222] provided by the R statistical software [219].

3.2.5.4 Gene correlation networks

The statistical software R was used to determine rank correlation coefficients between the subset of 48 genes for the 6 different single cell "sub-phenotypes" initially identified. A Spearman rank correlation coefficient cutoff of 0.4 was used to define whether or not two genes had a correlative relationship. Cytoscape (www.cytoscape.org) was used to visualize the correlative relationships.

3.3 Results

3.3.1 Transcriptional heterogeneity across single NTS neurons

Our results revealed significant variability in normalized gene expression across all single cells (Figure 3.5). Approximately two-thirds of the genes showed expression values spanning three orders of magnitude as measured across multiple

high-throughput qPCR runs, multiple rats, and in both hypertensive and baseline states.

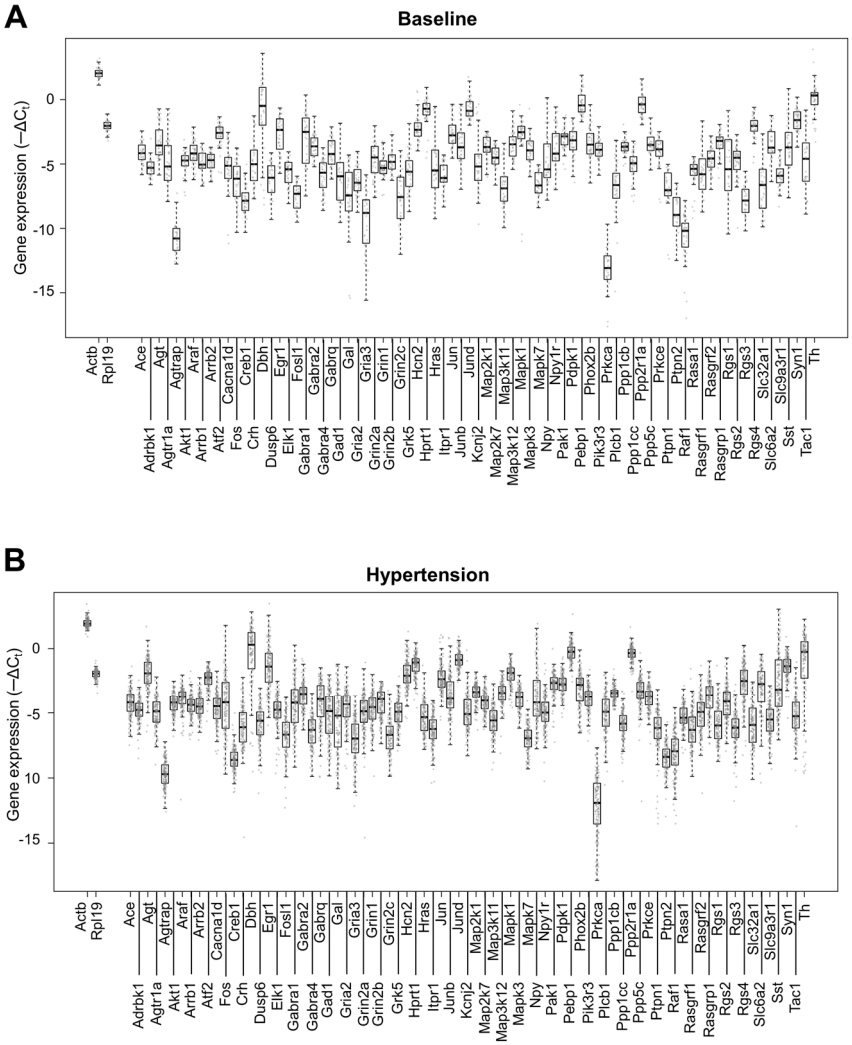

Figure 3.5 Gene expression and variance distributions. Boxplots overlaid with in-line scatter plots showing the spread of expression data for all genes ($-\Delta C_t$). Each grey dot corresponds to a particular gene expression level in a particular single cell sample. (A) Expression in neurons collected from baseline-normotensive rats, (B) Expression in neurons collected from hypertensive rats.

As outlined in § 2.5.2**,** a key step to analyzing large-scale gene expression data is to identify cluster gene expression data that may reveal underlying relationships within the data either across samples and genes. Initially we analyzed the variability in single cell gene expression using Principal Component Analysis (PCA) to identify clusters of gene expression data across the single-neuron samples, which may provide insight into the variability observed. Unfortunately, the PCA results did not reveal any clustering or structure to the variability observed in the cellular states, as illustrated in plots of the PCA scores along the first five principal components that accounted for 48.94% of the variability in the data, based on the cumulative sum of their corresponding eigenvalues (Figure 3.6).

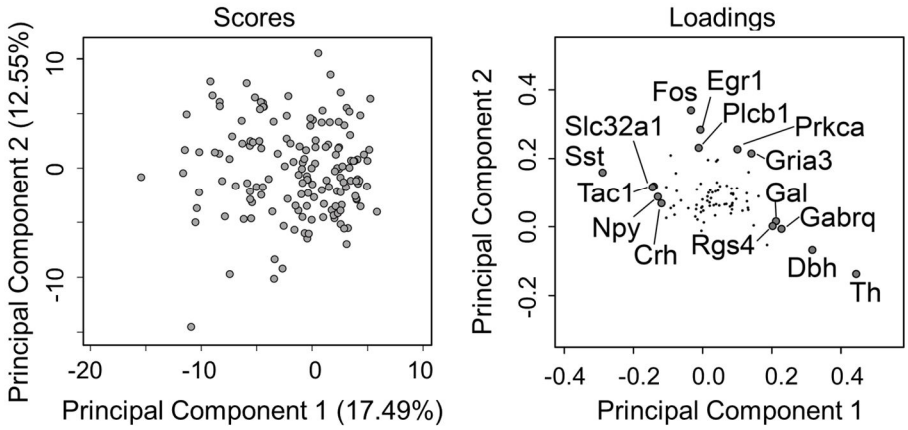

Figure 3.6 Principal component analysis of the gene expression data of single cells from hypertensive rats. (A) Projection of single cells (scores) along the first two principal components (PCs) is shown. Additional components were explored as well, but not shown in this figure. (B) Loading values of the genes along the first two PCs. Genes with the five highest and lowest loading values along PC 1 and genes with the five highest loading values along PC 2 are labeled. The highest and lowest genes along the multiple PCs explored provided the bases for the selection of a subset of 48 genes with significant contributions to variability observed in the data.

Despite the absence of any obvious clusters due to the large variation in express across the panel of genes measured, it is possible that focusing on a subset of genes that are the principal contributors to the data variation, i.e. reducing the dimensionality of the data, may reveal underlying clusters or structure that were not apparent initially. We subsequently derived a subset of 48 genes that significantly contributed to the observed variability by using the five highest and lowest corresponding loading values along the first five principal components as a basis for gene selection. Genes were rank-ordered based on their respective loading values, which were determined from PCA. The five highest and lowest ranked genes (10

genes total) from the first five principal components were identified as genes of interest for subsequent analysis (Appendix A.2).

Additionally, various subsets of the single cell data were analyzed based on gene functions (Appendix A.1). These subsets were analyzed in order to identify any other genes contributing to the variability that may have been overshadowed by a few genes. In other words, these functional gene subsets were analyzed through PCA in order to identify less dominant sources of variability. Some of the functional categorizations used to subset gene groups included ion channels, neuromodulatory regulators, and intracellular signaling. A rank ordered list of genes along the first five principal components and the respective gene functional subsets in which the single cell data was analyzed is tabulated in Appendix A.2. The genes with corresponding bolded values in Table A.2.1 represent 30 of the final 48 genes selected that created the 48-gene dimensional data set on which further multivariate analysis was performed. The additional 18 genes were selected on the basis of their loading values from PCAs performed on the various subsets of data as described previously. As several genes were repeatedly identified as either a high or low ranking gene along multiple principal components (Appendix A.3), a final set of 48 genes was selected.

3.3.2 MDS visualization of transcriptional states of single NTS neurons

Next, we analyzed the single cell states, characterized by this 48-dimensional gene expression (i.e. transcriptional) profile per cell, to determine the presence of any structure or organization subtending these seemingly disparate cell states. We

performed all possible pairwise comparisons of the single cells using a Spearman rank correlation. The high-dimensional data set of correlation coefficients were then converted to corresponding similarity values, which were projected into three dimensions using MDS (Figure 3.7).

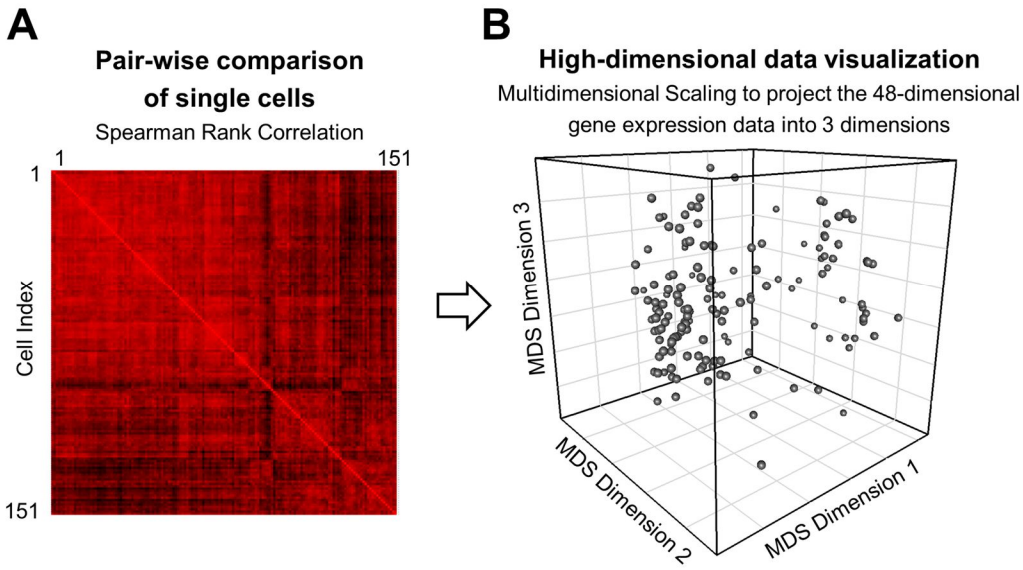

Figure 3.7 Spearman rank correlation coefficients and multidimensional scaling of neurons from hypertensive rats. (A) Pairwise comparison of single cells based on Spearman rank correlation coefficients. Single cells are compared based on their respective 48-gene rank order. Red indicates a high correlation between cells while black represents no correlation between a pair of single cells. (B) The Spearman rank correlation coefficients are used to determine the similarity distance between each cell. The high dimensional set of similarity values between all possible single-cell pairs are then projected into three dimensions using Multidimensional scaling. A sphere in this 3D space represents a single neuron. The relative distance between two spheres in this 3D space corresponds to the relative (dis)similarity between two cells.

As outlined in § 2.5.2.2, MDS is useful to visualize similarities and dissimilarities of high-dimensional data in a lower dimensional space [189,223,224]. In this context, the proximity between any two cells in the MDS space corresponds to how similar or dissimilar the rank correlation of gene expression is between that particular cell pairing. Projecting the single-cell states resulted in an unstructured, distributed cloud in this MDS space (Figure 3.7), which revealed no obvious structures or organization to cell states. To analyze these multi-genic expression state (dis)similarities in the context of the synaptic input-types these NTS neurons receive, we subsequently analyzed the single-neuron variability with respect to gene expression of the two input-type markers *Fos* (transcript of FOS) and *Th*.

3.3.3 Synaptic-input based analysis of single-neuron transcriptional heterogeneity

We first considered the extremes of the single-cell multiplex gene expression distribution (Figure 3.7) with respect to the two input-type markers to identify and annotate two input-based subtypes (Figure 3.8): cells with *Fos* expression and minimal to no *Th* expression (*Th*-/*Fos*+) and cells with *Th* expression and minimal to no *Fos* expression (*Th*+/*Fos*-). A rank-ordering of *Th* expression levels ($-\Delta C_t$) showed a significant decrease in $-\Delta C_t$ values within the lower 15% quantile. A similar approach was applied to *Fos* expression levels, however the lower 30% quantile showed a significant drop in expression levels within the subset of hypertensive samples. Thus single neurons that fell within the lower 15% and 30% quantiles for *Th* and *Fos*

expression ranges were categorized as *Th-/Fos+* and *Th+/Fos-* respectively. Categorization based on immunoreactivity of the same single cells to the respective markers was nearly identical to categorization based on mRNA expression. Only six individual NTS neurons categorized as "*Fos-*" showed FOS immunoreactivity. Although a single cell may be labeled as "*Fos-*", this annotation is simply an indicator of low *Fos* mRNA levels in that particular neuron. Given the dynamic and transient nature of *Fos* regulation and expression, this slight discrepancy is unsurprising.

Applying the mRNA-based annotation of these single cell subtypes to the MDS visualization of cell states revealed a surprisingly structured organization. The two subtypes were distinctly clustered at the opposing extremes of the overall distribution of cells, as shown in Figure 3.8.

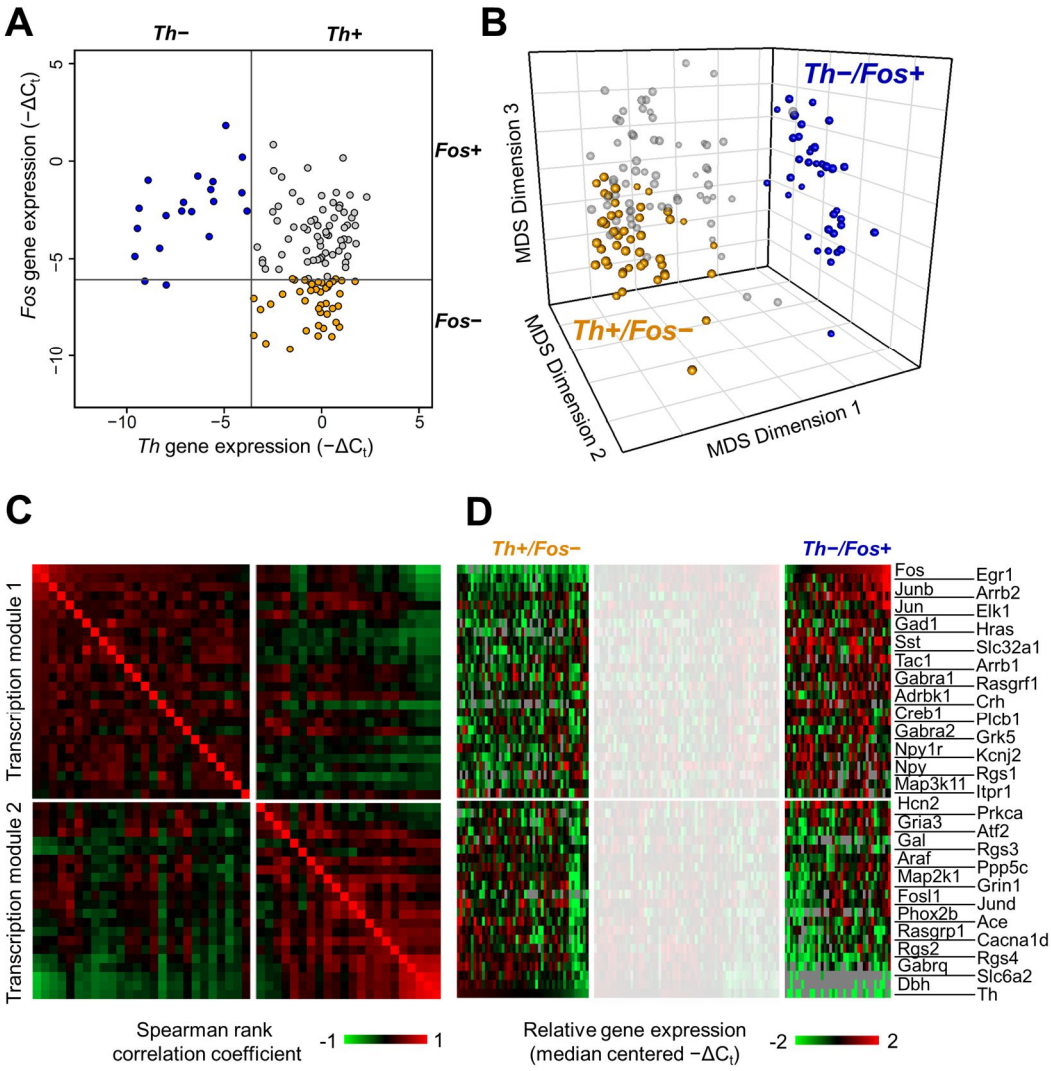
A
Th−
Th+
Fos+
Fos−
Fos gene expression (−ΔCt)
Th gene expression (−ΔCt)
B
Th−/Fos+
Th+/Fos−
MDS Dimension 3
MDS Dimension 2
MDS Dimension 1
C
Transcription module 1
Transcription module 2
Spearman rank correlation coefficient
-1
1
D
Th+/Fos−
Th−/Fos+
Fos
Junb
Jun
Gad1
Sst
Tac1
Gabra1
Adrbk1
Creb1
Gabra2
Npy1r
Npy
Map3k11
Hcn2
Gria3
Gal
Araf
Map2k1
Fosl1
Phox2b
Rasgrp1
Rgs2
Gabrq
Dbh
Egr1
Arrb2
Elk1
Hras
Slc32a1
Arrb1
Rasgrf1
Crh
Plcb1
Grk5
Kcnj2
Rgs1
Itpr1
Prkca
Atf2
Rgs3
Ppp5c
Grin1
Jund
Ace
Cacna1d
Rgs4
Slc6a2
Th
Relative gene expression (median centered −ΔCt)
-2
2

Figure 3.8 Input-driven extreme-phenotypes. (A) Input-based cell type identification. A bivariate plot of single cells obtained from hypertensive rats based on their normalized expression of *Th* and *Fos*. The extremes of the distributions for each gene were initially explored resulting in two extreme classes of single cells 1) cells with no *Th* expression and 2) cells with no *Fos* expression. The grey lines indicate the threshold criteria used to define the extreme subtypes *Th-/Fos+* (blue filled circles) and *Th+/Fos-* (orange filled circles). (B) Clustering of input-based cell types. A 3D MDS projection of single cells with the extreme phenotype classifications applied. These projects are based on the similarity of single cells with respect to their ranked expression order of the 48 gene subset. (C) Heat map of gene expression correlation coefficients and modules of highly correlated genes. The highly variable genes show that the underlying gene expression in these extreme subtypes can be organized into two correlative groups, or transcription modules. These transcription modules group genes that show higher correlations (upper left quadrant and lower right quadrant of the heat map) with each other across single cells of the extreme subtypes. Columns and rows with the same index representing a particular gene follow the row annotation in panel (D) Gene expression gradients in input-based cell types. Heat map of normalized gene expression data. An overall gene expression gradient can be observed in the gene expression profile of the 48 highly variable genes across the extreme subtypes. Focusing on the extreme regions to the left and right of the faded region on the heat map, opposite expression behaviors can be observed in the two transcription modules between the two extreme input-based subtypes. The upper set of genes in the heat map shows an overall decrease in gene expression in *Th+/Fos-* cells and an increase in *Th-/Fos+* cells. The opposite behavior is observed in the lower set of genes. The expression patterns of these extreme subtypes occupy opposite ends of the gene expression gradient observed.

Neurons categorized by their input-types (i.e., *Fos* or *Th* expression level) maintained close proximity to each other in the transcriptional space indicating that individual cells receiving a particular input-type share similar transcriptional profiles, an indicator of cell response. The separation of the two extreme subtypes was found to be statistically significant as no such clustering was observed in randomized

permutations of the data. Additional details on the permutations performed are discussed in § 3.3.6.

This structured organization supports a novel perspective that diverse inputs to individual cells may drive variation in the transcriptional profiles of NTS neurons. It is interesting to note that the highly variable genes identified using PCA were rank correlated across many single cells categorized by the two input-type markers (Figure 3.8C). Gene expression was organized into two gene groups (which we refer to as *transcription modules*) where gene expression across samples within a group correlated with *Fos* and *Th* expression profiles. The correlation shared among genes with *Fos* and *Th* suggests that the expression patterns of *Fos* and *Th* serve as exemplars for each transcription module that distinguish the two populations of NTS neurons (Figures 3.8C-D). It is also worth noting that the expression of other key genes relevant to catecholaminergic function (e.g. *Dbh* and *Slc6a2*) correlated most highly with *Th* gene expression, consistent with the well-regarded expectation that these genes are co-regulated [225–231]. This result serves as an internal validation of our analysis. The alignment of the two input-type markers with the variation seen in the measured transcriptional profiles of NTS neurons implies a causal relationship where inputs to individual cells play a major role in shaping the transcriptional profiles. This relationship supports the hypothesis that inputs influence neuronal transcriptional state, which is substantiated by the quantitative nature of this relationship.

3.3.3.1 Intermediate neurons

While the majority of the cells expressed either *Fos* or *Th*, there were smaller populations with lower expression of one or both input-type markers. We interpret these various expression levels as indications of different populations with respect to the two input types. For example, some subset of *Th*-expressing cells may respond weakly to baroreceptor inputs through interactions with interneurons yielding variable *Fos* expression in those cells. If so, the NTS neuron types may form a continuous distribution with respect to strength of input from different sources, and by implication a continuous distribution of expression patterns may result. With this expectation, we categorized cells with *Th* and *Fos* expression levels lower than threshold used to define *Th*+ and *Fos*+ neurons, based on median expression for each input-type marker to yield four "intermediate" subtypes, shown in Figure 3.9. The $-\Delta C_t$ ranges for *Th* and *Fos* for these double positive cells were split into two groups respectively. A 30% quantile value of the *Th* expression range across the remaining samples not classified as *Th*- neurons was used to define a threshold dividing Th^{high} and Th^{low} cells while the median expression of the intermediate range of *Fos* expression levels was used to determine Fos^{high} and Fos^{low} cells. Using this binary classification of expression levels, the remaining double positive cells could be classified in one of 4 groups, Th^{low}/Fos^{low}, Th^{low}/Fos^{high}, Th^{high}/Fos^{low}, and Th^{high}/Fos^{high}.

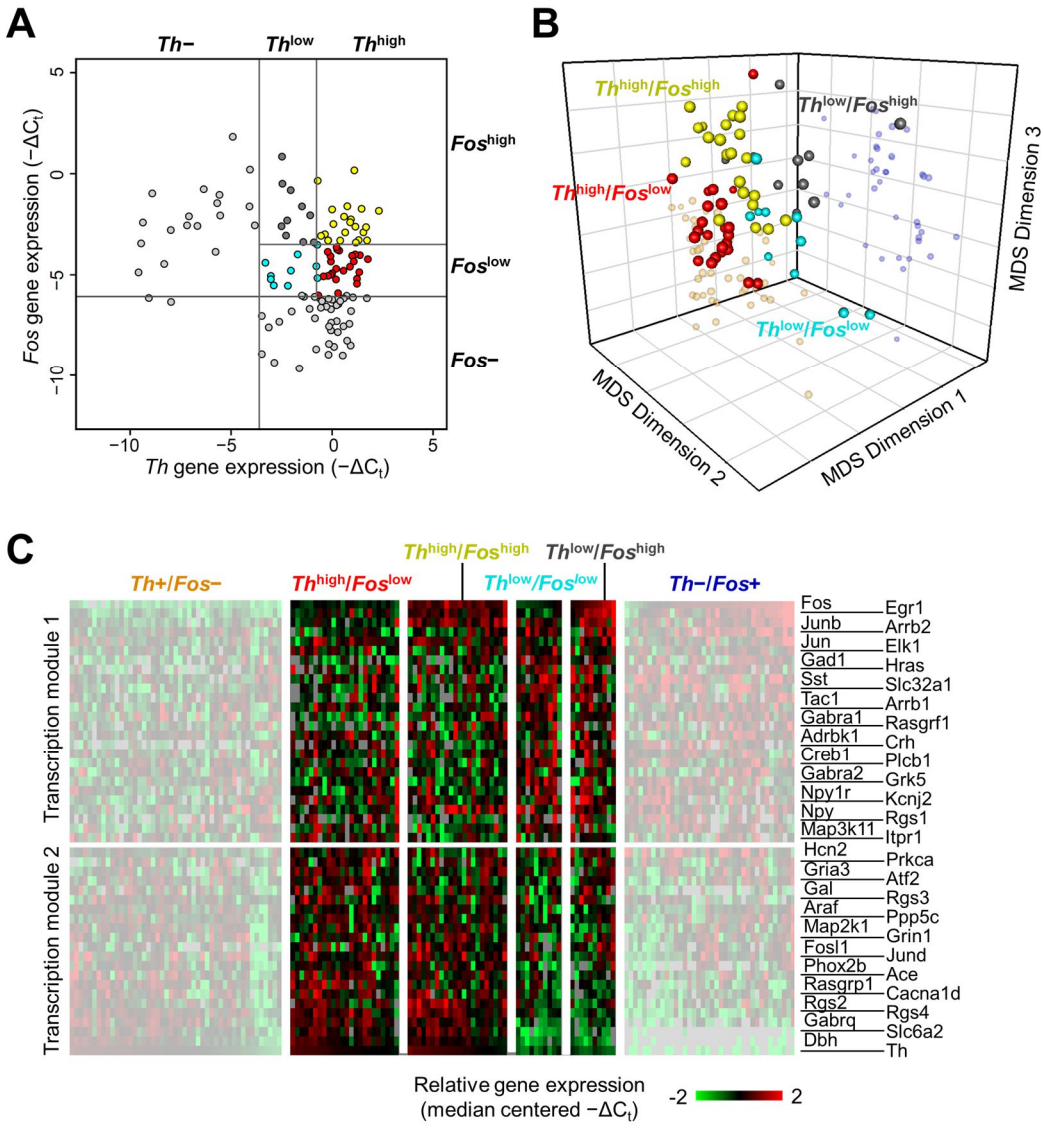
A
Th−
Thlow
Thhigh
Foshigh
Foslow
Fos−
Fos gene expression (−ΔCt)
Th gene expression (−ΔCt)
B
Thhigh/Foshigh
Thlow/Foshigh
Thhigh/Foslow
Thlow/Foslow
MDS Dimension 3
MDS Dimension 2
MDS Dimension 1
C
Th+/Fos−
Thhigh/Foslow
Thhigh/Foshigh
Thlow/Foslow
Thlow/Foshigh
Th−/Fos+
Transcription module 1
Transcription module 2
Fos
Junb
Jun
Gad1
Sst
Tac1
Gabra1
Adrbk1
Creb1
Gabra2
Npy1r
Npy
Map3k11
Egr1
Arrb2
Elk1
Hras
Slc32a1
Arrb1
Rasgrf1
Crh
Plcb1
Grk5
Kcnj2
Rgs1
Itpr1
Hcn2
Gria3
Gal
Araf
Map2k1
Fosl1
Phox2b
Rasgrp1
Rgs2
Gabrq
Dbh
Prkca
Atf2
Rgs3
Ppp5c
Grin1
Jund
Ace
Cacna1d
Rgs4
Slc6a2
Th
Relative gene expression
(median centered −ΔCt)
-2
2

Figure 3.9 Input-driven intermediate-phenotypes. (A) Intermediate input-based cell types. Bivariate plot of single cells obtained from hypertensive rats (Fig. 2A) based on their expression of *Th* and *Fos*. Finer classifications of single cells that express both input-type markers are included. The grey line segments in the upper right quadrant of the plot represent the threshold limits used to define four intermediary cell subtypes 1) Th^{high}/Fos^{low} (red circles), 2) Th^{high}/Fos^{high} (yellow circles), 3) Th^{low}/Fos^{low} (cyan circles), and 4) Th^{low}/Fos^{high} (grey circles) cells. A 30% quantile limit of *Th* expression of the single cells from hypertensive rats was used to define which cells would be classified as Th^{low} and Th^{high}. The median *Fos* expression value of the intermediary cells was used to define Fos^{low} and Fos^{high} cells. (B) Locating intermediate cell types in multidimensional gene expression space. 3D MDS projection of single cells with the four intermediate subtype classifications applied. These intermediate subtypes lie in-between the extreme groups (smaller more transparent spheres). Neurons with higher *Th* expression are positioned closer to the extreme *Th+/Fos-* subtypes while cells with more dominant *Fos* expression are positioned closer to the extreme *Th-/Fos+* subtypes group. (C) Gene expression gradients in intermediate cell types. Gene expression gradient pattern observed in heat map across intermediate cell groups. Focusing on the middle region in-between the whited-out sections of the heat map, gene expression gradient patterns occur across the 'intermediate' input-based cell groups. Moving from left to right, the overall expression patterns of genes in transcription module 1 and transcription module 2 shift from one extreme subtype to the other. Single cells that have more dominant *Th* expression have gene expression profiles more similar to cells within the *Th+/Fos-* subtypes while cells with more dominant *Fos* expression have expression patterns similar to the *Th-/Fos+* subtypes.

Mapping these annotations onto the MDS visualization of cell states revealed that the subtypes showing lower *Th* or *Fos* levels were located in between the two extreme cell types (Figure 3.9B). Similarly, subtypes showing higher levels of *Th* or *Fos* aligning closer to the corresponding extreme input-based subtype. Additionally, these results indicate that the 48 highly variable genes show correlated expression within these intermediate subtypes (Figure 3.9C). The gene expression in the

intermediate subtypes was correlated based on the same modules observed in the cases of the extreme *Th*+/*Fos*- and *Th*-/*Fos*+ subtypes, as shown in Figure 3.10.

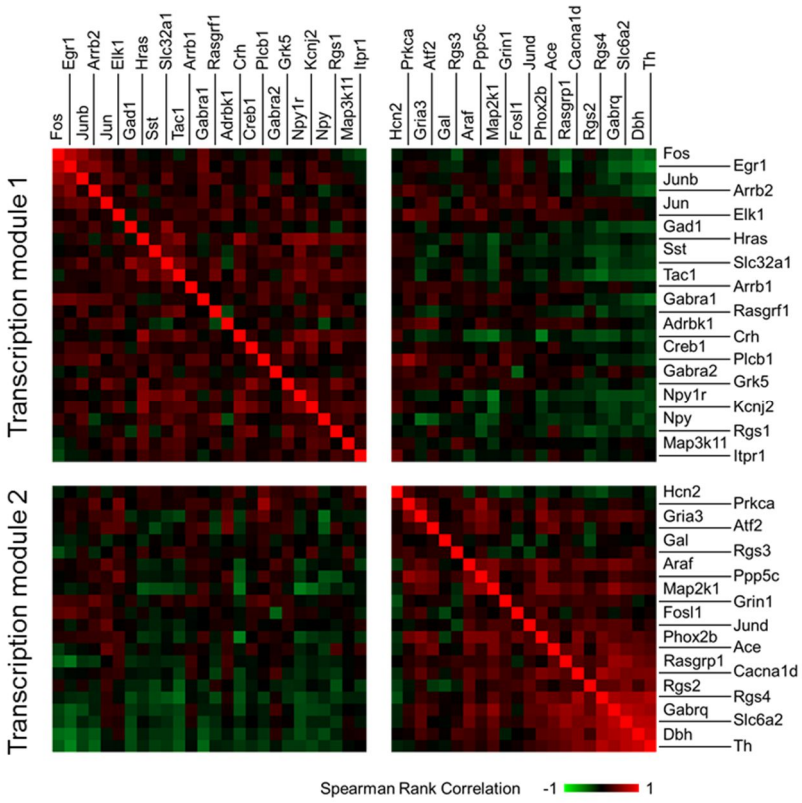

Figure 3.10 Gene-to-gene spearman rank correlations. Spearman rank correlation coefficients were calculated for pairwise comparisons of the subset of 48 genes across single cells having expression of both *Th* and *Fos* (i.e., cells in the intermediate groups). The Spearman correlation coefficients (ranging from –1 to 1) between all pairs are shown in the heat map. Genes within transcription module 1 have a slightly higher correlation coefficient with each other than with those in module 2 and vice versa. However, the overall values of the spearman correlation coefficients are lower than those calculated between genes across single cells of the extreme subtypes (*Th*+/*Fos*- and *Th*-/*Fos*+ groups).

3.3.3.2 Assessment of *Th* and *Fos* quantile limits

We further tested the causal relationship of *Fos* and *Th* by varying the threshold limits used to define the neuronal subtypes. Threshold levels applied to *Th* and *Fos* expression levels ranging from a 5% to 25% quantile limit were used to redefine the subtypes. Using the new subtype classification, it is clear that regardless of the quantile limit used, cells classified in the extreme subtypes continue to cluster into extreme groups in the MDS space while the intermediate groups remain clustered in-between these extreme groups, as illustrated in the following series of figures (3.11-3.14).

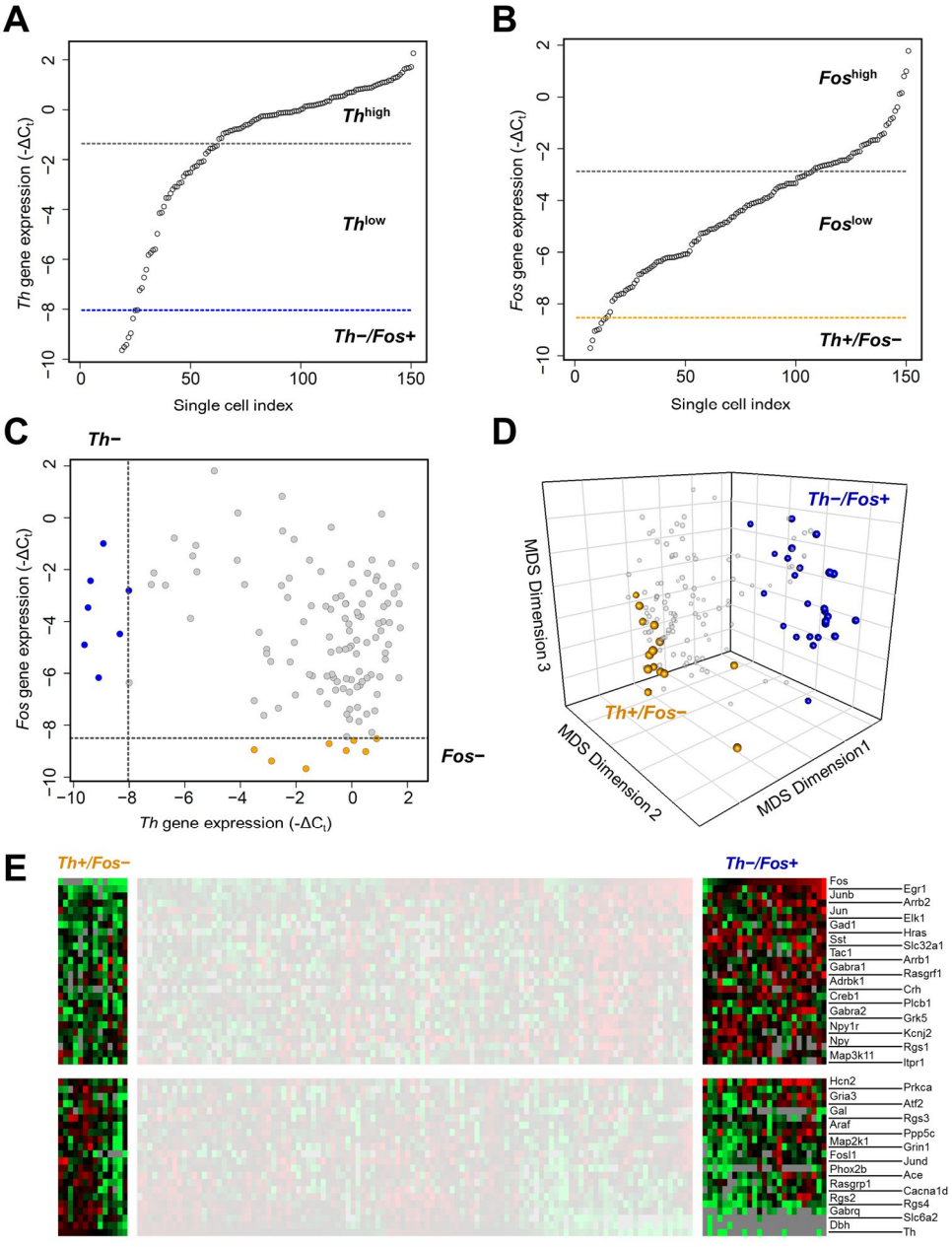
A
Th gene expression (-ΔCt)
Thhigh
Thlow
Th−/Fos+
Single cell index
B
Fos gene expression (-ΔCt)
Foshigh
Foslow
Th+/Fos−
Single cell index
C
Th−
Fos gene expression (-ΔCt)
Fos−
Th gene expression (-ΔCt)
D
Th−/Fos+
Th+/Fos−
MDS Dimension 3
MDS Dimension 2
MDS Dimension1
E
Th+/Fos−
Th−/Fos+
Fos
Junb
Jun
Gad1
Sst
Tac1
Gabra1
Adrbk1
Creb1
Gabra2
Npy1r
Npy
Map3k11
Egr1
Arrb2
Elk1
Hras
Slc32a1
Arrb1
Rasgrf1
Crh
Plcb1
Grk5
Kcnj2
Rgs1
Itpr1
Hcn2
Gria3
Gal
Araf
Map2k1
Fosl1
Phox2b
Rasgrp1
Rgs2
Gabrq
Dbh
Prkca
Atf2
Rgs3
Ppp5c
Grin1
Jund
Ace
Cacna1d
Rgs4
Slc6a2
Th

Figure 3.11 Varying *Th+/Fos-* and *Th-/Fos+* thresholds (5% quantile limits). Specified quantile values were used to define the limits used to categorize single cells within the subtypes. Single cell projections in the MDS space were examined under various quantile limits used to categorize single cells in the two extreme subtypes. (A) 5% quantile limit for *Th+* expression is represented by the blue dashed line. Cells below the blue dashed line are categorized as *Th-/Fos+* cells. Single cells above the blue dashed line are categorized as either Th^{high} or Th^{low} cells. The green dashed line represents the 30% quantile limit used to determine which cells are Th^{high} (above green line) or Th^{low} (below green line). (B) 5% quantile limit for *Fos+* expression is represented by the orange dashed line. Single cells below the orange line are categorized as *Th+/Fos-* cells. The green dashed line represents the median expression value of the remaining single cells and is used to determine which remaining single cells are Fos^{high} or Fos^{low}. (C) The resulting bivariate plot showing the scatter of single cells and what cells are categorized in the two extreme subtypes. (D) The resulting 3D MDS visualization of single cell correlations based on rank ordered gene expression. Note how the newly defined single cells continue to be projected at opposite extremes of the MDS space. (E) The corresponding rearranged heat map representing the scaled gene expression data. Rows represent genes while columns represent single cells. Single cells within each subtype are rank ordered by their respective *Th* or *Fos* expression level.

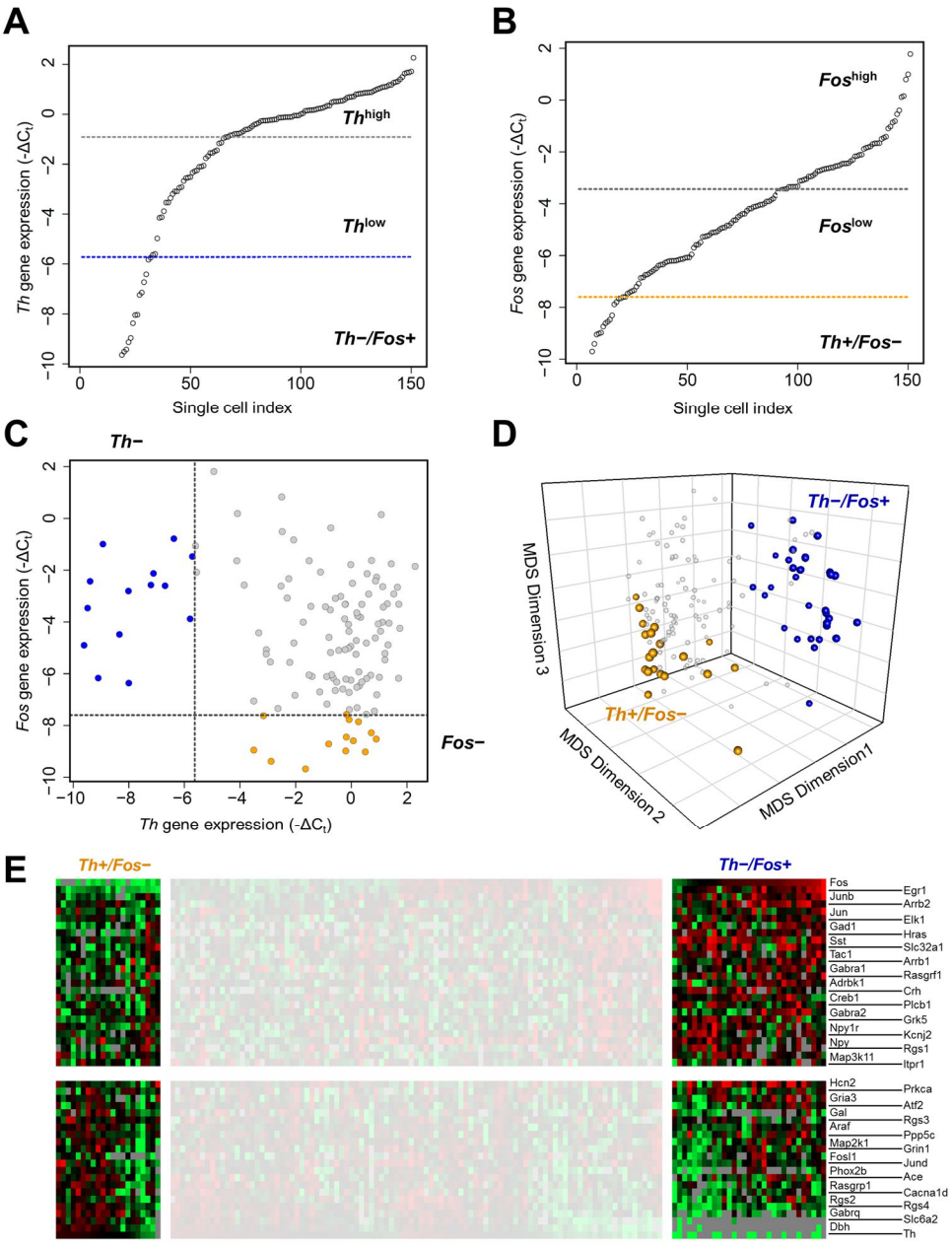

Figure 3.12 Varying *Th+/Fos-* and *Th-/Fos+* thresholds (10% quantile limits). Stepwise process of defining expression limits for *Th* and *Fos* and how the resulting cells are projected into the 3D MDS space based on their similarity (or dissimilarity) in rank ordered gene expression of the 48 genes identified from PCA. Annotation is identical to Figure 3.11.

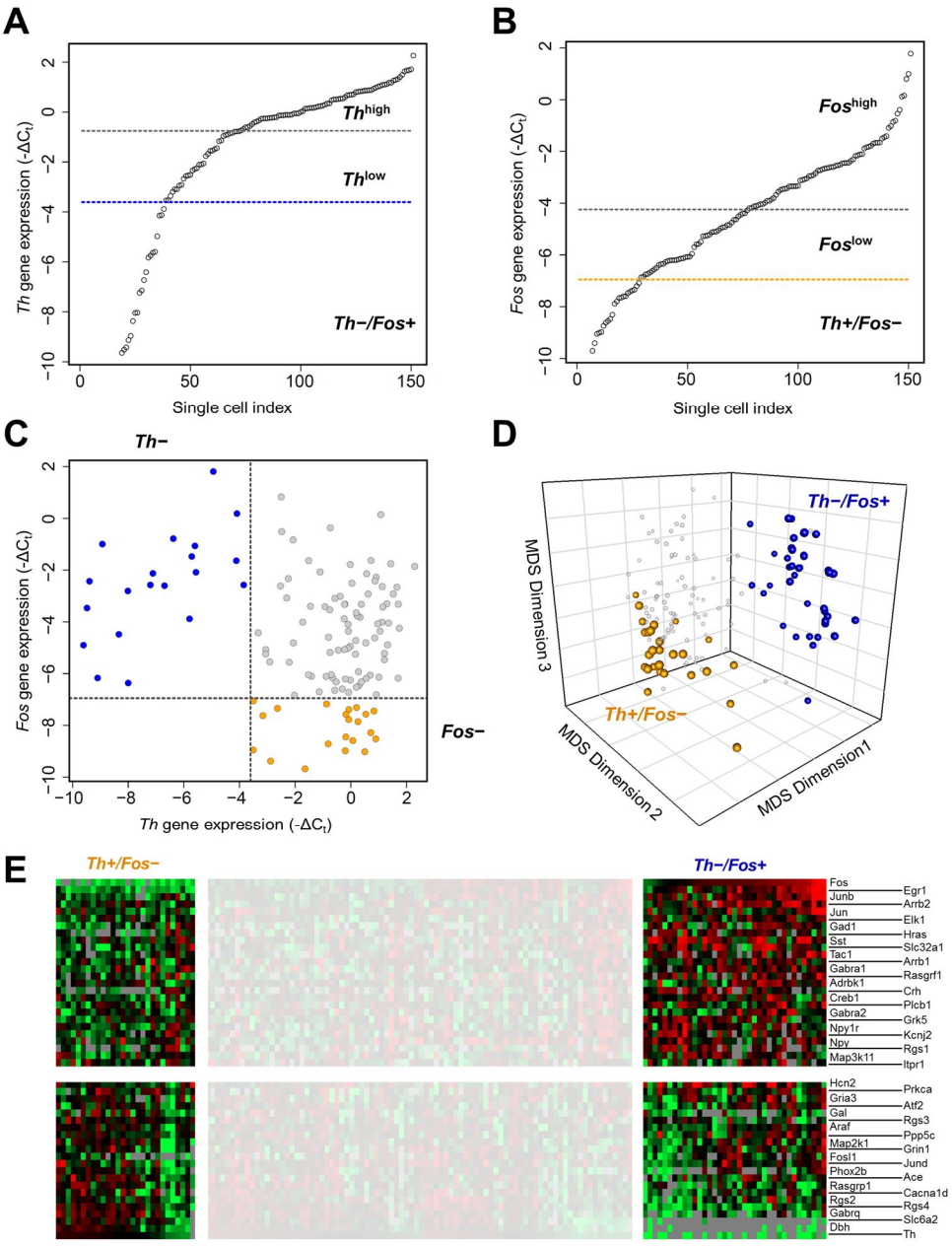

Figure 3.13 Varying *Th+/Fos-* and *Th-/Fos+* thresholds (15% quantile limits). Stepwise process of defining expression limits for *Th* and *Fos* and how the resulting cells are projected into the 3D MDS space based on their similarity (or dissimilarity) in rank ordered gene expression of the 48 genes identified from PCA. Annotation is identical to Figure 3.11.

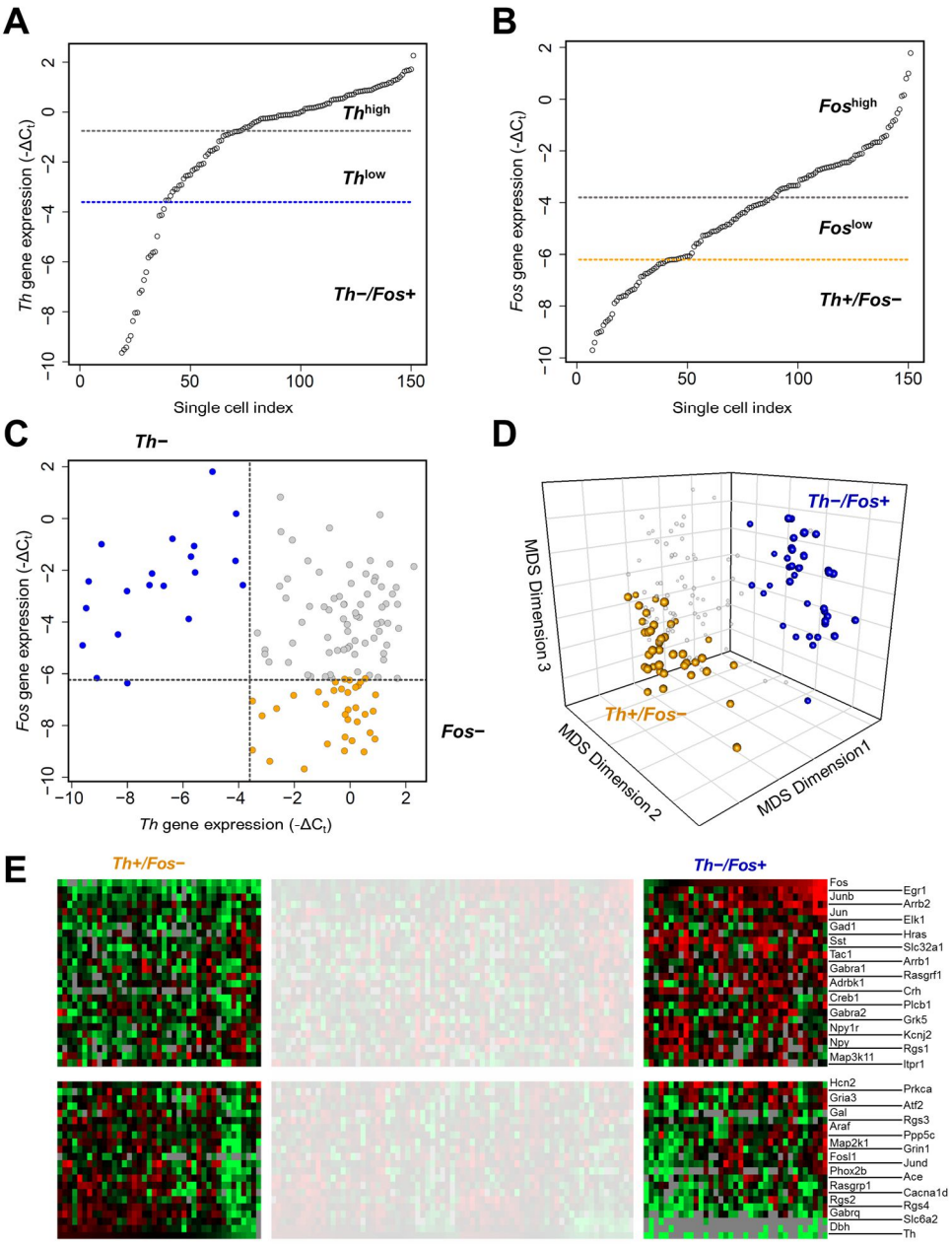

Figure 3.14 Varying *Th+/Fos-* and *Th-/Fos+* thresholds (15% and 25% quantile limits). Stepwise process of defining expression limits for *Th* and *Fos* and how the resulting cells are projected into the 3D MDS space based on their similarity (or dissimilarity) in rank ordered gene expression of the 48 genes identified from PCA. A 15% quantile value is used to define *Th+* cells while a 25% quantile value is used to define *Fos+* cells. Annotation is identical to Figure 3.11.

The persistent placement of single cells at the extreme regions in the MDS space indicates that this multiplex gene gradient behavior across single cells is indeed strongly correlated to the strength and magnitude of the inputs received. Regardless of the *Fos* expression or *Th* expression threshold level used, cells with the highest *Fos* or highest *Th* expression tended to be the same cells having extreme expression of the 48 variable genes highlighted by PCA.

3.3.4 Distinct gene correlation network structures

The coordinated gene expression patterns within the gene groups, or transcription modules (Figures 3.8), further differentiate the expression states of cells. The various active states that lie along the gradient structure are governed by underlying gene regulatory networks, which can be used to further distinguish these states. A comparison of rank correlative gene networks, a surrogate for the regulatory interactions occurring in single cells within the extreme states illustrated in Figure 3.8C, shows distinct structures of correlative gene expression behavior, which is shown in Figure 3.15.

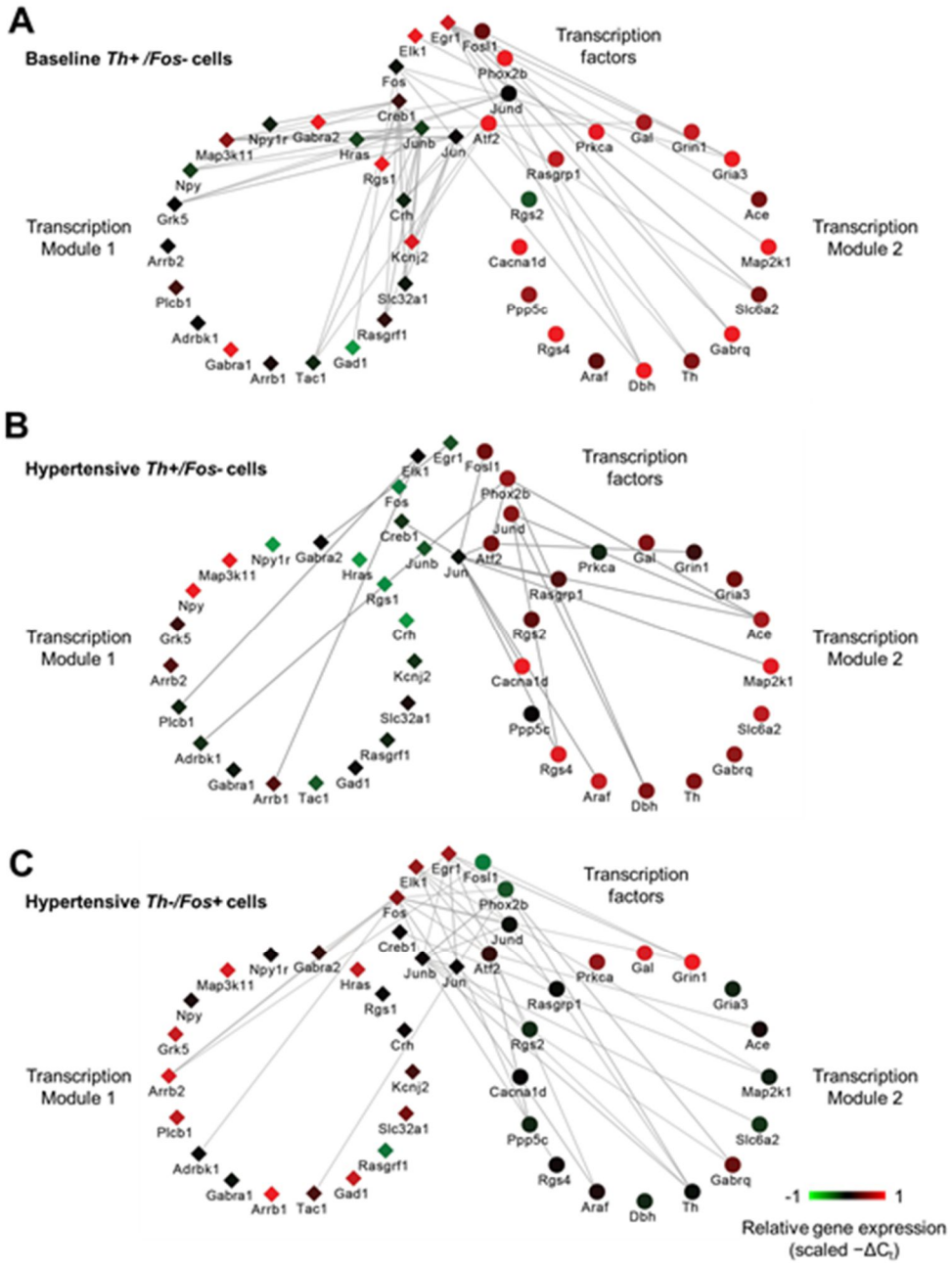
A
Baseline Th+ /Fos- cells
Transcription factors
Transcription Module 1
Transcription Module 2
Egr1
Elk1
Fosl1
Fos
Phox2b
Jund
Creb1
Junb
Jun
Atf2
Npy1r
Gabra2
Map3k11
Hras
Rgs1
Prkca
Gal
Grin1
Rasgrp1
Gria3
Npy
Grk5
Crh
Rgs2
Ace
Arrb2
Kcnj2
Cacna1d
Map2k1
Plcb1
Slc32a1
Ppp5c
Slc6a2
Adrbk1
Rasgrf1
Rgs4
Gabrq
Gabra1
Gad1
Araf
Arrb1
Tac1
Dbh
Th
B
Hypertensive Th+/Fos- cells
Transcription factors
Transcription Module 1
Transcription Module 2
C
Hypertensive Th-/Fos+ cells
Transcription factors
Transcription Module 1
Transcription Module 2
-1
1
Relative gene expression
(scaled −ΔCt)

Figure 3.15 Gene correlation networks. The correlative network structures represent correlative relationships shared between TFs and target genes of each module across the three cell types: baseline *Th*+, hypertension *Th*+, hypertension *Fos*+. Cytoscape software was used to visualize the correlative network relationships. Edge opacity represents the strength of the correlation shared between genes across the respective sample subset (e.g., *Th+/Fos*- single cells), the darker the edge, the higher the correlation coefficient values. These network structures illustrate the pairwise spearman rank correlative relationships among the subset of 48 genes. Transcription factors (TFs) are separated from the subset while the remaining genes are organized into their respective transcription modules 1 and 2 (figure 3.8C). The correlation network is based on pairwise gene correlations across various subsets of single cells. Only pairwise Spearman correlation coefficients ≥ 0.4 were included. Node colors represent scaled $-\Delta C_t$ values of from a representative single cell sample from the respective neuronal subtype. (A) Pairwise gene correlation network across normotensive single cells. Note the high number of correlative relationships shared between TFs and genes from both modules 1 and 2. (B) Correlation network based on hypertensive *Th+/Fos*- single cells show a significant change in the number of correlative relationships between TFs and downstream target genes and the majority of these relationships exist between TFs and genes within module 2. Similarly, this same shift in pairwise relationships occurs in *Th-/Fos*+ single cells, shown in (C). This shift in relationships suggests that a physiological perturbation, in this case acute hypertension, causes a shift in the correlative relationships between TFs and downstream genes.

In the baseline *Th*+/*Fos*- network, transcription factors (TFs) showed a high degree of connectivity, i.e., correlative relationships, with genes across both transcription modules. However, under the hypertensive challenge, the relationships between TFs and genes within the transcription modules were reduced and shift mainly to genes in transcription module 2 in the *Th*+/*Fos*- (higher-order input cell) and *Th*-/*Fos*+ (second-order input cell) networks.

3.3.5 Comparison of single NTS neurons across treatment conditions and animals

These input-driven shifts in expression correlation and potential gene regulation effects were also reflected in the constrained space occupied by hypertensive *Th+/Fos-* cells relative to the *Th+* cells from control animals at baseline blood pressure levels. The constrained transcriptional response of the hypertensive *Th+/Fos-* cells are shown in Figure 3.16. The constrained transcriptional space occupied by hypertensive *Th+/Fos-* cells suggests that neurons in response to an acute hypertensive challenge are forced into constrained functional states, potentially reducing the adaptive response of these neurons.

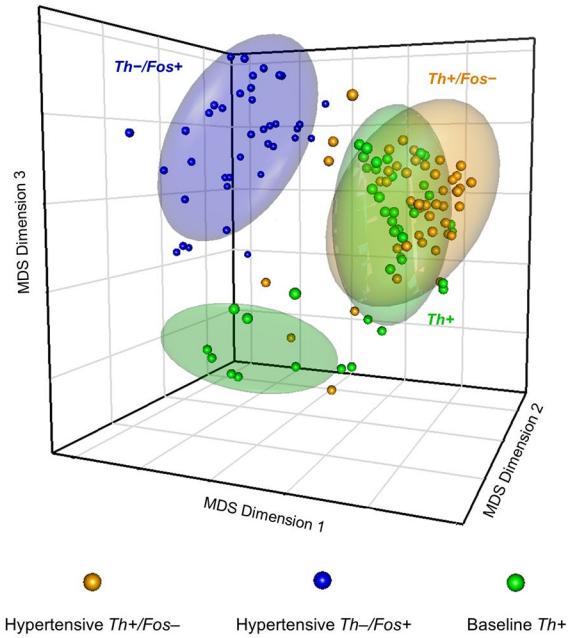

Figure 3.16 Constrained transcriptional behavior of hypertensive cells. A projection of the similarity values of single cells (based on rank ordered gene expression of the 48 genes identified in PCA). Normotensive *Th*+ single cells (green spheres) are included along with hypertensive *Th+/Fos*- single cells (orange spheres) and *Th-/Fos*+ single cells (blue spheres). The ellipsoids represent the 65th percentile of the single cell density for each subtype. Outliers within each subtype (single cells outside of the 95th percentile density for each subtype) were not included when defining these ellipsoids. In the case of the normotensive ellipsoids, two ellipsoids were included to represent the space occupied the normotensive single cells. The hypertensive *Th+/Fos*- cells occupy a smaller constrained space than their normotensive counterparts.

Although there was some individual rat-to-rat variability within these transcriptional modules, each neuronal subtype is composed of samples from multiple rats. If animal variability were the dominant source of single-neuron transcriptional heterogeneity, then we would expect that each subtype identified would be composed mainly of samples from one anima. However, that is not the case as samples from

multiple animals comprise each of the neuronal subtypes; the same pattern of structured variation across input classes is present in each animal, represented in Figure 3.17.

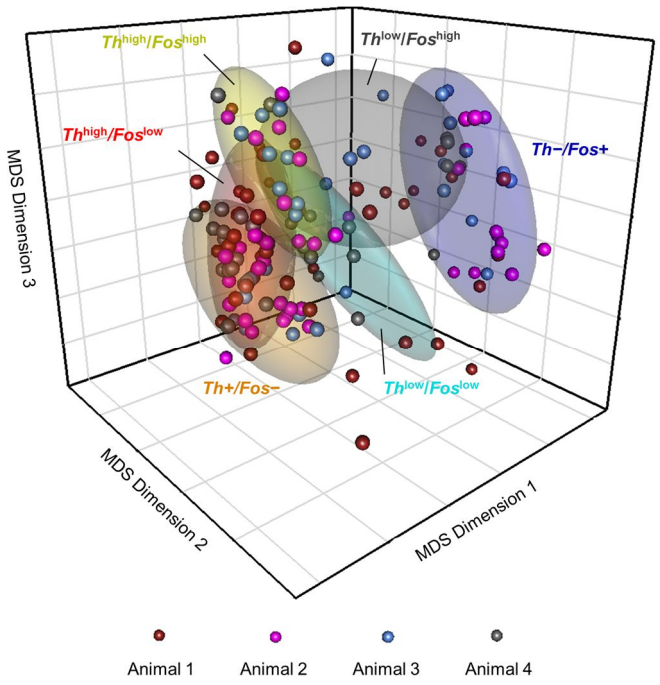

Figure 3.17 Subtype clusters maintained across animal subjects. Single cells in the 3D MDS space are annotated with the respective animal subjects from which they were taken from. Ellipsoids were added to represent the input-type defined subtypes originally identified (orange: *Th+/Fos-*, red: Th^{high}/Fos^{low}, yellow: Th^{high}/Fos^{high}, cyan: Th^{low}/Fos^{low}, grey: Th^{low}/Fos^{high}, blue: *Th-/Fos+*). The ellipsoids represent the 65th percentile of the single cell density for each subtype. Outliers within each group (single cells outside of the 95th percentile population density for each subtype) were not included when defining these ellipsoids. Single cells from their respective animal subjects are scattered throughout all subtypes and are not concentrated to one particular ellipsoid indicating that these clusters are not an artifact of animal variability.

3.3.6 Statistical significance of *Th* and *Fos* quantile limits and neuronal subtype organization

In order to determine the statistical significance of the molecular organization identified, as exemplified by the clustering of NTS neurons into transcriptional subtypes (Figure 3.8-3.9), we determined the likelihood of whether similar extreme neuronal subtypes would form randomly from the existing data set. Towards this goal, we performed the same statistical analysis described in § 3.2.5.3 (pairwise spearman rank gene correlation and MDS visualization of the dissimilarity data) on random permutations of the 48-gene "vectorized" data set of the single cells analyzed.

Permutation of the data consisted of randomly shuffling the gene expression values ($-\Delta C_t$) within a single cell sample. For example, the original *Fos* expression value would be randomly switched with the expression value of *Atf2, Th* switched with *Tac1*, and so on and so forth. This random shuffling of gene expression data was performed on each single neuron resulting in a single iteration of a random permutation of the data. Using the randomly shuffled data set, all possible pairwise comparisons between single cells were made to determine the Spearman rank correlation coefficient. This was then converted into a distance metric and projected into a three dimensional space using MDS.

The same *Th* and *Fos* quantile limits were used to define the two extreme sub-types identified in our original analysis (*Th*+ limit: 15% quantile, *Fos*+ limit: 30% quantile). Thus the 15% quantile limit was defined by the randomized set of *Th* and

Fos expression values. The input-type annotation was then applied to the projected data for the extreme *Th+/Fos-* and *Th-/Fos+* cell groups. We then characterized the relationship between the two extreme cell groups using two quantitative measures typically used to characterize clusters, centroid distance and minimum distance. In this case the centroid distance is defined as the distance between the center of mass (i.e., centroid) within a subtype (using neurons falling within the 95% of the density distribution for the respective subtype). The minimum distance is simply the minimum distance between any two neurons projected within the 3D MDS space. We repeated this permutation and cluster characterization process 1000 times with the existing data set to determine empirical distributions of the centroid and minimum distances.

We then posed the null hypothesis, which states that the Euclidean distance (centroid or minimum distance) between the original extreme neuronal subtypes (within the MDS space) is no different than the distance measure between subtypes identified from the randomly shuffled data set. The alternative hypothesis in this case is that the distance measures between the original subtypes are greater than the distances from the shuffled data set. An example of a permutation and identification of the extreme subtypes and the resulting distributions are shown in Figure 3.18.

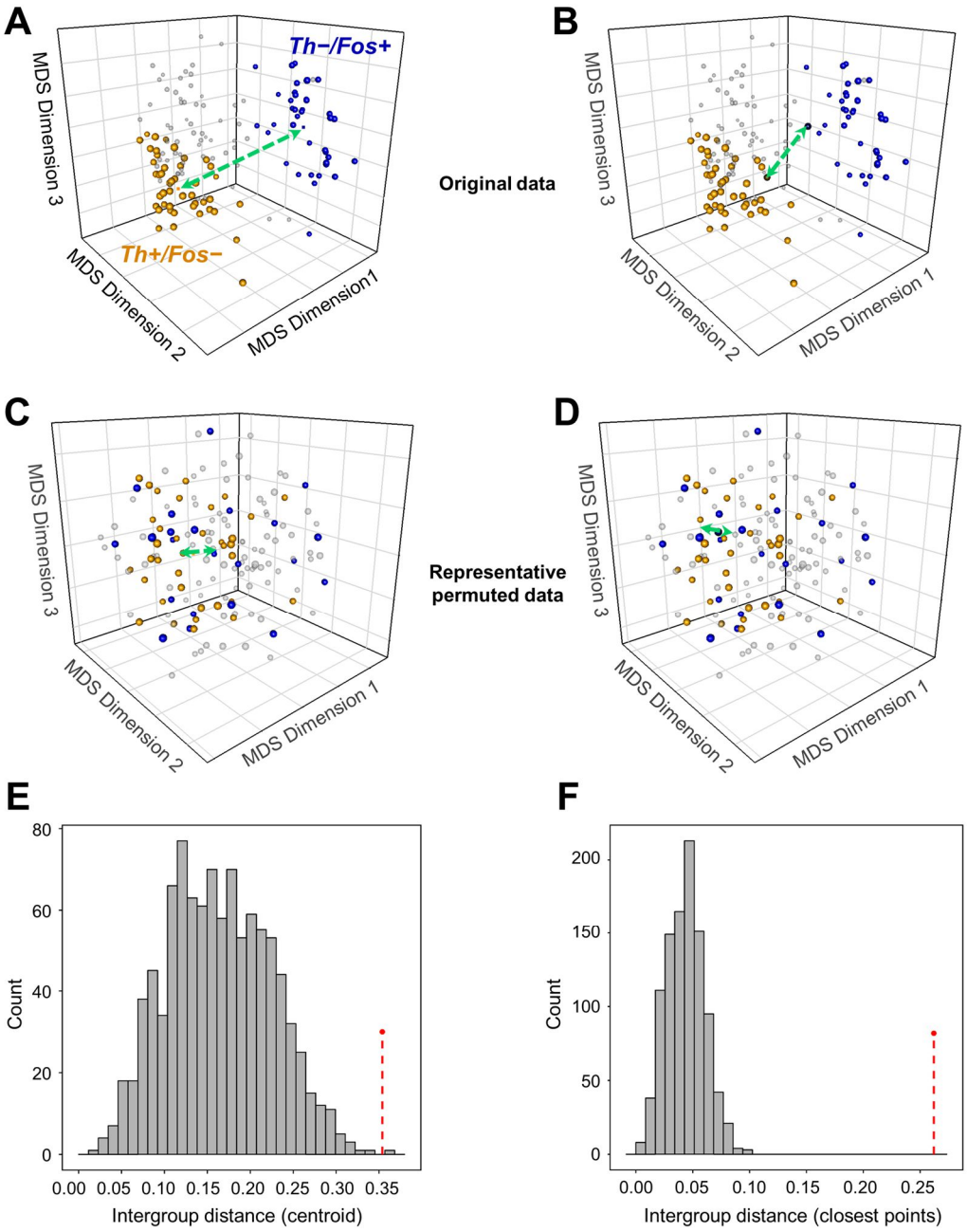
A
Th−/Fos+
Th+/Fos−
MDS Dimension 3
MDS Dimension 2
MDS Dimension1
B
Original data
MDS Dimension 3
MDS Dimension 2
MDS Dimension 1
C
MDS Dimension 3
MDS Dimension 2
MDS Dimension 1
Representative
permuted data
D
MDS Dimension 3
MDS Dimension 2
MDS Dimension 1
E
Count
0
20
40
60
80
0.00 0.05 0.10 0.15 0.20 0.25 0.30 0.35
Intergroup distance (centroid)
F
Count
0
50
100
150
200
0.00 0.05 0.10 0.15 0.20 0.25
Intergroup distance (closest points)

Figure 3.18 Statistical significance of *Th+/Fos-* and *Th-/Fos+* thresholds. Normalized gene expression data was permuted over 1000 iterations to determine the possibility of similar extreme groups forming randomly. The centroid distance and minimum distance between the extreme subtypes were used to characterize their relative positioning. The centroid distance is the distance between central points of each group in the 3D MDS space while minimum distance is the distance between the two closest points between the two groups. (A) Intergroup distance (centroids). The minimum distance (green dashed line segment) between the two extreme subtypes from the original data set. (B) Intergroup distance (closest points). The minimum distance (green dashed line segment) between the two extreme subtypes from the original data set. (C) Intergroup distance of permuted data (centroids). A representative example of a permuted data set and the resulting *Th+/Fos-* (orange spheres) and *Th-/Fos+* (blue spheres) groups. The green dashed line represents the centroid distance while the green dashed line in (D) Intergroup distance of permuted data (closest points). The minimum distance between clusters generated from the permuted data set. (E) Distribution of the centroid distances calculated from the 1000 iterations performed. Only one random permutation achieved the formation of two extreme groups having a centroid distance equal to or greater than the distance found in the original data, shown by the red dashed line (p=.001). (F) Distribution of the minimum distances calculated from a permutation step. None of the iterations produced a minimum distance as large as the distance found in the original data set, shown by the red dashed line (p=0.000).

Of the 1000 iterations performed to generate the distribution of centroid distances, only one permutation of the data was able to achieve a distance between the extreme neuronal subtypes equal to or greater than the distance between the originally defined *Th+/Fos-* and *Th-/Fos+* neuron groups (Figure 3.18). Similarly, none of the permutations resulted in a minimum distance greater than the minimum distance between the original groups. Thus the empirically defined p-value of the centroid and minimum distance between the *Th+/Fos-* and *Th-/Fos+* cell groups are 0.001 and 0,

respectively allowing us to reject the null hypothesis. These values give no reason to suspect that these extreme subtypes or clusters are a result of random chance.

3.4 Discussion

The present analysis of in vivo individual NTS neuron samples of the same neuroanatomical phenotype, examined in the context of specific neuronal input connectivity, revealed that post-developmental neuronal cell type is strongly associated with the specificity of connections. Studying gene expression profiles of NTS neurons at the single cell level provided us with the appropriate resolution to distinguish cell types with respect to the inputs they received. Our results support the importance of connectivity in defining a cell type, through the transcriptional regulation of neurons by their inputs. Viewing the distribution of neuronal cell types as a function of specific inputs allowed us to interpret cell-to-cell variability as structured heterogeneity rather than noise around a mean.

This single cell variability likely reflects cellular functional heterogeneity [26], influencing a cell's position along the gradient of the observed multiplex gene expression (Figure 3.8D). This structure is evident in the MDS visualization where single cells fall into input-defined clusters of cells that are positioned along an expression pattern gradient (Figure 3.8D, 3.9C). Since input-history of an individual cell influences the cell's transcriptomic state, we postulate that the cumulative input-history of a neuron provides a driving force for adjustment or analog tuning of the transcription modules, placing neurons within interchangeable, stable states along the

gradient of catecholaminergic (*Th*+/*Fos*-) and non-catecholaminergic (*Th*-/*Fos*+), hypertension-responsive neurons states.

Visualization, using MDS, of gene expression gradients, dynamic landscapes, and analog tuning of expression defining cell development and function is a recent application used most notably in hematopoietic and embryonic stem cells, and cell signaling systems, such as NFKB signaling [52,53,232]. Our application of such techniques and concepts to ostensibly terminally differentiated single cells is novel as far as we are aware. The input-based ordered structure within the heterogeneous gene expression of single neurons in the MDS space now allows us to contextualize single cells along transcriptional module gradients, suggesting a plastic rather than a discrete cell phenotype. Finding correlated gene expression modules delineated by inputs is consistent with transcriptional phenotypes that result from combinatorial inputs. Subsequent variability within a given phenotype results from differences in input type and strength to each cell. In this context, any additional variability within a sub-phenotype, reflected in the spread of single cells of that particular group, may reflect variability of other inputs to the cell population. Additional input-driven analysis would be expected to further fractionate the phenotype.

Our results, which suggest an input-based organization of the NTS neuronal phenotype within a cloud of cellular states, raise intriguing possibilities as to the mechanisms through which such a gene expression gradient could be tuned in individual neurons. It is likely that combinatorial actions of transcriptional and post-

transcriptional regulatory processes are involved in transducing cellular inputs into the downstream regulation of transcriptional state. Such regulatory network coordination to generate complex patterns of gene expression has been well described with respect to developmental dynamics, and typically involves a unique combination of regulatory factors for each cell type [11–13,233,234]. It is possible that such formalism extends into post-developmental gene expression variability between neuronal phenotypes. We should also consider alternative regulatory schemes where graded gene expression spanning the spectrum of cellular states may be driven by a set of regulators in common to the NTS neuronal phenotypes, with inputs tuning cell-to-cell differences in regulatory activity and combinatorial action. Given the 1 h duration of the hypertension perturbation in our study, it is unlikely for the transcriptional regulatory network to influence neuronal network connectivity in such a short period. Hence, such feedback cannot serve as an alternative explanation of association between cellular inputs and correlated gene regulatory states.

These interchangeable cell states can be schematically represented as a dynamic gene expression landscape populated by individual cells based on their transcriptional response, illustrated in Figure 3.19A-B. The contour plots and 2D figures are used to help illustrate the concepts of distinct cell states and the influence inputs have in determining these states. The contour pots are a projection of the single cells in the 3D MDS space onto a 2D plane (Figure 3.19A-B).

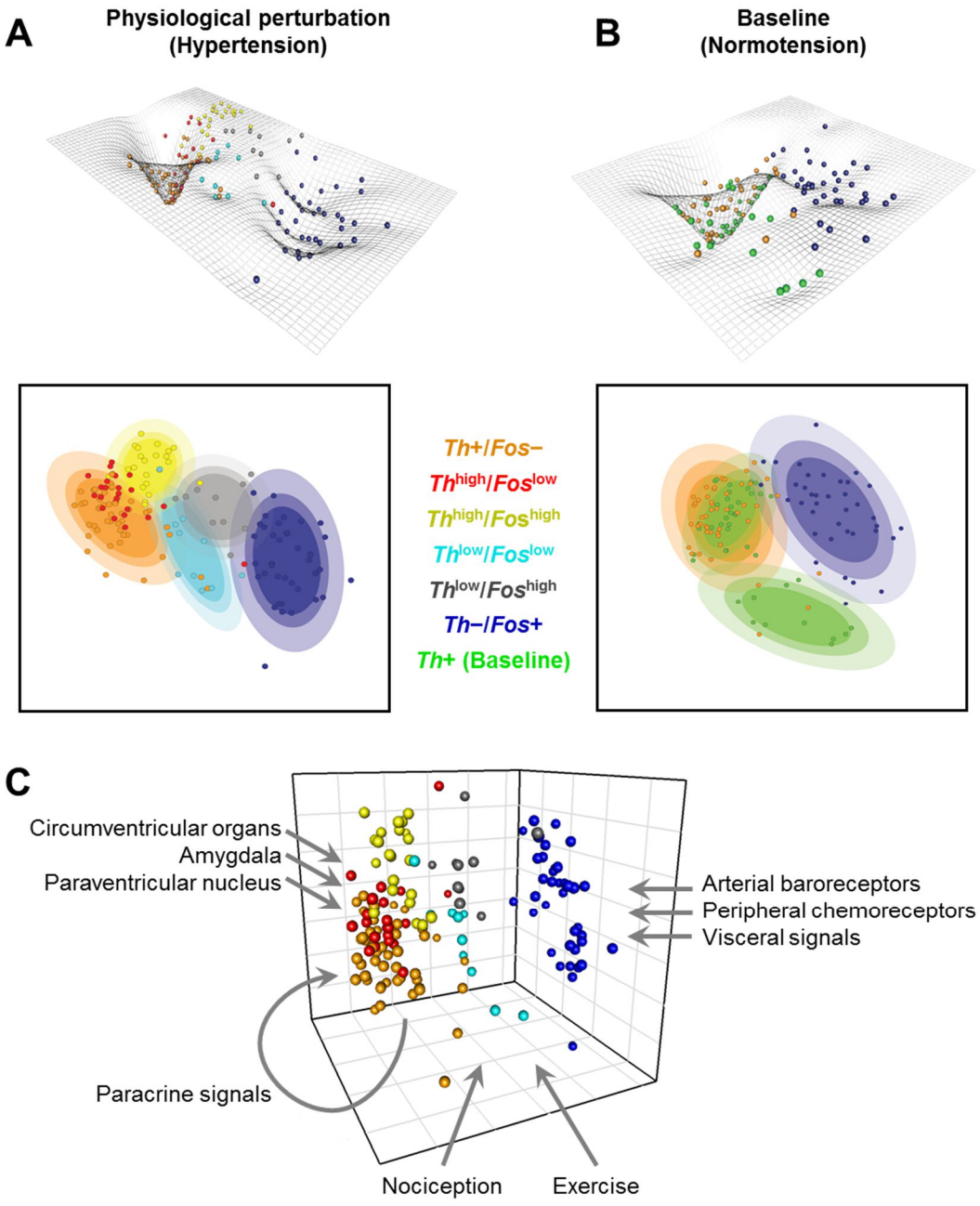
A
Physiological perturbation
(Hypertension)
B
Baseline
(Normotension)
Th+/Fos−
Thhigh/Foslow
Thhigh/Foshigh
Thlow/Foslow
Thlow/Foshigh
Th−/Fos+
Th+ (Baseline)
C
Circumventricular organs
Amygdala
Paraventricular nucleus
Arterial baroreceptors
Peripheral chemoreceptors
Visceral signals
Paracrine signals
Nociception
Exercise

Figure 3.19 Reversible cell states within the phenotype landscape shaping the variability and organization of single cell states. Contour plots are used to illustrate the concepts of distinct cell states and the influence inputs have in determining these states. The contour pots are a projection of the single cells in the 3D MDS space onto a 2D plane. The landscape topography is based on an inversion of the probability densities of single cells. Cell states are represented by wells in the landscape and ellipsoid regions in the 2D contour plot. The colored ellipsoids capture these states and symbolically represent potential "attractor"-like states within this landscape. These contour and landscape topographies were created for single cells collected from rats undergoing an acute hypertension challenge (A) and from baseline normotensive rats (B). Comparing these two landscapes (A and B) shows that the well in which catecholaminergic cells (orange spheres in A and B) lie is much more constrained and local under the hypertensive challenge than in the baseline state. The changing landscape between the two physiological states suggests that physiological perturbation (e.g., hypertension) influences not only the state of the single cells, but the very nature of the landscape in which they exist. Thus inputs have significant impact on transcriptional behavior and ultimately the phenotypic state of a cell. (C) Input-based gene expression phenotypes in NTS. Schematic of the influence of various inputs into the NTS shaping the cellular state and organization within a "homogeneous" single cell phenotype. Integrative inputs place demands on homeostasis such as those conveying visceral states, pain, posture, exercise, temperature, circadian time, mood etc. NTS neurons must integrate distinct combinatorial input sets. Our data revealed that gene expression variability across single neurons reflects their combinatorial inputs.

This perspective provides a further reduction of the high-dimensional dissimilarity data set. Moreover, the contour plots provide a simplified perspective on how the various input-type groups are positioned relative to one another. The placement of the *Th+/Fos-* and *Th-/Fos+* groups are clearly positioned at the extremes of the entire region, or landscape, while the intermediate groups occupy the intermediate region in-between the two extreme groups. This schematic also illustrates

the idea of how a single cell may transition between respective cell states and the likelihood of such a transition occurring. Cell states that share a high degree of overlap, as is the case with the *Th+/Fos-* and Th^{high}/Fos^{low} are more likely to have single cells transition between these states as opposed to distinct states that are much farther apart. The various colored contours represent the 65th, 95th, and 99th percentile of the single cells for any given input-type group. Outliers, defined as cells falling outside of the 95th percentile of all single cells classified within a subtype, were not included in defining the 65th, 95th, 99th percentile. The majority of cells lie within the inner most contour region in this topology (65th percentile – Figure 3.19A-B).

To further emphasize the dominant transcriptional states and how these states relate to one another, a landscape topography was created. The landscape topography is based on an inversion of the probability densities of single cells. When there is a greater concentration of cells in a particular region, such as those found in the 65th percentile of a particular input-type group, the probability density is much higher and decreases as one moves away from these regions of high single cell concentration. A topographical plot based on the probability densities was then inverted in order to create regions of lower values or valleys in this landscape to highlight the stability associated with these dominant transcriptional or potential "attractor"-like states. As a single cell moves away from the inner most contour or deep well, it is transitioning away from the well and climbing up towards a less stable state, which is less occupied by the single cells. Depending on the inputs received, single cells may occupy these various stable valleys and intermediate levels within these valleys.

The landscape figures and 2D contour plots help illustrate the distinct cell states and the influence of inputs. Such a conceptualization is an evolution of the Waddington's concept of "canalization" (§ 1.3), which describes developmental phenotypes [26,56] and was employed to organize the interrelationships between various cell types that emerge through dynamic expression changes during development [26]. The contour plots are a projection of the single cells in the 3D MDS space onto a 2D plane. The 'depth' of a well along the landscape at any given location was derived from the local density of cells so that a cluster of many cells is deeper and indicates a potential local "attractor" reflecting constrained gene expression in those particular cells. In this representation, these valleys and wells, or "attractor"-like states, correspond to dominant expression states of relatively stable expression modules (e.g., those corresponding to *Th*+/*Fos*- and *Th*-/*Fos*+ extreme subtypes). The remaining topography corresponds to potential intermediary states that may be transient in response to input histories of individual cells and physiological perturbations. The path that these cells take along the gene expression landscape is a function of the input(s) received and is likely to be as varied as the input(s) themselves. The exposure to a hypertensive challenge changes the constraints (Figure 3.16) and distribution of cells within the gene expression landscape (Figure 3.19A-B), consistent with phenotypes that are determined by distinct state-dependent responses. Ultimately, the type of inputs received alters the regulatory network resulting in constrained cell states, akin to a phenotype being an adaptive product of cellular input.

Plausibly, NTS *Fos*+ cells plausibly receive particular combinatorial inputs

beyond blood pressure and integrate variable sets of cardiovascular homeostasis modulators such as pain, temperature, exercise or mood, all of which affect cellular state and input-processing. The influence of various inputs on NTS cell state is symbolically represented in Figure 3.19C [109,210,235–237]. Such input-based influences imply that NTS neurons are individually gated in dynamic responses to combinatorial inputs, rather than behaving as a homogeneous population and integrating all inputs into a population rate code. NTS neurons dynamically responding to inputs drive a mechanism of blood pressure homeostasis based on the selection or gating of particular NTS neurons activated by combinatorial demands on blood pressure.

Similarly demonstrating a functional meaning to variability, Marder and collaborators have shown that variability extends to the levels of electrical and neural network function [100]. In this mechanism, the "neural code" by which blood pressure regulation is performed would be based on molecular states of individual neurons. This novel explanation of blood pressure homeostasis in terms of parallel distinct functional response pathways is something not found when assuming a rate code control by a homogeneous neuronal population. A mechanism of this kind is consistent with the presence of variable activity and absence of a blood pressure rate code observed in NTS baroreceptor neurons [114,141,238].

The principles of input-structured phenotype described in this chapter may extend to other central neuronal phenotypes. Large populations of neurons with multiple sources of inputs, adaptive response to inputs and variable activity of single

neurons are common in the brain. Measures of adaptive variability within a neuronal phenotype may enable development of a molecular physiology interacting with higher-level functions. This expectation of the influence of input history on neuronal cell type and function across the brain is supported by the emerging perspective reflected in the recently announced BRAIN initiative (§ 1.1.1). With the convergence of sophisticated experimental techniques and accurate and precise high-throughput technologies we have a unique opportunity to develop "*…an integrated view of molecular identity (DNA sequence, single-cell transcriptomes, epigenomic information, and protein expression). This picture, in combination with information on anatomical connectivity and functional measures (e.g. physiology) will afford an unprecedented view of the vertebrate brain.*" [40].

Based on the analyses and results described in this chapter, an alternative hypothesis can now be proposed on how a neuronal population and more generally a cellular population supports robust biological function: functional robustness is achieved through the development of distinct neuronal subtypes that exhibit graded cellular responses, rather than a uniform population response. The functional consequence of an adaptive neuronal response will be explored further via mathematical modeling in Chapter 5. The results detailed in this chapter expand the definition of a neuronal cell type to include post-developmental plasticity and highlights the role of transcriptional regulation in shaping these phenotypes. In a related manner, as correlated gene expression is indicative of underlying regulatory network influences, it is conceivable that the identification of cell-type-specific gene

network topologies may be facilitated by organizing the variable transcriptional responses of individual cells into distinct cellular subtypes. Concomitantly, identifying the underlying gene regulatory interactions would aid to clarify the molecular mechanisms that contribute to the formation of these phenotypes, which is the focus of Chapter 4.

Chapter 4

GENE NETWORK IDENTIFICATION FROM VARIABLE SINGLE-CELL TRANSCRIPTOMIC DATA

In Chapter 3, a molecular framework was identified in which transcriptionally heterogeneous single neurons belonging to the same neuroanatomical phenotype of the NTS organize into distinct neuronal subtypes that align with synaptic input-types. These subtypes are characterized by graded, correlated gene expression, which suggests the influence of underlying gene regulatory network(s). The development of a methodology to identify and generate quantitative models of gene interaction networks from heterogeneous single-cell transcriptomic data is the subject of the current chapter.

4.1 Introduction

As discussed in Chapter 3, the variability observed in the transcriptional states of single brainstem neurons can be understood in terms of the distinct combinatorial synaptic inputs each neuron receives [105]. These inputs drive individual NTS neurons into distinct neuronal subtypes that lie along a transcriptional landscape characterized by a gene expression gradient. The correlated gene expression spanning the distinct neuronal subtypes described in Chapter 3 suggest an underlying regulatory

network is influencing this expression behavior [67,239,240]. Identifying the gene interactions that drive the observed correlated gene expression would provide insight into the molecular mechanisms that shape these neuronal subtypes and further elucidate the "integrated view of molecular identity" of neurons within the brain [40]. There is a need, however, for a robust approach to derive data-driven causal network hypotheses that can be used to interpret and predict the heterogeneous transcriptional behavior of single cells along this transcriptional landscape.

Inferring underlying gene regulatory networks via statistical analysis of single-cell transcriptional data is often complicated by extensive single-cell heterogeneity. However, information about underlying regulatory networks are often manifest in the form of correlations observed in gene expression patterns across single cells. Consequently, single-cell transcriptomic data sets provide a rich experimental sampling of transcriptional states over a wide range of cellular responses that can then be used to infer the underlying regulatory network structure [27,30,69,241]. Several methods have been previously developed for deducing regulatory network structures from gene expression data. Statistically-based approaches rely on correlational relationships and dependencies to cluster gene expression profiles, with the rationale being that co-expressed genes are likely to be functionally related [239,242]. One concern with these methods is that the correlational relationships confound direct and indirect effects and do not necessarily imply causal interactions.

Other approaches such as the popular method known as ARACNE overcome these limitations by employing information-theoretic approaches to distinguish

between direct and indirect gene interactions [205]. Alternatively, Boolean networks have been used successfully to identify regulatory interactions. Although Boolean models characterize genes in a simplified binary ON-OFF state, large-scale computable network models can be generated and analyzed for insights into signaling pathways and biological function [199,200]. Another network modeling approach involves the use of and Bayesian statistics. Bayesian network models provide a probabilistic framework that integrates gene expression data with *a priori* knowledge of the biological system. While Bayesian network models typically discretize expression data, though not necessarily in a binary manner as in Boolean networks, this approach has been successfully employed to identify gene interaction networks associated with cell function, regulation, and disease states [201–203]. The discretization of gene expression does not necessarily capture the graded responses that occur in biological systems, as observed in the transcriptional responses of NTS neurons for example (§ 3.3.1). Thus, often times, the complex, nonlinear relationships underlying gene expression and the transcriptional state of a cell are ignored. To overcome some of the limitations of the discretization-based methods, fuzzy logic approaches that consider the biologically relevant continuum of gene expression have been used to develop regulatory network models [214,243–246].

In this chapter, we develop an approach that builds upon the principles and prior applications of fuzzy logic [247–250] for analyzing high-throughput single-cell transcriptomic data to identify and model regulatory networks quantitatively. Using this approach, we identify and analyze the regulatory networks underlying the

structured variability of gene expression corresponding to the multiple neuronal subtypes described in Chapter 3. In the first section of this chapter, some background to fuzzy logic and its previous applications towards modeling gene networks is provided. This is then followed by an outline of the strategy used to adapt fuzzy logic towards developing quantitative gene interaction network models from single-cell transcriptomic data. These models are then used to investigate the potential sources of single-neuron transcriptomic heterogeneity. Results from quantitative model development and simulation analysis are presented. Finally, the implications of these results are discussed. The material in the current chapter has appeared in a journal article by the author [106].

4.2 Fuzzy Logic Modeling of Gene Regulatory Networks

4.2.1 Fuzzy logic background

Fuzzy logic is a form of multi-valued logic that deals with approximate reasoning via fuzzy sets [248]. Fuzzy sets contain a continuum of graded membership, ranging from 0 to 1, which allows a variable to transition gradually across multiple membership classes, as opposed to distinct binary membership (0 *or* 1). Fuzzy logic provides a method for describing complex systems using a set of linguistic rules, easily interpretable and expandable, that are derived from expert and/or *a priori* knowledge [243,245,251]. The inherent flexibility of "fuzzy" membership of a variable and the ability to expand rules that describe a system allow fuzzy logic

modeling approaches to deal with uncertain, vague, or incomplete information about a process or system of interest. These capabilities make fuzzy logic modeling a viable approach for modeling complex biological systems such as gene regulatory networks, as prior work has successfully shown [243,245,251–253].

A scalability issue, however, arises as the number of process variables and states increases: the proliferation of rules required to explore all possible combinatorial relationships results in computationally intractable models. Several strategies have been employed to address this issue. For example, prior work has demonstrated that constraining the number of rules produce accurate regulatory network models [245]. Optimization techniques such as genetic algorithms have been employed to derive an optimal number of rules [251,254,255]. The genetic algorithm utilizes principles of natural evolution in order to seek solutions in a large or possibly infinitely large search space [256]. Although a review of the genetic algorithm is beyond the scope of this work, however reviews outlining the specifics of the genetic algorithm can be found in [257,258].

More recently, Morris et al. [259] integrated these strategies into a "constrained fuzzy logic" (cFL) approach that enabled them to develop quantitative protein signaling network models, which they used to investigate protein-signaling network behaviors in response to various biochemical perturbations. A limitation for utilizing cFL to infer gene regulatory networks is that the approach developed by Morris et al. [259] was formulated from data measured in experiments that maximally stimulated or inhibited pathways via saturating doses of a ligand or drug. Such

targeted, binary-type perturbations do not mimic the continuous fluctuations and variability observed in single-cell transcriptomic data sets [105,260].

4.2.2 Adapting constrained fuzzy logic

In this study, we formulated a cFL approach applicable to single-cell transcriptomic data. Using these concepts and building on these previous efforts, we develop a methodology to model quantitatively gene regulatory networks based on *a priori* knowledge and context-specific single-cell transcriptomic data. An overall summary of the methodology is illustrated in Figure 4.1. In this chapter, *in vivo* gene expression measures that were analyzed in Chapter 3 are used.

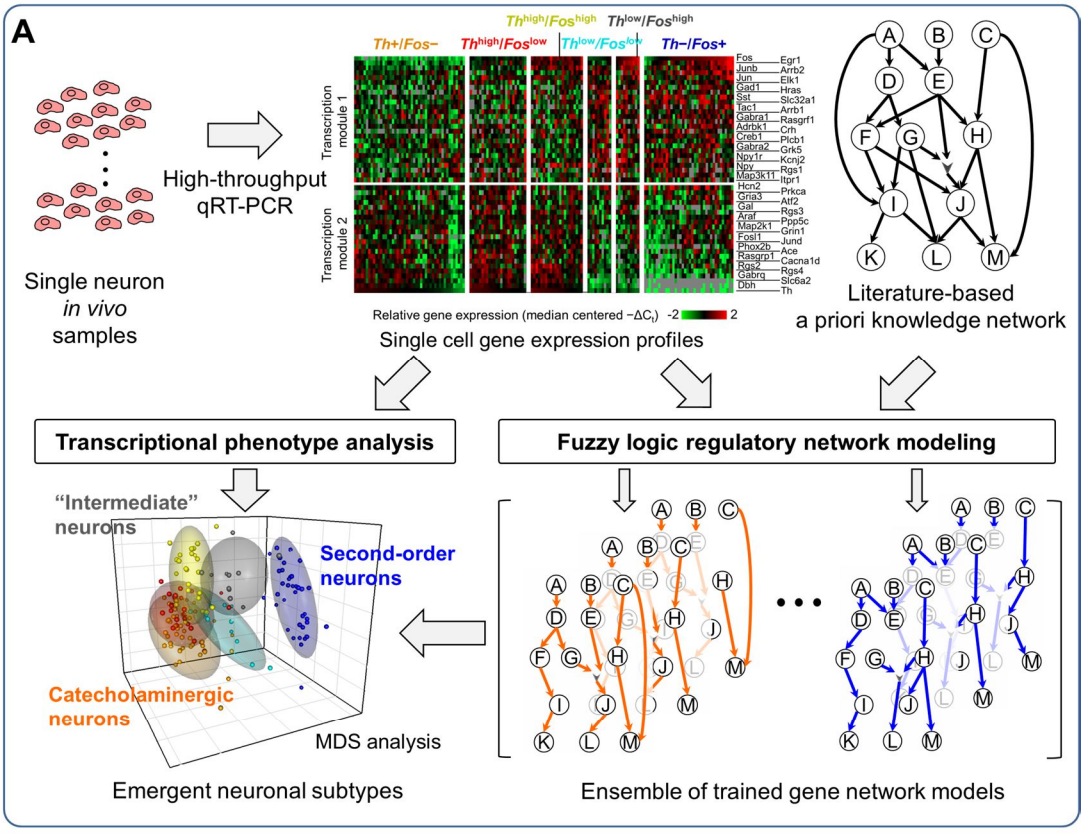
A
Single neuron
in vivo
samples
High-throughput
qRT-PCR
Th+/Fos−
Thhigh/Foslow
Thhigh/Foshigh
Thlow/Foslow
Thlow/Foshigh
Th−/Fos+
Transcription module 1
Transcription module 2
Fos
Junb
Jun
Gadd1
Sst
Tac1
Gabra1
Adrbk1
Creb1
Gabra2
Npy1r
Npy
Map3k11
Hcn2
Gria3
Gal
Araf
Map2k1
Fosl1
Phox2b
Rasgrp1
Rgs2
Gabrq
Dbh
Egr1
Arrb2
Elk1
Hras
Slc32a1
Arrb1
Rasgrf1
Crh
Ptcb1
Grk5
Kcnj2
Rgs1
Itpr1
Prkca
Atf2
Rgs3
Ppp5c
Grin1
Jund
Ace
Cacna1d
Rgs4
Slc6a2
Th
Relative gene expression (median centered −ΔCt) -2 2
Single cell gene expression profiles
Literature-based
a priori knowledge network
Transcriptional phenotype analysis
Fuzzy logic regulatory network modeling
"Intermediate"
neurons
Second-order
neurons
Catecholaminergic
neurons
MDS analysis
Emergent neuronal subtypes
Ensemble of trained gene network models

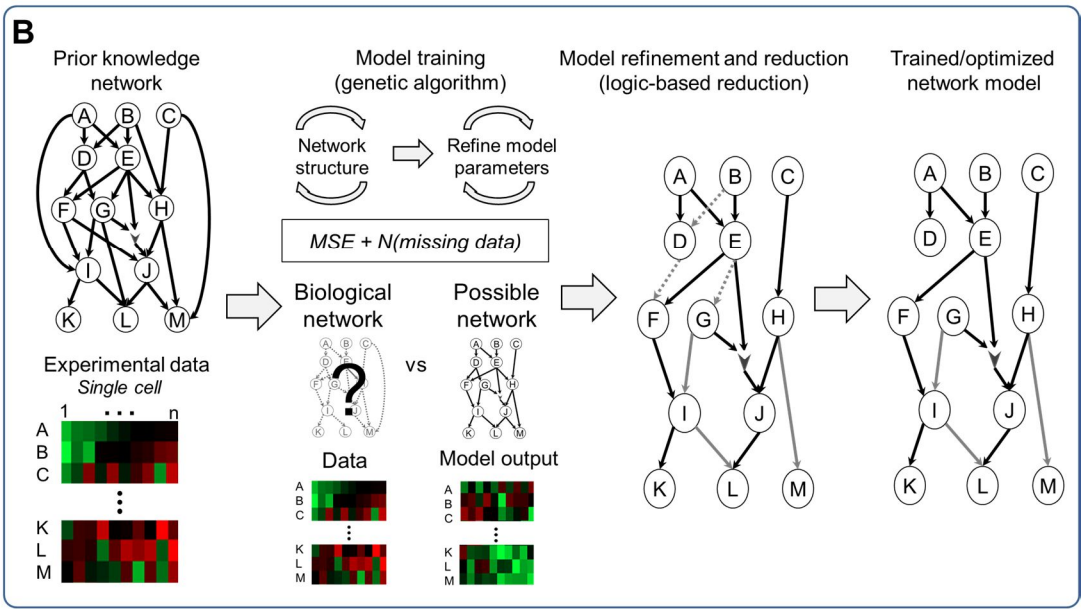
B
Prior knowledge
network
Model training
(genetic algorithm)
Network
structure
Refine model
parameters
MSE + N(missing data)
Model refinement and reduction
(logic-based reduction)
Trained/optimized
network model
Biological
network
Possible
network
vs
Experimental data
Single cell
1 . . . n
A
B
C
K
L
M
Data
Model output

Figure 4.1 Inferring gene regulatory networks via fuzzy logic. (A) Transcriptional profiles of 300 individual brainstem neurons taken from hypertensive rats were measured using the BioMark™ (Chapter 2). Multidimensional analysis of the single cell transcriptional data set revealed emergent neuronal subtypes that aligned with synaptic input-type and were composed of two sets of correlated gene expression modules. To infer the gene regulatory networks underlying these neuronal subtypes, an *a priori* network is trained against the single-cell transcriptional data set using principles of fuzzy logic modeling. Multiple quantitative regulatory network models are generated from the fuzzy logic methodology and are considered as part of a network ensemble that quantitatively characterizes plausible gene interactions and influences driving the highly variable transcriptional state of individual neurons. (B) The fuzzy logic methodology involves training an *a priori* network composed of gene interactions and influences curated from literature and transcription factor databases against context-specific gene expression data. Using a genetic algorithm, the initial a priori network is optimized such that unnecessary interactions (or edges) are removed while maintaining the network model's ability to fit the experimental data (below a certain error threshold). The trained network is then refined, where network model parameters (Figure 4.2) are optimized to improve model fit. A final reduction step is then performed where redundant directed edges not necessary for the model to fit the experimental data are removed to generate a simplified regulatory network model.

The *a priori* gene regulatory network, shown in Figure 4.1B consists of direct and indirect causal interactions curated from *i)* literature, *ii)* transcription factor databases, and *iii)* gene pairs with high correlation in the single neuron expression profiles. We are interested in exploring multiple gene regulatory pathways and therefore include a large number of potential gene interactions. Similar to the earlier cFL approach of Morris et al. [259], each interaction within the network is modeled as an "input-output" reaction, where an input-output pairing refers to gene nodes connected by a directed edge, mathematically defined by a transfer function. In order

to model biologically relevant nonlinear gene interactions, transfer functions approximating Hill functions were used.

To address reactions involving multiple gene inputs and facilitate development of a computable model, the fuzzy logic framework relies on Zadeh fuzzy logic gates (Figures 4.2B, 4.3B) [261,262] to determine the output of multi-gene interactions. The network identification approach utilizes a limited number of Hill-function parameter sets spanning a wide range of linear to near-binary ON-OFF-type relationships to define quantitatively a particular interaction. The specific Hill-function parameter values are identified based on the experimental data in a subsequent training step.

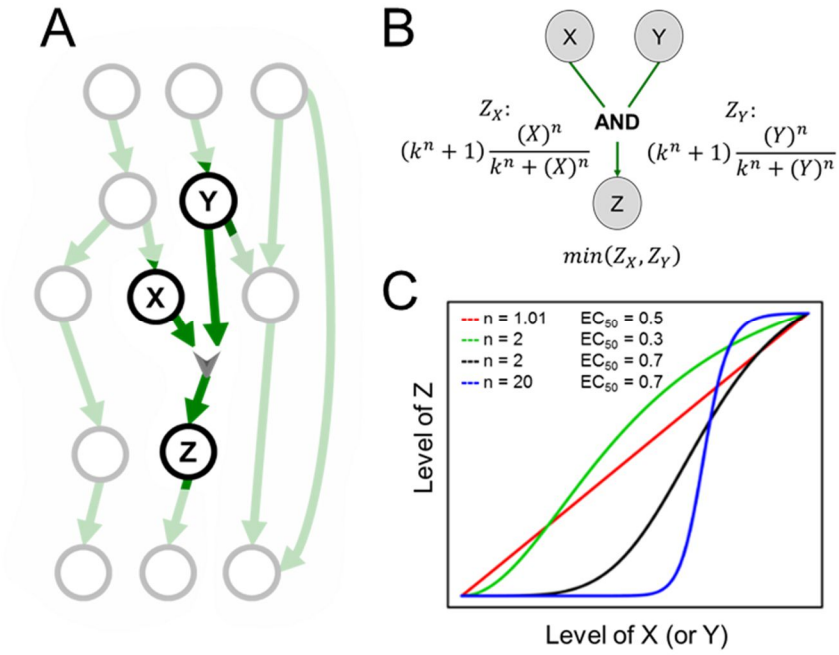

Figure 4.2 Modeling input-output gene interactions. (A) Schematic of a representative, causal (i.e. directed) gene regulatory network. In this network, both gene X and gene Y are required to "activate" gene Z. (B). An example of a Hill function equation used to model nonlinear input-output relationships and a Zadeh logic AND gate used to determine which input will determine the output from gene Z. n is the Hill coefficient and determines the sensitivity (i.e. sharpness of the curve), k represents the input level at which half of the maximal output response is achieved (EC_{50} in panel C). (C) Representative sigmoidal curves characterizing saturating input-output relationship among the genes.

Once the *a priori* gene regulatory network is specified, it is then trained against the experimental transcriptional data set via a genetic algorithm to determine an optimal network structure capable of fitting the experimental data below a predetermined error threshold. The mean square error (MSE) was used as a measure of the fit and predictive capability of the network model. Following the optimization scheme of Morris et al. [259], each independent run of the genetic algorithm generated

a population of regulatory network models (referred to as optimized *unprocessed* models), with the "best" network model (i.e., lowest MSE) selected for further refinement. The Hill-function parameters in the selected unprocessed model were then further refined using a non-linear optimization scheme based on the subplex algorithm [263], which produces an *unprocessed-refined* network model.

Although the training step removes reactions not supported by the data, we observed a number of redundant reactions, i.e. different input components activating the same output, included in the original a priori network remained in the unprocessed-refined network. In order to simplify the model further, the unprocessed-refined network model went through a final model reduction step. Here, the frequency of input selection for each gene interaction (as defined by the Zadeh gates − Figures 4.2B, 4.3B) was determined from simulations performed during the training step. These calculated frequencies were translated into edge weights that indicated the relative "dominance" of a particular gene interaction. In certain cases, some redundant gene interactions were not removed during the optimization step of the model training. These non-dominant or unused gene interactions were removed in order to generate a final *unprocessed-refined-reduced* gene regulatory network model.

Due to the stochastic nature of the genetic algorithm, multiple plausible network solutions can be generated that fit the data equally well, each representing a plausible network of regulatory interactions corresponding to the experimentally measured transcriptional states of single cells. Similar to prior fuzzy logic-based model development approaches, we considered an ensemble of network model

solutions that are generated through multiple iterations of the training, refinement, and reduction processes [245,259,264]. The abundance or lack of a particular gene interaction across individual network models within an ensemble was interpreted as the likelihood of the particular relationship driving that specific response [264,265].

4.3 Modeling Methodology

In this section, the statistical analysis, data-type, and computational platforms used to develop this methodology and analyze single-neuron transcriptomic data are described in detail.

4.3.1 Statistical analysis and significance of the network ensemble

To assess the fit and predictive capabilities of each unprocessed-refined-reduced network model, an *n*-fold cross validation procedure was performed. In this process, two-thirds of the data set was defined as the training subset used to train, refine, and reduce the a priori network. The remaining one-third was set aside as a validation subset that would be used to evaluate the predictive capabilities of the unprocessed-refined-reduced network. Within an iteration of the cross-validation process, the training-refinement-reduction step was repeated five times in order to identify several different plausible models generated by the genetic algorithm. This step was then repeated forty times resulting in a total of 200 potential network-model solutions. Network models with the corresponding lowest twenty-five MSE values were selected to form a network ensemble.

In addition to cross-validating the *a priori* network, we performed a series of tests to determine the statistical significance of the ensemble of regulatory network models. We compared the network ensemble of unprocessed network models to unprocessed models trained against randomized data or unprocessed network models derived from randomized a priori networks. The randomized *a priori* networks were generated either by *i)* randomizing directed edge placement throughout the a priori network, or *ii)* generating a randomize network topology. Both types of randomized networks maintained a directed acyclic structure. This constraint was placed on the network randomization process to avoid the inclusion of any feedback interactions, the effects of which would not be observable in a single time point. Consequently training a network with feedback interactions against the single time point data set would falsely increase the MSE of the unprocessed randomized cyclic network. *A priori* network training with random edge removal was also performed to evaluate the dependence of the training process on the *a priori* network structure.

4.3.2 Simulation and analysis of single neuronal transcriptional states

To elucidate the structure of the underlying gene regulatory networks corresponding to neuronal subtypes, we trained the a priori network against *i)* the scaled gene-expression data for each neuronal subtype identified in our prior analysis, and *ii)* the scaled gene-expression data set spanning all neuronal subtypes [105]. Comparing regulatory network model fits of the network ensembles produced from training by either type of data set would provide insight into whether a common

regulatory network or distinct regulatory networks underlie the experimentally observed distribution of neuronal transcriptional states.

Next, we investigated the response of the network ensemble to a range of randomly generated regulatory network stimuli levels using Latin hypercube sampling (LHS). We analyzed the simulated single-cell transcriptional states generated from our network ensembles using non-metric multidimensional scaling (MDS), as described in § 2.5.2.2 and applied in Chapter 3.

4.3.3 Single-cell gene expression data normalization

While the same normalized $-\Delta C_t$ data analyzed in Chapter 3 is used in the present modeling efforts, an additional scaling step is performed on the $-\Delta C_t$ data such that the gene expression data exist in a range of [0, 1] to prevent a subset of genes that are expressed much more dramatically than others from biasing the modeling results. Expression levels for each gene were normalized by subtracting the minimum expression value across all single-neuron samples and dividing the difference by the corresponding expression level range. This normalization/scaling technique has been used in previous fuzzy logic analyses of gene expression data [243,244,253].

4.3.4 Computational platforms

Genetic algorithm training and network ensemble simulations were performed in the R statistical software using various functions with the *CellNOptR* and *CNORfuzzy* packages [199,259]. Several functions within these packages were

modified to account for continuous levels of network inputs, applicable to the present single cell transcriptional data set. MDS analysis and Latin hypercube sampling was performed using the *MASS* package [220] and lhs package respectively, in the R statistical software. All regulatory network figures were generated using Cytoscape v2.8.3 [266].

4.4 Results

4.4.1 A priori network of the AT1R-mediated pathway

We employed the developed fuzzy-logic methodology to infer a gene-regulatory network involved in the angiotensin type 1 receptor (AT1R)-mediated pathway. AT1R mediates central autonomic control of blood pressure by the octapeptide angiotensin II (AngII) via modulation of NTS neurons. The activation of AT1R (initiated upon binding with AngII) triggers a signaling cascade resulting in an increased activation of transcription factors (TFs) such as ELK1, FOS, and JUN [267,268], as well as an increase binding activity of AP-1, consisting of phosphorylated FOS and JUN proteins. AP-1 binds to target promoters leading to changes in gene expression of tyrosine hydroxylase (*Th*), dopamine β-hydroxylase (*Dbh*), and norepinephrine transporter (*Slc6a2*), all critical to the production and release of the catecholamine norepinephrine. These changes result in neuromodulation of catecholamines as well as enhanced inhibitory GABAergic transmission, both associated with hypertension [269].

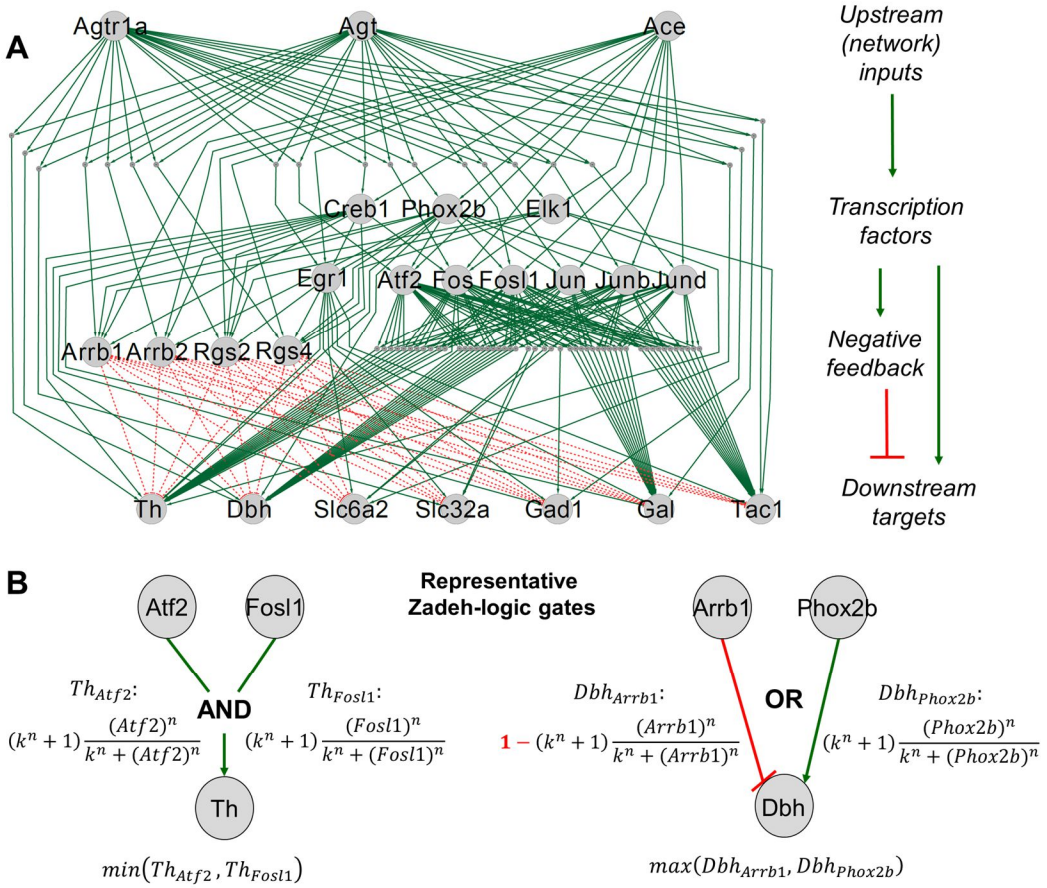
A
Agtr1a
Agt
Ace
Creb1
Phox2b
Elk1
Egr1
Atf2
Fos
Fosl1
Jun
Junb
Jund
Arrb1
Arrb2
Rgs2
Rgs4
Th
Dbh
Slc6a2
Slc32a
Gad1
Gal
Tac1
Upstream (network) inputs
Transcription factors
Negative feedback
Downstream targets
B
Representative Zadeh-logic gates
Atf2
Fosl1
AND
Th_{Atf2}:
$(k^n+1)\frac{(Atf2)^n}{k^n+(Atf2)^n}$
Th_{Fosl1}:
$(k^n+1)\frac{(Fosl1)^n}{k^n+(Fosl1)^n}$
Th
$min(Th_{Atf2}, Th_{Fosl1})$
Arrb1
Phox2b
OR
Dbh_{Arrb1}:
$1-(k^n+1)\frac{(Arrb1)^n}{k^n+(Arrb1)^n}$
Dbh_{Phox2b}:
$(k^n+1)\frac{(Phox2b)^n}{k^n+(Phox2b)^n}$
Dbh
$max(Dbh_{Arrb1}, Dbh_{Phox2b})$
C
Catecholaminergic neurons
"Intermediate" neurons
Second order neurons
Ace
Agtr1a
Agt
Upstream inputs
Fos
Elk1
Atf2
Jun
Jund
Phox2b
Creb1
Fosl1
Junb
Egr1
Transcription factors
Arrb1
Rgs2
Arrb2
Rgs4
Negative feedback
Th
Slc6a2
Gad1
Tac1
Dbh
Slc32a
Gal
Downstream targets
Scaled gene expression (median centered $-\Delta C_t$)
0.0 0.5 1.0

Figure 4.3 The *a priori* network model of the AT1R-mediated regulatory network. (A) Gene interactions and influences associated with the AT1R-mediated pathway used to formulate the *a priori* network. The network consists of four tiers − *i)* upstream network inputs, *ii)* transcription factors, *iii)* negative feedback, and *iv)* downstream targets – hierarchically layered to capture the signaling cascade that occurs when AT1R is stimulated by AngII binding. Genes of interest are assigned to each tier according to their functional role in this pathway (Table 4.1). Because the transcriptional dataset consists of a single time point, the *a priori* network is formulated as a directed acyclic network, where negative feedback influences regulating Agtr1a, are modeled as direct inhibitory interactions with downstream targets. (B) Examples of transfer functions and Zadeh logic gates used in the *a priori* network. Multi-input reactions are modeled using either an AND or OR Zadeh logic gate. In the AND gate example, the minimum value of *Th*, as calculated by the two transfer functions (Th_{Atf2} and Th_{Fosl1}), determines the resulting *Th* value. The minimum value is used in order to represent the effects a limiting input substrate would have in a multi-input reaction. In the OR gate example, the maximum value of *Dbh,* as calculated by the two transfer functions (Dbh_{Arrb1} and Dbh_{Phox2b}), determines the resulting *Dbh* value. Here, the maximum value simulates a competitive reaction, where the input having greater influence on the output determines the reaction output. (C) Heat map of scaled $-\Delta C_t$ gene expression values used to train the *a priori* network. Both neuronal subtype-specific data subsets and the entire $-\Delta C_t$ data set were used to train the *a priori* network.

In order to model the AT1R mediated regulatory network, we formulated a four-tiered hierarchically structured *a priori* set of gene interactions derived from relevant literature and constrained within the bounds of the gene set measured across the single-neuron samples. Since the transcriptional changes previously described occur upon AT1R activation, the corresponding gene, *Agt1r* was positioned in the first tier of the hierarchical structure. And while AT1R mediates the effects of AngII, the latter is the product of the enzymatic reaction between the angiotensin-converting enzyme (ACE) and angiotensinogen (*Agt*). Therefore the genes *Ace* and *Agt* were

placed alongside *Agt1r* as upstream-signal (i.e. "network") inputs. Stimulating these three first-tier network inputs activates the second tier of TFs. These TFs interact with two gene groups referred to as "feedback" and "downstream target" genes, forming a third and fourth tier, respectively. Additional genes were added to the TF-, feedback-, and downstream-target- tiers as supported by literature and computational analysis of promoter-gene regions using the PAINT software and the TRANSFAC database [79]. The nodes in the *a priori* network and the relevant literature implicating the role for each network node are summarized in Table 4.1.

Table 4.1 AT1R *a priori* regulatory network genes

Upstream (network) inputs • Ace, Agt, Agtr1a – [268,270]
Transcription factors • Phox2b, Egr1, Atf2 – [271] • Fos, Jun – [268,271] • Fosl1, Junb, Jund – [271,272] • Creb1 – [271–273] • Elk1 – [268,271,273]
Negative feedback • Arrb1, Arrb2 – [274,275] • Rgs2, Rgs4 – [276]
Downstream targets • Th, Dbh – [268,269] • Slc32a – [79,277] • Slc6a2 – [268,269,271] • Gad1 – [114] • Gal – [268,271,278] • Tac1 – [137,279,280]

The fuzzy logic input-output interactions cannot handle cycles in the regulatory network due to their unidirectional nature of the Hill-like function used to model quantitatively these gene interactions. To address this issue, feedback interactions were considered as affecting the target gene expression levels as a functional consequence of signaling regulation. In the directed acyclic graph, direct feedback inhibition on *Agt1r* coming from *Arrb1, Arrb2, Rgs2, and Rgs4* was rearranged to inhibit expression of *Agt1r* target genes as shown in Figure 4.3.

4.4.2 Network ensembles recapitulate single-neuron transcriptional variability

Using the cross-validation procedure previously described in § 4.3.1 we evaluated the fit and predictive capabilities of the unprocessed-refined-reduced network models. With the exception of the second-order neuronal subtype-specific network ensemble, each subtype-specific ensemble produced lower MSE values than the common, or general, network ensemble. However, comparing the fit of the general network ensemble to the second order neuronal-specific data subset revealed a higher MSE than the corresponding subtype-specific network ensemble MSE, shown in Figure 4.4. The result indicated that the subtype-specific networks better fit the data.

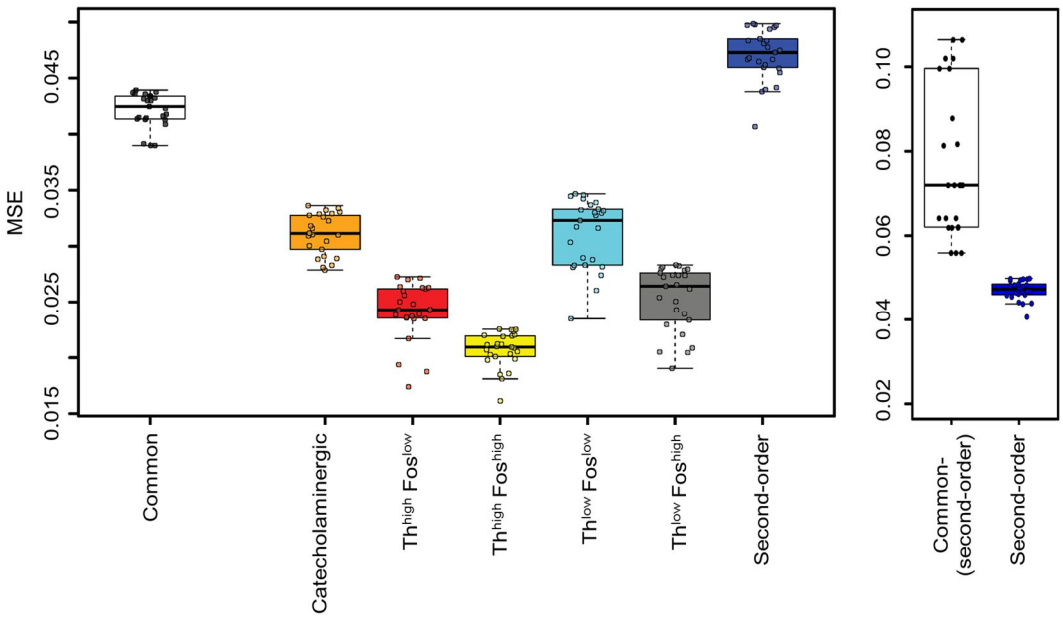

Figure 4.4 Trained regulatory network performance. Boxplots showing MSE values, representing a trained network model's overall ability to fit experimental data, of the general network ensemble and neuronal subtype-specific network ensembles. With the exception of the second order network ensemble, the subtype-specific network ensembles produced lower MSE values than the general network ensemble. When assessing the general network ensemble's ability to fit the second order subtype-specific data subset, however, the general network ensemble produced a higher MSE value (rightmost boxplot). Therefore, all subtype-specific ensembles fit the experimental data better than the general ensemble.

We further assessed the predictive capabilities of these models by using heat maps for simple visual interpretation. Comparison of the simulated transcriptional states generated by a representative unprocessed-refined-reduced network model and the corresponding experimental test data show similar transcriptional behavior across single cells and genes, further corroborated by the low absolute difference between data and simulation (i.e., residuals), as illustrated in the heat maps in Figure 4.5

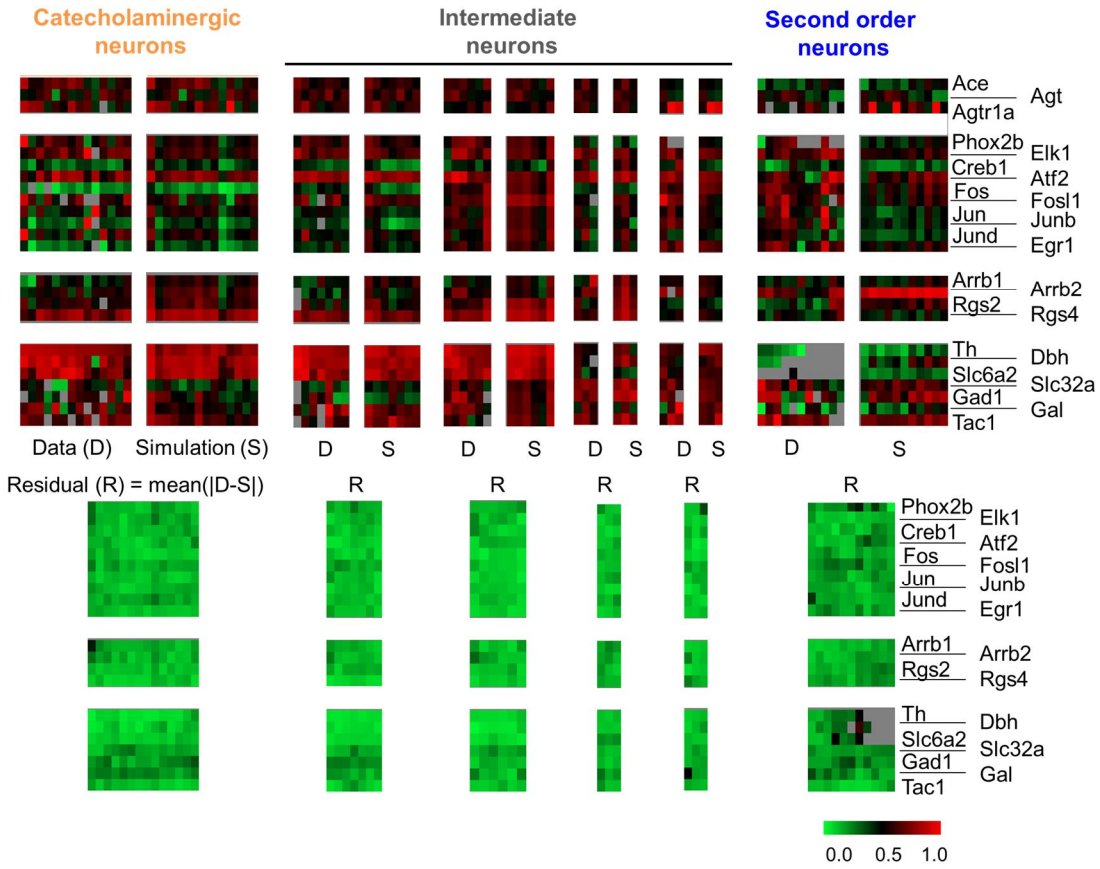

Figure 4.5 Simulated gene expression. Heat maps (top row) were used to visually assess the predictive capabilities of the subtype-specific trained networks. Each pair of heat maps consists of the "validation" data subset, set-aside during the cross-validation procedure, and the corresponding simulated scaled gene expression data of single neurons from a representative trained network from the subtype-specific network ensemble. Heat maps in the bottom row visualize the absolute difference between the "validation" subset and corresponding simulated scaled gene expression of single neurons. The mean absolute residual was calculated across all networks within a subtype-specific ensemble and averaged. Gray pixels represent instances where data was unavailable (failed qPCR reactions).

A similar performance of model simulations to experimental data was observed across all neuronal subtypes modeled. The improved ability of the subtype-

specific network ensembles to fit the transcriptional profiles of individual neurons indicates that the previously observed transcriptional gradient [105] is not driven by some common regulatory network, but rather by distinct networks corresponding to these neuronal subtypes.

4.4.3 Distinct regulatory network topologies define neuronal subtypes

When comparing the ensemble network topologies of the extreme neuronal subtypes (catecholaminergic, i.e. higher-order, and second-order subtypes), several distinct network structures distinguished these two extreme neuronal subtypes. For example, the transcriptional states of *Agt* and *Agtr1a* strongly influence the transcriptional output of the catecholaminergic ensemble network, which corresponds with previous expectations of AT1R mediated effects of AngII on catecholaminergic neurons. These *Agt-Agtr1a* influences, however, were reduced in the second-order ensemble network where *Ace* shows a stronger influence on subsequent transcription factors, as indicated by edge thickness (Figure 4.6). This shift in influence suggests that *Agtr1a*-mediated effects were more dependent upon the availability of AngII. Alternatively, the prominent influence of *Ace* in the individual neurons of the second order neuronal-subtype may reflect the direct effects *Ace* has on intra-neuronal signaling [281].

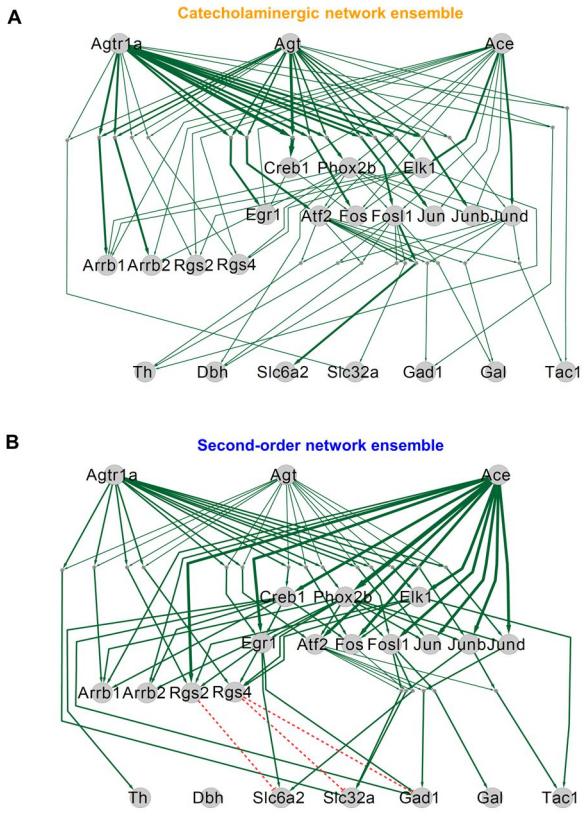

Figure 4.6 Comparison of catecholaminergic (higher-order) and second order neuronal network ensembles. The unprocessed-refined-reduced network ensembles underlying the (A) catecholaminergic (higher-order) and (B) second-order neuronal subtypes are depicted in the first and second panel. Edge thickness represents the strength (i.e. frequency across all networks within an ensemble) of a particular interaction determined during the training process. Edge color represents stimulatory (green) or inhibitory (red) interactions. Multiple interactions were pruned from the original *a priori* network structure, particularly in the interactions between transcription factors and downstream target genes. The frequency of edges (x) was classified into three bins: *i)* $0.12 \leq x \leq 0.4$, *ii)* $0.4 < x \leq 0.7$, and *iii)* $0.7 < x \leq 1.0$. Only edge frequencies $x \geq 0.12$ were included in network ensemble images in order to focus on more dominant interactions and aid in visual interpretation.

Additionally, the prominent TF interactions (*Atf2, Fosl1, and Jund*) regulating *Th* and *Dbh* expression in the catecholaminergic-specific ensemble differentiated this

subtype from the second order neuronal network ensemble (Figure 4.6). The presence of the AP-1 interactions in the catecholaminergic ensemble and absence in the second-order ensemble matches previous reports of increased AP-1 activation in catecholaminergic neurons [269]. Second-order neurons do not express *Th* and *Dbh*, and hence the interactions corresponding to AP-1 activation of *T*h and *Dbh* expression were absent in the second-order ensemble. Likewise, an increase in TF stimulatory interactions for *Gal, Gad1,* and *Tac1* was observed in the second-order ensemble. Second-order neurons may play an inhibitory role in blood pressure regulation [269]. Our modeling results, which predict an increased number of TF interactions in the second-order network ensemble, suggest a causal link between AT1R-mediated pathway activation and neuronal inhibitory transmission.

The signaling feedback interactions were another distinguishing feature of the network ensembles; second-order neuron networks support the presence of inhibitory interactions, which were not observed in the catecholaminergic ensemble. As an example, *Rgs2* and *Rgs4* inhibit downstream target genes, such as *Gad1*. These distinct interactions mediating the effects of *Agt*, *Agtr1a*, and *Ace* in catecholaminergic vs. second-order neurons indicate that these subtypes are driven by distinct regulatory networks. Consistent with these results, the regulatory networks corresponding to the intermediate neuronal subtypes also showed a subset of distinct causal interactions that drive the transcriptional states of individual neurons along a gene expression gradient, previously discussed in §3.4.4. The individual networks corresponding to the intermediate neuronal subtypes is shown in Figure 4.9.

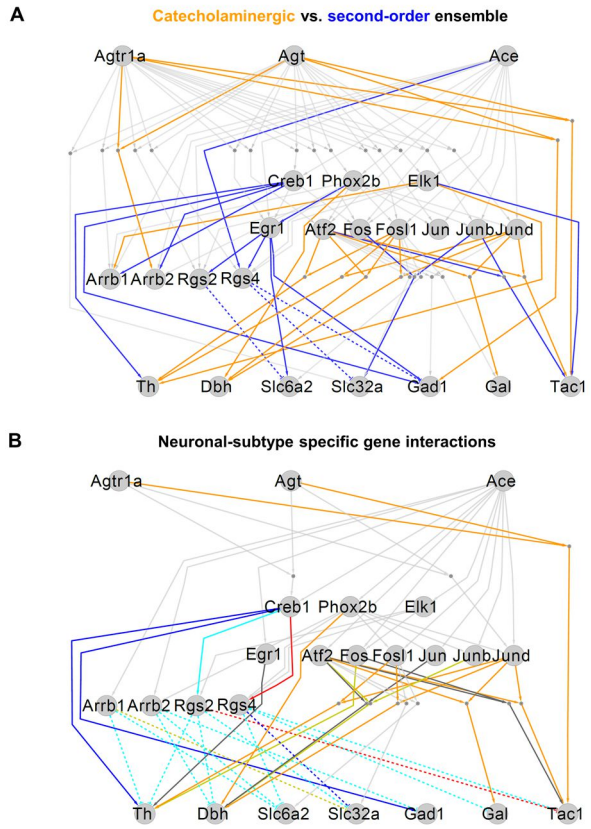

Figure 4.7 Distinct gene regulatory networks distinguish neuronal subtypes. (A) Network figure depicts both common and unique edges between the catecholaminergic (higher-order) and second-order ensembles. Gene interactions unique to catecholaminergic neurons (orange) depict a greater number of AP-1 transcription factor related interactions affecting *Th* and *Dbh* while interactions specific to second-order neurons (blue) depict distinct transcription factor regulation of downstream target genes. (B) As neurons traverse the intermediate neuronal subtypes that lie along the transcriptional landscape [105], distinct causal gene interactions are driving these transcriptional states. Unique directed edges for the intermediate neuronal subtypes are colored as follows: Th^{high} Fos^{low} (red), Th^{high} Fo^{shigh} (yellow), Th^{low} Fos^{low} (cyan), Th^{low} Fos^{high} (dark grey). Directed edges common to all neuronal subtypes are shown in light grey. Edge frequency is not accounted for in these network visualizations.

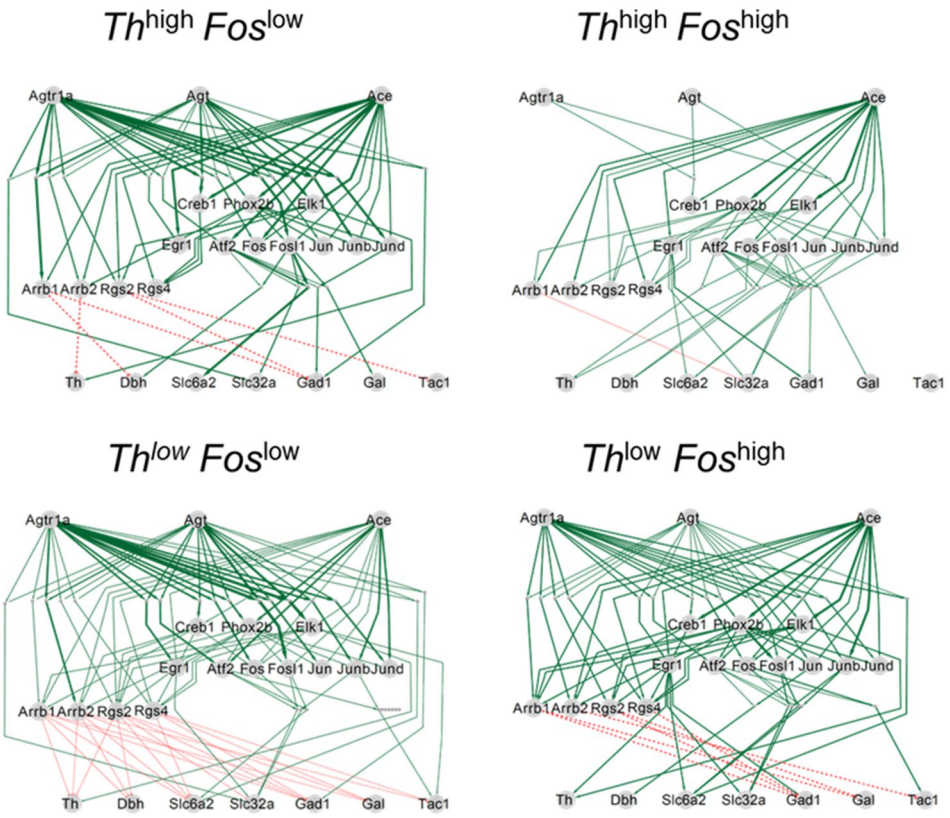

Figure 4.8 Gene network ensembles for intermediate neuronal subtypes identified in the NTS. The resulting unprocessed-refined-reduced network ensemble generated from the fuzzy logic process. Color and edge thickness annotations are identical to what was described in Figure 4.6.

4.4.4 Distinct network topologies and stimuli support a distribution of single-neuron transcriptional states

To investigate how distinct regulatory networks drive the emergent neuronal subtypes, we simulated the transcriptional states of individual neurons by stimulating the network ensembles with the same set of randomly selected stimuli levels of *Agt, Agtr1a,* and *Ace*. Using our network ensemble models we reproduced the distribution of neuronal subtypes, as visualized via MDS analysis (Figure 4.9).

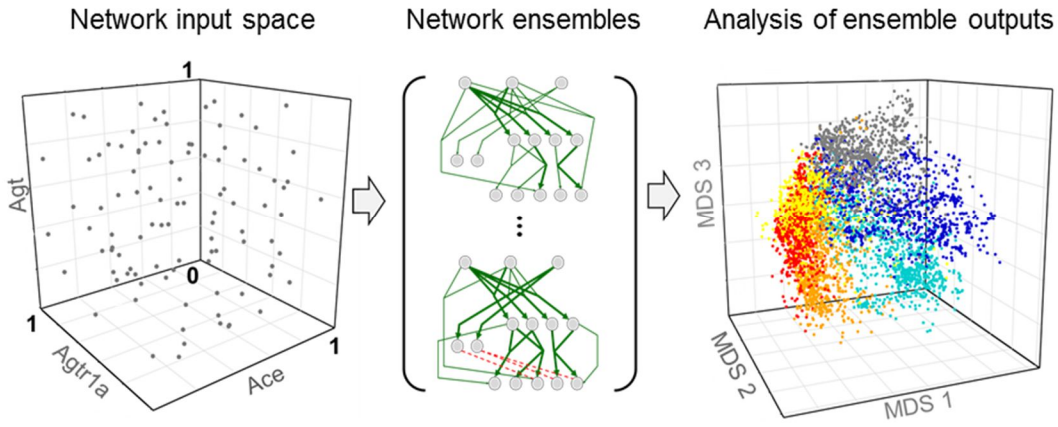

Figure 4.9 Interpreting single cell variability via multidimensional scaling of network simulations. Schematic of the simulation workflow using network ensembles and subsequent analysis via multidimensional scaling (MDS). Random network input values (scaled gene expression values) for *Ace*, *Agt*, and *Agtr1a* were selected from the multidimensional network input space using Latin hypercube sampling. This set of randomly selected network input values was used to stimulate all subtype-specific network ensembles, as in Figure 4.5. Using multidimensional scaling (Chapter 3), the simulated single-cell transcriptional states was then projected into a 3D MDS space.

Similar to the previous analysis presented in Chapter 3, our analysis of simulated transcriptional states yielded distinct clusters of neurons segregated by the regulatory network subtype. The differences between transcriptional states are driven by subtype-specific regulatory networks receiving a similar overall spectrum of inputs. Within each subtype, we observed a wide distribution of neuronal transcriptional states indicated by the large area covered by each subgroup in the MDS space. In certain cases, the pairwise distance between the transcriptional states of simulated neurons is shorter across neuronal subtypes than within a neuronal subtype despite differences in the underlying regulatory networks.

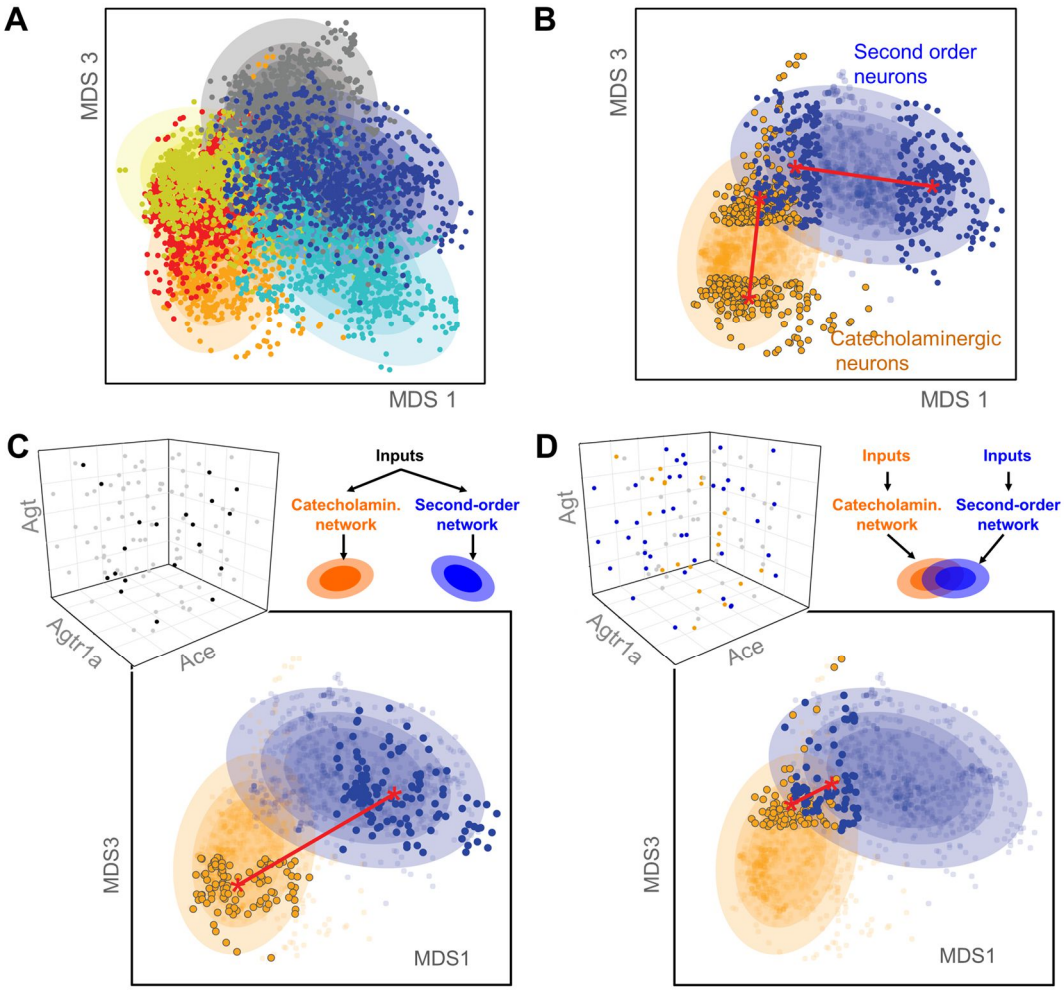
A
MDS 3
MDS 1
B
MDS 3
Second order neurons
Catecholaminergic neurons
MDS 1
C
Agt
Agtr1a
Ace
Inputs
Catecholamin. network
Second-order network
MDS3
MDS1
D
Agt
Agtr1a
Ace
Inputs
Inputs
Catecholamin. network
Second-order network
MDS3
MDS1

Figure 4.10 MDS visualization of simulated transcriptional states. (A) The first and third MDS coordinates capture the variability across single neurons. Subsequent analysis was performed along MDS coordinate axes 1 and 3. (B) Significant variability is reproduced in the network ensemble simulations, indicated by the spread of the data points within and across neuronal subtypes. However, an overlap between neuronal subtypes is also observed. Focusing on the catecholamine. (catecholaminergic, i.e. higher-order) and second-order neuronal subtypes, the intra-subtype Euclidean distance between simulated neurons within the upper 75%- and lower 25%-quantile of the population density (along MDS axis 3) is nearly twice the distance between higher-order neurons in the 75%-quantile and second-order neurons within the lower 25%-quantile of the population density (along MDS 1; 0.3391 vs. 0.1764). This larger intra-subtype distance also holds for the second-order neuronal subtype (0.5481 vs. 0.1764). Distances were determined between centroids for each quantile-group. To investigate the causes of this variability, transcriptional states generated from distinct network inputs stimulating the catecholaminergic and second-order regulatory network ensembles were examined. (C) Subtype-specific network responses to similar network inputs yielding distinct transcriptional states. (D). Second-order subtype-specific network response to distinct network inputs yield similar transcriptional states.

In these instances, distinct network inputs appear to drive the differing regulatory networks towards a similar transcriptional state (Figure 4.10). Thus, our fuzzy-logic network modeling predicts that the pervasive transcriptional variability observed *in vivo* is likely a product of distinct regulatory network interactions as well as response to distinct network stimuli [70,86,93,192,282,283]

4.4.5 Statistical significance and predictive capabilities of network ensembles

To further test and verify the predictive capabilities of the fuzzy logic-based models, we evaluated how well a particular subtype-specific ensemble would predict the transcriptional states of catecholaminergic neurons captured and measured

independently from the data set used to cross-validate the a priori regulatory network. Simulations of the catecholaminergic-specific network ensemble using the scaled network input levels measured from the independent neurons reproduced the experimentally measured transcriptional states remarkably well, illustrated in Figure 4.11.

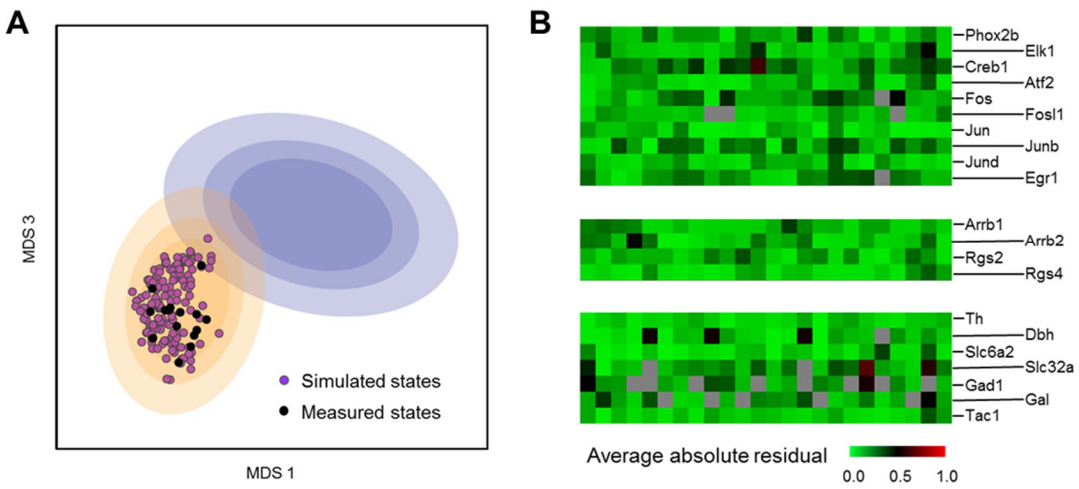

Figure 4.11 Predictive capabilities of catecholaminergic-subtype network ensemble. (A) A refined-reduced network ensemble was used to predict the transcriptional states of neurons independently measured from the transcriptional data set used for cross-validation. Gene expression profiles from fifteen single brainstem neurons of the catecholaminergic phenotype were measured using the BioMark™. The scaled gene expression of *Ace*, *Agt,* and *Agtr1a* were used to stimulate the higher-order network ensemble. Using Spearman rank correlation distances and MDS, we visualized the simulated transcriptional states with those of the independently sampled neurons Because the network ensemble consists of twenty-five plausible network models, an excess of predicted states was generated (relative to the fifteen independent brainstem neurons). Both the simulated and experimentally measured transcriptional states of neurons fall within the 65%-quantile population density and overlap considerably. This overlap suggests reasonable performance of the catecholaminergic-specifc network ensemble and increases the confidence of the other network ensembles derived using this fuzzy logic approach. (B) The average absolute residuals between the simulated and experimentally measured transcriptional states of the independently captured catecholaminergic neurons from a separate rat are visualized in a heat map. The predominantly low value for each scaled gene expression level across all single-neuronal samples further corroborates the predictive capabilities of the catecholaminergic-specific network ensemble.

Further statistical analysis and comparison of the unprocessed network ensembles revealed that nearly all subtype-specific unprocessed network models were indeed statistically significant. All other randomized *a priori* network structures resulted in higher MSE values (empirically determined p values < 0.05).

Table 4.2 Statistical significance of subtype-specific unprocessed a priori networks and dependence of training process on *a priori* network structure (p-values)

	Catecholaminergic neurons (Th+ Fos-)	Th^{high} Fos^{low} neurons	Th^{high} Fos^{high} neurons	Th^{low} Fos^{low} neurons	Th^{low} Fos^{high} neurons	Second order neurons (Th- Fos+)
Randomized data	0.032	0.010	0.048	0.058	0.000	0.006
Randomized edge placement	0.000	0.000	0.000	0.004	0.002	0.020
Random *a priori* network	0.000	0.000	0.000	0.002	0.000	0.002

In only one instance did a p-value > 0.05 occur (Th^{low} Fos^{low} network ensemble, p-value = 0.058). While this may not meet the statistical threshold of significance typically used, a p-value of 0.058 indicates a low probability that similar or better network predictions could be obtained from a network trained against randomized data

4.5 Discussion

In this chapter, we developed a fuzzy logic modeling approach that supports the inference of causal gene regulatory networks from highly variable in vivo single-neuron transcriptomic data. This approach treats the single-neuron transcriptomic data set as an abundant source of information about underlying gene regulatory

interactions, which manifest as correlated gene expression patterns across hundreds of single neurons. [105]. The quantitative regulatory network models developed in this study allow us to interpret how regulatory network interactions drive, in part, the structured organization of neuronal subtypes from a distribution of heterogeneous single neurons; distinct regulatory network topologies and their responses to distinct network inputs drive individual neurons through a range of transcriptional states.

In comparison to other approaches based on fuzzy logic, we find that our fuzzy logic modeling approach provides a robust technique to infer quantitative regulatory network models from variable single-cell gene expression data. Previous fuzzy logic modeling has identified only qualitative gene regulatory networks from microarray data, in the context of activators, repressors, and target gene triplets [243,245]. In instances where quantitative network models have been developed, these models relied on data generated under defined, binary-type experimental perturbations [259], which do not capture the continuous changes in network inputs observed *in vivo*. The fuzzy logic approach developed in this work, however, accounts for continuous levels of gene regulatory network inputs and allows us to model single-cell gene expression responses to more subtle changes occurring under physiological conditions. This methodology is a novel approach to infer quantitative regulatory network models that provide insight into the regulatory mechanisms contributing to the heterogeneous nature of single cells.

4.5.1 Distinct regulatory networks underlying heterogeneous responses at the single-cell level

The presence of distinct regulatory structures underlying neuronal variability posits implications as to how a neuronal population will respond to a targeted gene intervention. Apart from the variability one would expect given the stochastic nature of gene expression [86], manipulating a specific gene within a neuronal regulatory network is likely to differentially affect neuronal subtypes. As opposed to an "analog" or population response to a targeted gene intervention, our models suggest a more "discrete" or subpopulation-specific response based on their respective and distinct network topology. Our model-based prediction aligns with previous results demonstrating heterogeneous dose response across single cells, as in the case of NF-kB in response to TNFα [232]. Similarly, heterogeneous responses to drug treatment have been observed in clonal cancer cell lines [284]. With multiple studies repeatedly demonstrating a large degree of heterogeneity among individual cells, our network modeling approach provides a path towards understanding the regulatory network topology of cellular subtypes.

Individual cells naturally respond to a variety of environmental cues and stimuli in order to develop properly and perform specific cellular functions (§ 1.2.3 and § 2.2.1.2). These developmental and functional responses are supported by distinct genetic programs and regulatory network rewiring. While gene regulatory networks are often cast as static snapshots, regulatory networks are cell-, tissue-, and condition-specific and exhibit dynamic adaptation in response to both internal and external

signals [282]. For instance, in the context of disease such as cancer, regulatory network adaptation is highly prevalent in the differential response between normal and diseased cells. One example of this network adaptation involves a drug treatment that targets the intracellular ERK signaling pathway. While the drug inhibits the ERK pathway and effectively removes tumors in melanomic patients with an oncogenic BRAF mutation [285], the same drug activates the ERK pathway in cells with wild-type BRAF, potential promoting tumors in those cells [286]. Moreover, experimental evidence in yeast strains has shown that widespread changes occur in gene interaction networks and the pathways they represent during cellular response to DNA damage [287]. These reorganized interactions demonstrate that cells rely upon the ability to rewire regulatory network programming in order govern dynamic cellular functions in response to changing environments, stress, and stimuli.

4.5.2 Distinct stimuli and regulatory networks drive single cells across a transcriptional landscape

Within the brain, distinct gene regulatory network activity and genetic programs are critical in modulating the transcriptional state of neurons. Specific transcriptional mechanisms shape the developmental trajectory of neurons, which contributes to overall neuronal diversity and connectivity [12,13,233]. Not only are specific genetic programs critical to neuronal development, changes and adaptations of regulatory networks continue to play an essential role in post-mitotic neurons. In

response to cellular inputs, distinct regulatory network interactions direct individual neurons into distinct subtypes to support physiological functions.

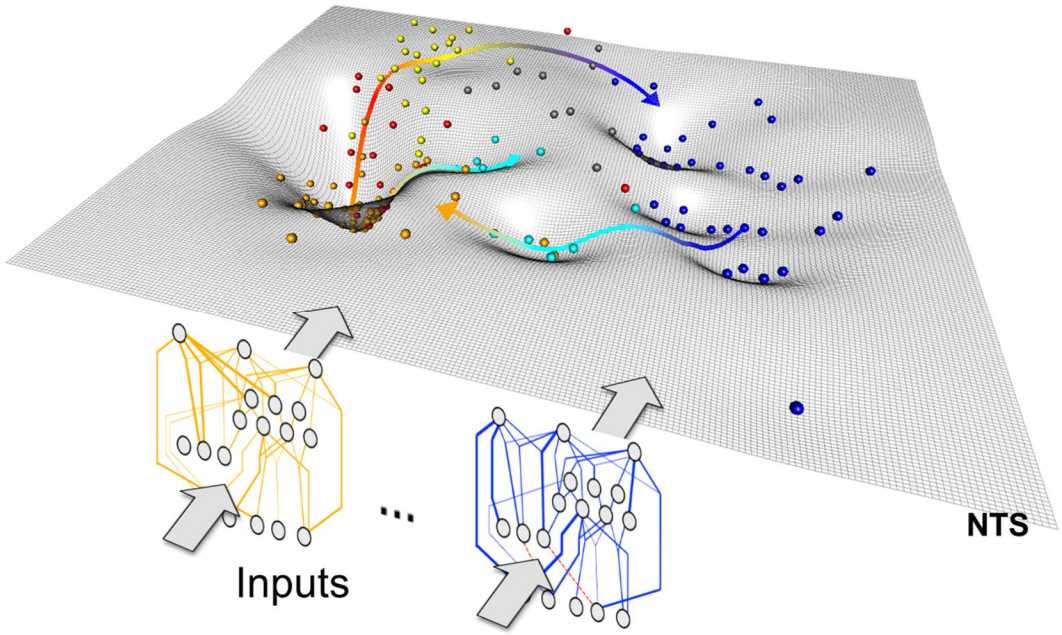

Figure 4.12 Dynamic transcriptional states of NTS neurons. This schematic, similar to the transcriptional landscape in Figure 3.19, represents the idea that both distinct gene interaction networks and the input stimuli that operates on them drive an individual neuron through a range of transcriptional states along this landscape.

Relating this back to the transcriptional landscape described in § 3.5, these distinct regulatory networks drive neurons towards specific transcriptional states. In addition, distinct network inputs stimulating subtype-specific regulatory networks can drive seemingly divergent neuronal subtypes towards similar transcriptional states, with likely impact on physiological function. Our simulations indicate that the

transcriptional states of individual neurons can be tuned via graded inputs to the subtype-specific regulatory networks, suggestive of an adaptive response. The transcriptional (i.e. functional) flexibility and diversity of individual neurons provide a mechanistic explanation to the experimentally observed plasticity of mature neurons [103,104]. Furthermore, the tunable nature of the transcriptional states of individual neurons poses intriguing possibilities regarding the dynamics of how neurons traverse across subtype-specific transcriptional states. Similar to developmental trajectory, are there critical regulatory interactions that can shift an individual or a subpopulation of neurons to a different trajectory towards a particular state in the development of disease? Likewise, how does the tunable, i.e. adaptive nature of these individual post-mitotic neurons and neuronal subtypes affect central regulation of physiological functions, such as those involved in maintaining cardiovascular homeostasis? While answers to the former question require time course data from single neurons as well as modifications to our approach to consider dynamics, the second question can be explored further via mathematical modeling, which is the subject of the next chapter.

4.5.3 Modeling assumptions

Our trained network ensembles contain likely gene interactions and influences that fit in vivo gene expression data remarkably well. The biological scope of the regulatory interactions and mechanisms predicted by the network ensembles is limited to the data types used to train the network models. The approach could be expanded to include additional regulatory mechanisms such as post-translational regulation and

micro RNA (miRNA) interactions, which have been recently reported to have a significant impact on neurogenic hypertension development [288]. While the mRNA levels of key genes have been shown to correlate with corresponding protein levels and neuronal function [61,96], this remains an assumption inherent to the hypothesized gene regulatory interactions derived from the experimental data sets from the transcriptomic domain. However, a significant advantage of fuzzy logic models lies in their flexibility and capacity to easily expand the *a priori* network. Additional regulatory components and interactions can therefore be incorporated with relative ease. By adding the appropriate gene-miRNA interactions to the *a priori* network, for instance, we can extend the biological scope of the regulatory mechanisms involved in gene regulation and the transcriptional heterogeneity present from neuron to neuron or cell to cell. Our study enables new opportunities to employ the fuzzy logic-based network models to inform future experimental design and iteratively refine the network ensembles to further elucidate the mechanisms that support neuronal and other cell-type diversity within the central nervous system.

4.5.4 Concluding remarks

In this chapter, the development and application of a novel fuzzy logic-based approach to analyze single-cell in vivo transcriptomic data is described. Using this methodology, we have been able to identify the contributions of regulatory network interactions and those of cellular inputs have in shaping the transcriptional states of neuronal subtypes. The results described in this chapter support a new approach that

builds upon the identification of neuronal subtypes based on their transcriptomic profiles (Chapter 3). The approaches developed and utilized in this chapter defines neuronal subtypes not only by transcriptional profiles, but on the regulatory networks and gene interactions that drive their transcriptional states. While the work presented in the current chapter reveals the presence of an organizational framework in which distinct neuronal subtypes are shaped, in part, by distinct gene network responses to synaptic input-types received, the functional significance of these distinct neuronal subtypes and the adaptive responses supported by these networks within the NTS remain unclear. The functional relevance of distinct NTS neuronal subtypes and adaptive responses of neuronal subtypes to inputs is explored in the broader functional context of cardiovascular homeostatic regulation in the following chapter.

Chapter 5

INVESTIGATION OF THE EFECTS OF BRAINSTEM NEURONAL ADAPTATION ON BARORECEPTOR REFLEX REGULATION OF CARDIOVASCULAR HOMEOSTASIS

Single-cell analysis of brainstem neurons indicate that single-neuron transcriptional heterogeneity in the brainstem represents the adaptive responses of individual brainstem to the various synaptic inputs received. These results are further supported by quantitative modeling and analysis of underlying gene networks, which suggest that inputs to individual neurons can drive them across a range of transcriptional states. In this chapter, the functional relevance of adaptive responses in brainstem neurons is explored in the functional context of baroreceptor reflex regulation of cardiovascular homeostasis via mathematical modeling. A closed-loop control system model characterizing baroreceptor reflex regulation of cardiovascular functions is developed and used to test the functional role neuronal adaption fulfills under the simulated condition of systolic heart failure.

5.1 Introduction

In Chapters 3 and 4, analysis and results were presented that reveal an underlying molecular organizational framework in which the transcriptional states of an in individual neuron aligns with the synaptic inputs received. Consequently, these

neurons form distinct neuronal subtypes that populate a transcriptional landscape defined by graded, correlated gene expression. Further analysis showed that distinct gene regulatory networks subtend these neuronal subtypes. Taken together, these findings suggest that the transcriptional heterogeneity observed across NTS neurons is due in part to the adaptation of individual neurons to the inputs they receive over the course of its post-developmental history. From these results, we propose that the presence of distinct neuronal subtypes and adaptation of neuronal subtypes support robust biological function through graded cellular responses. In this chapter, we test this proposal by examining the functional impact that neuronal adaptation of input-driven subtypes has on cardiovascular function via mathematical modeling. Towards this goal, we develop a mathematical model that incorporates distinct input-driven neuronal subtypes within the context of the baroreceptor reflex, referred to as the baroreflex, the physiological control mechanism that regulates arterial blood pressure. A brief summary of this physiological system can be found in § 2.2.1.

Despite extensive investigation and characterization of the baroreflex, understanding the behavior of this control system as a whole remains a challenge. Some of the main difficulties in understanding this system lie in the nonlinear behavior of individual components and nonlinear interactions among these components. Consequently, the behavior of the overall system is likely to be different from the sum of the individual parts. Mathematical modeling has provided valuable insight into the nonlinear relationships occurring in the baroreceptor reflex and how they affect cardiovascular function [289–293].

Autonomic regulation, mediated by sympathetic and parasympathetic nerves that innervate cardiovascular organs such as the heart and vasculature, manifests in linear and nonlinear ways [294–298]. The two branches of the autonomic nervous system (ANS) interact nonlinearly in such a way that the activity of one branch of the ANS simultaneously enhances the antagonistic effects of the other branch on the innervated organ. This *accentuated antagonism* has been experimentally observed to affect key cardiac (i.e. heart) effector functions. For example, parasympathetic tone, which reduces heart rate, has a much larger inhibitory effect in the presence of sympathetic tone [299]. Ventricular contractility (i.e. *inotropy*), another cardiac function, is affected in a similar manner [296,300,301]. Despite extensive experimental evidence that emphasize the importance of parasympathetic tone on cardiac functions beyond heart rate (i.e. *chronotropy*), which is mediated by vagal innervation of the heart (Figure 5.1, [131]), a majority of prior models focus primarily on sympathetic influence on cardiovascular functions. Of the mathematical models that do account for parasympathetic effects, they primarily focus on parasympathetic influence on heart rate or its inverse, heart period [291,293,302–304].

Recent clinical evidence suggests that parasympathetic activity, manipulated by vagal nerve stimulation, has profoundly positive effects in cases of treating heart failure [305]. In this context, elevated parasympathetic, or vagal, tone has been shown to be therapeutic and provides cardioprotective effects. Conversely, a decrease in vagal tone has been associated with many forms of heart disease and may even precede many of the actual symptoms [306]. The cellular and molecular mechanisms

that determine vagal output to the heart present an area of major significance for treating heart disease. The mechanisms underlying vagal-mediated cardioprotection represent potential targets for early diagnosis and novel palliative therapy. As the control center regulating autonomic tone, the NTS and the neuronal subtypes within project to multiple brainstem nuclei including the nucleus ambiguus (NA) and dorsal motor nucleus of the vagus (DMV) to regulate parasympathetic tone. Experimental evidence has shown that the NA and DMV act as the sources of vagal tone and affect distinct cardiac functions [38,126,130,131,307,308] and represent two targets of continued investigation with respect to vagal regulation of cardiac function.

The addition of these extra components related to the neuroanatomic organization of vagal outflow certainly increases the complexity of any baroreflex model. However, the added complexity represents features that have not been explicitly examined within the broader context of the cardiovascular system, to our knowledge. Including these features in a mathematical model enables us to understand more clearly how various interactions and adaptation to NTS neuronal subtypes and neuronal populations in the NA and DMV affect vagal tone and overall parasympathetic influence on cardiovascular functions. Since adaptation is a process occurring in response to a changing environment, or challenged state, we investigate what the functional consequences of neuronal adaptation are under an impaired i.e. diseased cardiovascular state – systolic heart failure post myocardial infarction. Before details of the model are presented, a brief review on the key physiological components of the cardiovascular system, as it pertains to this model, is provided for additional

context about the physiological system modeled in this study. This is then followed by a brief review of previous modeling efforts that have formed the foundation of the current model used in this chapter.

5.2 Physiological Components Involved in Cardiovascular Homeostasis

5.2.1 Autonomic regulation and the cardiovascular system

The principal purpose of the cardiovascular system is to circulate blood throughout the body in order to transport oxygen, carbon dioxide, hormones, and nutrients to and from cells and maintain homeostasis (defined in § 1.2.3). Key physiological variables of the cardiovascular system include arterial blood pressure, blood gas composition, and circulating blood volume. These variables are regulated in part by the baroreflex, which is primarily responsible for short-term regulation of arterial blood pressure and manipulates cardiovascular effector functions by varying sympathetic and parasympathetic tone. Parasympathetic regulation of this reflex, mediated by the vagus nerve, provides rapid (milliseconds), inhibitory regulation on cardiac functions such as heart rate (i.e. *chronotropy*) and ventricular contractility (i.e. *inotropy*) and balances the stimulating effect the sympathetic regulation has on cardiac function, which occurs on a slightly longer time-scale (seconds).

As described in § 2.2.1, blood pressure, aspects of respiration, and blood volume are measured either directly or indirectly by *i)* baroreceptors located in the aortic and carotid arches, *ii)* cardiopulmonary stretch receptors found in cardiac

regions such as the atria, cardiac ventricles, and pulmonary vessels carrying blood from the lungs to the heart, and *iii)* slowly adapting lung stretch receptors located in smooth muscle fibers of the lung airways [309,310]. These receptors respond to distension by triggering neuronal firing patterns that are sent the glossopharyngeal and vagus nerve. These nerves terminate in the NTS where these signals are integrated with other higher order signals that results in a subsequent signaling cascade that determines sympathetic and parasympathetic tone, which affect cardiovascular effector functions such as heart rate, cardiac contractility, and peripheral resistance of the vasculature.

The activation of these receptor-types in isolation or in combination triggers distinct effector function responses. For example, baroreceptor activation, representative of increases in arterial blood pressure, lead to decreases in heart rate and ventricular contractility [311,312]. Activation of cardiopulmonary baroreceptors, a subset of baroreceptors that measure low pressure points in the circulation, result in the inhibition of efferent sympathetic outflow, which decreases heart rate and modulates peripheral resistance of vascular beds in the body. These changes, in combination of others that occur in response to the demands placed on the cardiovascular system ultimately result in changes in arterial blood pressure.

Multiple lung stretch receptor types exist including slowly adapting receptors (SARs), rapidly adapting receptors (RARs), and bronchopulmonary C fibers. These receptor types reflect a subset of cardiorespiratory mechanisms that affect cardiovascular function and each type has distinct effects on cardiovascular function

such as heart rate. For the purposes of this study, modeling efforts focused on SAR inputs to the NTS. Activation of slowly adapting receptors (SAR) have varying effects on cardiac function, which has been shown to be dependent upon the rate of SAR activation, history of SAR activation, and duration of SAR activation. In this model, we use data generated by Greenwood et al. [313] and Hainsworth [314], which shows that SAR activation leads to *tachychardia* , an increase in heart rate above the normal resting heart rate, and reduces ventricular contractility [310].

5.2.2 The pumping heart and the cardiac cycle

The heart is one of the primary components of the cardiovascular system. It is a muscular organ that pumps blood through the pulmonary and systemic circulatory systems. It is composed of four main compartments: *i)* upper right atrium, *ii)* lower right ventricle, *iii)* upper left atrium, and *iv)* lower left ventricle. Both the right side of the heart (right heart) and left side of the heart (left heart) include two valves, an atrioventricular valve, which separates the atrium and ventricle, and a semilunar valve, which separates the ventricles from the main arteries. The atrioventricular valves, which include the tricuspid valve (right heart) and mitral valve (left heart), and the semilunar valves, which include the pulmonary valve (right heart) and aortic valve (left heart), ensure a unidirectional blood flow from the atria to the ventricles to the main arteries. The heart pumps blood in a rhythmic manner that is determined by a group of pacemaking cells in the sinoatrial node (SA node, Figure 5.1). These cells generate an electrical impulse that travels though the atrioventricular node, which

conducts electrical signals to the atria and ventricles. The generation of these impulses initiates a heartbeat, or *cardiac cycle*. Although the SA node spontaneously generates electrical impulses, sympathetic and parasympathetic nerves innervate this node and regulate the rate of impulses generated, thus regulating heart rate.

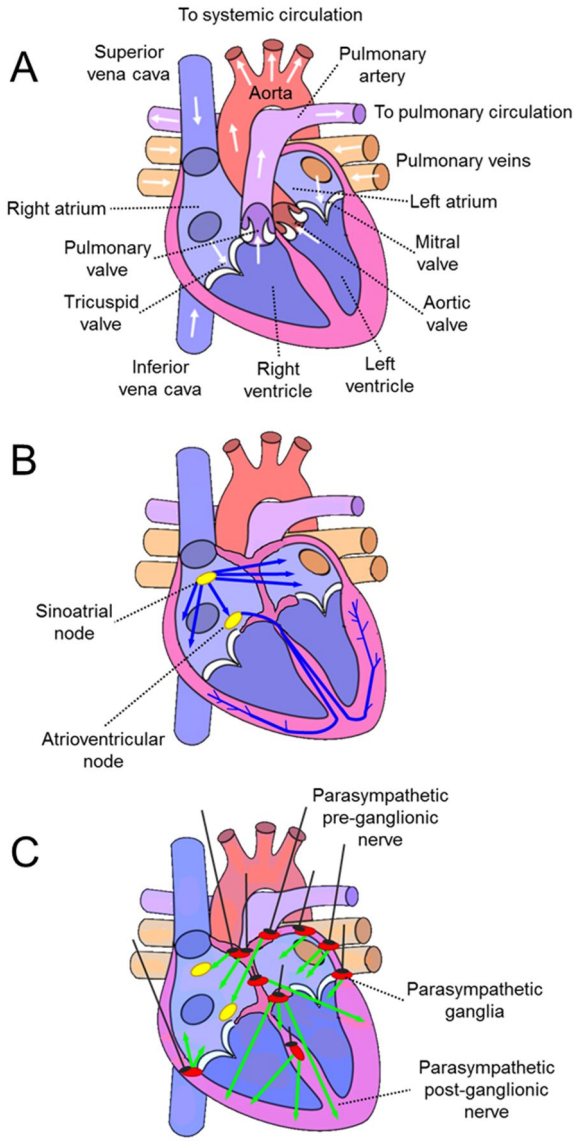

Figure 5.1 Anatomy of the heart. (A) The basic anatomical components of the heart. White arrows indicate direction of blood flow (B) The sinoatrial node is located in the wall of the right atrium. This group of pacemaker cells generate electrical impulses that cause the heart to contract. These impulses are conducted through the heart and are coordinated by the atrioventricular node, which electrically connects the atrial and ventricular chambers. (C) Schematic diagram indicating the multiple regions of the heart that are innervated by the vagus. The diagram of the heart has been modified from [315]. The schematic of vagal innervation is based on a diagram from [316].

The cardiac cycle, or the generation and completion of a single heartbeat, involves two main phases, the *diastole* (relaxation of the heart), when blood pressure decreases and *systole* (contraction of the heart) where blood pressure rises and reaches its maximum level (Figure 5.2).

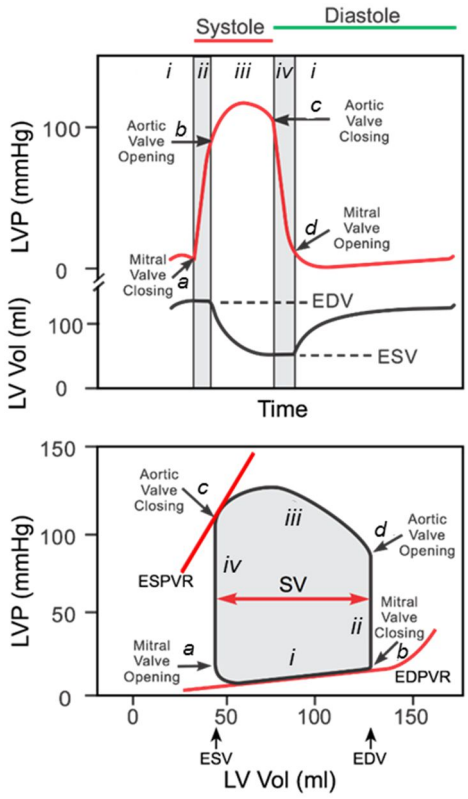

Figure 5.2 Cardiac cycle. Top panel: left ventricular pressure (LVP) and volume (LV volume) plotted over the four main steps of the cardiac cycle: *i)* diastolic filling, *ii)* isometric contraction, *iii)* ejection, and *iv)* isovolumetric (isometric) relaxation. The pressure at the end of diastole is indicated by *(a)*. This is when ventricular filling completes and the ventricle has reached its end diastolic volume (EDV). Once ventricular pressure exceeds aortic pressure *(b)*, the aortic valve opens and ejection begins. When the aortic valve closes, ejection ends and the ventricle has reached its end systolic volume (ESV). Subsequently the ventricle begins to relax isometrically *(c)*. Finally, when ventricular pressure drops below atrial pressure, the mitral valve opens up and the ventricle begins to fill with blood *(d)*. Bottom panel: pressure-volume relationship (PV loop) during the cardiac cycle. The red line in the upper left corner represents the end systolic pressure volume relationship (ESPVR). The slope of this line represents the maximal contractile state of the ventricle and is represented by the variable E_{max} in the model. The red curve along the bottom of the PV loop represents the end diastolic pressure volume relationship (EDPVR), or the passive filling of the ventricle. ESV – end systolic volume, EDV – end diastolic volume. The figure of the cardiac cycle has been modified from [317].

These two phases consist of four basic steps, *i)* diastole, which includes atrial systole, *ii)* isovolumetric contraction, *iii)* ventricular ejection, and *iv)* isovolumetric (i.e. isometric) relaxation time. During diastole the semilunar valves connect to the left and right atria close, the atrioventricular valves open, and the muscle fibers of the heart relax. This is then followed by systole, where the left and right atria contract, sending blood into the ventricles. Subsequently, the atrioventricular valves close and the ventricles begin to contract, with no change in ventricular volume during the isometric contraction stage. Following isometric contraction, the ventricles continue to contract as the blood empties out and flows into the pulmonary artery (from right ventricle) to oxygenate blood or the ascending aorta (from the left ventricle) to provide blood for systemic circulation. Concomitantly, the semilunar valves to the atria open. Finally, in isometric relaxation, the heart muscle fibers relax, ventricular pressure decreases while ventricular volume remains constant and the atria refill with blood.

5.2.3 The venous system

Beyond heart rate and cardiac contractility, the baroreflex actively regulates the venous system, another key physiological component that affects blood flow, or *hemodynamics* [290]. The venous system returns blood from the periphery to the heart and to store blood, acting as a capacitor to maintain filling of the heart with blood. Veins account for approximately 70% of the total blood volume, the arteries account for approximately 18%, and terminal arteries and arterioles account for approximately 3%. The ability of the venous system to store blood, or its capacitance, varies for

different vascular compartments. Similarly, the volume of blood stored within a blood vessel is dependent upon its *compliance* – the ability of a blood vessel to expand and contract passively with respect to changes in *transmural pressure* (difference between the internal and external pressures of the vessel). Consequently, the blood volume in a vessel when the transmural pressure is zero is referred to as the *unstressed volume*. The blood volume at a non-zero transmural pressure is referred to as the *stressed volume* [318].

Veins are the most compliant compartment in the body and can easily accommodate changes in blood volume. Veins that run through the internal organs of the abdomen, or *splanchnic* compartment are some of the most compliant veins in the body and thus act as reservoirs for blood. Veins outside of the splanchnic compartment, or *extrasplanchnic* veins are less compliant. In particular, the systemic and pulmonary arteries through blood from the heart flows to the pulmonary and systemic circulation, respectively, have very low compliances. Conversely, vascular resistance, which reduces blood flow and increases pressure, differs among the various vascular compartments as well.

These variables play affect cardiac function based on their ability to modulate circulation and blood flow into the heart, they play a central role in affecting cardiac function. Moreover, changes to these variables in different compartments have varying effects on cardiac function and arterial blood pressure. For instance, an increase in arterial resistance causes a significant increase in arterial blood pressure. However, a similar increase in venous resistance results in a decrease in blood flow to the heart

(venous return) and affects how much blood is ultimately pumped out to the arteries. Thus vascular compliance, unstressed and stressed volumes, and vascular resistance are key physiological variables that affect hemodynamic behavior and cardiovascular state [290,292].

The nonlinear manner in which these various mechanisms behave make it difficult to predict the overall behavior of the cardiovascular system, whose function is based on the superimposed functions of these previously described mechanisms. Moreover, the nonlinear regulatory effects imposed by the sympathetic and parasympathetic branches of the ANS increases the complexity of this system. However, because the baroreflex is a physiological control system, providing negative feedback regulation on arterial pressure, we take a control systems engineering approach to systematically and quantitatively characterize the complexities of these various nonlinear components and interactions, as illustrated in Figure 5.3. Further, a control systems engineering approach provides a framework within which to explore the effects adaptations to neuronal subtypes and neuronal populations within the brainstem have on cardiovascular function and state.

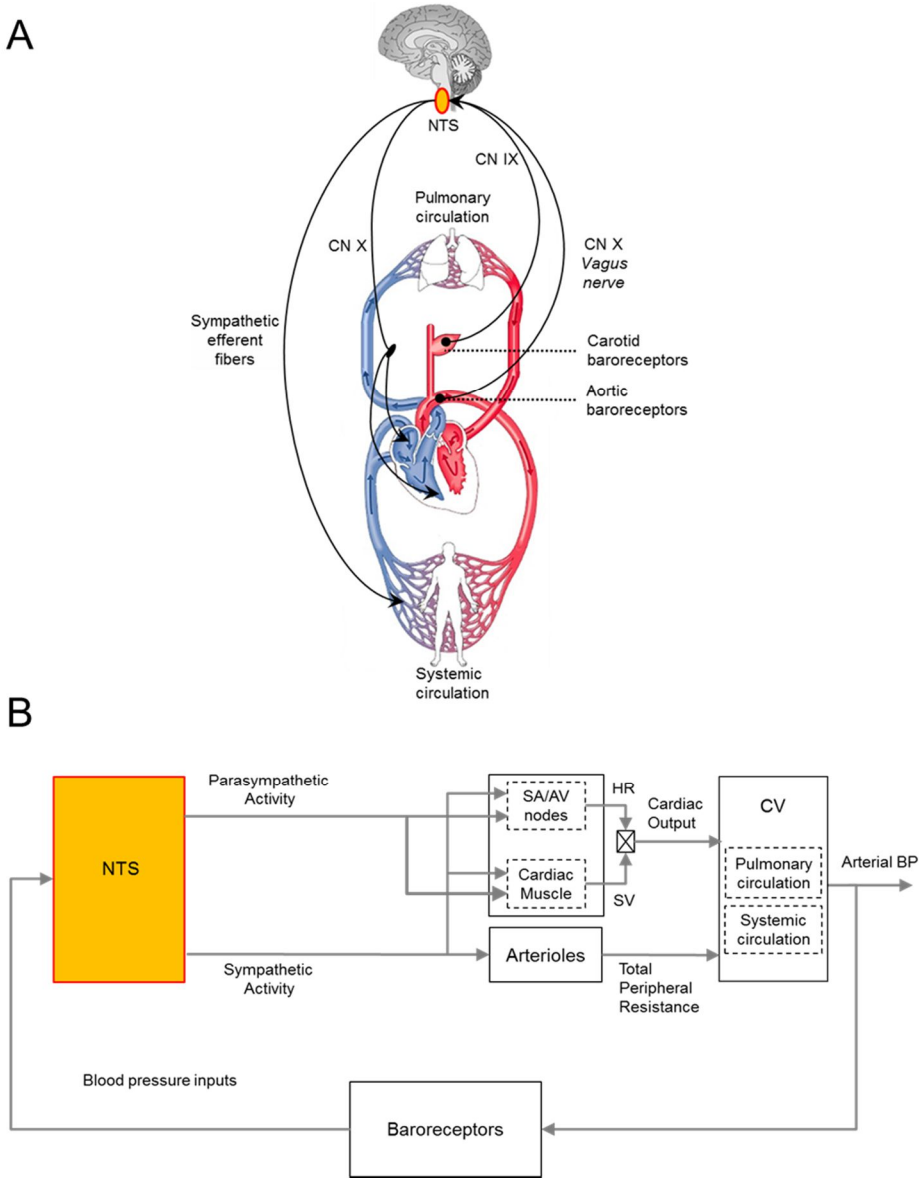

Figure 5.3 Autonomic innervation of the cardiovascular system. (A) Schematic illustrating representative sympathetic and parasympathetic innervation of target organs and tissue in the cardiovascular system. Afferent information from the carotid and aortic baroreceptors is sent along the glossopharyngeal (CN IX) and vagus nerves (CN X). The vagus is the primary nerve that carries parasympathetic afferent and efferent signals. (B) Corresponding control block diagram of the cardiovascular system shown in (A). This diagram represents information flow involved in the autonomic regulation of the cardiovascular system.

In the next section, a brief review is provided of a few select models of interest exploring key aspects of baroreceptor reflex regulation and the behavior of central physiological components including the heart and vasculature.

5.3 Previous Modeling Efforts

Because the baroreflex is a physiological control system, quantitative approaches from the field of control systems theory provide methodologies with which to systematically characterize and model this physiological reflex. Several efforts have focused on analyzing the sources of the oscillatory nature of blood pressure, which varies between a maximum systolic pressure and minimum diastolic pressure, and the stability of this oscillatory behavior. Burgess et al. [319] developed a first-order linear feedback model describing the response of mean arterial pressure to changes in sympathetic drive. The model includes a proportional controller representing neural control mechanisms and a sensor or "feedback" gain. Using their model, Burgess et al. showed that high-frequency oscillations (~4 Hz) observed in the blood pressure of rats could be accounted for by the time-delays associated with the sympathetic response to blood pressure changes. One implication to this simple yet elegant model, is that a strict relationship between the vasculature and sympathetic tone must exist to maintain stable blood pressure oscillations. Stimuli that would alter the gain in the feedback loop (e.g. altered baroreflex gain) would cause the system behavior to become either unstable (gain increase) or asymptotically stable (gain decrease) [319,320]. Therefore,

in order to maintain stable oscillatory behavior, the linear feedback model suggests that continuous adaption must occur in the system.

Subsequent work by Ringwood and Malpas [320] included nonlinear input-output relationships describing the central nervous system and vasculature components within the feedback model. By incorporating nonlinearities into the feedback model, Ringwood and Malpas determined that oscillatory behavior at a low frequencies, (~0.3Hz) can be maintained via nonlinear input-output relationships within the CNS over a wide range of gain changes that could occur at various points in the feedback loop. In other words, nonlinearities in the CNS afford greater stability to the oscillatory behavior of blood pressure.

Additional baroreceptor modeling efforts have further emphasized the nonlinear nature of the baroreceptor response to blood pressure changes [293,321,322]. Interestingly, it has been shown in closed-loop simulations of baroreflex regulation of heart rate, baroreceptor, sympathetic, and parasympathetic nerve firing follows a hysteresis curve (time dependence of system outputs to present and past inputs). Moreover, the hysteresis loop associated with model conditions simulating healthy normotensive adults is wider than those associated with model conditions simulating hypertensive cases. This suggests some maladaptation (or lack of adaptation) in conditions associated with hypertension development [293].

A key physiological component to cardiovascular system that affects blood flow and pressure is the vasculature or venous system. Despite its complexity, many models have successfully utilized simple yet effective models that rely on concepts

from electrical circuit design to characterize venous blood flow. A commonly used model that captures key hemodynamic properties is the Windkessel model [323]. Originally used to describe aortic blood flow from the heart, it likens the heart and aortic flow to a closed hydraulic circuit that includes a water pump (i.e. heart) connected to a chamber. This modeling approach has been used effectively to incorporate hemodynamic effects on blood pressure [292].

In addition, the respiratory system is intertwined with the cardiovascular system and affects heart rate variability. Although an examination of the cardiorespiratory system is beyond the scope of this work, modeling work has shown that respiratory sinus arrhythmia has beneficial effects, including reducing the work load of the heart while maintaining physiological levels of CO_2 [324].

Finally, several previous efforts have integrated these neurogenic and physiological mechanisms into a more comprehensive models. An example of such a model is a closed-loop hemodynamic model of baroreceptor reflex regulation of arterial blood pressure developed by Ursino [291]. This model is of particular interest because this model includes many of the physiological and neural regulatory mechanisms involved in regulating arterial blood pressure. Multiple cardiovascular effector functions are included such as pulsatile heart rate, cardiac contractility, hemodynamics, and autonomic regulation of vascular system properties like vascular resistance. In addition, compartmentalized physiological structures are integrated into this model in order to provide a more accurate representation of the physiological components affecting hemodynamics and blood pressure. For example, Ursino

incorporated a compartmentalized vascular system composed of components characterized by distinct capacitances; resistances; and unstressed volumes. Using this model, Ursino showed that the pulsatile perfusion of the carotid sinus leads to an overall decrease in baroreflex gain and that venous unstressed volumes in the vasculature play a larger role in hemodynamic responses to acute blood loss (hemorrhaging) than does systemic resistance or heart rate [291]. This model has since been modified to study cardiovascular functions under various conditions, including exercise-induced stress [325], and univentricular flow resulting from right heart-bypass operations as a treatment for congenital heart disease [289].

5.4 Baroreceptor Reflex Model Structure

In this study, we extend the models developed by Ursino [289,291,326] to include additional components representing neuronal subtypes in the brainstem involved in regulating vagal outflow. Additional details regarding the original Ursino model are provided in Appendix B.

5.4.1 Modeling the brainstem nuclei and their role in regulating vagal outflow

Multiple transfer functions are included to represent the molecular organization identified in Chapter 3, the neuroanatomical organization of the vagal efferent sources, and the neuronal projections they receive from the neuronal subtypes within the NTS. We include distinct input-output transfer functions to represent specific input-driven NTS neuronal subtypes, as identified in Chapter 3. In our extended model, we focus

on three neuronal subtypes corresponding to three types of peripheral signals that affect cardiovascular function: *i)* carotid baroreceptors, *ii)* cardiopulmonary receptors, and iii) SAR lung-stretch receptors. Similarly, transfer functions were included to represent the signal processing and vagal regulatory functions of the NA and DMV. Each transfer function models the input-output relationship characterizes neuronal response to a given input signal as a sigmoidal relationship to capture the biologically relevant behavior associated with neurons active in the baroreflex [141,291,327]. Because vagal outflow has been shown to increase monotonically with activity in the sinus nerve with an upper saturation, sigmoidal functions, similar to those used in Chapter 4, are used to describe the input-output responses of these components. The sigmoidal relationship is described by the following equation:

$$f_{out,j} = \frac{f_{min,j} + f_{max,j} * exp\left(\frac{f_{input,j} - f_{midpt,j}}{k}\right)}{1 + \exp\left(\frac{f_{input,j} - f_{midpt,j}}{k,j}\right)} \qquad 5.1$$

Here, $f_{min,j}$ and $f_{max,j}$ represent the firing frequency output range of the j^{th} neuronal subtype or neuronal population. $f_{input,j}$ refers to the firing frequency from the respective receptor-type to which that the specific neuronal subtype is responding. $f_{midpt,j}$ represents the input firing frequency value that would trigger a firing frequency response that is half of the maximum firing frequency output. Finally k_j represents the input sensitivity of the neuronal subtype. A large *k*-value represents low input sensitivity, i.e. a gradual increase in output over a range of inputs whereas a smaller *k*-

value represents a higher input sensitivity. A *k*-value of unity results in a near-binary switch-like response profile.

This sigmoidal model was chosen due to minimal number of parameters required and the physiological relevance and interpretability of the parameters. It is important to note that our findings in Chapter 3 do not necessarily support the use of a population rate code, which conflicts with the use of firing frequencies as the input and output type for these transfer functions. However, firing frequencies are used here because they represent a straightforward manner with which to represent the information transmitted to and processed by distinct neuronal subtypes and neuronal populations in the brainstem.

5.4.2 Functional connectivity in the brainstem

Physiological experiments have shown that the NA and DMV modulate specific cardiac effector functions. The NA modulates heart rate and to a lesser extent ventricular contractility while the DMV primarily affects contractility [38,307,328–330]. The connection between these brain nuclei and the NTS neuronal subtypes were defined based on experimentally established electrophysiological characteristics of the NA and DMV. Firing patterns of the NA have been shown to align with the respiratory cycle suggesting that neuronal populations within the NA are in part dependent upon synaptic signals relaying information related to respiration. Alternatively, firing patterns within the DMV have been shown to be independent of respiration [131,331], suggesting respiratory rhythms have minimal influence on the

DMV. Taking together, these results suggest that neuronal populations in the NA and DMV have specific effects on effector functions. Based on these findings, we propose a particular connectivity between the NTS subtypes, NA, and DMV, as illustrated in Figure 5.4.

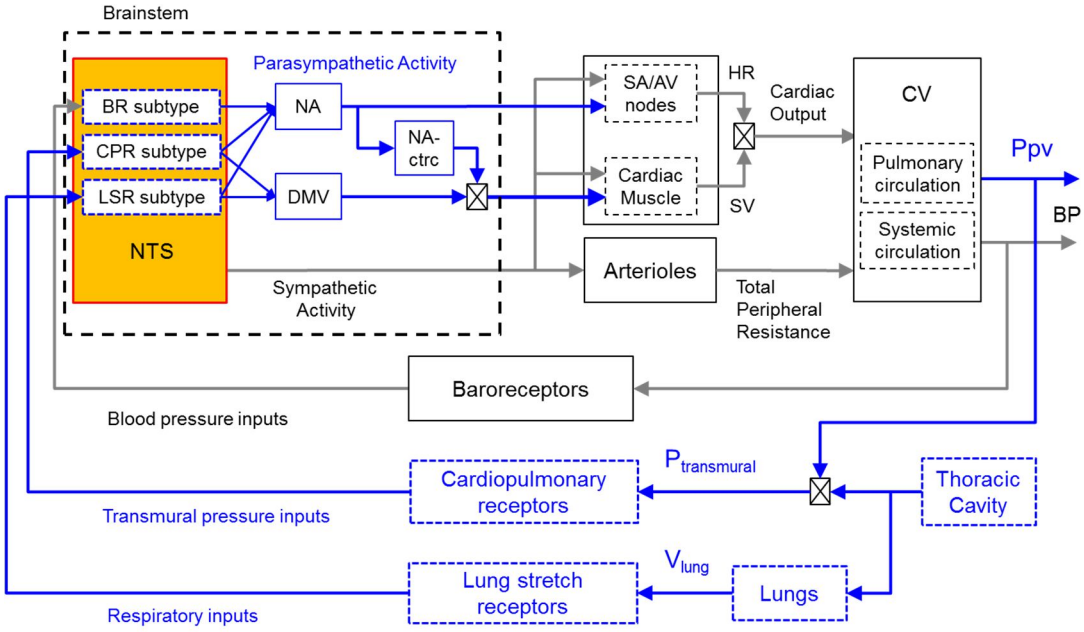

Figure 5.4 Control block diagram of revised model. Components outlined in blue represent the new components incorporated into the model. A sigmoidal function (Equation 5.1) is used to represent the input-output transfer functions for the neuronal subtypes and neuronal populations added in the brainstem. NA-ctrc refers to the influence neuronal populations in the NA have on ventricular contractility.

5.4.3 Vagal efferent outflow

The extended model includes vagal efferent effects on the end systolic ventricular pressure volume relationship, which is a measure of ventricular elasticity.

This addition represents a novel extension to the previous models as no other model has examined vagal influence on cardiac function beyond that of heart rate to our knowledge. The elasticity measure (E_{max}) in this model represents the linear relationship between end systolic pressures and volume [311]. Experimental evidence has established E_{max} as a robust correlate of contractility, independent of changes to blood flow that are known to affect other measures of ventricular contractility [311,332]. Similar to heart rate, elasticity is regulated by the accentuated antagonistic interplay between sympathetic and vagal activity [298,333].

By including vagal efferent effects on ventricular contractility, we are now able to capture the accentuated antagonistic effect that vagal and sympathetic tone have on ventricular contractility. To capture quantitatively this antagonistic effect, sympathetic and vagal tone were modeled to affect the inverse of elasticity. This value is a mathematical relationship used to capture the nonlinear effects of combined sympathetic and vagal tone on elasticity and not a calculation of ventricular compliance, which corresponds to the stiffness of the cardiac muscle. Ursino was able to replicate this accentuated antagonistic effect on heart rate by modeling a linear relationship between heart period (the inverse of heart rate) and autonomic tone [291].

5.4.4 Sympathetic efferent outflow

Sympathetic efferent outflow is modeled using a monotonically decreasing exponential curve to capture the decrease in sympathetic activity (represented by firing frequency) in response to increased baroreceptor activity [291]. Both sympathetic and

parasympathetic activity and their effects on modulating effector functions are associated with time delays, with parasympathetic efferent effects having a much shorter time delay (~milliseconds), than sympathetic efferent effects (~seconds).

5.5 Parameter Selection

Because the primary goal of this study is to investigate the effects of neuronal adaptations, we focus on the modeling efforts required to incorporate the presence of neuronal subtypes in the NTS and neuronal populations in the brainstem and tune the parameters corresponding to the transfer functions characterizing these components. Additional details regarding parameter values corresponding to the multiple physiological components are included in Appendix B.2 for additional information.

5.5.1 Brainstem model parameter selection

Since this model formulation and detail related to autonomic (i.e. parasympathetic) regulation has heretofore not been modeled, parameters were tuned to fit relevant experimental data. A central issue in parameter tuning involved selecting the appropriate data and experimental design from which this data was generated. Because model parameters for afferent components (i.e. receptors) have been previously determined [289–291,326], experimental data for parameter tuning of the brainstem neuronal components required controlled stimulation of afferent receptors and measures of effector function output. For example, to tune parameters describing the baroreceptor input-driven NTS subtype and its effect on ventricular

contractility, experimental data relating arterial pressure to ventricular contractility would be ideal. Thus brainstem parameters were tuned to simulate changes in heart rate and ventricular contractility measured in relevant physiological experiments [311].

Based on the model structure (Figure 5.4), the transfer functions representing the NA, DMV, and the NA's effect on contractility, i.e. $NA_{contractility}$, occur downstream of the transfer functions representing the NTS neuronal subtypes. As a result, multiple parameter values could potentially be selected for these downstream transfer functions, depending on the experimental data used. To address this issue, only one set of parameters for the downstream transfer functions were used based on the parameter values that best fit data related to baroreceptor effects on heart rate and contractility. These set parameters were subsequently used when defining parameters for the transfer functions representing the remaining NTS neuronal subtypes.

Baroreceptor input-driven subtype parameters were tuned to simulate experimental data generated by Suga et al. [311] who measured the percent change (relative to control conditions) in heart rate and left ventricular contractility (E_{max}) in response to changes in arterial pressure (Figure 5.5). Lung stretch receptor input-driven subtype parameters were tuned to simulate data from Greenwood [313] and Hainsworth [314]. In both cases, Greenwood and Hainsworth measured changes in heart rate relative to control conditions (Figure 5.6). While these experiments were conducted in canines, we assumed that similar changes would apply to the human model, where baseline heart rate and ventricular contractile values were based on

physiological data taken from healthy humans. It is important to note that when tuning both sets of parameters, they were adjusted in open-loop model structures mimicking the open-loop conditions of the experiments from which the data was generated. Once acceptable parameter values were defined, based on simulation fit to experimental data, these parameters were then used to determine the parameter set associated with the cardiopulmonary receptor neuronal subtype, which was tuned in a closed loop model structure.

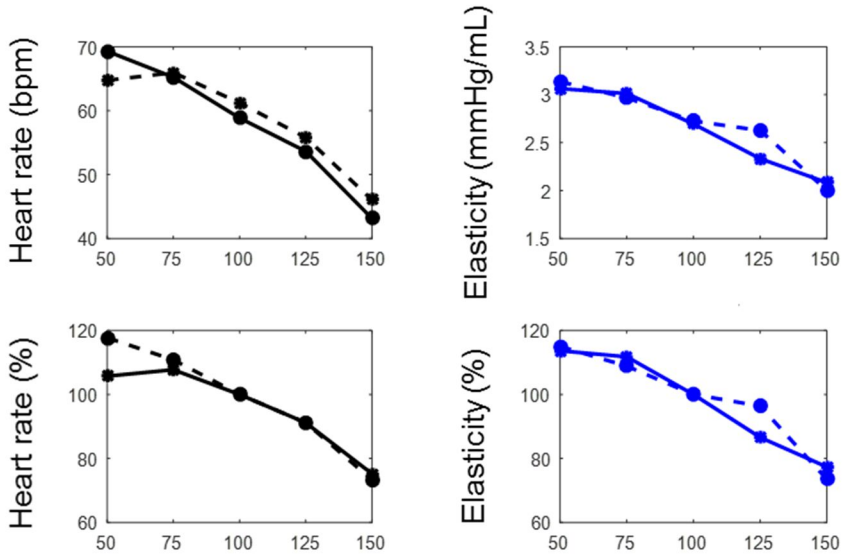

Figure 5.5 Parameter fitting for baroreceptor input-driven subtype, NA, $NA_{contractility}$, and DMV parameters. The simulated effects (dashed lines) of arterial pressure on heart-rate and ventricular contractility are shown with fitted parameters and compared against experimental results measuring percent changes in heart rate and contractility in canines (solid lines). Percent changes were scaled to physiological values corresponding to adult males using baseline heart rate and contractility values of 61.2 bpm and 2.695 mmHg/mL, respectively. Parameters were tuned in open-loop model conditions emulating the experimental design used to measure the changes in heart rate and contractility.

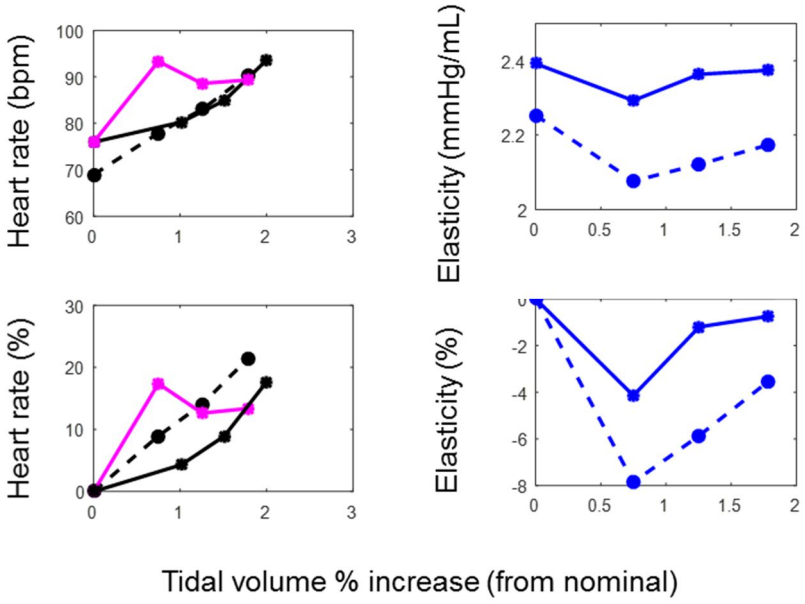

Figure 5.6 Lung stretch receptor input-driven subtype parameter fits. The simulated effects of lung volume on heart-rate and ventricular contractility are shown with fitted parameters and compared against experimental results measuring changes in heart rate and contractility in canines per experimental data found in [313] (purple lines) and [314] (black lines). Changes in heart rate and contractility were scaled to physiological values corresponding to adult males using baseline heart rate and contractility values of 84.6 bpm and 2.392 mmHg/mL, respectively (experimental – solid, simulated – dashed). Baseline parameters were drawn from simulations using the original model by Ursino [289,291] mimicking the open-loop conditions used in the experimental design, which differed from those used in [311]. Parameters were tuned in open-loop model conditions emulating the experimental design used to measure the changes in heart rate and contractility.

To tune parameters related to the cardiopulmonary baroreceptor input-driven subtype, experimental data generated by Frey [297] were used. In this case, experimental data was collected from adult females placed in a lower body negative chamber, which causes blood to pool in the lower body and results in a deactivation or

unloading of cardiopulmonary receptors. Therefore, these parameters were tuned in a closed loop model structure.

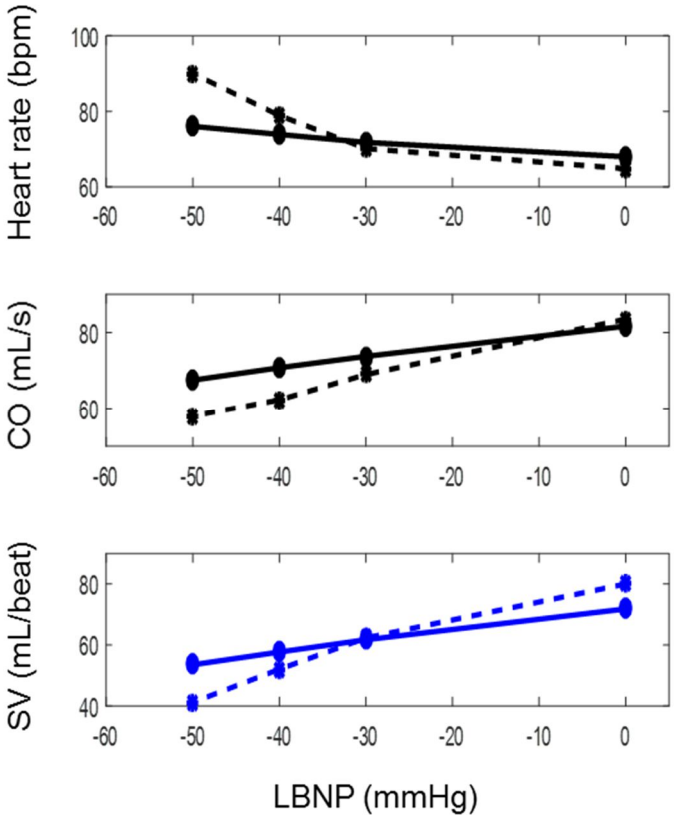

Figure 5.7 Cardiopulmonary receptor input-driven subtype parameter fits. The simulated effects of different lower body negative pressures on simulated heart-rate, cardiac output, and stroke volume (dashed lines) are shown with fitted parameters and compared against experimental results (solid lines) measuring these parameters in adult females placed in a lower body negative chamber [297]. Because the lower body negative chamber is a non-invasive technique that leads to changes in circulating blood volume, parameters were tuned in closed-loop model conditions, using the fitted parameters identified for the NA, $NA_{contractility}$, DMV, baroreceptor-, lung stretch receptor-neuronal subtypes from the previous model fitting results (Figures 5.5, 5.6). Experimental data (solid lines) and simulated fits (dashed lines) are shown.

We recognize that because multiple parameters are involved in influencing the vagal effects on heart rate and contractility, resulting in an over-parameterized model, multiple parameter sets are likely to yield reasonable fits to experimental data. However, because the model extensions only include a single input-output transfer function to represent neuronal populations from the NA and DMV that influence heart rate (NA) and ventricular contractility ($NA_{contractility}$ and DMV), we included only one set of parameters for each of the three transfer functions in order to constrain the possible parameter space. For reference, a comprehensive list of model parameters and supplementary text describing the original Ursino model and related equations are included in Appendix B.2.

5.5.2 Accentuated antagonistic effects on ventricular contractility

Previous experimental methods have demonstrated the nonlinear effects that simultaneous sympathetic and vagal drive have on cardiac functions beyond chronotropy. We use a similar technique to capture the nonlinear effect that combined sympathetic and vagal drive have on heart rate. Based on the resulting parameter values identified from the model fitting efforts, the model is able to capture the accentuated antagonistic effects that modulate ventricular contractility, as illustrated in Figure 5.8.

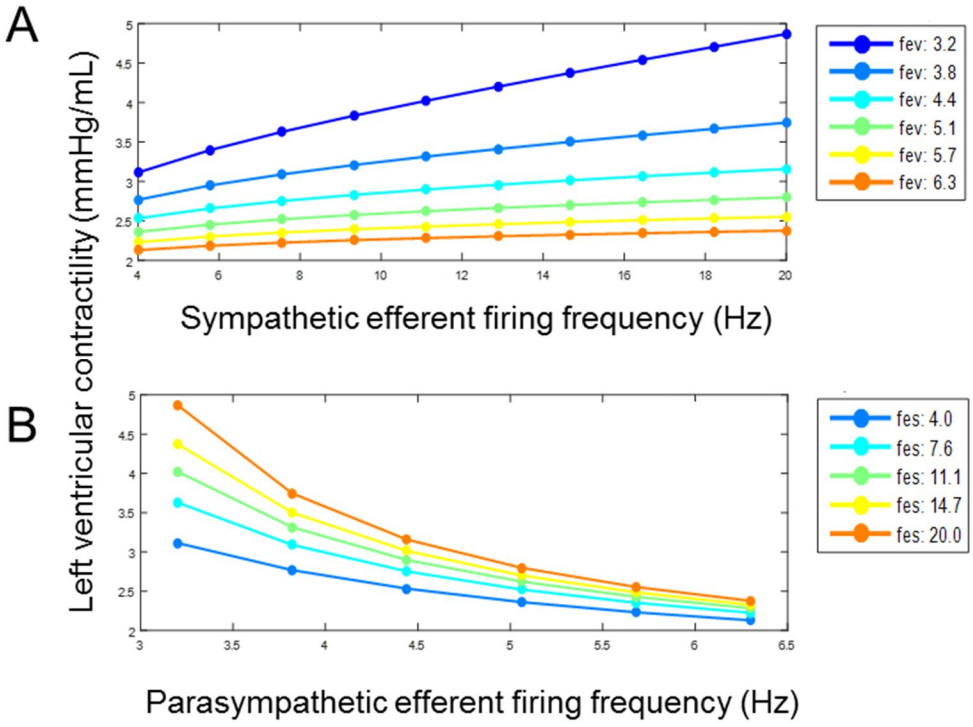

Figure 5.8 Accentuated antagonistic sympathovagal effects on ventricular contractility. Simulations were conducted to show the effect that (A) increasing vagal tone (fev), as represented by firing frequencies (Hz), has on contractility at different levels of sympathetic tone and (B) the effect increasing sympathetic tone has on contractility at different levels of vagal tone. Note that at higher sympathetic levels (fes), vagal tone has a larger inhibitory effect on contractility, as indicated by the larger drop in contractility (orange plot in A).

5.6 Simulation Results

The computational model described herein includes input-output transfer functions that reflect the input-driven neuronal subtype organization recently identified (Chapter 3), known neuroanatomical organization of parasympathetic efferent origins, and vagal efferent effects on multiple effector functions including heart rate and ventricular contractility. Given the closed-loop nature and complexities

associated with this system, including distinct time-delays characterizing sympathetic and vagal efferent effects and multiple interacting compartments, the model was developed in the SIMULINK environment (MathWorks®), which facilitates the modeling of these dynamic and interacting components. Ordinary differential equations incorporated into this model were solved using ODE15s, with an error tolerance of 1e–3.

5.6.1 Simulation of physiological conditions

Prior to using the model to explore the impact of neuronal adaptation under the disease state of systolic heart failure post myocardial infarction, simulations were conducted to evaluate the model's ability to recapitulate hemodynamic and cardiovascular behavior consistent with healthy physiology of a 70 kg adult. To evaluate simulated cardiovascular performance, multiple hemodynamic parameters were used, including end diastolic pressure and volume (EDP and EDV, respectively) and end systolic pressure and volume (ESP and ESV, respectively). These values are traditionally visualized as the pressure-volume loop associated with the cardiac cycle. Additional parameters left ventricular pressure, left ventricular flow rates, ejection fraction, which measures the fraction of blood pumped out of the ventricle after systole, and cardiac output, which is a measure of the total volume of blood pumped by the heart per unit time. Some clinically relevant cardiovascular parameters and their acceptable ranges, based on hemodynamic measures observed in literature, are provided in Table 5.1.

Table 5.1 Hemodynamic parameters for adult females(64 kg)

Parameter	Value		(units)	Reference
SBP	123	(11)	mmHg	[334]
DBP	72	(8)	mmHg	[334]
EDV	118	(19)	mL	[334]
ESV	43	(11)	mL	[334]
EDP	9	(3)	mmHg	[335]
ESP	120	(20)	mmHg	[335]
EF	0.64	(0.08)	--	[334]
CO	85	(21)	mL/s	[334]
SV	75	(15)	mL/beat	[334]

Values in parenthesis represents standard deviation as reported in sources. Abbreviations: systolic blood pressure (SBP), diastolic blood pressure (DBP), end diastolic volume (EDV), end systolic volume (ESV), end diastolic pressure (EDP), end systolic pressure (ESP), ejection fraction (EF), cardiac output (CO), and stroke volume (SV)

These values, measured in adult females [334], were used as reference to compare model simulations against. Because the mass of the females varied around 64 kg, their hemodynamic measures would be more appropriate to use as a reference for the model, which was based on parameters scaled to an 70 kg adult [291]. Hemodynamic simulations of the cardiac cycle demonstrate that the model does simulate cardiovascular behavior that lies well within the expected range of hemodynamic measures associated with healthy adults, with an approximate mass of 70 kg.

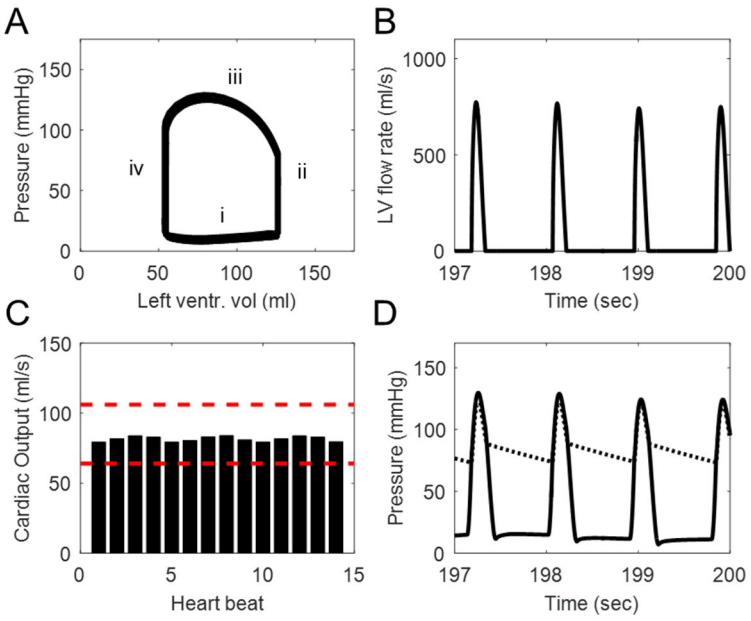

Figure 5.9 Hemodynamic performance of left ventricle over multiple cardiac cycles. (A) The pressure volume relationship, P-V loop, is shown for the extended model. The various steps of the cardiac cycle represented include, *i)* filling phase, *ii)* isometric contraction, *iii)* ejection, and *iv)* isometric relaxation. The variability observed in the P-V loop is due to the effects of respiration, which is captured in changes in thoracic pressure that affects flow into the right atrium. (B) Flow rate of blood pumped out of the left ventricle. (C) Bar plot of cardiac output (mL/s). The dotted red lines represent the physiological ranges of cardiac output for healthy adults, approximately 70 kg [334]. (D) Systemic pressure (P_{sa}, black dashed line) and left ventricular pressure ($P_{max,lv}$, solid black line) over the course of multiple cardiac cycles.

5.6.2 Simulating systolic heart failure due to myocardial infarction

Simulating a diseased or impaired cardiovascular state would present a situation that could potentially cause dramatic changes in the synaptic inputs received by brainstem neurons. In this study we chose to examine the effects of neuronal adaptation under closed-loop conditions mimicking systolic heart failure due to

myocardial infarction. This condition was chosen for two main reasons: *i)* damages incurred from myocardial infarction affect left ventricular structure and functions can be simulated by modifying corresponding physiological parameters of the heart in this model, and *ii)* relevant animal models exist that can be used to simulate systolic heart failure post myocardial ischemia, which will enable us to test and verify experimentally predictions made based on model simulations and analysis.

Systolic heart failure following a myocardial infarction is characterized by ventricular remodeling that results in an enlarged left ventricle. In addition, ventricular contractility is reduced, which results in an impaired ability to pump blood out of the heart and a subsequent reduced ejection fraction, where an ejection fraction less than 0.5, which is considered to be the clinical threshold for classifying reduced ejection fraction [305,336,337]. These changes lead to increases in EDV and ESV and result in reduced cardiac output, reduced cardiovascular health and increases the risk of a reoccurrence of a myocardial infarction. However, both systolic and diastolic blood pressures continue to exist within ranges considered to be normotensive [338]. To simulate these physiological characteristics, parameters associated with left ventricular contractility, resistances, unstressed volumes, and sympathetic tone to the heart were modified to match qualitatively the physical changes that are known to occur in the heart following a myocardial infarction. Modified parameters are included in Appendix B.2.

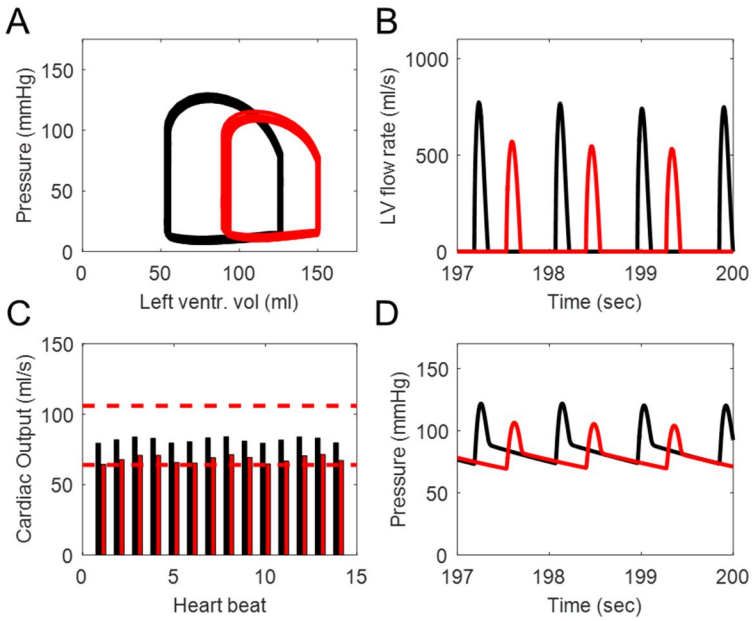

Figure 5.10 Simulating systolic heart failure due to myocardial infarction. Hemodynamic performance of the left ventricle under the nominal (black) and diseased state (red) is shown, as in Figure 5.9, including the (A) P-V loop, (B) flow rate of blood pumped out of the left ventricle, (C) cardiac output (mL/s), and (D) systemic (P_{sa}) and left ventricular pressure ($P_{max,lv}$).

5.6.3 Compensatory effects of brainstem neuronal adaptations

To simulate neuronal adaptations, we modified parameters, defined in Equation 5.1, to change various aspects of the nonlinear sigmoidal behavior of the neuronal subtypes and specific populations included in the model. Using the cardiovascular measures outlined in Table 5.1 as reference for hemodynamic parameters in healthy adults (i.e. nominal values), we evaluate how parameter changes to the transfer functions can potentially compensate for or worsen cardiovascular state under the simulated conditions of systolic failure.

Initial simulation efforts focused on modifying parameters associated with all brainstem neurons included in the model to determine the extent to which neuronal adaptation could potentially compensate for impaired cardiac function. We explored a parameter space encompassing a 10-fold increase or decrease of the nominal parameters tuned to fit experimental data. We used a Sobol sampling technique to generate 1000 randomly selected parameter sets to explore the parameter space and evaluate the corresponding effects on hemodynamic behavior. Simulation analysis revealed that only few parameter sets were able to compensate adequately for impaired cardiac function, an example of this compensatory effect is illustrated in Figure 5.11.

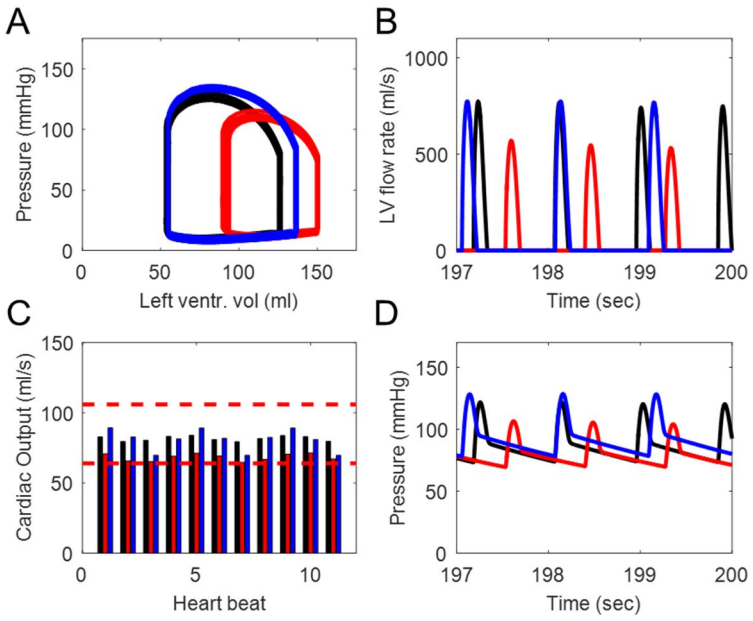

Figure 5.11 Hemodynamic performance based on representative neuronal adaptations in the brainstem. Hemodynamic performance of the left ventricle under the nominal (black), diseased state (red), and adapted state (blue) are shown. Hemodynamic behavior illustrated include (A) P-V loop, (B) flow rate of blood pumped out of the left ventricle, and (C) cardiac output (mL/s), and (D) systemic (P_{sa}) and left ventricular pressure ($P_{max,lv}$). Based on these neuronal adaptations, the resulting ejection fraction is 0.635.

In this example, changes to parameters associated with all brainstem transfer functions were able to shift the pressure-volume relationship from the diseased state back towards the nominal hemodynamic condition. Ejection fraction, EDV, EDP, ESV, and ESP were brought back to near nominal levels. Although a slight increase in systolic and diastolic pressures occurred, these pressures were well within normotensive blood pressure ranges. A closer examination of the behavior of the

modified brainstem transfer functions show that multiple changes to input-output response, as illustrated in Figure 5.12.

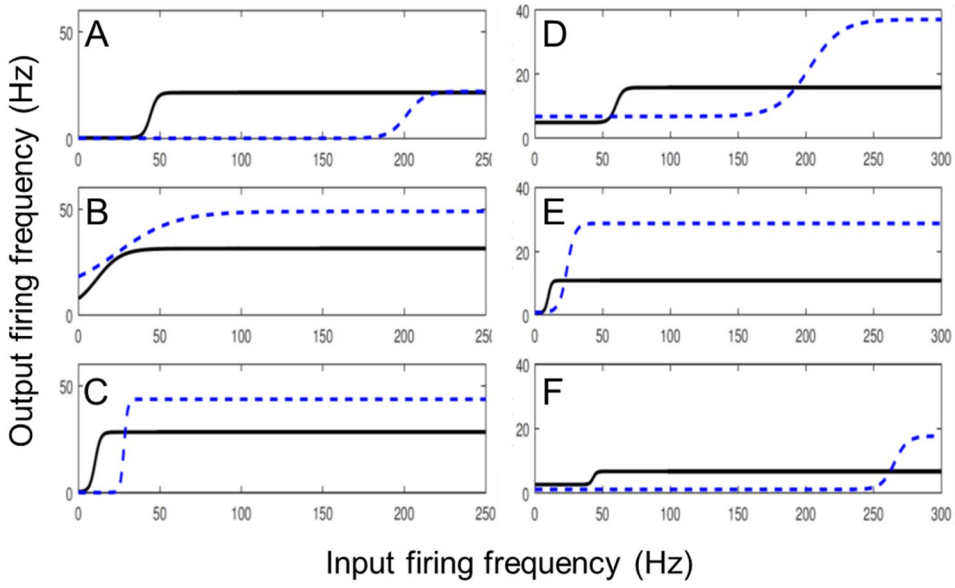

Figure 5.12 Representative adapted input-output transfer function relationships of neuronal subtypes and populations modeled in the brainstem. Changes to the sigmoidal input-output relationships describing neuronal function are shown for the input-driven neuronal subtypes and neuronal brainstem populations included in the brainstem portion of the model. Nominal (solid black line) and adapted (dashed blue line) input-output behavior is shown for the (A) baroreceptor subtype, (B) lung stretch receptor subtype, and (C) cardiopulmonary subtype. Additional brainstem neuronal populations included those in the (D) NA, primarily affecting heart rate, (E) $NA_{contractility}$, primarily affecting ventricular contractility, and (F) DMV, which primarily affects ventricular contractility.

Changes included increases in the dynamic response range of these neuronal populations. The rightward shift of the sigmoidal curve indicates an increase in the range of input values to which these populations are sensitive. Moreover, the

sensitivity of these neuronal populations, indicated by the slope of the curve, changes as well. To gain a better understanding of how these changes affected vagal tone, we analyzed the time-dependent changes to the various inputs and outputs associated with these neuronal populations. The corresponding input and output firing frequencies are compared in Figure 5.13.

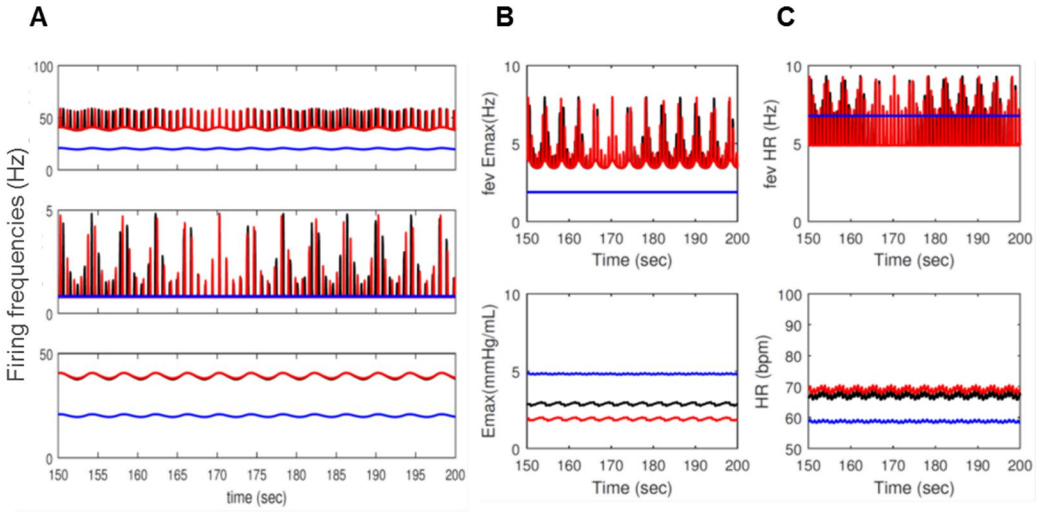

Figure 5.13 Input signal characteristics in brainstem due to adaptations occurring throughout the brainstem. Firing frequency outputs are shown over the last 50 secs of the 200 sec simulation for the nominal (black), diseased (red), and adapted (blue) states. In (A), the top subpanel illustrates the input firing frequency received by the neuronal population in the NA that primarily affects heart rate. Middle panel: Input firing frequency signal to the neuronal population in the NA that primarily affects contractility. Bottom panel: Input firing frequency signal to the neuronal population in the DMV that affects contractility. (B) Top panel: firing frequency representing vagal tone (*fev*) that modulates contractility (E_{max}). This firing frequency represents the sum of the output signals generated by brainstem neuronal populations represented by the $NA_{contractility}$ and DMV transfer functions. Bottom panel: the resulting contractility of the left ventricle. (C) Top panel: firing frequency representing the vagal tone that modulates heart rate. Bottom panel: resulting heart rate.

From the results, it is apparent that regardless of the higher input firing frequencies to the NA, DMV, or $NA_{contractility}$, lower firing frequencies are generated by these neuronal populations resulting in decreased vagal tone. This decrease in vagal tone results in a corresponding increase in ventricular contractility and a slight increase in heart rate. Ultimately, this leads to a desirable increase in cardiac output and improved ejection fraction (0.635, Figure 5.11).

Having demonstrated that compensation could be achieved through neuronal adaptation in the brainstem, we next sought to determine whether this compensatory effect could be localized to a particular neuronal subtype or population. Based on the functional importance the NTS plays in blood pressure regulation and the distinct roles that the NA and DMV have in regulating vagal outflow, we divided and examined the brainstem into two distinct sections, *i)* the NTS, and neuronal subtypes therein, and *ii)* the NA and DMV. We therefore examined the effects of adaptation to the NTS and associated neuronal subtypes separate from adaptive changes occurring to the neuronal populations mediating the effects the NA and DMV have on heart rate and contractility. Similar to the initial simulation analysis, we preformed simulation analysis using randomly selected parameter sets for each division of the brainstem. Our analysis revealed that of the 1000 independently selected parameter sets tested, none were able to complete compensate and return hemodynamic behavior of the cardiovascular system. However, several parameter sets were able to improve hemodynamic behavior, decreasing EDV and ESV while increasing ejection fraction to values nearing 0.5 (ejection fraction = 0.425), an example of which is shown in

Figure 5.14, along with the corresponding changes to the input-output transfer function behavior in Figure 5.15.

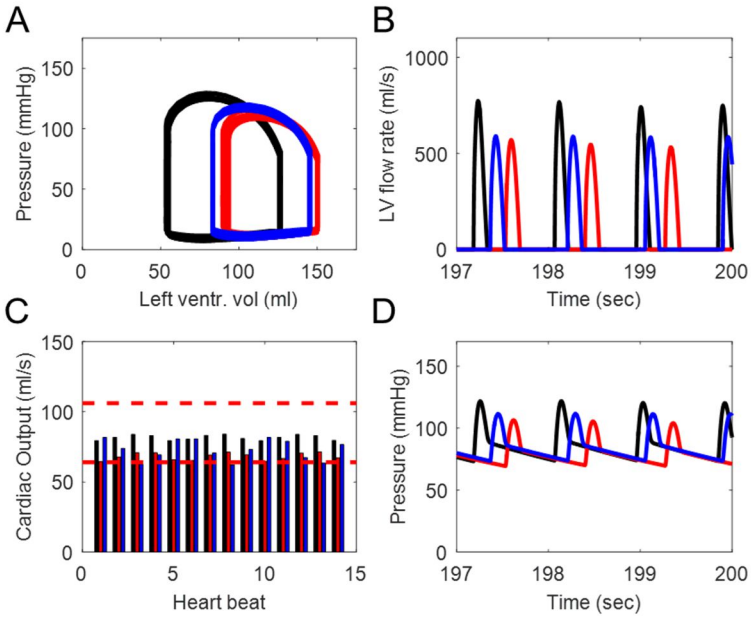

Figure 5.14 Hemodynamic performance based on representative neuronal adaptations in the NTS. Hemodynamic performance of the left ventricle are shown based on neuronal adaptations occurring only in the NTS neuronal subtypes. Nominal (black), diseased (red), and adapted states (blue) are represented with (A) P-V loop, (B) flow rate of blood pumped out of the left ventricle, and (C) cardiac output (mL/s), and (D) systemic (P_{sa}) and left ventricular pressure ($P_{max,lv}$). Based on these neuronal adaptations, the resulting ejection fraction is 0.425.

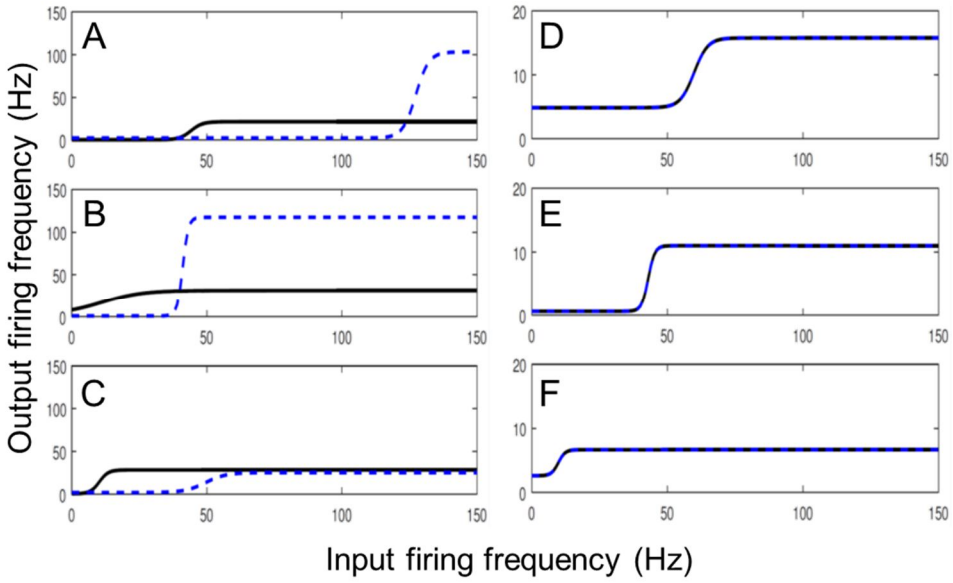

Figure 5.15 Representative adapted input-output transfer function relationships of neuronal subtypes in the NTS. Changes to the sigmoidal input-output relationships describing neuronal function are shown for the input-driven neuronal subtypes in the NTS. Nominal (black), diseased (red) and adapted (dashed blue line) input-output behavior is shown for the (A) baroreceptor subtype, (B) lung stretch receptor subtype, and (C) cardiopulmonary subtype. Note that the nominal and adapted transfer functions in (D-F) overlap each other because no changes were made to the NA, $NA_{contractility}$, and DMV transfer functions.

In this particular case, it is interesting to note that in Figure 5.15, the baroreceptor-driven neuronal subtypes experience a large rightward shift is observed, larger than any shift observed in the other neuronal subtypes. In addition, the increase in the dynamic response range of this subtype and the lung-stretch-receptor-driven neuronal subtype is much larger than the adaptation required to compensate for systolic heart failure when all neuronal populations in the brainstem were modified. The

corresponding input and output firing frequencies associated with adaptation occurring only in the NTS are provided in Figure 5.16.

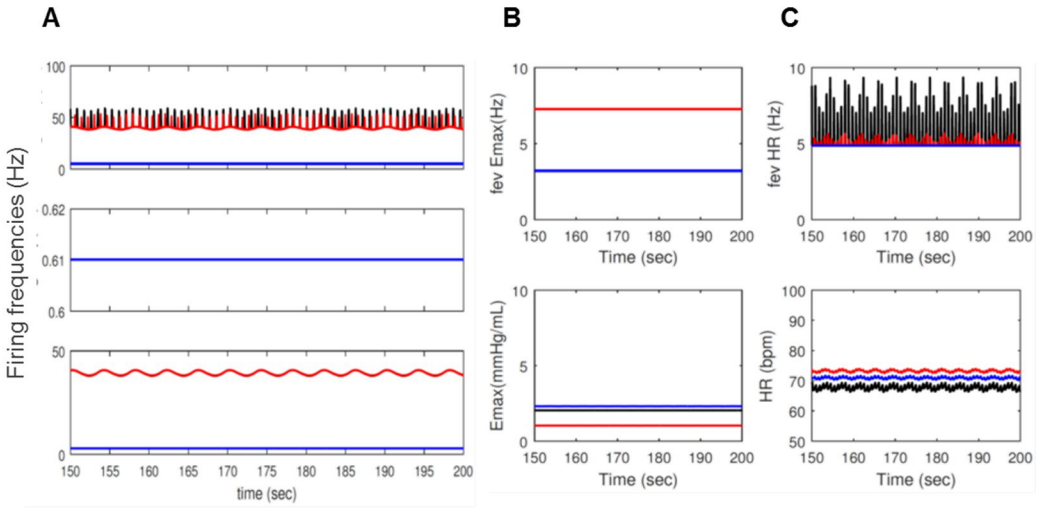

Figure 5.16 Input signal characteristics in brainstem due to adaptations occurring in neuronal populations outside of the NTS. Firing frequency outputs are shown over the last 50 secs of the 200 sec simulation for the nominal (black), diseased (red), and adapted (blue) states. (A), Top panel: input firing frequency received by the neuronal population in the NA that primarily affects heart rate. Middle panel: Input firing frequency signal to the neuronal population in the NA that primarily affects contractility. Bottom panel: Input firing frequency signal to the neuronal population in the DMV that affects contractility. (B) Top panel: firing frequency representing vagal tone that modulates contractility. This firing frequency represents the sum of the output signals generated by brainstem neuronal populations represented by the $NA_{contractility}$ and DMV transfer functions. Bottom panel: the resulting contractility of the left ventricle. (C) Top panel: firing frequency representing the vagal tone that modulates heart rate. Bottom panel: resulting heart rate.

The figures above, comparing the corresponding firing frequencies of the nominal, diseased, and near-compensated state, show a similar reduction in vagal tone

affecting ventricular contractility and heart rate. It is interesting to note that the firing frequencies received by the NA are much lower and more stable than the input firing frequencies in the previous example, where all brainstem parameters were modified. This reduction in firing frequencies is due, in part, to the large rightward shift observed in the baroreceptor-driven NTS neuronal subtype. Because the input frequency required to achieve half of the maximum response output increased dramatically, it effectively desensitized this subtype to any inputs generated by the baroreceptors. This in turn resulted in the decreased output from this NTS subtype and decreased the overall input to the NA, which subsequently decreased vagal tone. While the adaptations differ from those that occurred from the initial parameter adjustment study, the effects are the same – a reduction in vagal tone leading to an increase in ventricular contractility.

Finally, simulations involving parameter modifications to only the NA, $NA_{contractility}$, and DMV revealed that hemodynamic behavior can be restored to nominal ranges. An example of compensatory effects of neuronal adaptation in these neuronal populations is presented in Figures 5.17-5.18:

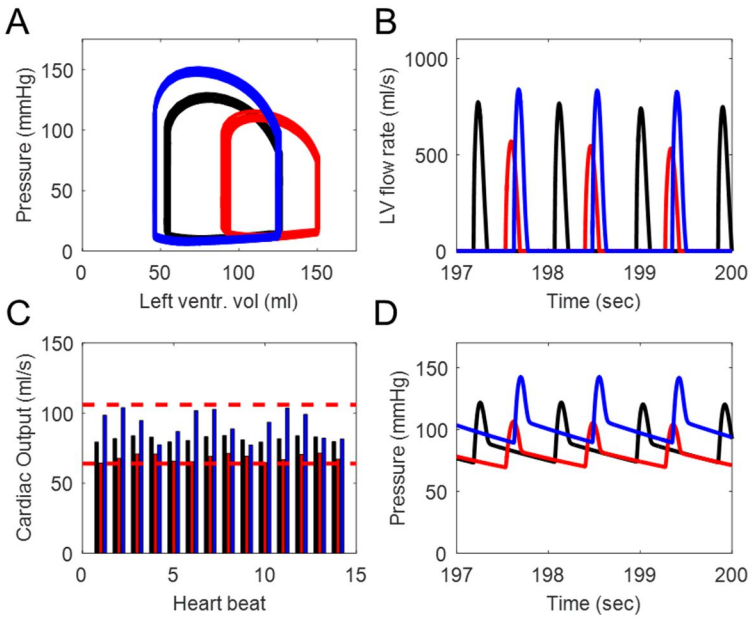

Figure 5.17 Hemodynamic performance based on representative neuronal adaptations in the NA, $NA_{contractility}$ and DMV neuronal populations. Hemodynamic performance of the left ventricle are shown based on neuronal adaptations occurring only in the NTS neuronal subtypes. Nominal (black), diseased (red), and adapted states (blue) are represented with (A) P-V loop, (B) flow rate of blood pumped out of the left ventricle, and (C) cardiac output (mL/s), and (D) systemic (P_{sa}) and left ventricular pressure ($P_{max,lv}$). Note the increase in systemic pressure due to the adapted state. This is likely due to the increased flow from the left ventricle. Based on these neuronal adaptations, the resulting ejection fraction is 0.630.

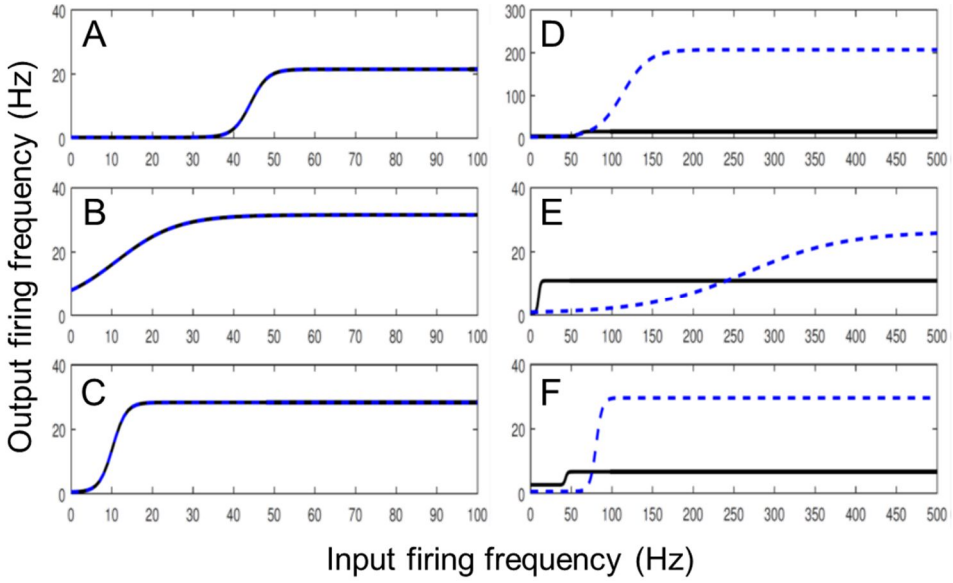

Figure 5.18 Representative adapted input-output transfer function relationships of brainstem neuronal subtypes outside of the NTS. Changes to the sigmoidal input-output relationships describing neuronal function are shown for the input-driven neuronal subtypes in the NTS. Nominal (black), diseased (red) and adapted (dashed blue line) input-output behavior is shown in the input-driven NTS subtypes in (A-C). Note that no changes are observed as parameters associated with these subtypes remained constant in this representative example. Nominal and adapted states are shown for (D) NA, (E) $NA_{contractility}$, and (F) DMV transfer functions, i.e. neuronal populations.

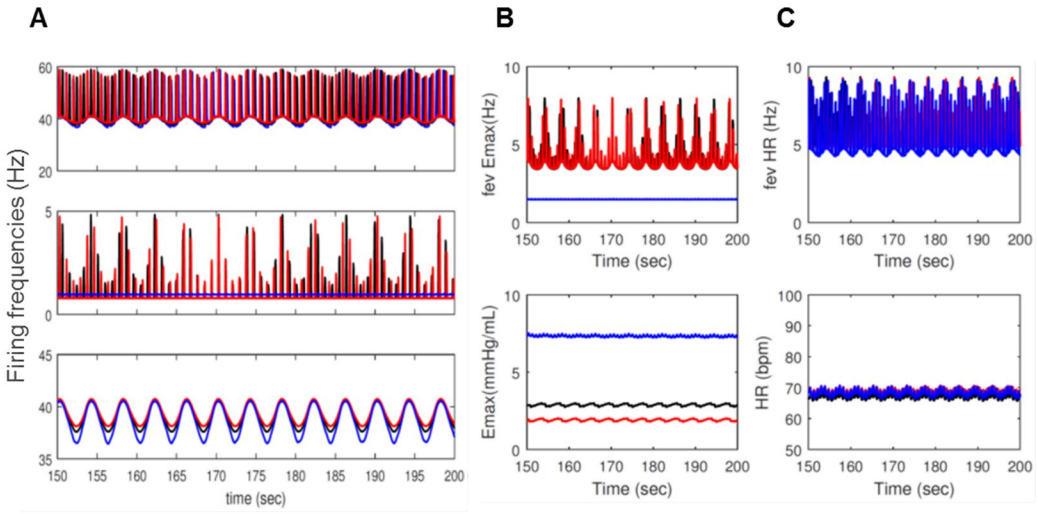

Figure 5.19 Input signal characteristics in brainstem due to adaptations occurring in neuronal populations outside of the NTS. Firing frequency outputs are shown over the last 50 secs of the 200 sec simulation for the nominal (black), diseased (red), and adapted (blue) states. (A), Top panel: input firing frequency received by the neuronal population in the NA that primarily affects heart rate. Middle panel: Input firing frequency signal to the neuronal population in the NA that primarily affects contractility. Bottom panel: Input firing frequency signal to the neuronal population in the DMV that affects contractility. (B) Top panel: firing frequency representing vagal tone that modulates contractility. This firing frequency represents the sum of the output signals generated by brainstem neuronal populations represented by the $NA_{contractility}$ and DMV transfer functions. Bottom panel: the resulting contractility of the left ventricle. (C) Top panel: firing frequency representing the vagal tone that modulates heart rate. Bottom panel: resulting heart rate.

Although hemodynamic behavior were restored to levels within nominal ranges, there was a corresponding increase in blood pressure (systolic blood pressure = 142 mmHg, diastolic blood pressure = 89 mmHg), a result due to change in cardiac output, which was above nominal conditions. Similar to other conditions that improved or returned hemodynamic behavior, vagal tone was decreased, which led to

an increase in contractility and in increase in cardiac output. Vagal tone affecting heart rate showed a much more dynamic profile than the vagal tone affecting contractility. This difference was due to the presence of distinct transfer functions (neuronal populations) that affect either heart rate or contractility. The parameter changes affecting the NA neuronal population modulating contractility caused a larger shift in the input threshold, effectively minimizing the response output of this population to the input firing frequencies received. The parameter changes associated with the NA neuronal population affecting heart rate did not shift the input threshold as dramatically and thus this neuronal population would generate output firing frequencies that mimic the dynamics of the input signal received.

5.7 Discussion

In this study, we investigated the functional relevance of adaptation occurring to distinct neuronal subtypes within the context of baroreceptor reflex regulation of arterial blood pressure. By developing a closed-loop control model of short-term baroreflex regulation of distinct cardiovascular functions, we were able to examine how adaptation of neuronal subtypes within the NTS and brainstem affect vagal tone and compensate for changes associated with a diseased state. By modifying the parameters characterizing the left heart, we were able to reproduce hemodynamic behavior corresponding to systolic heart failure induced by myocardial infarction.

The results from the simulation analysis suggest that neuronal adaptation is necessary to compensate for the impaired systolic function of the left heart. These

compensatory changes are the result of reduced vagal tone which ultimately results in increased ventricular contractility, cardiac output, and improved ejection fraction. Based on the organization of the brainstem and the distinct connections of neuronal populations affecting specific cardiac functions, heart rate was not as dramatically affected in compensated conditions as ventricular contractility.

A common theme across the compensated conditions under the impaired cardiovascular state induced by systolic heart failure was reduced vagal tone. These results align with current knowledge, which dictates that cardiac vagal activity is diminished and unresponsive in diseased states [38]. Impaired vagal activity is typically coupled with increased sympathetic activity, leading to many symptoms observed in heart disease. However, our results indicate that this decreased vagal activity acts as a short-term compensatory mechanism by which brainstem neurons seek to improve hemodynamic behavior and cardiovascular state. This short-term compensatory response aligns with the expected physiological changes associated with systolic heart failure following myocardial infarction. Because the compliance of the heart decreases, i.e. cardiac muscle fibers become "stiffer" as a result of the infarction, the contractility of the heart decreases [339,340]. To compensate for the resulting lowered cardiac output, a possible mechanism to increase cardiac output is to increase neuronal excitation (or similarly decrease neuronal inhibition) of the ventricles to increase contractile efforts. This can be achieved by increasing sympathetic tone and, as suggested by our model simulations, by decreasing vagal tone and the inhibitory influence of parasympathetic innervations to the ventricles.

Despite the compensatory effects decreased vagal tone may have in the short-term, sustained impairment of vagal tone is undesirable, so much so that it has become prognostic indicator of heart health [341]. In addition, clinical evidence supports the benefits of elevating vagal tone in heart disease, which provides cardioprotective effects. As our model indicates what neuronal adaptations occur to provide a short-term compensatory effect, it is possible that these changes are somehow sustained and continue to inhibit vagal tone long-term. By understand the adaptive changes that occur initially, it may be possible to investigate and target these mechanisms to improve vagal drive.

Our simulation analysis provides several interesting insights into these neuronal mechanisms. Because the NTS, NA, DMV, and the neuronal subtypes within these nuclei are connected and modulate vagal tone [38], neuronal adaptation may affect multiple neuronal populations within the brainstem and affect vagal tone. Our results indicate that neuronal adaptation, represented by parameter changes to the corresponding transfer functions, must occur in multiple brainstem neuronal populations to compensate for impaired systolic function. Adaptations occurring only in NTS neuronal subtypes were not enough to fully compensate for the impaired state nor improve cardiac output and ejection fraction to nominal levels. While the parameter space explored in our analysis involved a 10-fold increase/decrease from the nominal parameter values, exploring a larger parameter space would unlikely lead to different results or conclusions. This is due to the structure of signal flow occurring from the NTS to the NA and DMV and the sigmoidal input-output transfer functions

used. Reducing vagal tone in the context of this model would require decreasing output firing frequencies from the NTS neuronal subtypes. However, minimum firing frequencies tested in our simulations included near-zero firing levels. Thus, it is unlikely that exploring a larger parameter space would result in the identification of parameter sets representative of neuronal adaptations that would fully compensate for systolic heart failure. The need for adaptations to occur in the neuronal populations of the NA and DMV supports the importance that these nuclei play in regulating cardiovascular function and state.

The neuronal changes occurring in the transfer functions representing the neuronal populations in the NA and DMV indicate that they minimize the outputs generated by the NTS. These adapted neuronal populations appear to act as filters or synaptic gates, modulating the input signals generated by the neuronal subtypes in the NTS, as seen in Figures 5.13, 5.16, and 5.19. Neuronal adaptations that lead to this gating effect may be a potential area to focus. Targeting molecular mechanisms contributing to this sustained gating effect by neuronal populations in the NA and DMV may improve or reverse this neuronal gating behavior by the NA or DMV that when sustained, leads to the impaired vagal tone and overall autonomic imbalance associated with heart disease.

Several molecular mechanisms associated with autonomic imbalance in other conditions of heart disease and cardiac dysfunction have focused on ion-channels affecting membrane potential. One example includes the Kv1.1 Shaker-like potassium channel encoded by the Kcna1 gene. Gene knockout studies investigating sudden

unexplained death in epilepsy (SUDEP) have shown that this gene plays a central role in primary neurogenic cardiac dysfunction, affecting neural signaling between the brain and heart [342]. Specifically, increased parasympathetic tone as a result of deficient or absent Kcna1 expression in the vagal nerve fibers was found to contribute to the neurocardiac defect in mouse models. In this context, a sustained overexpression of Kcna1 in neurons within the NA and DMV may contribute to the reduced vagal drive observed in the model simulations. Another ion channel related target includes N-type Ca^{2+} channels (NCCs). Pharmacological studies performed in dnNRSF-Tg mice, a transgenic mouse model of cardiomyopathy, revealed that blocking NCCs improved autonomic imbalance by reducing sympathetic overdrive as well as improving parasympathetic drive [343]. Although the molecular mechanisms underlying this autonomic modulation remain unclear, it is believed that blocking NCCs affect the interaction between the sympathetic and parasympathetic arms of the ANS. Thus characterizing expression of genes coding for NCCs and the associated regulatory interactions affecting expression in the NA and DMV may reveal potential novel therapeutic targets for improving parasympathetic drive.

While this model represents a quantitative characterization of brainstem neuronal components involved in cardiovascular regulation that have not been modeled to this extent, as far as we know, there are limitations to this model worth discussing. While only a few select afferent input-types were included in this model, the NTS receives a diverse array of afferent and higher-order inputs. For example, chemoreceptor afferents terminate in the NTS and play a major role in cardiovascular

regulation. Although chemoreceptors have a larger influence in regulating pH and oxygen levels in the blood and certainly impact cardiovascular and respiratory function. Furthermore, neuronal populations in the DMV have been shown to generate spontaneous rhythmic firing patterns. These pacemaker neurons play a critical role in modulating heart rate and respiration, both of which impact cardiovascular function as well [131,331]. While these omissions limit what types of physiological conditions can be explored with this model, they provide future opportunities to improve the model and enable one to use this model to explore additional conditions such as neuronal mechanisms involved in impaired response to exercise-induced stress in those suffering systolic heart failure post myocardial infarction.

Despite these limitations, this model provided a platform with which to examine the functional relevance of neuronal adaptation, as suggested from the single-neuron analysis of the NTS. The adaptive responses generated by input-driven neuronal subtypes and neuronal populations in the brainstem provide a mechanism through which the autonomic nervous system is able to provide short-term compensation for changes or impaired function, such as the case of systolic heart failure. These results suggest that neuronal adaptation provides a mechanism which enables robust short-term regulation of cardiovascular homeostasis by the brain. Further analysis is required to explore how or why these neuronal adaptations, which lead to this gating effect that inhibits vagal tone, are potentially sustained in cases of systolic heart failure. Possible model extensions and simulation work are provided in the final chapter of this dissertation.

Chapter 6

MOLECULAR AND CELLULAR ORGANIZATION UNDERLYING THE CIRCADIAN PHASE SHIFT RESPONSE IN THE SUPRACHIASMATIC NUCLEUS

In this chapter, the approaches and concepts developed in Chapters 3 and 4 are applied towards identifying an organizational framework in which transcriptionally heterogeneous single neurons form neuronal phenotypes within the suprachiasmatic nucleus. A statistical analysis is also performed to identify paracrine signaling mechanisms through which these phenotypes form a cellular interaction network that underlies the response of the suprachiasmatic nucleus to a light-induced circadian phase-shift.

6.1 Introduction

The work presented in this chapter represents a departure from the NTS and the neurons within. In Chapters 3 and 4, experimental and multivariate analytical approaches were applied to identify transcriptional phenotypes amid the transcriptional heterogeneity pervasive across single NTS neurons. Analyzing the heterogeneous transcriptional states of these neurons with respect to their functional connectivity revealed distinct input-driven neuronal subtypes, which respond adaptively to the inputs received. Using similar approaches, we test the generality of

this type of molecular organization by studying another brain nucleus, the suprachiasmatic nucleus (SCN). In this study, the transcriptional heterogeneity of single SCN neurons is analyzed to identify not only what neuronal phenotypes may exist in the SCN, but to determine how these neuronal phenotypes may organize into larger more complex cellular networks, which are critical in maintaining SCN function.

As discussed in § 2.2.2, the principal biological clock in mammals resides in the suprachiasmatic nucleus (SCN). This nucleus synchronizes physiological and behavioral processes throughout the body to cycles with periods of approximately twenty-four hours, i.e. *circadian rhythms*. Synchronization, which enables coordinated anticipation of the 24 h daily light/dark cycle, results from coherent, rhythmic output signals generated and adjusted by the SCN in response to photic inputs. This cyclic behavior of the SCN arises from single neurons, which exhibit autonomous circadian rhythms, interacting with one another via synaptic and paracrine signaling mechanisms to form cellular interaction networks that synchronize the oscillatory behavior of individual SCN neurons [108]. Consequently, SCN tissue is able to generate synaptic and molecular signals that are more precise and rhythmic than those of individual neurons. Because synchronization results in part from emergent properties of the cell-interaction networks underlying SCN function, a better understanding of such properties requires knowledge of the functional behavior of these cellular networks and how their constituent components (i.e., single neurons) are organized.

Prior studies characterizing SCN neurons relied on intrinsic neurochemical features and spatial localization, connecting SCN regional phenotypes to biomolecular signaling mechanisms. Immunohistochemical (IHC) staining of neurons expressing vasoactive intestinal polypeptide (VIP) or arginine vasopressin (AVP) have shown that these neurons mainly localize within the ventrolateral (core) or dorsomedial (shell) regions of the SCN, respectively [148,344,345]. VIP+ and AVP+ neurons differ in the expression of cell-surface receptors and genes involved in circadian regulation (i.e. core clock genes) in response to light stimuli. Distinct spatial localization and transcriptional responses in VIP+ and AVP+ neurons have made these neuropeptides convenient neuronal phenotypic markers that have provided insight into the function and spatial organization of the photic input-oscillator-output system that entrains the SCN to a light/dark cycle [346–349].

However, single-cell level analyses have shown that individual neurons comprising SCN cell-networks are heterogeneous across multiple functional levels, as exemplified in single neuron firing patterns, which occur at different phases of the circadian cycle [350], and in the period of oscillatory gene expression programs, which varies from 22 h to 30 h [98,273,351]. Additionally, while most VIP+ and AVP+ neurons exhibit intrinsic rhythmic firing rates and transcriptional programs, not all neurons (*in vitro)* exhibit circadian behavior. In the absence of synaptic signaling, these behaviors can become unstable, resulting in some neurons losing their intrinsic rhythmicity while others can spontaneously gain rhythmicity [352]. Further, waves of gene expression travel through cultured SCN tissue in an orderly fashion [353]

indicating that a complex phase relationship exists among neuronal oscillators, even when functionally coupled.

Understanding how neurons interact and form cell-interaction networks regulating circadian behavior is further confounded by the inherent transcriptional heterogeneity exhibited by single neurons, as reported in [27,93] and analyzed previously in Chapters 3 and 4. The results obtained from the analysis of single NTS neurons in Chapter 3 suggests that single-neuron transcriptional heterogeneity may be understood in terms of the synaptic and neuromodulatory inputs that drive neurons into distinct transcriptional states [106]. Concomitantly, recent work has shown that phase-shift behavior in the SCN arises from the expression behavior of multi-genic networks [149,156,157,159]. These results, when considered with the input-driven nature of photosensitive SCN neurons and their region-specific peptide expression behavior, suggest that analyzing both the transcriptional responses of individual SCN neurons to photic inputs and their spatial distribution throughout the nucleus would provide insight into the neuronal phenotypic states and organization of these states comprising the cell-networks that drive the robust and synchronized outputs of this brain nucleus.

In this chapter, an analysis of the SCN is performed to reconcile the heterogeneous behavior of individual SCN neurons with the coordinated behavior of the SCN. A combined experimental and computational approach, similar to those described in Chapter 3, are applied. The transcriptional and spatial diversity of single SCN neurons are analyzed in mice experiencing a light-induced phase-shift in their

circadian rhythms and a neuronal interaction network model is developed, which is used to interpret the single-cell heterogeneity in the context of tissue-level function [22]. Towards this objective, hundreds of individual SCN neurons are sampled, using laser capture microdissection [33,105,354,355], while their *in situ* positions are tracked simultaneously. These neurons are subsequently characterized, independent of prior knowledge of known SCN neuron-types, using their transcriptional states across a panel of circadian-related genes in order to characterize neurons more comprehensively than might be possible from a single biomarker or a select few biomarkers [94]. Given the previous extensive characterization of the transcriptional regulation of circadian rhythms [156,158,356,357], the current study focuses on analyzing the expression levels of 96 genes relevant to intercellular signaling and gene expression programs previously identified to contribute to neuronal phase-shifting behavior [149,156,157,159]. Prior studies have shown that gene panels of similar scale and functional diversity provide a sufficient basis to define a framework within which to interpret the transcriptional heterogeneity of single cells in the brain [97,105]. Single SCN neurons from dark-adapted mice or mice experiencing a light-induced (light-pulsed) phase shift in their circadian rhythms. Using multivariate analytical techniques and a particular technique from the field of graph network theory known as community structure detection, we analyzed the transcriptional states of these neurons and identify a molecular organizational framework within which distinct functional groups of SCN neurons function and interact. The material in the current chapter has appeared in a journal article co-written by the author.[358]

6.2 Experimental and Computational Methods

6.2.1 Animal Model

The objective of this study was to study the in vivo transcriptional responses of SCN neurons to a light-induced circadian phase-shift. To this end, C57BL/6J male mice between 4–6 weeks (Charles River Laboratories - Wilmington, MA) were housed within 12 hour light, 12 hour dark cycles and given free access to food and water. Warm white fluorescent bulbs (150 lux) were used for the light cycle. After 10 days of light/dark cycle entrainment, the lights were switched off. On the second day of the constant dark period, animals were given a one-hour light exposure (150 lux of white light) at Zeitgeber time (ZT) 14 h, 2 hours into their subjective dark period, and sacrificed one hour later at ZT 15 (light-pulsed). SCNs were also collected from non-light-pulsed animals at ZT 15 (dark-adapted). Animals were euthanized by carbon dioxide asphyxiation in dim red light, and brains were extracted in light. Hypothalamic tissue blocks were dissected and embedded in Optimal Cutting Temperature (OCT) embedding medium and frozen on dry ice. OCT-embedded tissue samples were stored at –80°C prior to sectioning and laser capture microdissection. All protocols were approved by the TJU Institutional Animal Care and Use Committee.

6.2.2 Staining and immunofluorescent analysis

In order to minimize RNA degradation and maintain quality of the tissue samples for laser capture microdissection the rapid immunofluorescent staining

protocol described in § 2.4.2 was used. In this study, the primary antibody anti-NeuN 1:25 (Millipore®) and the secondary antibody Alexa-488 anti-mouse 1:50 diluted in PBS containing 2% BSA were used to identify SCN neurons. The slides, again washed with PBS, subsequently underwent a standard dehydration process (75% ethanol, 30sec; 95% ethanol, 30 sec; 100% ethanol, 30 sec; 100% ethanol, 30 sec), rinsed briefly in Xylenes (Sigma-Aldrich) for 1 min, and then transferred into another bath of fresh Xylenes for 5 min to further remove any trace of ethanol. Finally, the slides were air-dried for 5 min prior to laser capture microdissection.

6.2.3 Sample collection and spatial tracking

We collected 352 single SCN neurons from the light-perturbed or dark-adapted mice (also referred to as dark-dark mice as they are housed in constant darkness as opposed to being exposed to a 12 h light – 12 h dark cycle) using laser capture microdissection [33]. Neurons throughout the SCN were selected in an unbiased fashion and their anatomic location recorded. Within each coronal section collected, beginning with the first appearance of the rostral SCN, based on the identification of anatomical landmarks referenced against the mouse brain atlas, spatial coordinates within a 10 μm by 10 μm grid system were recorded to determine neuron location in each coronal section of the SCN. To indicate the grid location, 7 divisions were used beginning laterally from brain midline and dorsally from the ventral SCN border with the optic chiasm. Seven divisions were used along each axis to indicate the grid location.

6.2.4 cDNA preparation and high-throughput qRT-PCR

Using the procedures described in § 2.4.5, the expression levels of 96 genes were measured using the BioMark™ high-throughput qPCR platform. Primer-probe assays were developed using the Universal Probe Library (Roche, Indianapolis, IN). A detailed list of probe and primer sets is included in Appendix C. These gene/primer pairs were pre-validated by both standard PCR and qPCR analysis using cDNA generated from mouse hypothalamic RNA (Clontech Laboratories Inc., Mountain View, CA).

The same sample preparation procedures required for high-throughput qPCR analysis were used, as described in § 2.4.4 and as applied in the analysis of NTS neurons. Raw C_t values generated from qPCR analysis in the BioMark™ were subject to quality assessment prior to analysis.

6.2.5 Gene selection

Genes included in this study were chosen based on their functional relevance in the transcriptional programs underlying the oscillatory behavior of SCN neurons. Previous efforts in this laboratory exploring the multi-genic expression programs involved in circadian phase-shifts provided the foundation from which the 96 gene panel was designed [149]. Expression measurements included transcripts involved in intracellular signaling pathways, regulated downstream targets, and core-clock functions (Appendix C)

6.2.6 Qualitative assessment of data

Due to the region-specific expression nature of certain SCN markers, we expected several samples to show minimal to no expression of certain genes (e.g. *Vip, Avp*). Therefore, individual reactions that failed were interpreted to represent either too low or no measurable amount of cDNA in the amplified sample. Consequently, a "minimum-1" value was substituted for that particular qRT-PCR reaction (the minimum value being the lowest $-\Delta\Delta C_t$ value across all DD and LP single neuron samples for a particular gene) [176].

6.2.7 Data normalization

Expression levels were normalized by using the $-\Delta\Delta C_t$ method, described in [171] and outlined previously in § 2.5.1. In this procedure, gene expression within a single neuron is first normalized relative to the average of three housekeeping genes, *Actb, Hprt,* and *Atp5b*, which do not show circadian expression rhythms [182,183,359,360]. In addition, these genes were shown to have the most stable expression across the single-neuron samples using geNorm [174]. Modified z-values were then calculated by means of dividing the $-\Delta\Delta C_t$ the standard deviation within a gene assay across all single-cell samples. Modified z-values were used for data visualization using heat maps.

6.2.8 Silhouette score

One of the main objectives in analyzing single SCN neurons is to identify groups or clusters of transcriptionally similar neurons, which are interpreted to represent a functional phenotype. To quantify the consistency across members within a designated transcriptional phenotype, a silhouette score is calculated using Equation 6.1 for each member within a cluster:

$$s(i) = \frac{b(i) - a(i)}{\max\{a(i), b(i)\}} \qquad 6.1$$

Here *a(i)* represent the average dissimilarity of member i relative to all other members within its designated cluster, the lower the value of *a(i)*, the better the cluster assignment. Average dissimilarity values of member *i* relative to all other clusters are then calculated, from which the lowest average dissimilarity value is chosen as *b(i)*. Based on Equation 6.1, silhouette scores fall within a range of $-1 \leq s(i) \leq 1$

A value approaching 1 indicates that the difference of a member across a distinct cluster is much larger than the difference within its designated cluster meaning that the member is well matched and vice-versa. In order to quantify the overall similarity across members within a cluster, the arithmetic average of all *s(i)* values is calculated within a group. Similar to an individual score, an average score approaching 1 indicates a well-defined cluster, −1 indicates an ill-defined cluster, and 0 represents a neutral clustering of members. Silhouette scores were determined using the silhouette function provided in the R package *cluster* [361].

6.2.9 Statistical significance of correlation thresholds

Pearson correlation coefficients, a measure of the linear correlation between two variables (i.e. genes) are used to quantify the correlated expression patterns of genes. To verify the statistical significance of pairwise Pearson correlation coefficients among genes (expression levels between gene pairs across neurons) and among cells (expression levels within pairs of neurons across genes), we permute the data (1000 times) to determine a distribution of correlation coefficient values. From this distribution, determined empirically, we identify a range of Pearson correlation coefficient values that are not likely to be repeated or achieved by random chance ($p < 0.05$). These statistically significant coefficient values represent potential threshold limits that can be used in determining what correlations are included in the networks developed in this study. Permutations are performed across DD neurons, LP neurons, and specific subsets of neurons.

6.2.10 Gene correlation networks

A Pearson correlation coefficient threshold of 0.5 is used to define a statistically significant relationship between a gene pair. This correlation value of 0.5 was empirically verified as a statistically significant threshold using repeated random permutations of the gene expression data within the various defined cell-types (described in § 6.3.7). All network figures visualizing the correlative relationships of interest were generated using Cytoscape version 2.8.4 (www.cytoscape.org).

6.2.11 Community structure detection

The development and analysis of gene networks have offered insights into gene interactions underlying distinct neuronal subtypes, an example of which was described in Chapters 3 and 4. As part of the multivariate analysis performed on individual SCN neurons, we apply the leading eigenvector community detection technique [198]. Briefly, this technique decomposes a modular matrix representation of a graph composed of edges and vertices, which may represent an individual neuron for example. The modular matrix is partitioned into a set of representative vectors (of cells or genes) that principally contribute to the modular structure "hidden" within the original network topology [198]. In this context, the representative vectors are considered to represent a module or group of similar neurons. The *igraph* package and associated functions in the R statistical software [219] were used to perform leading eigenvector community detection in the correlation networks developed in this work.

6.3 Results

6.3.1 Sample collection and quality assessment

We collected 352 single SCN neurons from mice kept either in constant darkness for 2 days (dark-dark or DD mice, n=2) or kept in darkness for 2 days and then exposed to a light-pulse (LP) at a clock time corresponding to 2 hours after lights-out of the previous 12 h light-dark cycle (Zeitgeber time [ZT] 14; LP mice n=6). Brains were collected after 1 hour of light exposure in the LP group and at the

corresponding clock time in the DD group (ZT15, Fig. 1A). Single-cell cDNA from these single neuron samples was analyzed with 30,624 individual qRT-PCR measurements. Numerous stringent quality control tests were used to assess the data and ensure that only high-quality single-cell data was included in the subsequent analysis, as described in § 3.3.4.4. Of the total single-neuron samples collected, 29 samples were excluded due to failed reactions, improper sample loading, or poor signal quality. Ultimately, 88 neurons from DD mice and 235 from LP mice were analyzed. Since expression levels were normalized to the mean expression level of three *Actb, Atp5b*, and *Hprt*, and six assays were excluded due to poor signal quality or assay contamination, neurons were characterized based on the normalized expression of 87 genes. Having assessed the quality of the single-neuron expression data and normalized the data to allow for an appropriate comparison of gene expression between treatment conditions, we performed various multivariate analytical methods to identify a molecular organizational framework that would enable us to interpret single-neuron heterogeneity in the context of the SCN's synchronizing functions.

6.3.2 Dark-adapted neurons exhibit multiple functional states

Our analysis revealed substantial transcriptional heterogeneity across neurons from the DD mice (referred to as DD neurons) evidenced not only in the wide range of expression levels of neuropeptide and membrane receptor genes but also in the combinations of several key neuropeptide genes expressed. For example, *Vip* showed

binary-like expression across DD neurons, of which 45% expressed *Vip* levels below the detection limit. Single neurons expressing *Vip* were localized within the ventral portion of the SCN (Figure 6.1), as expected [108,148,362].

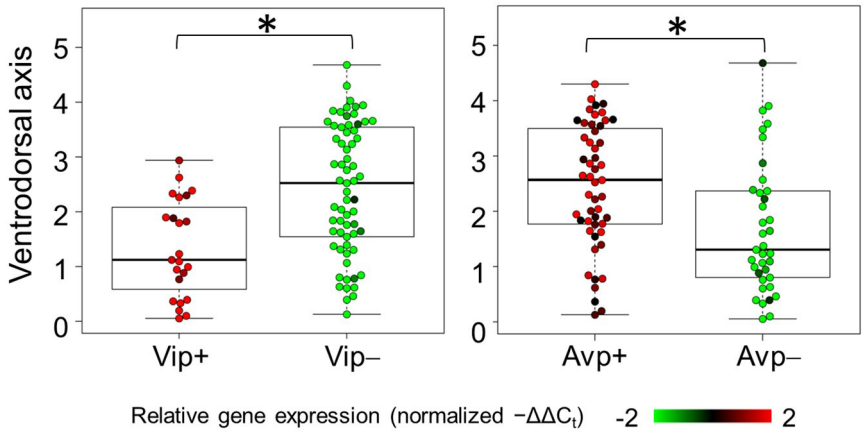

Figure 6.1 Distribution of *Vip*+ and *Avp*+ neurons along ventrodorsal axis. A box plot of the ventrodorsal positioning of individual *Vip*+ ($-\Delta\Delta C_t > 0$) and *Vip*- ($-\Delta\Delta C_t <= 0$) neurons. Circles represent individual data points (i.e. single SCN neurons) whose color reflect the normalized expression value of *Vip* or *Avp*, respectively, in each plot. A Wilcoxon rank sum test was performed to determine if there were significant differences in ventrodorsal positioning between the two neuron groups. A p-value of 1.78e–4 indicates that the null hypothesis can be rejected and that there is a statistically significant difference (*) between the ventrodorsal positioning of *Vip*+ and *Vip*- neurons. Similarly, significant differences in ventrodorsal positioning were observed between *Avp*+ and *Avp*- neurons (Wilcoxon rank sum test p-value = 1.14e–3).

Avp expression, however, spanned a 4000-fold expression range across the DD neurons. Surprisingly, gene expression of adenylate cyclase-activating polypeptide (*Adcyap1*), which codes for the neuropeptide PACAP (a molecular input signal

generated by primary ganglion neurons in the retinohypothalamic tract [RHT], which innervates the ventral regions of the SCN) occurred in approximately 25% of neurons sampled from DD mice, as observed in Figure 6.2. Contrary to previous results, which defined distinct SCN neuronal populations based on their exclusive production of VIP or AVP [142,352], many DD neurons sampled expressed combinations of *Vip, Avp*, and *Adcyap1*, as illustrated in Figure 6.2, suggesting that these neurons may exist in various functional states.

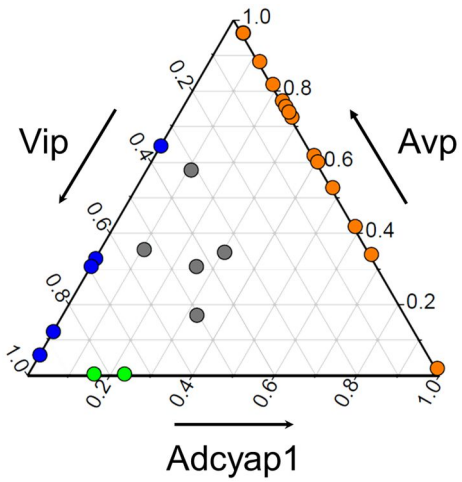

Figure 6.2 Multi-genic expression of *Vip, Avp*, and *Adcyap1* in subset of neurons collected from dark-adapted mice. Ternary plot of the proportional expression levels of the neuropeptide genes *Vip*, *Avp*, and *Adcyap1,* which sum to a total value of 1. Each circle represents an individual neuron's compositional *Vip-Avp-Adcyap1* expression profile. This sample subset of single neurons from dark-adapted mice exhibits positive normalized expression of the three genes of interest. Colored circles represent individual neurons with positive co-expression of *Vip/Avp* (blue), *Vip/Adcyap1* (green), *Avp/Adcyap1* (orange), and *Vip/Avp/Adcyap1* (grey).

Subsequent hierarchical clustering analysis based on 32 neuropeptide and membrane receptor genes, as well as 13 light-response genes, performed on the DD neurons revealed four neuronal subpopulations having distinct expression profiles (Figure 6.3). In addition to co-expressing combinations of *Vip, Avp*, and *Adcyap1*, these subpopulations were characterized by correlated expression patterns of three distinct groups of genes (i.e., transcription modules; Figure 6.3A) with Pearson correlation coefficient values greater than the statistically significant threshold (discussed in § 6.3.7). Despite showing no distinct expression patterns across the neuronal subpopulations, light-response genes including *Fos, Egr1, Egr2, Jun,* and *Junb,* forming a fourth transcription module, were included in Figure 6.3A to serve as a qualitative internal validation of our experimental approach and analysis. Because SCN neurons increase expression of these genes upon light-mediated activation [156,158,159], we expected downregulated expression of these genes in DD neurons, which was what was observed (Figure 6.3A). The remaining genes measured did not lead to further distinction of subpopulations were therefore not included when determining the four transcription modules heat map. The remaining genes are shown in Figure 6.3C. While correlations between gene expression states related DD neurons to a particular subpopulation, there was no clear spatial organization among these subpopulations (Figure 6.3B).

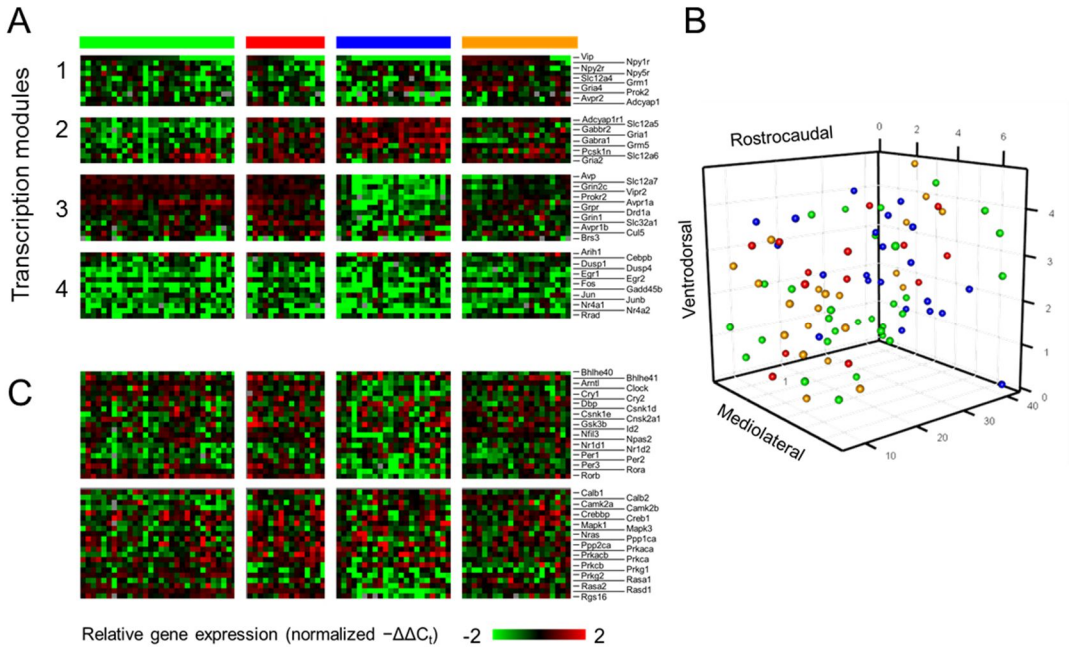

Figure 6.3 Clustering of neurons collected from dark-adapted mice. (A) Heat map visualizes relative expression levels ($-\Delta\Delta C_t$) of 32 key neuropeptide, receptor, and light-response genes measured in the 88 single neurons from DD mice. Hierarchical clustering, based on the Pearson correlation coefficient, revealed four groups of genes (transcription modules) showing correlated expression across four neuronal subpopulations (groups of columns) defined by gene expression profiles. Colored bars above each group correspond to specific subpopulations. (B) Mapping of SCN neuronal subpopulations. Color annotation of subpopulations identical to gene expression-based groups defined in (A). Single neurons were plotted based on their recorded spatial coordinates (Material and Methods) along the mediolateral, ventrodorsal, rostrocaudal axes of the SCN. (C) Remaining gene expression shown in heat map. The remaining 56 genes were arbitrarily sectioned into two groups for ease of visual interpretation and do not represent additional transcriptional modules.

Sample clusters of DD neurons were also supported by the presence of clusters of neurons detected from a principal component analysis (PCA) of these neurons (Figure 6.4).

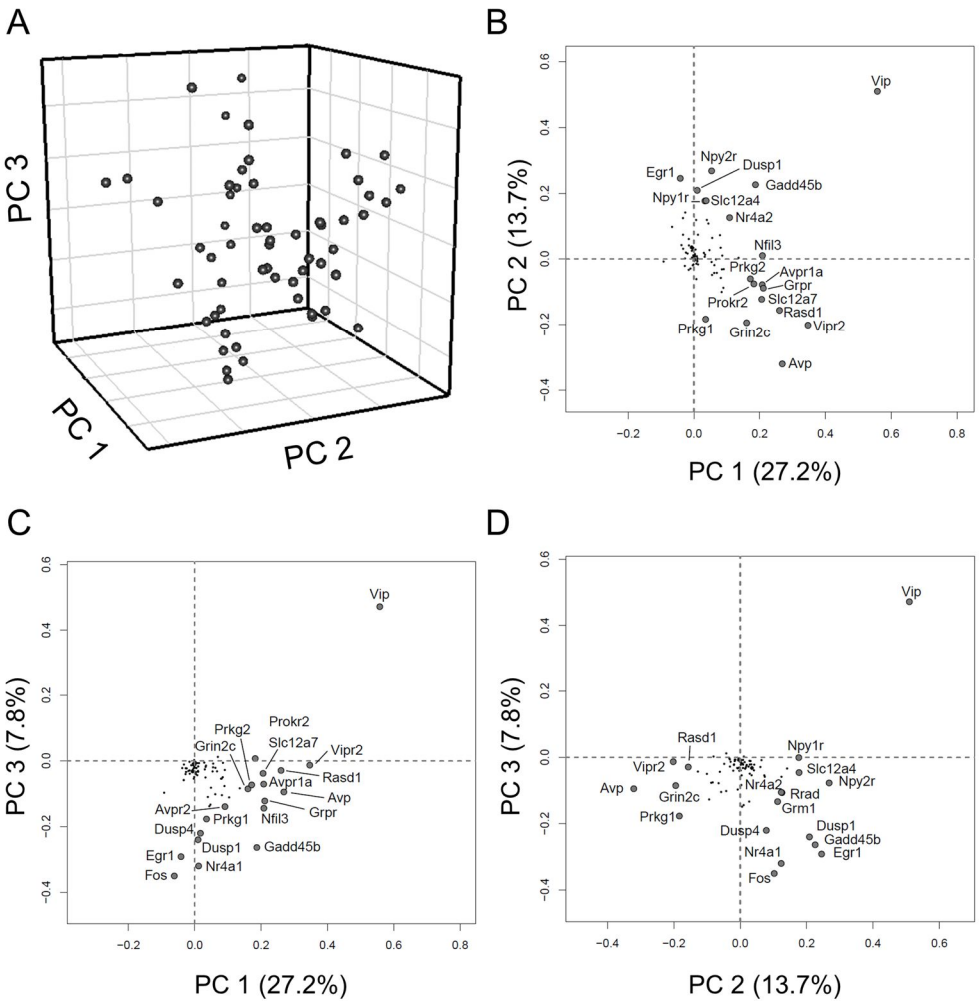

Figure 6.4 Principal component analysis (PCA) of neurons from dark-adapted mice. (A) Scores plot along the first three principal components obtained from PCA of transcriptional profiles of DD neurons (dark-grey spheres). The normalized $-\Delta\Delta C_t$ values were used in the PCA. Corresponding loading values of genes along PC 1 v. PC 2 (B), PC 1 v. PC 3 (C), and PC 2 v. PC 3 (D) are represented in the 2D plots. The labeled genes have a larger contribution to the variability observed in the dataset. The scattered positioning of the neurons in (A) suggest that several neurons cluster together and that there may be some transcriptional organization to these DD neurons.

6.3.3 Gene expression profiles distinguish dark-adapted from light-pulsed SCN neurons

Concomitantly, we compared the transcriptional states of the DD and LP neurons using several multivariate analytical techniques to verify light-mediated changes in neuronal state. The Pearson correlation coefficient was used as a measure of similarity between all possible pairs of transcriptional profiles of neurons, which we visualized in a heat map. This analysis revealed two distinct clusters composed predominantly of positive correlation coefficients among pairs of neurons within treatment groups indicating that transcriptional states were more similar within than across treatments (Figure 6.5A).

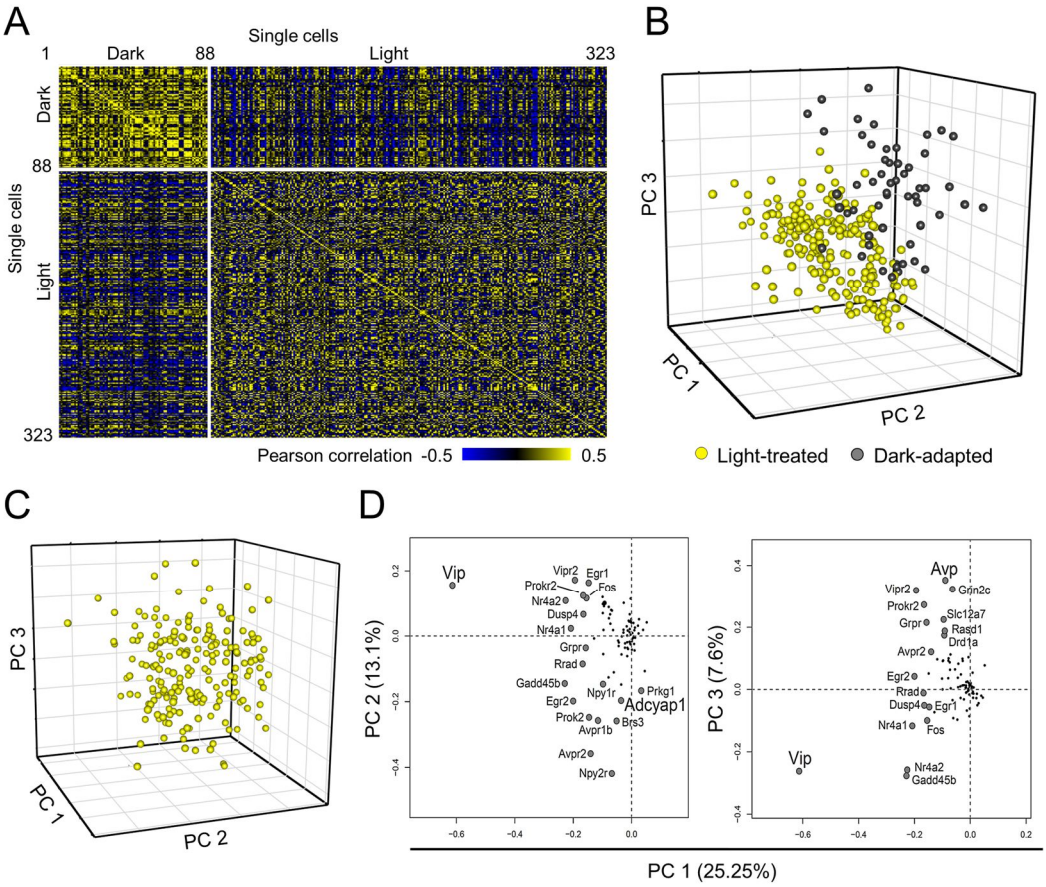

Figure 6.5 Comparing neurons from dark-adapted and light-treated mice. (A) Pearson correlation of 332 single neurons collected across dark-adapted (88 neurons) and light-treated (235 neurons) mice. (B) Scores plot obtained from a Principal Component Analysis (PCA) on the single neurons (spheres) sampled shows that neurons responding to the light pulse (yellow) form a distinct cluster from that of the dark-adapted neurons (dark-gray) along the first three principal components. The distinct clusters indicate distinct transcriptional states between these two treatment groups. (C) Scores plot obtained from PCA of only neurons from light pulsed animals shows a large amount of variability as indicated by the large spread of neurons. (D) Loading values obtained from the PCA analysis of neurons taken from light-perturbed animals are plotted for PC1 and PC2 and PC1 and PC3. The labeled genes contribute more to the observed variability in the data, with the signaling neuropeptide genes *Vip* and *Avp* having the largest contributions to neuronal variability along PC1 and PC2. *Adcyap1* and other labeled genes contribute to variability along PC3.

In a separate analysis, we used PCA to characterize the variation across the transcriptional states of DD and LP neurons by transforming the multi-genic expression states into a lower-dimensional gene expression space defined by new coordinate axes (i.e. principal components). We found that the first three principal components retained 46% of the variation in the original data, which was sufficient to distinguish neuronal states between the two treatment groups (Figure 6.5B). Next, we examined the weighted contributions (i.e. loadings) each gene had to each of the first three principal components to determine which genes had the largest influence on the distribution of transcriptional states of LP and DD neurons along these principal components. Genes having the largest influences (i.e. loadings with the largest magnitude values) along the first three principal components included light-induced genes such as *Per1, Egr1, Egr2, Fos,* and *Jun* [363–365], and GABA-associated inhibitory signaling genes such as *Gabra1* and *Slc12a5*, which are involved in phase-shifting responses in the SCN and synchronizing SCN neurons [144,366]. These results further support the idea that single-cell transcriptional profiles can be used to distinguish distinct functional states of neurons between treatment groups, as previously reported [31,105,367].

Although the transcriptional states of neurons between the two treatment groups were distinct, the large spread of transcriptional states of the LP neurons in the principal component space (PC 1-3) indicated that a large amount of variation within the LP neuronal dataset remained (Figure 6.5B yellow spheres). A PCA performed on the LP neurons indicated that variation across the transcriptional states of these

neurons were due in part to expression variations of *Vip, Avp*, and *Adcyap1* (Figure 6.5C-D). Interestingly, Adcyap1 expression was observed across multiple neurons throughout the SCN under both treatment conditions (Figure 6.6), suggesting that endogenous PACAP production, in addition to light-induced production in the RHT, may also play a role in synchronization.

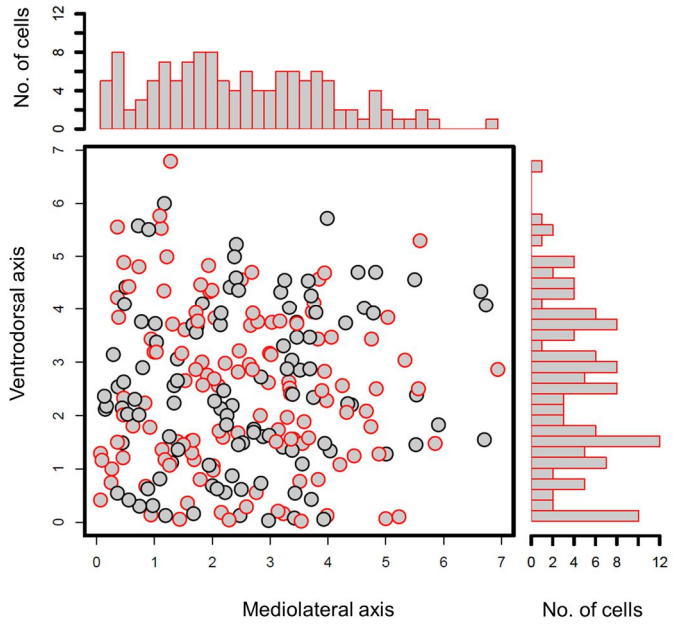

Figure 6.6 Spatial distribution of Adcyap1 expressing neurons. The combined scatterplot and histograms show light-treated cells with positive expression of Adcyap1 ($-\Delta\Delta C_t > 0$) are not localized to a particular location and are distributed throughout the SCN. The scatterplot depicts the ventrodorsal and mediolateral position of the single cells. Red-outlined circles indicate single neurons that display positive *Adcyap1* expression. The corresponding histograms show the distribution of cells with positive *Adcyap1* expression along the ventrodorsal and mediolateral axes.

As *Vip, Avp,* and *Adcyap1* are involved in circadian regulation and were some of the major contributors to gene expression variation in the LP neurons, supported by the loading values plotted in Figure 6.5D, we examined how well a biased classification approach, one based on the expression levels of these three genes, would be able to categorize transcriptional phenotypes of SCN neurons.

6.3.4 Neuropeptide-based classification poorly characterizes transcriptional states of light-pulsed neurons

Classifying neurons based on a binary classification of expression levels for *Vip, Avp,* and *Adcyap1,* with neurons either demonstrating positive ($-\Delta\Delta C_t$ > median gene expression) or negative expression ($-\Delta\Delta C_t$ <= median gene expression), yielded eight clusters (Figure 6.7A). Similar to the behavior of DD neurons, a small subset of LP neurons (10%) co-expressed *Vip, Avp,* and *Adcyap1* (Figure 6.7B), which aligns with prior observations of *Vip* and *Avp* co-expression reported by Romijn et al. [146] and Mieda et al. [145].

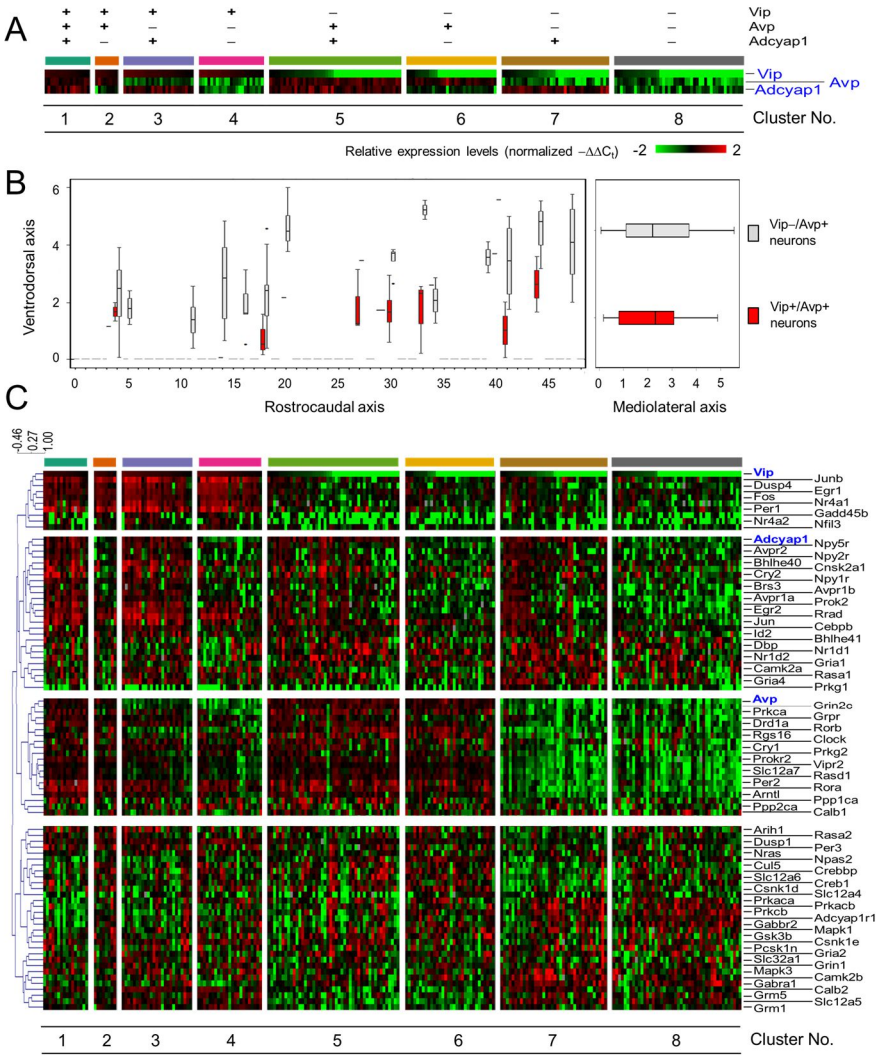

Figure 6.7 Sorted gene expression profiles of SCN neurons in light-pulsed (LP) mice with respect to *Vip, Avp,* and *Adcyap1*. (A) Heat map visualizing normalized gene expression of *Vip, Avp,* and *Adcyap1* across LP neurons. Neurons are categorized based on positive ($-\Delta\Delta C_{t,gene\text{-}i} > \text{median}(-\Delta\Delta C_{t,gene})$) or negative ($-\Delta\Delta C_{t,gene\text{-}i} <= \text{median}(-\Delta\Delta C_{t,gene})$) expression. (B) Boxplots show distribution of *Vip+/Avp+* neurons and remaining sampled neurons along ventrodorsal, mediolateral, and rostrocaudal axis of SCN. A majority of *Vip−/Avp+* neurons are positioned dorsally relative to the *Vip+/Avp+* neurons. (C) Heat map visualizing expression of 87 genes from across light-treated neurons. Neurons are organized as in (A). Dendrogram on left side of heat map indicates how genes were grouped was based on the Pearson correlation coefficient.

A heat map of the rearranged multi-genic profiles of LP neurons revealed four transcription modules that showed distinct, correlated expression patterns across several, but not all of the eight neuronal groups (Figure 6.7C). Since gene expression within the transcription modules appeared to correlate with *Vip, Avp,* and *Adcyap1* expression, we expected that these genes would act as central regulators or hubs in gene networks in which the expression of core clock and functional genes would be co-regulated. We subsequently identified statistically significant correlative relationships (Pearson correlation coefficient > 0.5) among all pairwise combinations of the 87 genes measured and developed gene correlation networks to investigate gene regulatory network behavior [368–370]. Gene correlation networks were developed from expression data across LP neurons and subsets of LP neurons, defined by positive normalized expression of key neuropeptide (*Vip+, Avp+, Adcyap1+*) and receptor genes involved in circadian rhythmicity and synchronization.

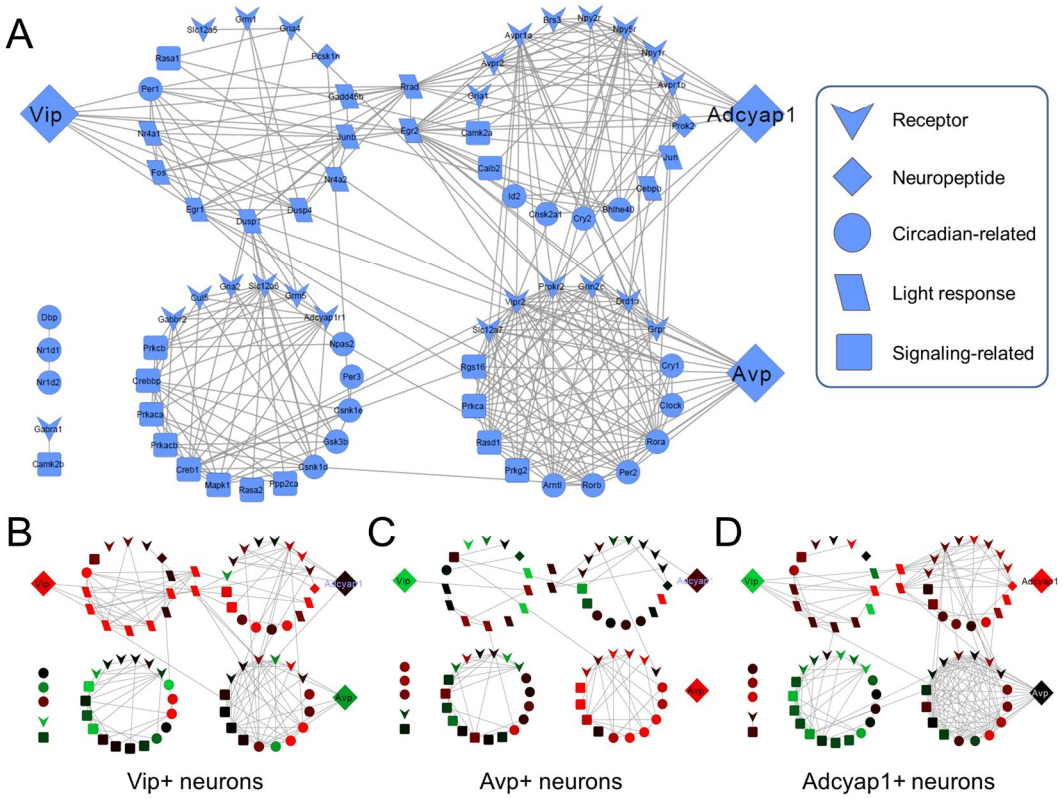

Figure 6.8 Gene correlation networks within specific SCN cell-types. (A) Combined gene correlation network across all genes and all subsets of neurons. Edges between nodes (genes) correspond to a Pearson correlation coefficient greater than 0.5, which was determined to be statistically significant (refer to Figure 6.20). *Vip, Avp,* and *Adcyap1* are separated from their highly interconnected gene clusters in order to highlight these specific neuropeptide genes. Node placement is identical in the subsequent correlation networks for specific neuron-types (B-D). (B) *Vip*+ neuron gene correlation networks. When *Vip* expression is upregulated, few correlations are shared with other genes whereas *Vip2r* shows a larger number of gene correlations when it is expressed at high levels. (C) *Avp*+ neuron gene correlation network. Similar correlation behavior among genes with respect to neuropeptides and receptors is observed. Moreover, minimal correlations are observed among genes with the receptors for *Avp (Avpr1a, Avpr2a)* in *Avp*+ neurons. (D) *Adcyap1*+ neuron gene correlation network. Gene correlation networks were constructed using Cytoscape version 2.8.4.

The gene correlation network across all LP neurons showed a large number of pairwise correlations involving *Vip, Avp,* and *Adcyap1* (Figure 6.8A). However, correlation networks within the subsets of LP neurons revealed few statistically significant correlations involving these three neuropeptide genes. Within *Vip*+ LP neurons, *Vip* shared correlations with only three other genes (Fig. 4B). Similarly, neither *Adcyap1* nor *Avp* shared any pairwise correlations in *Adcyap1*+ or *Avp*+ LP neurons, respectively (Figure 6.8C-D). Similar correlated behavior, or rather a lack of correlated expression behavior, was observed in neurons defined by positive expression of receptor genes, illustrated in Figures 6.9-6.11.

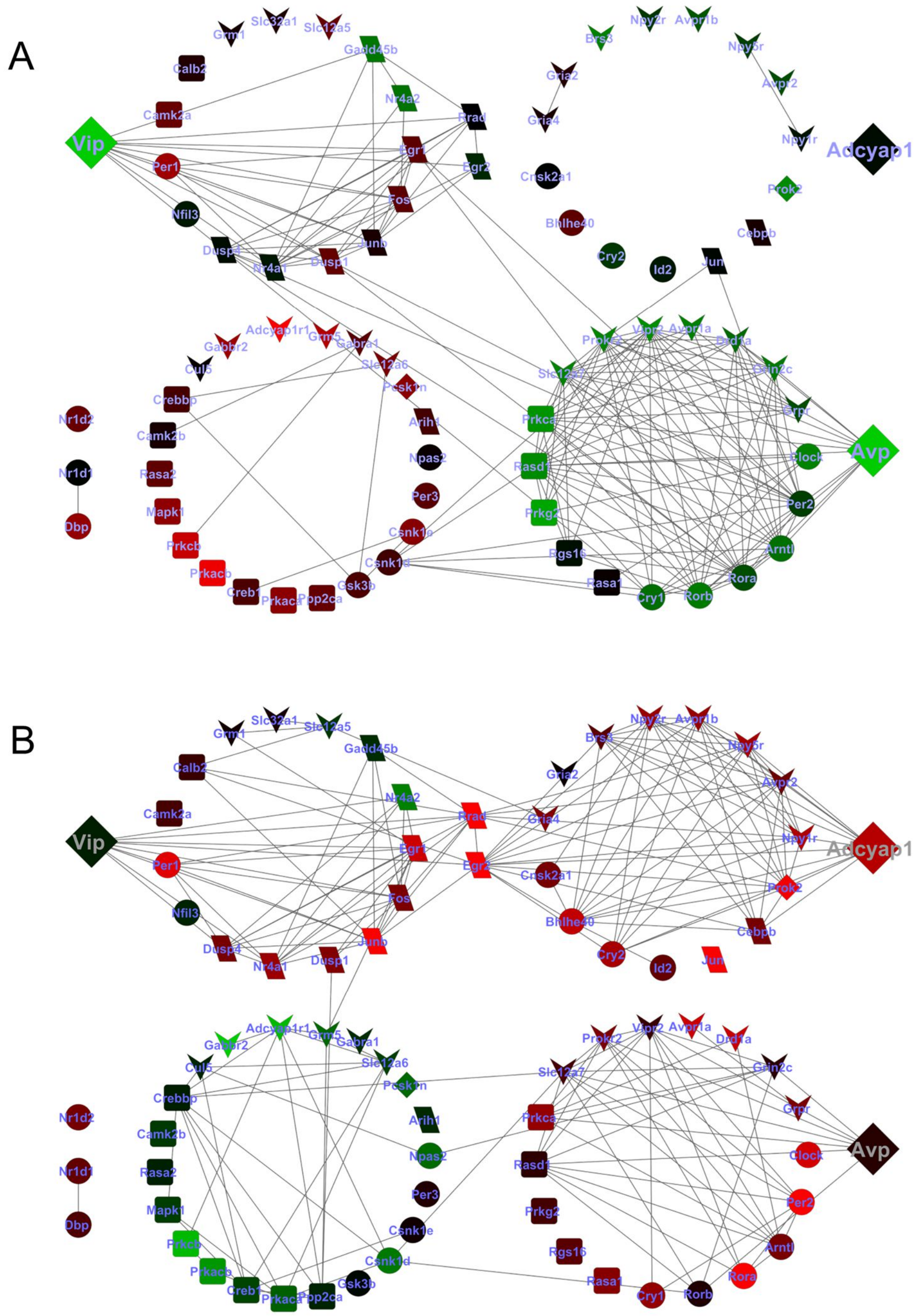
A
Grm1
Slc32a1
Slc12a5
Gadd45b
Calb2
Camk2a
Nr4a2
Rrad
Vip
Per1
Egr1
Egr2
Fos
Nfil3
Junb
Dusp4
Nr4a1
Dusp1
Brs3
Npy2r
Avpr1b
Npy5r
Gria2
Avpr2
Gria4
Npy1r
Adcyap1
Csnk2a1
Prok2
Bhlhe40
Cebpb
Cry2
Id2
Jun
Gabbr2
Adcyap1r1
Grm5
Gabra1
Cul5
Slc12a6
Pcsk1n
Crebbp
Arih1
Camk2b
Npas2
Rasa2
Per3
Mapk1
Csnk1e
Prkcb
Csnk1d
Prkacb
Gsk3b
Creb1
Prkaca
Ppp2ca
Nr1d2
Nr1d1
Dbp
Prokr2
Vipr2
Avpr1a
Drd1a
Slc12a7
Grpr
Prkca
Rasd1
Clock
Avp
Prkg2
Per2
Rgs16
Arntl
Rasa1
Rora
Cry1
Rorb
B

Figure 6.9 Gene correlation network within *Adcyap1r1*+ cells and *Avpr1a*+ cells. Gene correlation network across all genes in single LP neurons. Only correlative relationships (edges) with a Pearson correlation coefficient greater than 0.5 between genes (nodes) are included in network. Nodes are arranged in an identical manner as in Figure 6.8 and node colors represent median expression values of genes within the respective subsets of light-treated SCN neurons. (A) Gene correlation network across genes in single neurons expressing *Adcyap1r1* at levels greater than or equal to the normalized median expression level of *Adcyap1r1* across all cells. Receptor genes such as *Prokr2, Vipr2, Avpr1a, Drd1a,* and *Grin2c* show a greater number of correlative relationships among other genes than neuropeptide genes *Vip, Avp,* and *Adcyap1*. (B) Gene correlation network across all genes in single LP neurons expressing Avpr1a at levels greater than or equal to the normalized median expression level of Avpr1a across all cells. Receptor genes such as *Npy1r, Npy2r, Npy5r, Avpr2, Avpr2a, Prok2,* and *Vipr2* show a large number of correlative relationships among other genes suggesting that receptor gene expression plays a strong regulatory role driving the transcriptional states of specific SCN cell-types. Gene correlation networks were constructed using Cytoscape version 2.8.4.

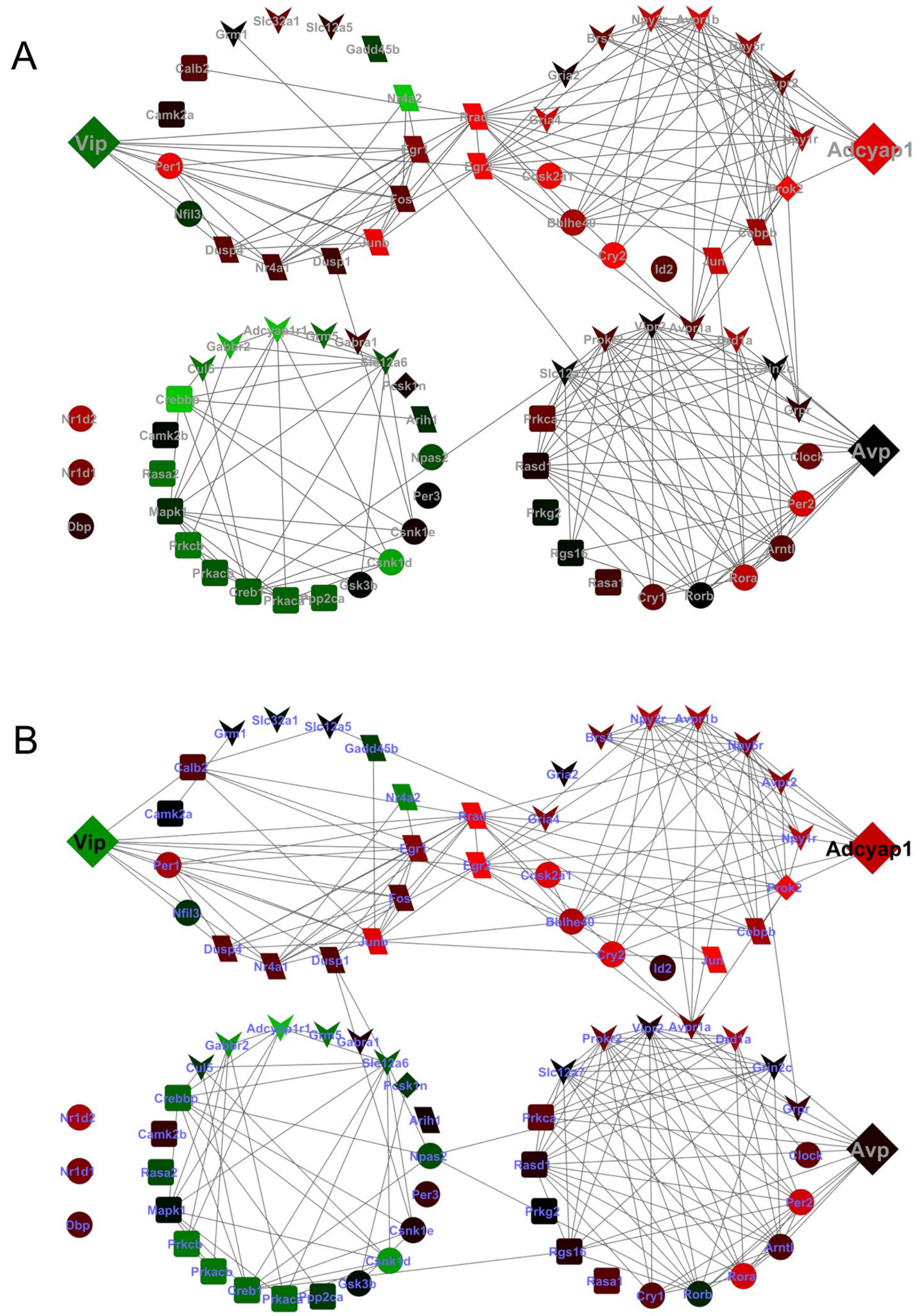
A
B
Vip
Adcyap1
Avp
Grm1
Slc32a1
Slc12a5
Gadd45b
Calb2
Nr4a2
Camk2a
Rrad
Egr1
Egr2
Per1
Fos
Nfil3
Junb
Dusp4
Nr4a1
Dusp1
Brs3
Npy2r
Avpr1b
Npy5r
Gria4
Avpr2
Npy1r
Csnk2a1
Prok2
Bhlhe40
Cebpb
Cry2
Id2
Jun
Prokr2
Vipr2
Avpr1a
Drd1a
Slc12a7
Grin2c
Grpr
Prkca
Rasd1
Clock
Per2
Prkg2
Arntl
Rgs16
Rora
Rasa1
Cry1
Rorb
Adcyap1r1
Gabbr2
Grm5
Gabra1
Cul5
Slc12a6
Pcsk1n
Crebbp
Arih1
Camk2b
Npas2
Rasa2
Per3
Mapk1
Csnk1e
Prkcb
Csnk1d
Prkacb
Gsk3b
Creb1
Prkaca
Ppp2ca
Nr1d2
Nr1d1
Dbp

Figure 6.10 Gene correlation network within *Avpr1b*+ cells and *Avpr2*+ cells. Gene correlation network across all genes in single LP neurons. Only correlative relationships (edges) with a Pearson correlation coefficient greater than 0.5 between genes (nodes) are included in network. Nodes are arranged in an identical manner as in Figure 6.8 and node colors represent median expression values of genes within the respective subsets of LP neurons. (A) *Avpr1b* at levels greater than or equal to the normalized median expression level of *Avpr1b* across all cells. Receptor genes such as *Npy2r, Npy5r, Vipr2, Avpr1a,* and *Avpr2a* show a large number of correlative relationships among other genes suggesting that receptor gene expression plays a strong regulatory role driving the transcriptional states of specific SCN cell-types. (B) Gene correlation network across all genes in single LP neurons expressing *Avpr2* at levels greater than or equal to the normalized median expression level of *Avpr2* across all cells. Receptor genes such as *Npy2r, Npy5r, Avpr1b,* and *Avpr2* show a greater number of correlative relationships among other genes than *Vip, Avp,* or *Adcyap1*. Moreover, *Vipr2, Prokr2*, and *Grin2c* also show a large number of correlative relationships further suggesting the regulatory relationships underlying specific cell-types are driven by the inputs the cell-type is responding to rather than the ligand or signal it is generating. Gene correlation networks were constructed using Cytoscape version 2.8.4.

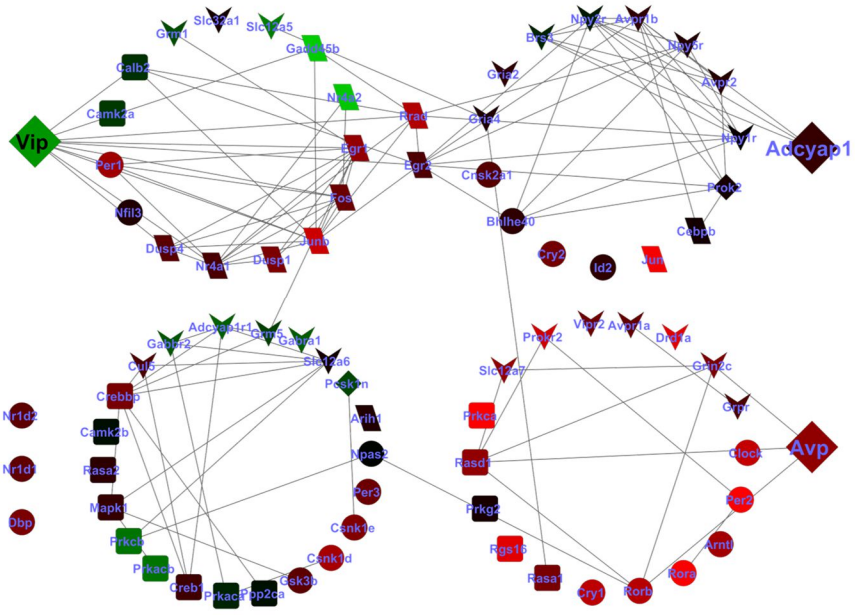

Figure 6.11 Gene correlation network within *Vipr2*+ cells. Gene correlation network across all genes in single LP neurons expressing *Vipr2* at levels greater than or equal to the normalized median expression level of *Vipr2* across all cells. Only Pearson correlation coefficients (edges) greater than 0.5 between genes (nodes) are included. Node colors represent median expression value of the gene across *Vipr2*+ LP neurons. Node arrangement is identical to that of Figure 6.8. Receptor genes such as *Npy2r, Npy5r, Avpr1b,* and *Avpr2* show a greater number of correlative relationships among other genes than *Vip, Avp,* and *Adcyap1*. Networks were constructed using Cytoscape version 2.8.4.

To further verify the ability (or inability) of this neuropeptide expression-based categorization to describe the transcriptional states of SCN neurons, we assessed both qualitatively and quantitatively how well the transcriptional states of these neurons clustered with respect to this categorization scheme. Multidimensional scaling (MDS), hierarchical clustering, and minimum spanning trees (Figure 6.12) repeatedly showed poor consistency across the transcriptional states within the eight clusters.

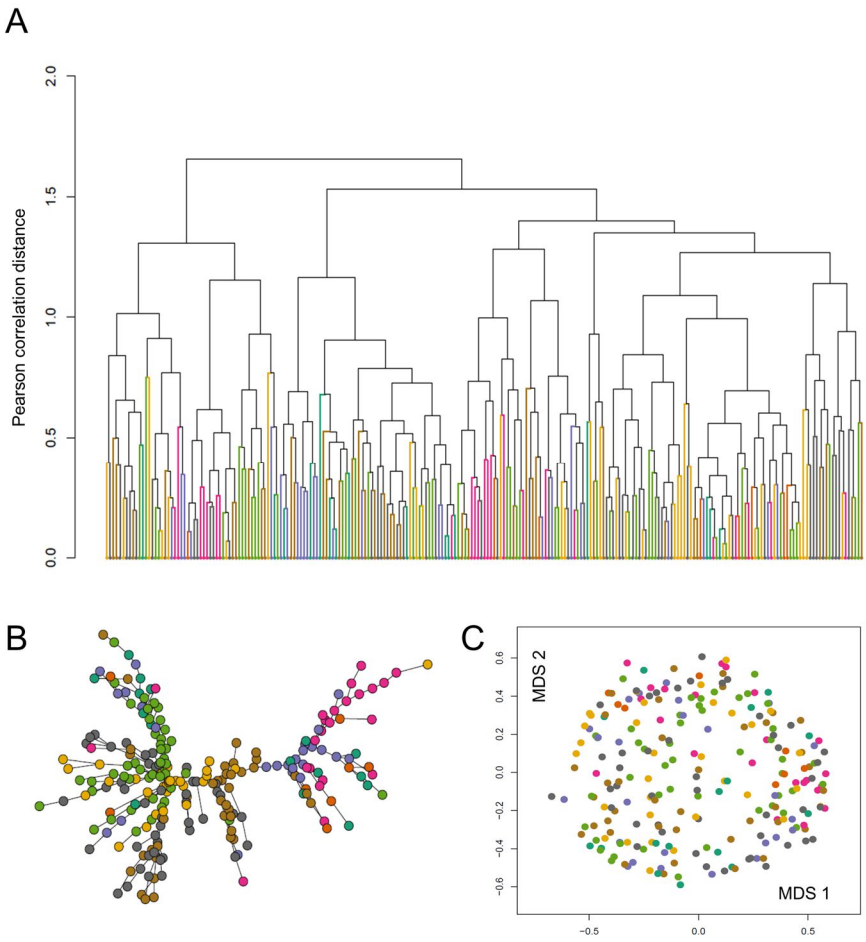

Figure 6.12 Neuronal hierarchical clustering (light-pulsed neurons). (A) Dendrogram of light-pulsed neurons based on the Pearson correlation coefficient distance. Cell-type definition based on neuropeptide gene expression does not align with hierarchical clustering indicating that the neuropeptide-based classifier does not accurately characterize the transcriptional states of single neurons. A minimum spanning tree (B) and a 2D MDS plot (C) further supported the inability of the *Vip/Avp/Adcyap1* expression-based categorization to group transcriptional states Color annotation corresponds to the cluster colors used in Figure 6.7A and 6.7C. Silhouette scores for each cluster represent an average of the silhouette scores calculated for each member within an assigned cluster (§ 6.2.8) – cluster 1 (–0.509), cluster 2 (–0.085), cluster 3 (–0.181), cluster 4 (–0.049), cluster 5 (–0.175), cluster 6 (–0.047), cluster 7 (0.104), cluster 8 (–0.075).

Furthermore, nearly all silhouette scores (Figure 6.12 legend), a quantitative measure of the similarity of transcriptional states within each group, were negative, indicating poor consistency across transcriptional states within these groups. These results suggest that despite their utility in defining SCN neuron-types, categorization of transcriptional states based on *Vip, Avp,* and *Adcayp1* expression is not comprehensive enough to describe the single-neuron heterogeneity observed.

6.3.5 Distinct single-cell transcriptional phenotypes in light-pulsed neurons

Due to the poor consistency of transcriptional states within clusters defined in the earlier approach, we sought an alternative way to characterize this transcriptional heterogeneity. Therefore we applied an approach that relied on the full extent of the multi-genic transcriptional states measured to group the LP neurons. Neurons sharing statistically significant similar transcriptional states (neuron-pairwise Pearson correlation coefficient ≥ 0.5, empirically determined to be statistically significant threshold using similar computational approaches outlined in § 6.2.9, the results of which are described in § 6.3.7), were assumed to exist in similar functional states and to form distinct neuronal phenotypes. We constructed a neuronal correlation network by connecting LP neurons having similar transcriptional states.

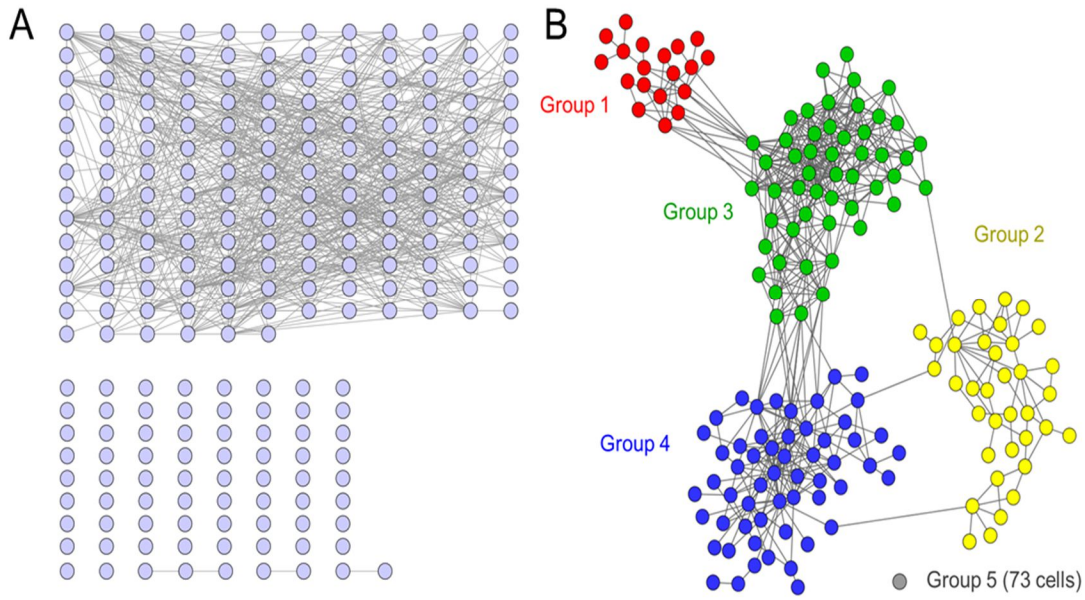

Figure 6.13 Community detection in correlation network. (A) Neuron correlation network based on Pearson correlation analysis across the multi-genic (87 genes) transcriptional states of the light-treated neurons. Each node represents an individual light-treated neuron (purple nodes). Edges indicate positive Pearson correlation coefficients > 0.5. An edge between two nodes represents a pairwise Pearson correlation coefficient between two neurons. The bottom portion shows neurons that did not correlate strongly ($\rho < 0.5$) with other neurons. (B) Reorganized graph network based on community structures identified using the leading eigenvector community detection algorithm [198]. Highly interconnected groups of neurons, representing community structures within the correlation network, are labeled and colored accordingly. A fifth group of neurons (representative gray node) showed little or no correlations with other neurons. Genes listed next to each group correspond to the five genes with the highest number of correlations with the other genes (across cells) within the defined neuronal group. The network map was created using Cytoscape version 2.8.4.

We subsequently performed a topological analysis [198,371] on the neuronal correlation network to identify highly interconnected modules within the network that were representative of neuronal phenotypes. We identified four highly interconnected

modules or neuronal groups and created a fifth group that consisted of neurons showing a minimal number of or no significant correlation with any other neurons, represented by the single gray node in Figure 6.13. A reorganized heat map of the transcriptional states based on this grouping revealed that nearly all neuronal groups possessed distinct expression motifs (Figure 6.14A), which was further supported by the more organized clustering of neurons, based on the newly identified group structures, in the 2D-MDS plot in Figure 6.14B.

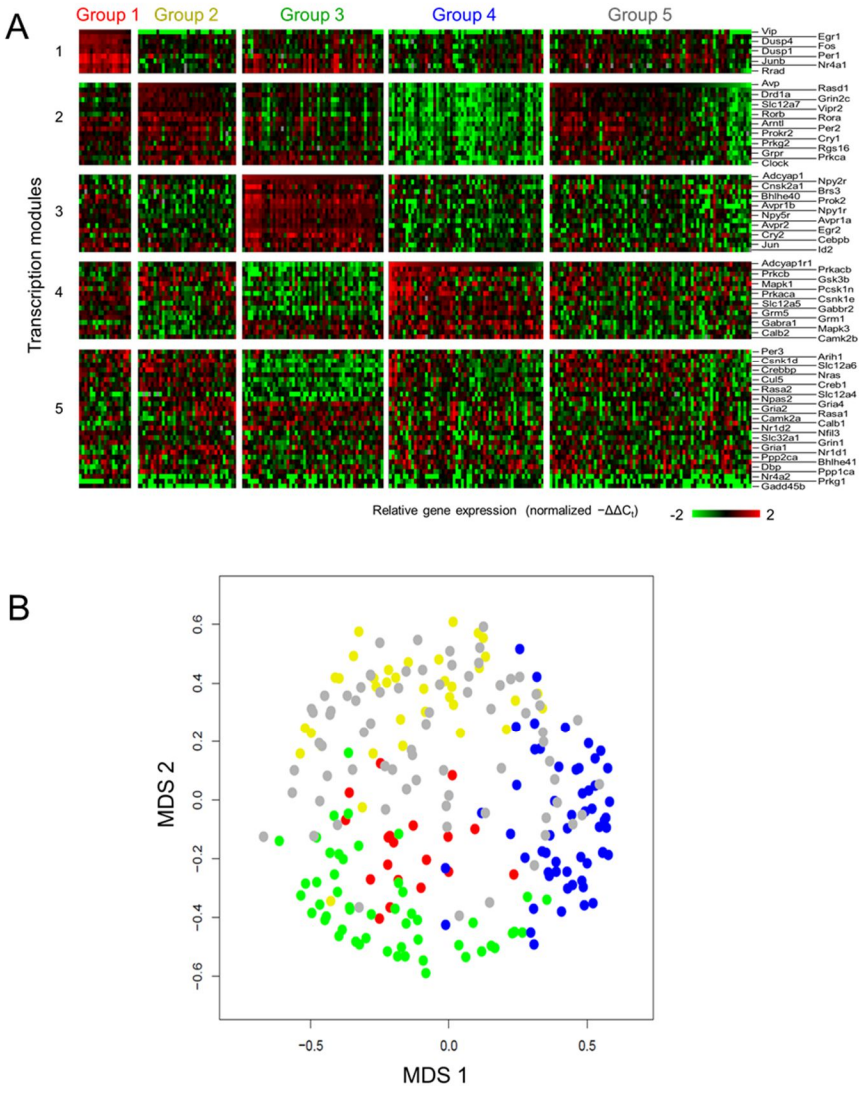

Figure 6.14 Heat map and MDS visualization of neuronal groups identified from community detection algorithm. (A) Heat map visualizing the underlying transcriptional states corresponding to the SCN neuronal subtypes identified in Figure 6.13B (B) 2D MDS plot of light-treated neurons, similar to that of Figure 6.12C, but with new neuronal group annotation (Figure 6.13B). Using the new neuronal group annotation, distinct clusters emerged, with the exception of Group 5, whose neurons are scattered throughout the plot, which reflects some of the similarities that these neurons share transcriptionally to the neurons of the other groups. Silhouette scores for the neuronal groups were calculated to be: Group 1 (0.554), Group 2 (0.239), Group 3 (0.321), Group 4 (0.324), and Group 5 (–0.258).

To verify these neuronal groups, we compared the expression behavior and spatial organization of these presumptive groups (Figure 6.15) aligned with the known intrinsic molecular behavior and regional specificity of SCN neuron-types.

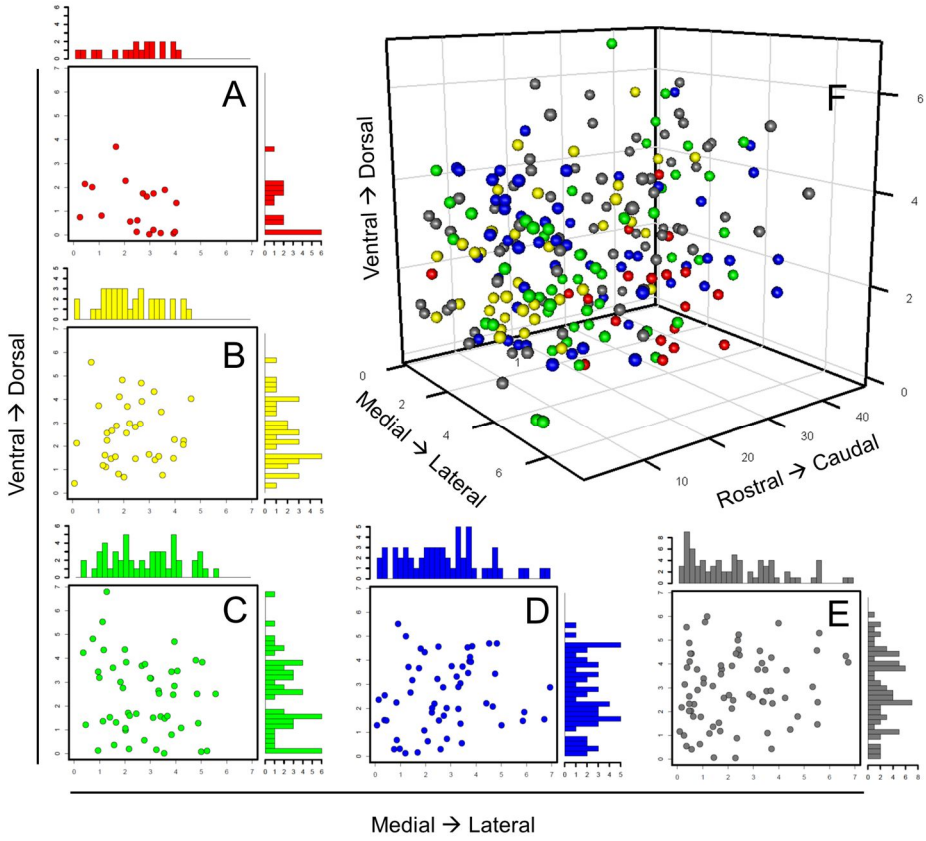

Figure 6.15 Spatial distribution of neuronal groups throughout SCN. Individual neurons are color-labeled with the same color annotation defined in Figure 6.13. The same anatomical coordinates were used to track spatial positioning of light-treated neurons throughout the SCNs from which they were collected. (A) − (E) Scatterplots with marginal histograms show the locations and relative density of these neuronal groups along the ventrodorsal and mediolateral axes. (F) All 235 neurons were plotted with respect to their anatomical position.

Our analysis revealed that gene expression behavior within these groups not only aligned with current understanding of the SCN, but also reflected nuanced expression behavior and spatial organization throughout the SCN, as illustrated in Figure 6.15 and Figure 6.16.

Group 1 consisted of 19 neurons that showed high *Vip, Per1,* and *Per2* expression, suggesting that these neurons responded directly to photic inputs from the RHT [148,365,372,373]. Concomitantly, immediate early genes including *Fos, Jun, Junb,* and *Egr2* were also upregulated. Group 1 neurons were also predominantly located in the SCN core, as illustrated in Figure 6.15. Further, upregulated expression of *Vip* and immediate early genes along with the localization of these neurons within the core (Figure 6.15A-B) agree with prior results that map VIP+ neurons in the SCN core [150,351].

Group 2 included neurons characterized by upregulated expression of *Avp* and *Per2*. Core clock genes were also upregulated including *Cry1, Rora, Rorb, Clock,* and *Arntl1* – all transcriptional regulators for *Avp* and *Per2*, which is co-expressed in AVP+ neurons upon light-induction [363]. Upregulated expression of VIP receptor gene, *Vipr2*, in these *Avp*+ neurons further relates our results to those of others showing interactions between VIP+ and AVP+ neurons [146,148]. Alignment between the core clock genes' expression behavior across the LP neuron samples and the previously identified molecular behavior of the SCN lend additional validity to our approach and results. Group 2 neurons tended to localize medially, spanning the ventrodorsal region of the SCN. Although several of these neurons were located more

ventrally than expected, given their upregulated expression of *Avp*, Group 2 neurons were mainly located dorsally to Group 1 (Figure 6.16), which agrees with the known region-specific arrangement of VIP+ and AVP+ neurons in the SCN [344,374].

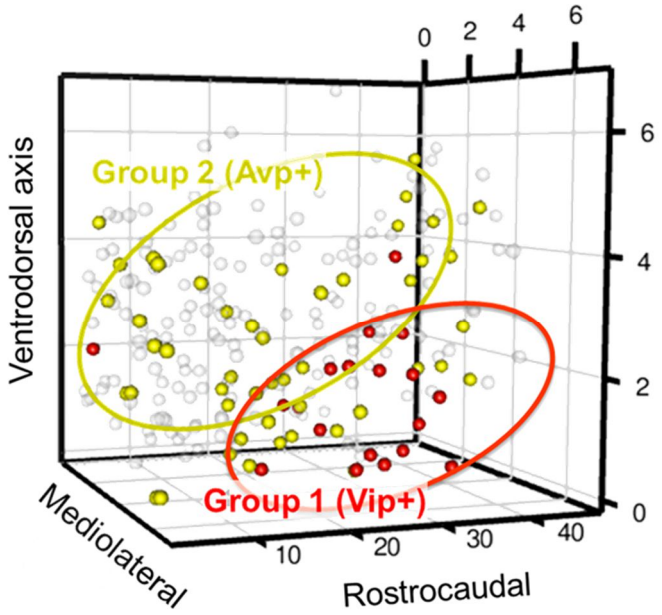

Figure 6.16 Spatial distribution of *Vip*+ Group 1 neurons and *Avp*+ Group 2 neurons. Neurons (spheres) are plotted according to their spatial coordinates within the SCN recorded during sample collection. Group 1 neurons (red) are predominantly ventral to the Group 2 neurons (yellow), aligning with the known organization of *VIP*+ and *AVP*+ neurons in the SCN.

Group 3 consisted of neurons exhibiting upregulated expression of *Adcyap1*. Since PACAP is produced in the RHT, the unexpected endogenous expression of *Adcyap1* prompted us to investigate the expression behavior of other circadian genes in this group more thoroughly. Cell surface receptor genes including *Avpr1b, Avpr2,*

Npy1r, and *Npy2r* were consistently upregulated across these neurons, suggesting that these neurons are receptive to both AVP and neuropeptide Y (NPY). Analysis of the spatial organization of these neurons revealed that they were distributed throughout the SCN, as illustrated in Figure 6.15D. This broad spatial distribution was further reflected in their nuanced gene expression behavior, which included gene expression specific to both core and shell regions. Genes traditionally understood to be expressed in the core, such as *Egr2, Cebpb, Jun, Rrad,* and the calbindin-related gene, *Calb2*, were all upregulated. However, other genes associated with core-specific expression such as *Crebbp* and *Creb1*, which are involved in CREB-mediated intracellular signaling [149,150], were downregulated across a majority of these neurons.

Group 4 neurons were characterized by upregulated expression of *Gabra1* and the PACAP receptor gene *Adcyap1r1*. Similarly, intracellular signaling genes including *Mapk3, Camk2b,* and *Prkaca* [149] and the neuropeptide signaling gene *Pcsk1n*, which codes for the precursor molecule of the peptide little-SAAS, were upregulated as well. Since little-SAAS has been reported to be involved in intercellular coordination within the SCN [375], this upregulated behavior suggests that Group 4 plays a synchronizing role in the SCN. Similar to Group 3, these neurons did not show any clear spatial organization as illustrated in Figure 6.15.

Finally, the fifth group consisted of 73 neurons not considered transcriptionally similar to those of other groups. However, these neurons did share some similar expression and spatial organizational characteristics associated with Groups 1-4. A subset of Group 5 neurons, for example, expressed levels of *Avp* similar to Group 2

neurons, a majority of which were located dorsomedially within the SCN. Similarly, several Group 5 neurons that exhibited upregulated expression of *Vip* and other core clock genes (e.g. *Per2, Cry1,* and *Clock*) mirrored both expression behavior and ventral localization of Group 1 neurons. However, differences in *Slc12a7* and *Grin2m* expression distinguished these neurons from those of Groups 1 and 2. Likewise, another subset of Group 5 neurons expressed increased levels of *Adcyap1r1* and decreased levels of *Vip* and *Avp*, similar to Group 4 neurons. However, decreased expression of *Pcks1n* differentiated these sets of neurons. It is possible that Group 5 neurons may represent functional variances of neurons within Groups 1-4 and add functional robustness [376] to the coordinated SCN response to photic inputs.

Of the five groups, Groups 1-4 included distinct transcription modules that were associated with upregulated expression of a key neuropeptide gene (Group 1 – *Vip*; Group 2 – *Avp*; Group 3 – *Adcyap1*; and Group 4 – *Pcsk1n*), which would appear to support current neurochemical criteria used to describe SCN neurons. However, the current criteria does not fully account for the underlying transcriptional states of these neurons, as evidenced by the presence of Group 5 neurons that express multiple neuropeptides and exhibit nuanced gene expression behavior. Moreover, a correlational analysis of the genes within each transcription module within Groups 1-4 revealed that of the five genes having the highest number of correlations (Pearson correlation coefficient >=0.5), none were neuropeptide genes (Table 6.1).

Table 6.1 Rank order of genes with highest number of correlations within each neuronal group (top five genes)

Gene	No. of Pearson correlations ($\rho \geq 0.5$)
Group 1	
Prokr2	15
GPer1	14
Gria4	14
Nr4a1	13
Brs3	13
Group 2	
Rasd1	12
Per2	11
Rasa1	11
Cry1	10
Gabra1	10
Group 3	
Rora	24
Drd1a	23
Prokr2	23
Arntl	22
Egr2	21
Group 4	
Csnk1e	11
Gsk3b	9
Adcyap1r1	9
Rora	8
Egr1	8

Furthermore, a quantitative reassessment of the reliability of this multi-genic approach to classify neuronal phenotypes showed that the silhouette scores for the newly annotated groupings of LP neurons in the MDS plane (Figure 6.14) did improve

(negative to positive scores), indicating better consistency among the transcriptional states within these groups (Figure 6.14 legend).

In summary, topological analysis of the neuronal-correlation network revealed distinct transcriptomic phenotypes that are likely involved in the phase-shift response in LP neurons. Although the correlational analysis elucidated presumptive functional groups within the neuron-interaction networks, this analysis does not provide any insight into possible inter-neuronal signaling mechanisms through which SCN cell networks are maintained. Given the established role that paracrine signaling plays in regulating circadian cycling [377] and the broad spatial distribution of neurons within Groups 3-5 throughout the SCN (Figure 6.15), which suggests the presence of possible paracrine signaling mediated interactions, we investigated what plausible signaling interactions may be connecting these functional groups.

6.3.6 Statistical inference of plausible group interactions in neuronal network

As part of the functional gene panel used to assess transcriptional states, several neuropeptides and corresponding receptor genes, such as *Vip*-*Vipr2* and *Avp*-*Avpr1b*, were measured. Utilizing this information, we examined the distributions of neuropeptide and corresponding receptor gene expression across the five groups to infer plausible neuronal group interactions. The bivariate expression behavior of neuropeptide-receptor pairs across LP neurons was divided into three distinct signaling expression regimes:

i) paracrine source: ($-\Delta\Delta C_{t,peptide} > 0$ and $-\Delta\Delta C_{t,receptor} <= 0$)

ii) paracrine target: ($-\Delta\Delta C_{t,peptide} <= 0$ and $-\Delta\Delta C_{t,receptor} > 0$)

iii) autocrine signaling: ($-\Delta\Delta C_{t,receptor} > 0$ and $-\Delta\Delta C_{t,receptor} > 0$).

The regime where low peptide and receptor gene expression occurred were not considered to play a dominant signaling role within this defined signaling scheme and were therefore ignored. These three regions are illustrated in a representative bivariate plot of ligand and receptor gene expression in Figure 6.17. In the interest of focusing on statistically significant group interactions, we used Fisher's exact test to identify which groups, if any, were statistically enriched in each signaling regime and to determine their potential signaling role (Table 6.2).

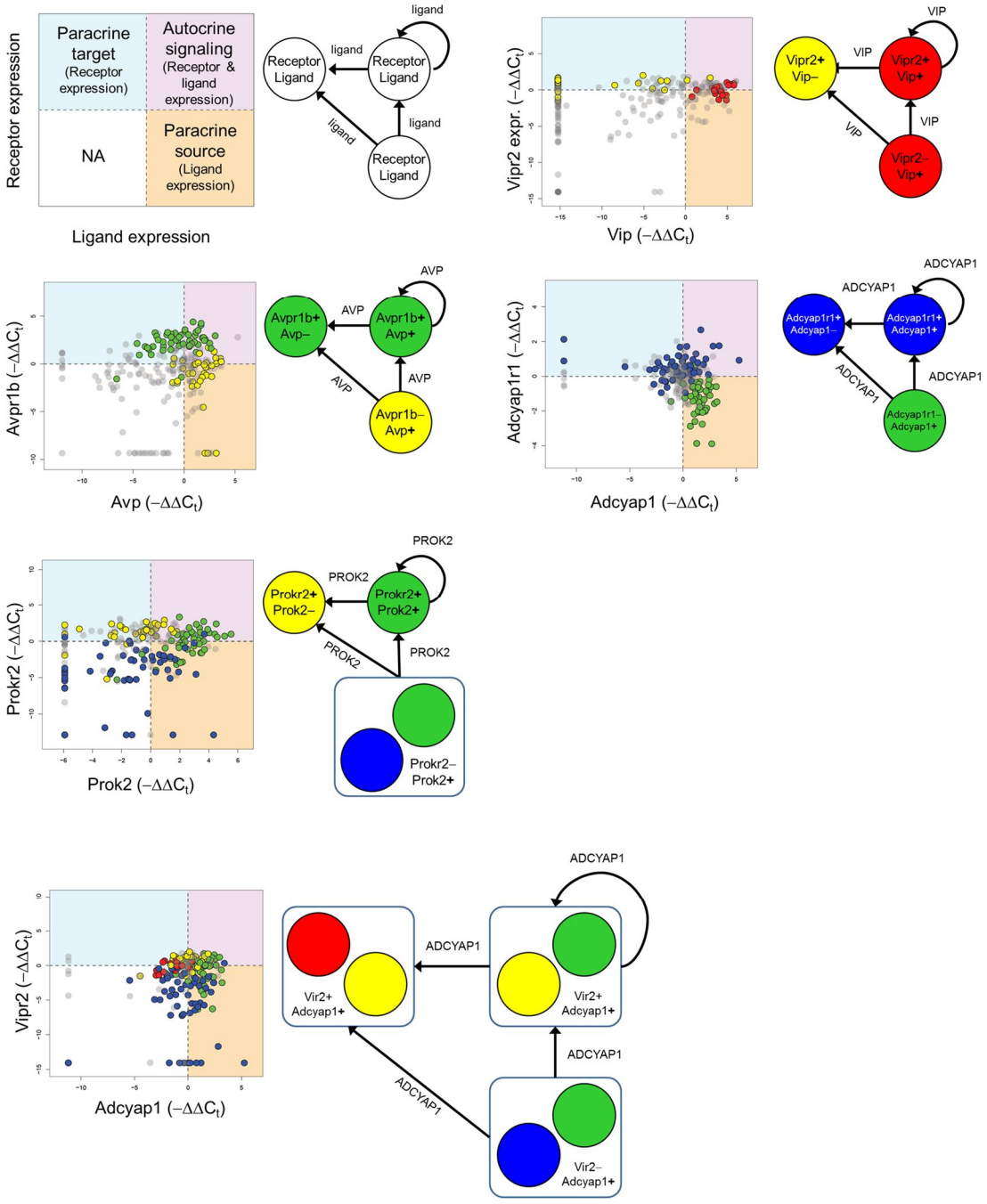
Receptor expression
Paracrine target (Receptor expression)
Autocrine signaling (Receptor & ligand expression)
NA
Paracrine source (Ligand expression)
Ligand expression
ligand
Receptor Ligand
Vipr2 expr. (−ΔΔCt)
Vip (−ΔΔCt)
VIP
Vipr2+ Vip−
Vipr2+ Vip+
Vipr2− Vip+
Avpr1b (−ΔΔCt)
Avp (−ΔΔCt)
AVP
Avpr1b+ Avp−
Avpr1b+ Avp+
Avpr1b− Avp+
Adcyap1r1 (−ΔΔCt)
Adcyap1 (−ΔΔCt)
ADCYAP1
Adcyap1r1+ Adcyap1−
Adcyap1r1+ Adcyap1+
Adcyap1r1− Adcyap1+
Prokr2 (−ΔΔCt)
Prok2 (−ΔΔCt)
PROK2
Prokr2+ Prok2−
Prokr2+ Prok2+
Prokr2− Prok2+
Vipr2 (−ΔΔCt)
Adcyap1 (−ΔΔCt)
Vir2+ Adcyap1+
Vir2+ Adcyap1+
Vir2− Adcyap1+

Figure 6.17 Inferring neuronal group interactions. Neurons expressing mRNA for neuropeptides (ligands) and their corresponding receptors are identified by $-\Delta\Delta C_t$ values and plotted in a bivariate plot. The combinatorial expression of the neuropeptide and receptor genes defines paracrine source/target and autocrine signaling roles. Each quadrant of the bivariate plot in the legend represents a particular signaling role a neuronal group may fulfill. If neuronal group(s) were determined to be statistically enriched within a particular quadrant (Fisher's exact test - Table 6.2) then the group(s) were defined to fulfill one of the following signaling roles: *i)* paracrine source ($-\Delta\Delta C_{t,ligand} > 0$ and $-\Delta\Delta C_{t,receptor} <= 0$), *ii)* paracrine target ($-\Delta\Delta C_{t,ligand} <= 0$ and $-\Delta\Delta C_{t,receptor} > 0$), or *iii)* autocrine signaling ($-\Delta\Delta C_{t,ligand} > 0$ and $-\Delta\Delta C_{t,receptor} > 0$) role. A representative set of neuronal group interactions are shown based on the following neuropeptide-receptor pairings: *Avp-Avpr1a, Vip-Vipr2, Adcyap1-Adcyap1r1, Prok2-Prokr2, Adcyap1-Vipr2*.

Table 6.2 Statistical enrichment of neuronal groups in signaling roles (Fisher's exact test)

Peptide-Receptor pair	Group #	Paracrine Source		Paracrine Target		Autocrine Signaling	
		Fraction of group	p-val	Fraction of group	p-val	Fraction of group	p-val
Avp-Avpr1a	1	0.16	7.60E-01	**0.53**	**9.41E-04**	0.05	9.95E-01
	2	**0.42**	**7.24E-04**	0.08	9.89E-01	**0.39**	**2.13E-02**
	3	0.04	9.99E-01	**0.41**	**5.70E-05**	**0.41**	**1.39E-03**
	4	0.05	9.99E-01	0.09	9.97E-01	0.02	9.99E-01
	5	**0.32**	**2.20E-03**	0.11	9.95E-01	0.26	3.54E-01
Avp-Avpr1b	1	0.08	8.14E-01	0.19	1.35E-01	0.03	9.93E-01
	2	**0.53**	**4.53E-06**	0.06	9.99E-01	0.28	2.47E-01
	3	0.00	1.00E+00	**0.51**	**1.22E-06**	**0.45**	**2.41E-05**
	4	0.04	9.99E-01	0.21	7.43E-01	0.04	9.99E-01
	5	**0.36**	**4.06E-04**	0.12	9.99E-01	0.22	5.83E-01
Avp-Avpr2	1	0.11	9.19E-01	**0.42**	**3.44E-02**	0.11	9.66E-01
	2	**0.44**	**1.68E-04**	0.06	9.99E-01	**0.36**	**5.13E-02**
	3	0	1.00E+00	**0.49**	**9.52E-07**	**0.45**	**1.15E-04**
	4	0.05	9.99E-01	0.14	9.68E-01	0.02	1.00E+00
	5	**0.34**	**2.10E-04**	0.12	9.97E-01	0.23	6.13E-01
Adcyap1-Vipr2	1	0.11	9.81E-01	**0.42**	**1.04E-02**	0.16	9.32E-01
	2	0.08	9.99E-01	**0.44**	**6.07E-05**	**0.42**	**3.10E-02**
	3	**0.49**	**6.69E-05**	0.00	1.00E+00	**0.49**	**1.34E-04**
	4	**0.41**	**4.40E-03**	0.02	1.00E+00	0.02	1.00E+00
	5	0.12	9.99E-01	0.25	6.74E-02	0.27	5.44E-01
Adcyap1-Adcyap1r1	1	0.05	9.99E-01	0.42	8.40E-02	0.21	6.07E-01
	2	0.31	6.66E-01	0.22	7.74E-01	0.19	6.88E-01
	3	**0.94**	**2.15E-26**	0.00	1.00E+00	0.04	9.99E-01
	4	0.04	1.00E+00	**0.41**	**3.35E-03**	**0.39**	**2.90E-04**
	5	0.03	9.99E-01	0.32	2.05E-01	0.30	6.34E-01
Prok2-Prokr2	1	0.21	6.07E-01	0.32	2.36E-01	0.37	1.93E-01
	2	0.00	1.00E+00	**0.53**	**1.35E-05**	0.31	3.10E-01
	3	**0.41**	**1.88E-04**	0.02	9.99E-01	**0.51**	**1.09E-05**
	4	**0.32**	**2.06E-02**	0.04	1.00E+00	0.02	1.00E+00
	5	0.10	9.99E-01	**0.34**	**3.92E-03**	0.22	8.67E-01

Bold values indicate statistically significant enrichment (conditions with p-val < 0.05).

Consistent with behavior of the established input-output pathway in which photic input stimulates VIP-producing neurons, which in turn stimulate AVP-

producing neurons to generate synaptic and molecular outputs, we observed an enrichment of Group 1 neurons as a VIP paracrine source that interacts with the paracrine target neurons of Group 2, which co-express the corresponding VIP receptor, *Vipr2,* and *Avp* (Figure 6.17). Paracrine feedback signaling between Group 2 and Group 1 via the AVP-AVPR2 pairing was supported by the data as well (Figure 6.17, Table 6.2). Moreover, increased expression of glutamate receptors *Grm1* and *Grm5* and glutamate receptor subunit *Grin1* across Group1 neurons suggest that these neurons are receptive to light-induced production of glutamate in the RHT.

In addition to recapitulating known neuron interactions mediated by VIP and AVP, our analysis revealed additional group interactions involving Group 3 neurons. Interactions between Group 3 and 2 neurons were supported by upregulated expression of the prokineticin 2 (*Prok2*) and PROK2 receptor, *Prokr2*, pairing (Figure 6.17). The upregulated expression of Prok2 across neurons of Group 3 suggest that this group fulfills PROK2-mediated roles including coordinating peptidergic output of the SCN [378,379]. Concomitantly, Group 3 neurons exhibited upregulated expression of glutamate receptor Gria4 and downregulated expression of PACAP-sensitive receptors *Adcyap1r1* and *Vipr2*. The diverging expression behavior of these receptor genes, when considered with the fact that these neurons were co-localized in the ventral region (Figure 6.15) where the RHT innervates the SCN, may indicate that this group is responsive to glutamate-specific signals generated by the RHT, in response to photic inputs.

Multiple interactions involving Group 4 also hinted at the interconnected nature of the neuronal network within the SCN. A plausible interaction between Group 4 and 3, mediated by the PACAP-ADCYAP1R1 pairing (Figure 6.17), was supported by the increased expression of *Adcyap1* in Group 3 and of *Adcyap1r1* in Group 4. Upregulated expression of *Adcyap1r1* also supports the possibility that Group 4 neurons respond directly to photic inputs via PACAP released from the RHT [143,380]. Additionally, the increased expression of *Pcsk1n* in Group 4 implies that this group may fulfill a synchronizing role. Previous studies have shown that *Pcsk1n* expression localizes in neurons located centrally within the SCN, overlapping with neurons producing gastrin-releasing peptide (GRP) [375]. Although Grp expression data was not included in our final analysis (due to assay contamination), assuming that Group 4 neurons co-express Grp, upregulated expression of gastrin-releasing peptide receptor (*Grpr*) in Groups 2 and 3 suggests that additional interactions occur between these groups and Group 4, further supporting its integrating role in the SCN.

By viewing plausible neuronal interactions in this manner, we can develop a more comprehensive neuron-interaction network that builds upon the established input-oscillator-output system. In addition to recapitulating known interactions between VIP+ and AVP+ neurons [142], our analysis suggests that paracrine signaling mechanisms connect neuronal phenotypes that are independent of the anatomical regions that have, in part, previously defined SCN neuron types (Figure 6.18).

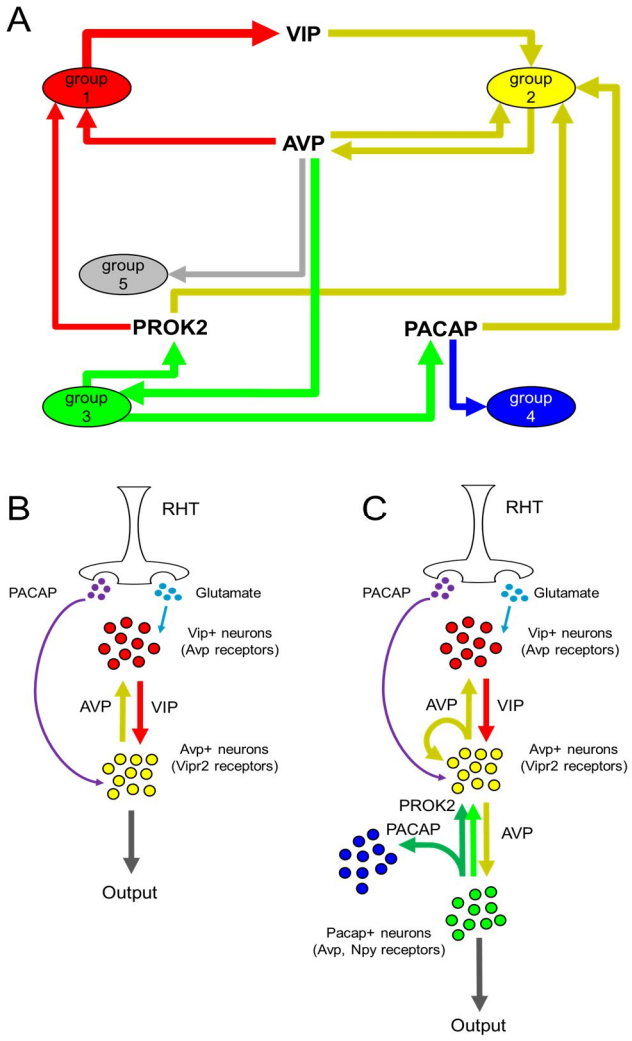

Figure 6.18 Proposed inter-neuronal SCN networks and input-output pathways. (A) Dominant interactions between presumptive neuronal groups. Nodes represent neuronal groups while directional arrows and neuropeptide labels represent mode of interaction between connected neuronal groups. Edge thickness corresponds to the fraction of single neurons within each group expressing a peptide or receptor involved in the interaction. Dominant interactions were identified as those having a Pearson correlation coefficient larger than those determined from random permutations of the peptide-receptor expression data across the LP neurons. (B) – (C) Comparison of one representation of the established input-output pathway of the SCN versus our proposed input-output pathway, based on the newly identified neuronal groups.

6.3.7 Statistical analysis of correlation thresholds

To determine statistically significant Pearson correlation coefficient values, from which a threshold limit was selected, a similar approach to that described in § 3.4.6 was used. Multiple permutation studies of were performed on the normalized gene expression data ($-\Delta\Delta C_t$) from DD neurons and LP neurons. From the gene expression data of the DD neurons, a distribution of all possible pairwise Pearson correlation coefficients between genes was determined over 1000 iterations. The resulting distribution of coefficients is illustrated in Figure 6.19.

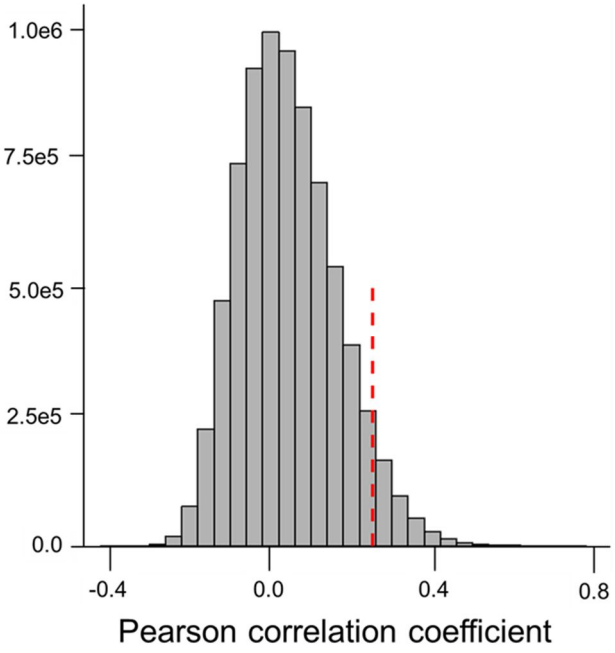

No.	Pearson correlation coefficient threshold	p-value
1	0	0.599
2	0.025	0.517
3	0.05	0.437
4	0.075	0.362
5	0.1	0.294
6	0.125	0.233
7	0.15	0.181
8	0.175	0.138
9	0.2	0.103
10	0.225	0.075
11	0.25	0.053
12	0.275	0.037
13	0.3	0.025
14	0.325	0.017
15	0.35	0.011
16	0.375	0.007
17	0.4	0.004

Figure 6.19 Empirical determination of significance threshold for Pearson correlation coefficient values in neurons from DD mice. Normalized gene expression data was permuted over 1000 iterations to determine the distribution of gene-gene correlations across the 88 cells collected from dark-adapted mice Given the sample size and variability in gene expression data present across the dark-adapted neurons, the empirically determined distribution of correlation coefficients suggests that Pearson correlation coefficient values >= 0.25 are statistically significant to a p-value of 0.053, marked by the red dashed line. Therefore positive Pearson correlation coefficients >= 0.25 determined within the dark-adapted neuronal data set are not likely to be a result of random chance. The adjacent table lists the number of significant correlations shared by the tabulated genes, which were depicted in the heat map of DD neurons (Figure 6.3). The adjacent table below lists the corresponding p-value, empirically determined, for the various Pearson correlation coefficient values from the permuted data.

Correlation coefficients greater than or equal to a value of 0.25 have an associated p-value of 0.053. Thus positive gene-to-gene Pearson correlation

coefficients determined across DD neurons with values greater than 0.25 were interpreted to not likely be a result of random chance.

The statistical significance of gene-gene and cell-cell correlation coefficients across LP neurons were determined in a similar fashion. Pearson correlation coefficients for all possible pairs were calculated using normalized gene expression data ($-\Delta\Delta C_t$) that was permuted over 1000 iterations for both gene-to-gene and cell-to-cell correlation coefficient distributions, which are shown in Figure 6.20.

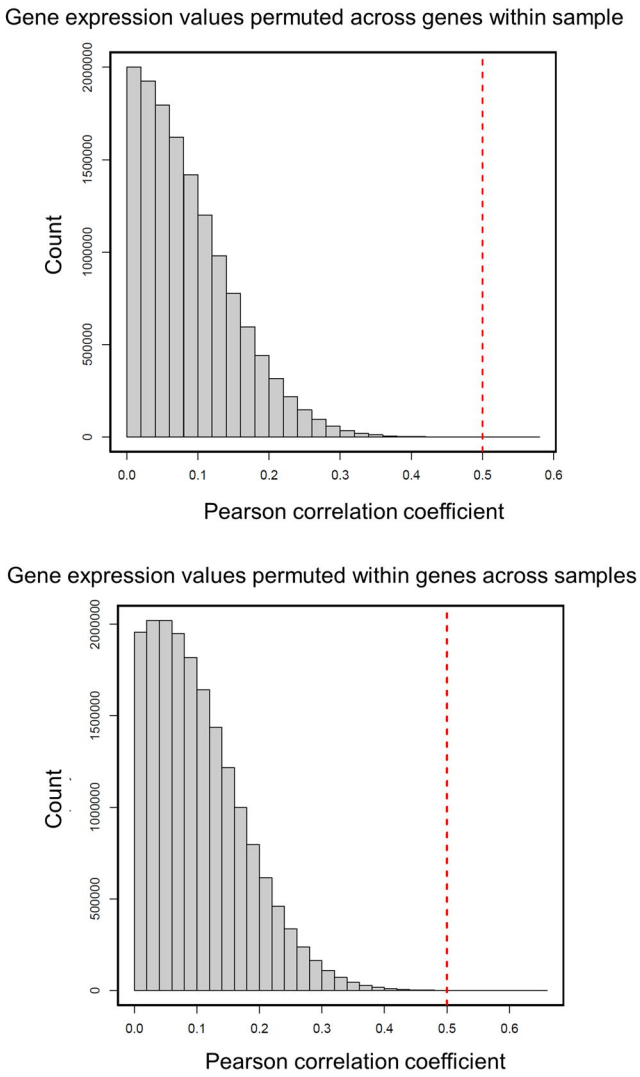

Figure 6.20 Empirical determination of significance threshold for neuronal correlation network. Normalized gene expression data was permuted over 1000 iterations to determine the possibility of generating a neuron-neuron correlation equivalent to or greater than those found in the data (i.e. pairwise neuron Pearson correlation coefficient >= 0.5). For each permutation, Pearson correlation coefficients were calculated for all pairs of LP neurons. The two histograms represent distributions of these Pearson correlation coefficients between various functional relationships determined from permuting gene expression across genes within a single neuron sample. None of the iterations resulted in a Pearson correlation coefficient equal to or larger than the correlations represented in the neuronal correlation network.

Of the 1000 permutations performed for determining either gene-to-gene or cell-to-cell correlation coefficients, not a single permutation-based coefficient was larger than 0.5. Thus, in the context of this study, Pearson correlation coefficients greater than 0.5 were interpreted to be statistically significant.

Despite the negligible possibility that a Pearson correlation coefficient between genes or cells greater than 0.5 could occur randomly across all genes and LP neurons assayed, it is possible that the correlation threshold of 0.5 may not be statistically significant in subsets of SCN neurons. The "noisy" nature of gene expression across the single SCN neurons reduces the strength of any underlying correlation between genes or cells. To address this concern, Pearson correlation coefficient distributions were determined across the subsets of SCN neurons identified in § 6.3.4. Like the statistical analysis performed on the LP neurons, a Pearson correlation coefficient of 0.5 was found to be statistically significant. Distributions of correlation coefficients developed from the permuted data subsets are presented in Figure 6.21.

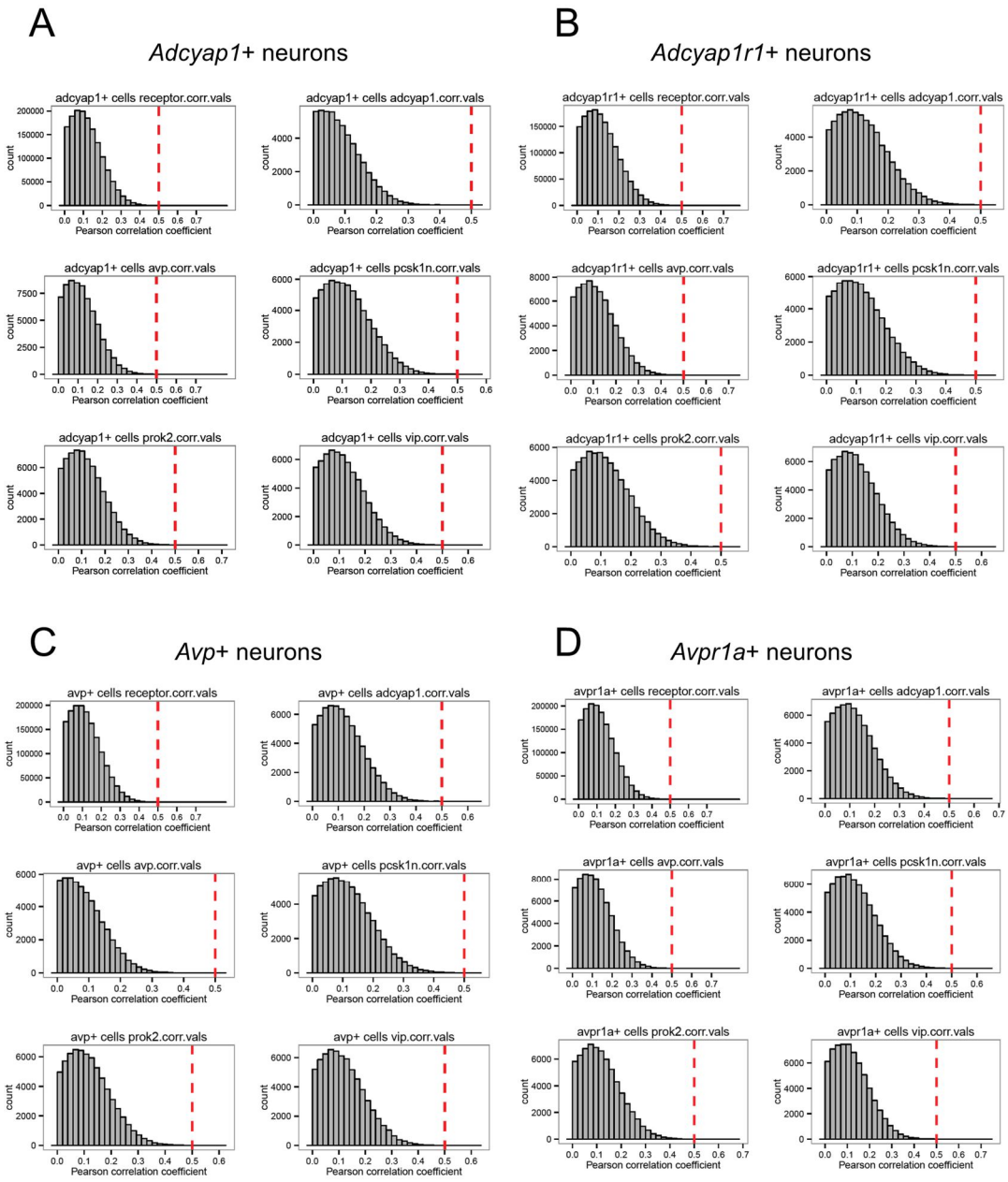
A
Adcyap1+ neurons
adcyap1+ cells receptor.corr.vals
adcyap1+ cells adcyap1.corr.vals
adcyap1+ cells avp.corr.vals
adcyap1+ cells pcsk1n.corr.vals
adcyap1+ cells prok2.corr.vals
adcyap1+ cells vip.corr.vals
B
Adcyap1r1+ neurons
adcyap1r1+ cells receptor.corr.vals
adcyap1r1+ cells adcyap1.corr.vals
adcyap1r1+ cells avp.corr.vals
adcyap1r1+ cells pcsk1n.corr.vals
adcyap1r1+ cells prok2.corr.vals
adcyap1r1+ cells vip.corr.vals
C
Avp+ neurons
avp+ cells receptor.corr.vals
avp+ cells adcyap1.corr.vals
avp+ cells avp.corr.vals
avp+ cells pcsk1n.corr.vals
avp+ cells prok2.corr.vals
avp+ cells vip.corr.vals
D
Avpr1a+ neurons
avpr1a+ cells receptor.corr.vals
avpr1a+ cells adcyap1.corr.vals
avpr1a+ cells avp.corr.vals
avpr1a+ cells pcsk1n.corr.vals
avpr1a+ cells prok2.corr.vals
avpr1a+ cells vip.corr.vals
count
Pearson correlation coefficient

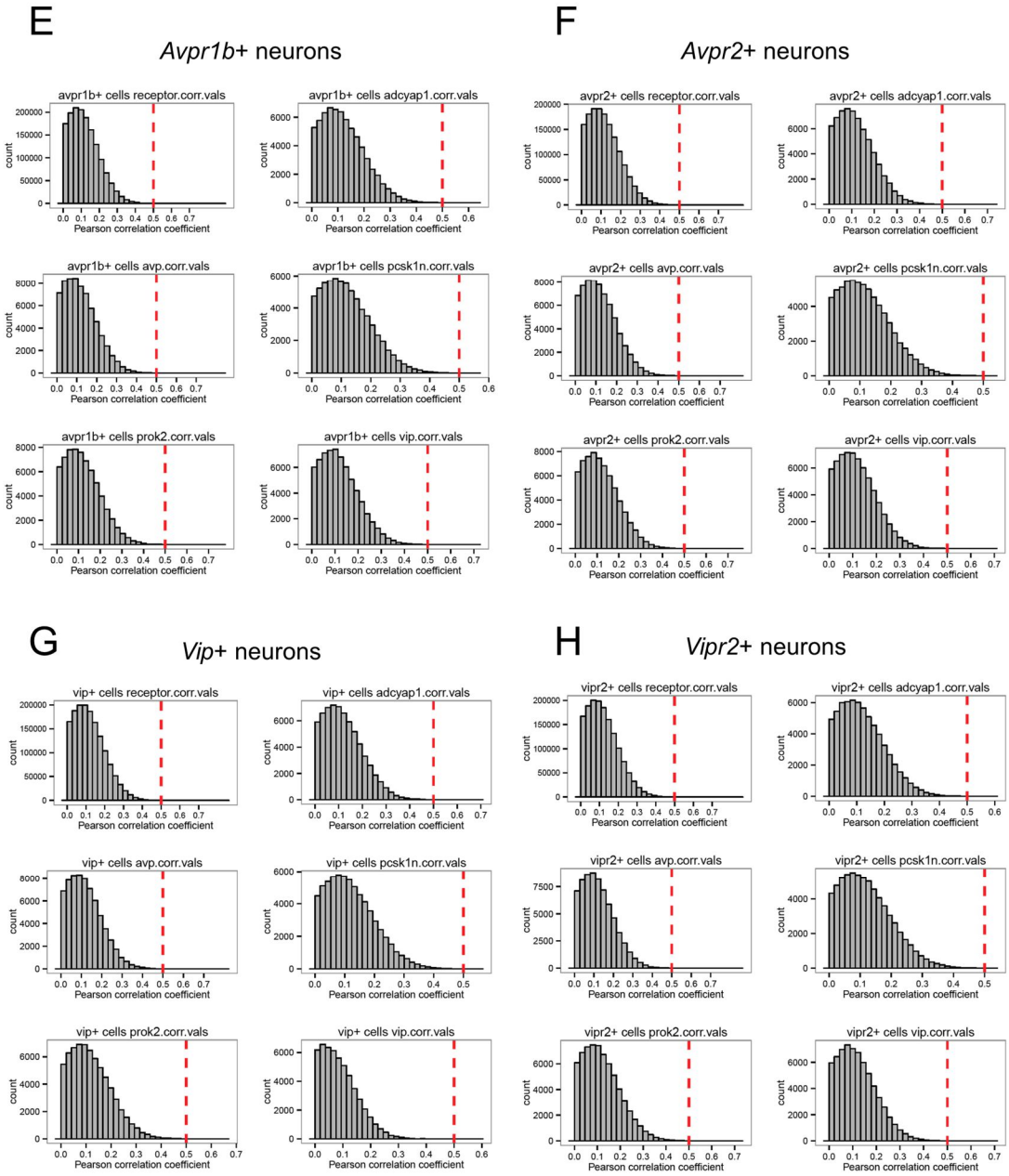
E
Avpr1b+ neurons
avpr1b+ cells receptor.corr.vals
avpr1b+ cells adcyap1.corr.vals
avpr1b+ cells avp.corr.vals
avpr1b+ cells pcsk1n.corr.vals
avpr1b+ cells prok2.corr.vals
avpr1b+ cells vip.corr.vals
F
Avpr2+ neurons
avpr2+ cells receptor.corr.vals
avpr2+ cells adcyap1.corr.vals
avpr2+ cells avp.corr.vals
avpr2+ cells pcsk1n.corr.vals
avpr2+ cells prok2.corr.vals
avpr2+ cells vip.corr.vals
G
Vip+ neurons
vip+ cells receptor.corr.vals
vip+ cells adcyap1.corr.vals
vip+ cells avp.corr.vals
vip+ cells pcsk1n.corr.vals
vip+ cells prok2.corr.vals
vip+ cells vip.corr.vals
H
Vipr2+ neurons
vipr2+ cells receptor.corr.vals
vipr2+ cells adcyap1.corr.vals
vipr2+ cells avp.corr.vals
vipr2+ cells pcsk1n.corr.vals
vipr2+ cells prok2.corr.vals
vipr2+ cells vip.corr.vals
count
Pearson correlation coefficient

Figure 6.21 Empirical determination of significance threshold for gene correlation network (LP neurons). Normalized gene expression data was permuted over 1000 iterations to determine the possibility of generating a gene-gene correlation equivalent to or greater than those found in the data (i.e. pairwise gene Pearson correlation coefficient >= 0.5). For each permutation, Pearson correlation coefficients were calculated for all pairs of genes. Histograms represent distributions of these Pearson correlation coefficients between various functional relationships including correlations shared with receptor genes and all the neuropeptide genes measured (*Adcyap1, Avp, Pcsk1n, Prok2,* and *Vip*). The dashed red line represents the correlation coefficient threshold used in generating the gene correlation network (Figure 4). These distributions were determined for gene-gene correlations within subset of SCN neurons including (A) *Adcyap1*+ neurons, (B) *Adcyap1r1*+ neurons, (C) *Avp*+ neurons, (D) *Avpr1a*+ neurons, (E) *Avpr1b*+ neurons, (F) *Avpr2*+ neurons, (G) *Vip*+ neurons, and (H) *Vipr2*+ neurons. None of the iterations resulted in a Pearson correlation coefficient equal to or larger than the correlations represented in the gene networks.

6.4 Discussion

A driving motivation for this dissertation is to understand how single-neuron heterogeneity, as defined by their heterogeneous transcriptomic state, relates to phenotypic function in distinct brain nuclei. Towards this goal, we analyzed and identified distinct transcriptomic phenotypes in the SCN and developed a molecular framework in which these distinct phenotypes organize into plausible cellular networks that contribute to and regulate SCN coordination of circadian rhythms. Although prior work relied on neurochemical criteria and physiological approaches to characterize SCN neuron types, functional heterogeneity across single SCN neurons conflicts with these classification approaches.

In this chapter, we analyzed the transcriptional and spatial organization of single SCN neurons from DD and LP treated mice. By integrating this precise spatial and gene expression data from hundreds of SCN neurons with multivariate mathematical techniques, we identified organizational frameworks (or lack thereof in the case of the DD neurons) that begin to reconcile the heterogeneous behavior observed in SCN neurons in dark-adapted and light-pulsed conditions. The absence of any clear anatomical organization in the DD neurons, relative to the structured anatomical organization between Group 1 (*Vip*+) and Group 2 (*Avp*+) LP neurons, suggests that photic inputs force a constrained transcriptional response. A diverse array of inputs, including non-hypothalamic neuronal innervations and paracrine signaling neuropeptides [377] are continually influencing and driving neuronal state and function [105]. The diversity of inputs is reflected in the wide range of transcriptional states exhibited by the DD neurons and random anatomical distribution through the SCN. Because the DD neurons are not receiving photic input, they are not forced to respond to this external constraining force and hence likely exist in a wider range of transcriptional states. Conversely, LP neurons exhibit more constrained and organized transcriptional states, due in part to the photic input received by these neurons. The anatomic organization between Groups 1 and 2 supports a spatially biased transcriptional response of SCN neurons to photic input. It is plausible that this spatial organization is due to RHT innervation of the SCN core. Such a cellular input-driven transcriptional response aligns with our previous findings from an analysis of

single NTS neurons responding to inputs from baroreceptors sensing changes in blood pressure [105].

In addition, we established a classification of SCN neurons, which provided a transcriptional basis from which we could infer cell-interaction network models from a population of heterogeneous neurons contributing to SCN function and robustness [108,147,351]. Our analysis not only recapitulated known neuronal phenotypes (Group 1-*Vip*+ neurons and Group 2-*Avp*+ neurons), but also revealed additional phenotypes that have not been described previously. While there is an extensive amount of literature detailing the various excitatory and inhibitory signaling mechanisms affecting the SCN, we have focused our single-cell transcriptomic analysis on the neuropeptides and paracrine signaling mechanisms deemed to regulate the circadian clock. Within the context of this paracrine signaling network (Figure 6.18), the neuronal phenotypes that arise from our unique single-cell transcriptomic data set represent neuron-types that add complexity to the paracrine signaling network underlying synchronization or circadian clock across the SCN. Our analysis and development of a neuronal network structure provides a model with which to interpret and understand more comprehensively the transcriptional heterogeneity pervasive across individual SCN neurons.

The multi-genic analysis of SCN neurons revealed greater molecular complexity across a population of SCN neurons than heretofore described [148,149,374]. This complexity manifested in several ways including *i)* the spatial organization of a subset of *Avp*+ Group 2 neurons, *ii)* the co-expression of *Vip* and

Avp, and *iii)* the endogenous expression of *Adcyap1* in neurons located throughout the SCN. One possible explanation for the larger than expected spatial distribution of *Avp*+ Group 2 neurons may be due to differences in the rhythmicity between mRNA and peptide expression [381]. AVP mRNA expression is robustly rhythmic while the corresponding peptide expression is less so. Therefore, some IHC studies have used the drug colchicine to inhibit release and promote accumulation of neuropeptides in the perikarya to enhance staining. Because single-cell qRT-PCR approaches measure mRNA, obviating the need for colchicine, it is possible that this approach revealed a subset of AVP mRNA-expressing neurons that lies outside of the dominant dorsomedial shell region identified by protein staining. Previous studies using *in situ* hybridization to map mRNA expression in the SCN have shown similar localization of AVP mRNA [344]. While co-expression of *Vip* and *Avp* is not characteristic of SCN neurons, our results and those of others [145,382] do support the idea that *Vip* and *Avp* co-expression does occur within a small subset of SCN neurons. Finally, the precise nature of LCM sampling, as demonstrated by results described in § 3.2.4.4, and the large spatial distribution of *Adcyap1*+ neurons throughout the SCN suggest that these results are not an artifact of any unlikely residual RHT processes contaminating the samples.

Despite the central roles neuropeptides play in circadian regulation, our gene correlational network analysis suggested that neuronal states are driven more by the inputs they receive rather than the peptidergic outputs they produce. This result parallels with the results described in Chapter 3. Concurrently, this receptor-based

transcriptional regulation occurring in SCN neurons may reflect a neuron's ability to sensitize itself to specific inputs. This sensitization or "gating" modulates SCN responsiveness to photic inputs at specific times during the circadian cycle [151,383,384]. Because transcriptional profiles were measured early in the dark cycle (ZT15 - a time when SCN neurons are more sensitive to phase-shifting photic inputs), it is possible that receptor-correlated expression reflects this gating behavior *in vivo* [151].

6.4.1 Study limitations

This analysis showed that nearly all neurons were associated with a particular neuronal phenotype, with the exception of Group 5 neurons. While we hypothesize that Group 5 may play multiple roles in the neuron-interaction network, the presence of these neurons brings to light some limitations of our sample set. Given the complex and dynamic nature of circadian regulation, SCN neurons are continually responding to multiple input types. Had we measured single-neuron transcriptional profiles at multiple times, our analysis would have likely revealed neuronal groups distinct from those identified herein.

Moreover, while the underlying transcriptional organization of most of the groups identified was independent of animal-animal variability, Group 3 was composed predominantly of neurons taken from one animal subject (Figure 6.22). Given the extent of transcriptional heterogeneity observed, which in many cases surpass animal-animal variability [31,105,367], it is surprising to see such a

concentration of neurons from one animal as no experimental biases or particular behavioral or physiological phenotypes were identified. Further, single-cell RNA sequencing of SCN neurons would have provided a comprehensive perspective of the transcriptional states of SCN neurons and potentially lead to the identification of additional neuron-types not included in our analysis.

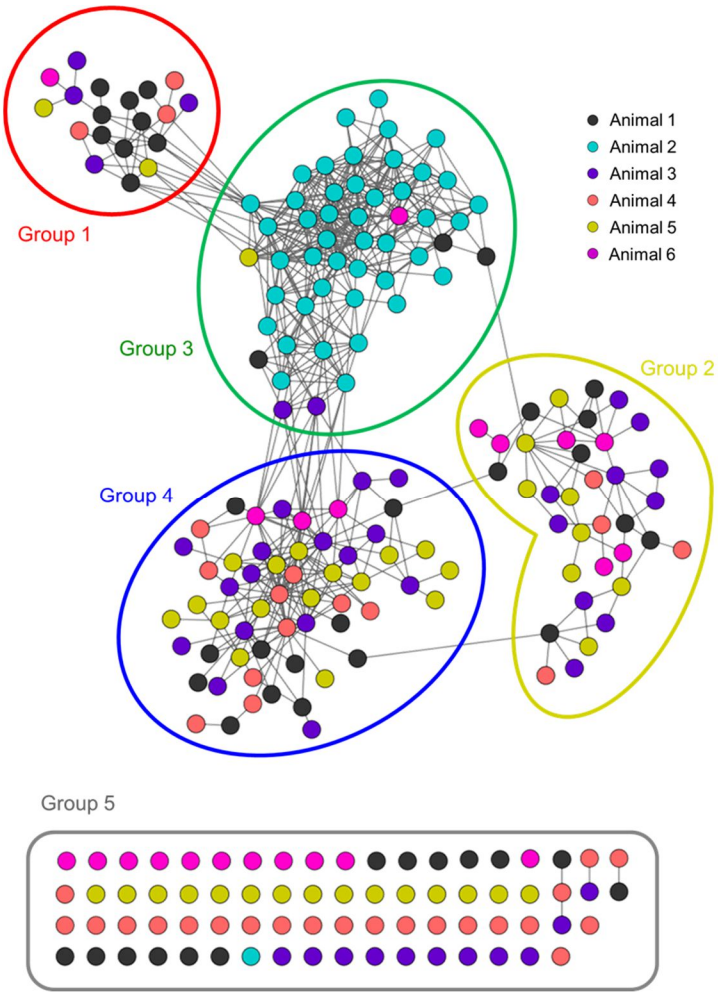

Figure 6.22 Animal variability across neuron correlation network. The same neuron-neuron correlation network (Figure 6.13) is annotated with the animal source from which the single neurons were sampled. Each group is outlined with their corresponding group color as in Figure 6.13. Although most groups are composed of neurons from multiple light-treated mice, Group 3 neurons were composed predominantly of neurons from Animal 2.

However, the main intent of this work was to provide a molecular framework from which to interpret the single-cell heterogeneity of SCN neurons. Given that the transcriptional components underlying circadian rhythms are well characterized

[156,356,357], our analysis focused on these and other functionally relevant genes to develop an organizational framework sufficient to reconcile SCN function and single-neuron transcriptional heterogeneity. While the data used in this study did not measure the complete transcriptome of the SCN neurons sampled, this study, along with previous efforts [97,105], suggests that the depth and breadth of the gene panel manually curated here is indeed able to infer a meaningful organizational framework. Given these limitations, further investigation - including single-cell RNAseq analysis across multiple time points in which photic input sensitivity and light/dark cycle durations differ - would provide valuable information regarding the function and organization of SCN networks.

The ability to interpret how single cells organize into functional interaction networks from heterogeneous cellular behavior not only provides fundamental insight into SCN organization, but also provides similar insights into the molecular organization of cellular networks and neuronal circuits of other tissues that regulate stable steady states, such as cardiovascular homeostasis, which was examined in Chapter 5. These neuronal circuits undergo distributed rearrangements throughout life yet are able to maintain stable behavior within an environment of continual perturbations [8]. Previous work has investigated how neuronal circuits and networks configure and self-regulate via synaptic connections, synaptic scaling, and permissive signaling that modulate cellular behavior [8,9]. And while current efforts continue to yield insight into network homeostasis, questions regarding how coordinated changes and phenotypic modulation that regulate network homeostasis remain. “The challenge

is to begin assembling an emerging molecular 'parts list'..." and "[specify] cell identity," in order to understand how neural activity is regulated [9]. The approaches developed in Chapters 3 and 4 and applied herein to analyze and develop a data-driven cellular network structure provides a methodology with which to interpret how single-cell heterogeneity contributes to cell network and neuronal circuit formation and has the potential to provide insight into the molecular parts list.

6.4.2 Concluding remarks

Our results show distinct functional phenotypes that exist outside the traditional neurochemical definitions of the SCN. Even though these neurochemical criteria are useful and conveniently describe key aspects of SCN function, they fall short of fully capturing the complexity and diversity of the neuronal components driving SCN function. Although our findings are limited to specific times chosen for this study, our approach provides a unique perspective of SCN functional networks that provide plausible explanations as to how these neuronal phenotypes and neuron-neuron interactions organize under dark-adapted and phase-shifting behavior.

These approaches and results discussed in this chapter provide a complementary perspective to the previous and more recent modeling work that characterizes the oscillatory molecular behavior of the SCN. Detailed work has modeled quantitatively the mechanistic roles of VIP [385,386], and the role that epidermal growth factor (EGFR) signaling plays in circadian regulation [387]. In addition, more recent work have applied techniques from information theory to

identify functional networks in the SCN based on the coupling of Per-luciferase expression in decoupled and coupled neurons [388]. These efforts are a few of the examples of some of the useful insight that have been gained in SCN function from focusing on a small set of genes. These methods can be applied towards understanding the multiple molecular mechanisms connecting the neuronal phenotypes identified in this chapter. As single-cell transcriptomic technologies continue to improve and become more widely accessible, it is important to have a viable methodology with which to analyze and interpret the heterogeneous transcriptional states underlying neuronal function. The single-cell analysis methodologies described in this chapter provide one such approach and thus may play a role in the continued study of the individual neurons in the SCN and their role in regulating circadian rhythms.

Chapter 7

CONCLUSIONS AND FUTURE DIRECTION

"A man would do nothing if he waited until he could do it so well that no one could find fault."

John Henry Newman (1801 – 1890), in *Lectures on the Present Position of Catholics in England* [389]

7.1 Conclusions

Throughout this dissertation, we have developed methodologies and an approach to analyzing and characterizing the molecular organizational principles underlying single-neuron heterogeneity in the mammalian brain. We applied a combined experimental and computational approach to analyze single-cell transcriptional heterogeneity in two distinct brain structures, the nucleus tractus solitarius and the suprachiasmatic nucleus, whose functional connectivity and spatial organization have been well characterized. From these efforts we have developed methodologies and quantitative models that characterize key molecular and physiological aspects of single-neuron heterogeneity in the brain.

The ultimate goal of this work, however, is not the analytical approaches or models themselves, but rather the insights gained from the application of these models

and methods. Through our analysis of transcriptionally heterogeneous neurons with respect to their functional connectivity and spatial organization, we have developed an alternative perspective from which to interpret and understand the functional relevance of transcriptionally heterogeneous single neurons. Rather than being primarily the result of intrinsic and extrinsic stochastic factors, transcriptomic heterogeneity provides functional robustness through a graded set of cellular responses, as opposed to some uniform population response. Transcriptional heterogeneity, which reflects the adaptive response of neurons, provides more nuanced responses and robust regulation of physiological functions critical to maintaining homeostasis.

In Chapter 2, rationale for studying the NTS and SCN as model brain nuclei to understand single-neuron transcriptional heterogeneity in their functional context was provided. To accomplish this task, details regarding the combined experimental and computational approach were provided. Well-established animal model systems, specific physiological perturbations triggering targeted transcriptional responses, precise sampling of single neurons via laser capture microdissection, and high-throughput qPCR platforms such as the BioMark^{TM} create the experimental foundation that enabled the characterization of transcriptionally heterogeneous neurons in their neuroanatomical and functional context. A critical aspect of the analysis of high-dimensional gene expression data includes data normalization, which removes systemic biases that affect subsequent analysis and prevents the appropriate interpretation of the data. To remove these biases, multiple normalization techniques were discussed. Two normalization techniques, geNorm and NormFinder [174,180],

used to identify multiple internal reference genes, was applied throughout the single-cell analysis described in this dissertation. Further, given the high-dimensional nature of gene expression that has been observed at the single-cell level, a brief summary was provided of the various multivariate analytical methods that could be used to identify organizational patterns that would help to clarify the relevance of single-neuron heterogeneity.

In Chapter 3, the combine experimental and computational approaches described previously were used to analyze single-neuron heterogeneity in the NTS. As alluded to in Chapter 2, the remarkable amount of heterogeneity observed across individual NTS neuron required multiple computational/multivariate techniques to analyze the data. Although the use of techniques such as PCA, MDS, and hierarchical clustering revealed a subset of genes that principally contribute to the transcriptional variation in the data, a meaningful interpretation of this transcriptional variability was only possible when the transcriptional profiles were analyzed in the context of the transcripts corresponding to intracellular markers of synaptic input-types received by these neurons. When individual neurons were classified by the types and strength of synaptic inputs received, distinct subtypes of transcriptionally similar neurons emerged from the high-dimensional gene expression data set. These neuronal subtypes were characterized by graded, correlated gene expression behavior of two underlying transcription modules. The presence of these input-driven subtypes suggests that the transcriptional heterogeneity of single neurons reflects their adaptive responses to these inputs. These results suggest an addendum be made to the canalized

developmental landscape initially proposed by Waddington [56,57]; once a cell reaches a differentiated state, the continual inputs it receives continually drives that cell along a dynamic transcriptional landscape populated with wells and valleys that represent various functional states in which a cell may exist. Furthermore, the graded and coordinated expression behavior across the two transcription modules suggest the presence of gene regulatory network(s) that coordinate this correlated behavior. The identification of these gene networks was the subject of Chapter 4.

Chapter 4 describes a systems identification approach that was developed to generate quantitative models of gene interaction networks that characterize plausible mechanisms underlying the emergent neuronal subtypes identified in Chapter 3. Despite the difficulties in analyzing highly variable gene expression of single cells, these heterogeneous transcriptional states can be viewed as providing distinct transcriptional response profiles across these single neurons. Concomitantly, taking advantage of *a priori* knowledge of causal gene interactions reported in literature, the single-cell transcriptional dataset represents input-output measures that can be used to develop a model of the underlying processes, i.e. gene interaction networks, driving these input-output responses. To develop quantitative models of these networks, a fuzzy logic-based modeling approach was developed and applied towards analyzing our single-neuron high-dimensional transcriptional data set. Hill-type functions, that can model near-linear to near-binary ON-OFF input-output relationships, were used to model quantitatively nonlinear gene interactions. An optimization technique known as the genetic algorithm, which is based on evolutionary principles, was subsequently

used to train, optimize, and refine the *a priori* network against the context specific single NTS neuron transcriptional data set.

Using this methodology, we developed and trained an *a priori* gene interaction network characterizing the AT1R functional pathway, which is heavily involved in blood pressure mechanisms in the brainstem. Our modeling and analysis of the AT1R pathway in NTS neurons revealed that distinct gene interactions were found to correspond to the distinct neuronal subtypes identified. Permutation studies and an n-fold cross-validation procedure were applied and verified the statistical significance of the *a priori* network structure and the predictive capabilities of the resulting trained network models. Simulation studies using these network models subsequently revealed that the response of these distinct network structures to distinct input stimuli can drive single-neurons across a range of transcriptional states. Taken together, these results indicate that both distinct network structures and distinct network inputs operating on these networks contribute to the transcriptional heterogeneity observed in single NTS neurons; these factors can drive an individual neuron along the transcriptional landscape that help define the functional states of NTS neurons. We interpreted this ability to exist in multiple transcriptional i.e. functional states to be representative of a neuronal adaptive response to received inputs. Based on these results, we proposed that this adaptive responses represents a mechanism that enables the brain to regulate robustly physiological functions, such as the maintenance of cardiovascular homeostasis.

In Chapter 5 a closed-loop control model of autonomic regulation of arterial blood pressure and relevant cardiovascular function was developed to test this proposal, specifically to explore what functional relevance adaptation of neuronal subtypes in the NTS and in the brainstem plays in the broader functional context of cardiovascular homeostasis. Using this closed-loop control model we simulated the diseased state of systolic heart failure due to myocardial infarction, which leads to an impaired cardiovascular state, to evaluate what effects neuronal adaptation would have on baroreflex regulation of cardiovascular performance. We then tested the effects of neuronal adaptation on short-term baroreflex regulation of the cardiovascular system by running multiple simulations using randomly selected parameters sets corresponding to the input-output transfer functions corresponding to the distinct neuronal subtypes in the brainstem. Simulation results revealed that neuronal adaptations can compensate for impaired cardiac function by reducing vagal tone that inhibits ventricular contractility. Although a sustained decrease in vagal tone is detrimental to overall cardiac health, decreased vagal drive provides a short-term compensatory mechanism that improves hemodynamic behavior and ejection fraction of the heart. In addition, these results suggest that neuronal adaptation must occur across multiple neuronal populations in the NTS, NA, and DMV to renormalize clinically relevant hemodynamic outputs like ejection fraction, cardiac output, diastolic, and systolic ventricular volumes. These results support our earlier proposal (§ 3.5) that neuronal adaptation, as observed across individual brainstem neurons, provides robust regulation cardiovascular homeostasis.

In Chapter 6 the input-driven organizational principles identified in the NTS, described in Chapters 3 and 4, and their utility in understanding single-neuron heterogeneity throughout the brain was examined in a distinct forebrain nucleus, the SCN. Despite extensive characterization of SCN neurons, based on neuropeptidergic and region-specific characteristics, single-neuron heterogeneity complicates our understanding of how SCN neurons interact and form cellular networks that regulate SCN function. By performing single-cell transcriptional analysis of the SCN, we were able to identify transcriptional signatures of neuronal phenotypes and paracrine signaling mechanisms using several multivariate techniques that were applied in Chapter 3 as well as techniques developed in the field of graph network theory.

Thorough examination of the gene expression behavior of single SCN neurons revealed multiple neuronal phenotypes whose gene expression behavior aligned with known SCN peptide production as well as support previously undescribed SCN neuron-types. An example of such a neuron-type includes neurons expressing *Adcyap1*, which were located throughout the SCN. With the exception of the *Avp*+ and *Vip*+ groups, these neuronal phenotypes were distributed throughout the SCN. However, analyzing gene expression corresponding to known ligand and receptor pairs involved in SCN paracrine signaling mechanisms revealed multiple plausible interactions among the identified neuronal phenotypes. Thus, these results suggest that transcriptionally heterogeneous SCN single neurons form distinct functional states in a molecular framework in which these neuronal phenotypes synchronize with one another through paracrine signaling mechanisms.

The above results demonstrate the utility of performing an analysis of single cells belonging to a complex organ such as the brain in the context of their *in vivo* neuroanatomical environment and functional connectivity. The combined experimental and computational approach described throughout this dissertation provides an overall platform that enables one to elucidate what neuron-types and how many exist in the brain and what functional roles they play. We have discovered an organizational framework within which individual neurons adaptively respond to the inputs they receive. Based on our single-cell analysis of the brain, we can now view a heterogeneous neuronal population as a mixture of distinct neuronal subtypes whose adaptive response to various inputs is driven by distinct regulatory networks. This adaptive response manifests as individual neurons transitioning across a range of transcriptional states that reflect an array of functional states that a neuron may exist in. Such adaptation provides robust regulation of physiological function, providing compensatory effects under challenged states. While these results provide the beginnings of how one may address the question of "what is a cell-type" and "what is the functional relevance of neuronal heterogeneity", significant work and opportunities remain.

7.2 Future Work

In this final section, several possible directions in which the work presented here can be taken are discussed. The present work only scratches the surface on

understanding transcriptional heterogeneity across single neurons and the role it plays in brain function and its regulation of physiological processes throughout the body.

7.2.1 Experimental techniques

High-throughput qPCR provides a broader molecular perspective on the state of an individual cell than what would be achieved using "reductionist" approaches, where a single gene or a particular signaling pathway is studied extensively. Although the analysis of the NTS and SCN in this dissertation involved brain nucleus-specific sets of 96 genes, which proved to be sufficient to identify distinct neuronal phenotypes, 96 genes represent only a fraction of a cell's transcriptome. Although these genes were carefully selected based on their functional relevance, as indicated by prior global microarray studies, investigating hundreds of genes is somewhat limited in scope. Technological advances that improve accuracy, precision, and availability of omics-scale assay platforms are continually being made. RNA sequencing of individual cells, or single-cell RNA-seq (scRNA-seq), a technique that sequences the entire transcriptome provides a comprehensive view of the molecular state of a cell.

During the completion of this dissertation, this technology has been applied effectively towards measuring single-cell transcriptomic heterogeneity [31,71,86,105,367] and will continue to be used to improve understanding of transcriptional heterogeneity underlying (dis)similarities existing between neuron-types. The approaches developed in this dissertation would benefit from applying scRNA-seq. Deeper profiling of individual neurons in the NTS and SCN with respect

to their functional connectivity and local neuroanatomical environment may reveal additional neuronal phenotypes supporting a more subtle and nuanced perspective of cell-types. Knowledge of the dominant and rare functional states in which neurons exist and how these states differ would provide additional mechanistic detail of physiological and pathological conditions, beyond what can be determined from analyzing hundreds of genes.

7.2.2 Acute hypertension model

Dynamics of single cell transcriptomic heterogeneity – Chapter 3 described work that demonstrated that an acute physiological perturbation such as an acute hypertension challenge can drive a change in the transcriptional landscape of NTS neurons. Although extensive sampling across multiple animals was performed in the analysis of the NTS, these results were based on a single time point, 60 min post-phenylephrine injection. While lateral sampling of single neurons would require a sampling scale that is beyond the scope of this dissertation, it is possible to consider the findings in Chapter 3 and create a plausible experimental design including a reasonable number of samples panning both animal replicates and multiple time points. Because the transcriptional variability observed across neurons within an animal was as large as, and in many cases larger than, the transcriptional variability observed across animals, it is plausible to suspect that cell-to-cell variability, rather than animal-animal variability, would be the dominant source of transcriptional heterogeneity within a time point. Consequently, a more thorough single-cell sampling

from one animal across multiple time points, with fewer single-cell samples collected across animals per time point would allow one to study transcriptional states and underlying organization of transcriptional states over time.

This proposed sampling approach can be applied to study single-neuron heterogeneity over time in established animal models of neurogenic disease. One example includes the spontaneously hypertensive rat (SHR) and its control counterpart, the Wistar Kyoto Rat (WKY). Analyzing single neurons in key brainstem nuclei would provide insight into the molecular mechanisms driving autonomic regulation in hypertension development. For instance, one can investigate the organizing principles of single neurons in the RVLM, the central nucleus regulating sympathetic outflow to the body, in SHRs and WKYs at key developmental stages of hypertension development including 4 weeks (pre-hypertensive), 6-8 weeks (hypertension development), 12 weeks (hypertension established) and 14-16 weeks (hypertension sustained). Such a study would potentially reveal how the molecular organization of single neurons persists or changes and how these changes drive the neurogenic aspects of hypertension pathology. This type of study may reveal transcriptional targets that may be manipulated to prevent a subset of neurons from adapting into a functional state associated with hypertension development. A similar longitudinal study was performed, which investigated microRNA states of multiple cell types in the brainstem and identified several microRNA targets that may prevent inflammatory pathways from reaching maladapted states that support hypertension progression [288].

Alternatively, another avenue of interest to pursue would not focus on the immediate transcriptional response of neurons to an acute hypertensive challenge, but rather investigate how individual neurons recover from such a challenge. Chapter 3 describes NTS neurons as having a constrained transcriptional response to an acute hypertensive challenge. However, it remains unclear whether these neurons revert back to some nominal state once the hypertensive challenge/perturbation dissipates. If neurons do not revert back to some nominal state, in what ways does this new state differ from the normotensive condition? This investigation would provide interesting insights into how neurons may (or may not) adapt to acute physiological challenges and what the effects of a challenge (or repeated challenges) may have on the functional state of brainstem neurons.

7.2.3 Gene regulatory network applications

Chapter 4 provides a methodology to identify gene interaction networks from inherently variability single-cell transcriptomic data. One logical step forward would be to perform sensitivity analysis on these network models. Determining how sensitive the gene interaction network system to the individual gene components, or combinations of genes, would provide additional insight into the underlying gene network. Identifying gene(s) having the largest impact on systemic responses would also provide plausible targets that can be further investigated either computationally or experimentally, through the use of targeted gene manipulation techniques in SHRs. It would be possible to study whether these targets can be manipulated to affect

transcriptional states of NTS neurons to rescue maladapted or dysfunctional neurons that affect physiology [34,390].

7.2.4 Circadian cellular network modeling

A simple extension of the single-neuron analysis of the SCN presented in Chapter 6 would be to apply fuzzy logic modeling, as described in Chapter 4, to the transcriptional profiles of SCN neurons. Detailed analysis revealed distinct neuronal phenotypes and applying the fuzzy logic modeling methodology may reveal distinct gene interaction networks underlying the functional states of these neuronal phenotypes. While the transcriptional programs underlying SCN circadian behavior are well established [108,142], this knowledge is based on tissue-level samples that average out the heterogeneity prevalent at the single-cell scale. If differences in gene interaction network structure were indeed present in SCN neurons, investigating differences among fuzzy-logic-based network models of different SCN neuronal populations would provide complementary information to recent results and ongoing studies focusing on the SCN.

As described in Chapter 6, one such example includes the study by Abel, et al. [388] which investigated the temporal dynamics of *Per* expression in single SCN cells using Per-luciferase. Their study revealed that small-world network structures, in which cells are sparsely connected, drive the temporal coordinated behavior of the SCN [388]. These cellular nodes in the small world networks may correspond to the distinct neuronal phenotypes identified in Chapter 6. Given the results presented in

Chapter 4, it is possible that distinct gene interaction networks correspond to the neuronal phenotypes identified in Chapter 6. Identifying and analyzing these gene networks would further help to distinguish these cell types and provide a model that can be used to study how these neuronal phenotypes may transition from one transcriptional phenotype to another in a small world network or other network structure.

Further, the cyclic nature of circadian rhythms strongly motivates a lateral study that investigates the changes of neuronal phenotypes at various time points during the circadian cycles. Questions regarding the persistence or adaptability of neuronal phenotypes, similar to those raised regarding the acute hypertensive challenge model and hypertension pathology apply to circadian rhythms as well.

The neuronal phenotypes identified from the single-neuron analysis of the SCN can also be integrated with previous modeling results that explore the oscillatory nature of VIP+ and AVP+ neurons [391]. In previous studies, oscillatory models examined how SCN synchronization could be explained by the interaction of these two neuron-types. Similar oscillatory models can be extended to include the previously unidentified neuronal phenotypes described in Chapter 6. Building a multi-phenotypic model that reflects the biological complexity observed in the SCN would be useful to explore what effects the presence of these neuronal phenotypes have on system sensitivity and robustness. Such a model can be used to generate hypothesis as to what gene, or group of genes, or even neuronal phenotype(s) would impact SCN synchronization for experimental testing *in vitro* and *in vivo*.

7.2.5 Baroreflex modeling

There are several possibilities in which this model can be used to further study autonomic regulation of blood pressure and cardiovascular homeostasis.

i) Including additional afferent inputs and corresponding neuronal subtypes in the NTS. These subtypes can be used to further explore how neuronal adaptation affects baroreflex regulation under other challenged cardiovascular states, such as exercise-induced stress. Patients suffering from systolic heart failure post myocardial infarction are reported to have impaired cardiovascular function in response to exercise-induced stress. Adding chemoreceptor inputs and additional components such as pacemaking neurons that align with the respiratory cycle will capture more accurately the interconnection between cardiovascular and respiratory processes may reveal potential neuronal populations and interactions that can be targeted to improve this impaired response.

ii) Limits of controller compensation – simulations showed that neuronal adaptation is able to compensate for an injured heart. However, the modified conditions represent one set of conditions emulating systolic heart failure. It is possible that more extreme changes to left heart function would causes changes that could not be fully compensated for by neuronal adaptation. Thus understanding what the compensatory limits of neuronal adaptation are would provide insight into what other systemic changes are required to compensate for the impaired disease state.

iii) Diastolic heart failure – there are multiple ways that impaired cardiac function manifests itself, with systolic heart failure following myocardial infarction representing one of multiple disease states. Diastolic heart failure is another disease state that associated with myocardial infarction and is characterized by impaired filling during diastole. In this case, ejection fraction is not affected as it is in systolic heart failure and is preserved. Understanding what compensatory changes result from diastolic heart failure and what neuronal responses are required to achieve such changes may provide additional insight into the array of neuronal adaptations associated with heart failure.

iv) Heart rate variability – although not included in the analysis in Chapter 5, the current model includes mechanisms through which respiration affects heart rate. This respiratory-induced variability in heart rate, or respiratory sinus arrhythmia, has been used a clinical measure of cardiac health as well as understanding the interplay between sympathetic and parasympathetic drive regulating heart rate. Thus, similar to using hemodynamic measures to examine the effects of neuronal adaptation, heart rate variability can potentially be used as a measure to examine the effects of neuronal adaptation on parasympathetic drive.

v) Incorporating gene regulatory networks – this model provides insight into what potential changes in neuronal behavior in the brainstem affects vagal drive. In Chapter 4, a methodology and quantitative models were developed characterizing brainstem neurons. Integrating these two types of models would provide a

molecular perspective on the mechanisms that may be causing the gating effect that was exhibited by the NA and DMV neuronal populations.

REFERENCES

[1] G.M. Shepherd, The Synaptic Organization of the Brain, Oxford University Press, USA, 2004.

[2] J. Nolte, The Human Brain: An Introduction To Its Functional Anatomy, Sixth, Elsevier, New York, 1988.

[3] S.B. Nelson, K. Sugino, C.M. Hempel, The problem of neuronal cell types: a physiological genomics approach., Trends Neurosci. 29 (2006) 339–45. doi:10.1016/j.tins.2006.05.004.

[4] N.N. Parikshak, M.J. Gandal, D.H. Geschwind, Systems biology and gene networks in neurodevelopmental and neurodegenerative disorders, Nat. Rev. Genet. 16 (2015) 441–458. doi:10.1038/nrg3934.

[5] Y. Ko, S. a Ament, J. a Eddy, J. Caballero, J.C. Earls, L. Hood, N.D. Price, Cell type-specific genes show striking and distinct patterns of spatial expression in the mouse brain., Proc. Natl. Acad. Sci. U. S. A. 110 (2013) 3095–100. doi:10.1073/pnas.1222897110.

[6] T.I. Lee, R.A. Young, Transcriptional Regulation and Its Misregulation in Disease, Cell. 152 (2013) 1237–1251.

[7] M.H. Hastings, A.B. Reddy, E.S. Maywood, A clockwork web: circadian timing in brain and periphery, in health and disease, Nat. Rev. Neurosci. 4 (2003) 649–661. doi:10.1038/nrn1177.

[8] A. Maffei, A. Fontanini, Network homeostasis: a matter of coordination, Curr. Opin. Neurobiol. 19 (2009) 168–173. doi:10.1016/j.conb.2009.05.012.

[9] G.W. Davis, Homeostatic Signaling and the Stabilization of Neural Function, Neuron. 80 (2013) 718–728. doi:10.1016/j.neuron.2013.09.044.

[10] R. Yuste, The discovery of dendritic spines by Cajal., Front. Neuroanat. 9 (2015) 18. doi:10.3389/fnana.2015.00018.

[11] A.I. Chen, J.C. de Nooij, T.M. Jessell, Graded Activity of Transcription Factor Runx3 Specifies the Laminar Termination Pattern of Sensory Axons in the Developing Spinal Cord, Neuron. 49 (2006) 395–408.

[12] I. Kramer, M. Sigrist, J.C. de Nooij, I. Taniuchi, T.M. Jessell, S. Arber, A Role for Runx Transcription Factor Signaling in Dorsal Root Ganglion Sensory Neuron Diversification, Neuron. 49 (2006) 379–393.

[13] A. Friese, J.A. Kaltschmidt, D.R. Ladle, M. Sigrist, T.M. Jessell, S. Arber, Gamma and alpha motor neurons distinguished by expression of transcription factor Err3., Proc. Natl. Acad. Sci. U. S. A. 106 (2009) 13588–93. doi:10.1073/pnas.0906809106.

[14] D.C. Crawford, J.M. Acuña, S.L. Sherman, FMR1 and the fragile X syndrome: human genome epidemiology review., Genet. Med. 3 (2001) 359–371. doi:10.1097/00125817-200109000-00006.

[15] C. Landles, G.P. Bates, Huntingtin and the molecular pathogenesis of Huntington's disease. Fourth in molecular medicine review series., EMBO Rep. 5 (2004) 958–63. doi:10.1038/sj.embor.7400250.

[16] R.A.C. Roos, Huntington ' s disease : a clinical review, (2010) 2–9.

[17] M. Thattai, a van Oudenaarden, Intrinsic noise in gene regulatory networks., Proc. Natl. Acad. Sci. U. S. A. 98 (2001) 8614–9. doi:10.1073/pnas.151588598.

[18] M.A. Savageau, Design principles for elementary gene circuits: Elements, methods, and examples., Chaos. 11 (2001) 142–159. doi:10.1063/1.1349892.

[19] G.M. Miller, B.A. Ogunnaike, J.S. Schwaber, R. Vadigepalli, Robust dynamic balance of AP-1 transcription factors in a neuronal gene regulatory network., BMC Syst. Biol. 4 (2010) 171. doi:10.1186/1752-0509-4-171.

[20] D.E. Zak, R.K. Pearson, R. Vadigepalli, G.E. Gonye, J.S. Schwaber, F.J. Doyle, Continuous-time identification of gene expression models., OMICS. 7 (2003) 373–86. doi:10.1089/153623103322637689.

[21] J. Kim, J. Eberwine, RNA: state memory and mediator of cellular phenotype., Trends Cell Biol. 20 (2010) 311–8. doi:10.1016/j.tcb.2010.03.003.

[22] J. Eberwine, J.-Y. Sul, T. Bartfai, J. Kim, The promise of single-cell sequencing, Nat. Methods. 11 (2013) 25–27. doi:10.1038/nmeth.2769.

[23] S.D. Ginsberg, I. Elarova, M. Ruben, F. Tan, S.E. Counts, J.H. Eberwine, J.Q. Trojanowski, S.E. Hemby, E.J. Mufson, S. Che, Single-Cell Gene Expression Analysis: Implications for Neurodegenerative and Neuropsychiatric Disorders, Neurochem. Res. 29 (2004) 1053–1064. doi:10.1023/B:NERE.0000023593.77052.f7.

[24] B.M. Kadakkuzha, S. V Puthanveettil, Genomics and proteomics in solving brain complexity., Mol. Biosyst. 9 (2013) 1807–21. doi:10.1039/c3mb25391k.

[25] J. Eberwine, J. Kim, Cellular Deconstruction: Finding Meaning in Individual Cell Variation, Trends Cell Biol. 25 (2015) 569–578. doi:10.1016/j.tcb.2015.07.004.

[26] T. Enver, M. Pera, C. Peterson, P.W. Andrews, Stem cell states, fates, and the rules of attraction., Cell Stem Cell. 4 (2009) 387–97. doi:10.1016/j.stem.2009.04.011.

[27] J.P. Junker, A. van Oudenaarden, Every cell is special: genome-wide studies add a new dimension to single-cell biology., Cell. 157 (2014) 8–11. doi:10.1016/j.cell.2014.02.010.

[28] M.D. Adams, J.M. Kelly, J.D. Gocayne, M. Dubnick, M.H. Polymeropoulos, H. Xiao, C.R. Merril, A. Wu, B. Olde, R.F. Moreno, A.R. Kerlavage, W.R. McCombie, J.C. Venter, Complementary DNA sequencing: Expressed sequence tags and human genome project, Science (80-.). 252 (1991) 1651–1656.

[29] E.P. Consortium, An integrated encyclopedia of DNA elements in the human genome., Nature. 489 (2012) 57–74. doi:10.1038/nature11247.

[30] G. Guo, M. Huss, G.Q. Tong, C. Wang, L. Li Sun, N.D. Clarke, P. Robson, Resolution of cell fate decisions revealed by single-cell gene expression analysis from zygote to blastocyst., Dev. Cell. 18 (2010) 675–85. doi:10.1016/j.devcel.2010.02.012.

[31] R. Durruthy-Durruthy, A. Gottlieb, B.H. Hartman, J. Waldhaus, R.D. Laske, R. Altman, S. Heller, Reconstruction of the mouse otocyst and early neuroblast lineage at single-cell resolution, Cell. 157 (2014) 964–978. doi:10.1016/j.cell.2014.03.036.

[32] B. Treutlein, D.G. Brownfield, A.R. Wu, N.F. Neff, G.L. Mantalas, F.H. Espinoza, T.J. Desai, M.A. Krasnow, S.R. Quake, Reconstructing lineage hierarchies of the distal lung epithelium using single-cell RNA-seq, Nature. 509 (2014) 371–375. doi:10.1038/nature13173.

[33] V. Espina, J.D. Wulfkuhle, V.S. Calvert, A. VanMeter, W. Zhou, G. Coukos, D.H. Geho, E. Petricoin, L. Liotta, Laser-capture microdissection, Nat. Protoc. (2006) 586–603.

[34] H. Duale, H. Waki, P. Howorth, S. Kasparov, A.G. Teschemacher, J.F.R. Paton,

Restraining influence of A2 neurons in chronic control of arterial pressure in spontaneously hypertensive rats., Cardiovasc. Res. 76 (2007) 184–93. doi:10.1016/j.cardiores.2007.06.018.

[35] J.P. Card, S. Fitzpatrick-McElligott, I. Gozes, F. Baldino, Localization of vasopressin- , vasoactive intestinal polypeptide-, peptide histidine isoleucine- and somatostatin-mRNA in rat suprachiasmatic nucleus, Cell Tissue Res. 252 (1988) 307–315.

[36] J.P. Card, L. Rinaman, J.S. Schwaber, R.R. Miselis, M.E. Whealy, A.K. Robbins, L.W. Enquist, Neurotropic properties of pseudorabies virus: uptake and transneuronal passage in the rat central nervous system., J. Neurosci. 10 (1990) 1974–94.

[37] A. Standish, L.W. Enquist, J.S. Schwaber, Central Neuronal Circuit Transneuronal Transport Innervating the Rat Heart Defined by of Pseudorabies Virus, J. Neurosci. 15 (1995).

[38] J. Wang, M. Irnaten, R. a Neff, P. Venkatesan, C. Evans, a D. Loewy, T.C. Mettenleiter, D. Mendelowitz, Synaptic and neurotransmitter activation of cardiac vagal neurons in the nucleus ambiguus., Ann. N. Y. Acad. Sci. 940 (2001) 237–246. doi:10.1111/j.1749-6632.2001.tb03680.x.

[39] C. Bargmann, W. Newsome, D. Anderson, E. Brown, K. Deisseroth, J. Donoghue, P. MacLeish, E. Marder, R. Normann, J. Sanes, M. Schnitzer, T. Sejnowski, D. Tank, R. Tsien, K. Ugurbil, Brain 2025, A Scientific Vision, 2014.

[40] NIH RFA-MH-14-215, BRAIN Initiative: Transformative Approaches for Cell-Type Classification in the Brain (U01), (2013). http://grants.nih.gov/grants/guide/rfa-files/RFA-MH-14-215.html.

[41] OpenStax, Parts of the Nervous System, OpenStax CNX. (2015). https://cnx.org/contents/fb1b3b55-ef15-44f3-9d52-df597ba53b4d@6.

[42] P. Nemes, A.M. Knolhoff, S.S. Rubakhin, J. V. Sweedler, Single-cell metabolomics: Changes in the metabolome of freshly isolated and cultured neurons, ACS Chem. Neurosci. 3 (2012) 782–792. doi:10.1021/cn300100u.

[43] S.S. Rubakhin, E.J. Lanni, J. V. Sweedler, Progress toward single cell metabolomics, Curr. Opin. Biotechnol. 24 (2013) 95–104. doi:10.1016/j.copbio.2012.10.021.

[44] M. Jove, M. Portero-Otin, A. Naudi, I. Ferrer, R. Pamplona, Metabolomics of

Human Brain Aging and Age-Related Neurodegenerative Diseases, 73 (2014) 640–657.

[45] A. Bayés, S.G.N. Grant, Neuroproteomics: understanding the molecular organization and complexity of the brain., Nat. Rev. Neurosci. 10 (2009) 635–46. doi:10.1038/nrn2701.

[46] S.B. Nelson, C. Hempel, K. Sugino, Probing the transcriptome of neuronal cell types, Curr. Opin. Neurobiol. 16 (2006) 571–576. doi:10.1016/j.conb.2006.08.006.

[47] M.K. Shin, J.M. Levorse, R.S. Ingram, S.M. Tilghman, The temporal requirement for endothelin receptor-B signalling during neural crest development., Nature. 402 (1999) 496–501. doi:10.1038/990040.

[48] J. Jacob, C. Maurange, A.P. Gould, Temporal control of neuronal diversity: common regulatory principles in insects and vertebrates?, Development. 135 (2008) 3481–3489. doi:10.1242/dev.016931.

[49] J.S. Odorico, D.S. Kaufman, J. a Thomson, Multilineage differentiation from human embryonic stem cell lines., Stem Cells. 19 (2001) 193–204. doi:10.1634/stemcells.19-3-193.

[50] I. Muñoz-Sanjuán, A.H. Brivanlou, Neural Induction, The Default Model and Embryonic Stem Cells, 3 (2002) 1–10. doi:10.1038/nrn786.

[51] M. Mingueneau, T. Kreslavsky, D. Gray, T. Heng, R. Cruse, J. Ericson, S. Bendall, M.H. Spitzer, G.P. Nolan, K. Kobayashi, H. von Boehmer, D. Mathis, C. Benoist, A.J. Best, J. Knell, A. Goldrath, V. Jojic, D. Koller, T. Shay, A. Regev, N. Cohen, P. Brennan, M. Brenner, F. Kim, T.N. Rao, A. Wagers, K. Rothamel, A. Ortiz-Lopez, N. a Bezman, J.C. Sun, G. Min-Oo, C.C. Kim, L.L. Lanier, J. Miller, B. Brown, M. Merad, E.L. Gautier, C. Jakubzick, G.J. Randolph, P. Monach, D. a Blair, M.L. Dustin, S. a Shinton, R.R. Hardy, D. Laidlaw, J. Collins, R. Gazit, D.J. Rossi, N. Malhotra, K. Sylvia, J. Kang, A. Fletcher, K. Elpek, A. Bellemare-Pelletier, D. Malhotra, S. Turley, The transcriptional landscape of αβ T cell differentiation., Nat. Immunol. 14 (2013) 619–32. doi:10.1038/ni.2590.

[52] S.C. Bendall, E.F. Simonds, P. Qiu, E.D. Amir, P.O. Krutzik, R. Finck, R. V Bruggner, R. Melamed, A. Trejo, O.I. Ornatsky, R.S. Balderas, S.K. Plevritis, K. Sachs, D. Pe'er, S.D. Tanner, G.P. Nolan, Single-cell mass cytometry of differential immune and drug responses across a human hematopoietic continuum., Science. 332 (2011) 687–96. doi:10.1126/science.1198704.

[53] S.R. Hough, A.L. Laslett, S.B. Grimmond, G. Kolle, M.F. Pera, A continuum of cell states spans pluripotency and lineage commitment in human embryonic stem cells., PLoS One. 4 (2009) e7708. doi:10.1371/journal.pone.0007708.

[54] K.J. Mitchell, The genetics of brain wiring: from molecule to mind., PLoS Biol. 5 (2007) e113. doi:10.1371/journal.pbio.0050113.

[55] E. Pujadas, A.P. Feinberg, Regulated noise in the epigenetic landscape of development and disease., Cell. 148 (2012) 1123–31. doi:10.1016/j.cell.2012.02.045.

[56] C.H. Waddington, Canalization of Development and the Inheritance of Acquired Characters, Nat. Publ. Gr. (1942).

[57] C.H. Waddington, Principles of Embryology, New York :Macmillan, 1956.

[58] S. Huang, G. Eichler, Y. Bar-Yam, D.E. Ingber, Cell Fates as High-Dimensional Attractor States of a Complex Gene Regulatory Network, Phys. Rev. Lett. 94 (2005) 128701. doi:10.1103/PhysRevLett.94.128701.

[59] K. Takahashi, S. Yamanaka, Induction of Pluripotent Stem Cells from Mouse Embryonic and Adult Fibroblast Cultures by Defined Factors, Cell. 126 (2006) 663–676. doi:10.1016/j.cell.2006.07.024.

[60] J.-Y. Sul, C.K. Wu, F. Zeng, J. Jochems, M.T. Lee, T.K. Kim, T. Peritz, P. Buckley, D.J. Cappelleri, M. Maronski, M. Kim, V. Kumar, D. Meaney, J. Kim, J. Eberwine, Transcriptome transfer produces a predictable cellular phenotype., Proc. Natl. Acad. Sci. U. S. A. 106 (2009) 7624–9. doi:10.1073/pnas.0902161106.

[61] M. Toledo-Rodriguez, B. Blumenfeld, C. Wu, J. Luo, B. Attali, P. Goodman, H. Markram, Correlation maps allow neuronal electrical properties to be predicted from single-cell gene expression profiles in rat neocortex., Cereb. Cortex. 14 (2004) 1310–27. doi:10.1093/cercor/bhh092.

[62] T.K. Kim, J.-Y. Sul, N.B. Peternko, J.H. Lee, M. Lee, V. V Patel, J. Kim, J.H. Eberwine, Transcriptome transfer provides a model for understanding the phenotype of cardiomyocytes., Proc. Natl. Acad. Sci. U. S. A. 108 (2011) 11918–23. doi:10.1073/pnas.1101223108.

[63] D.K. Singh, C.-J. Ku, C. Wichaidit, R.J. Steininger, L.F. Wu, S.J. Altschuler, Patterns of basal signaling heterogeneity can distinguish cellular populations with different drug sensitivities., Mol. Syst. Biol. 6 (2010) 369. doi:10.1038/msb.2010.22.

[64] O.N. Suslov, V.G. Kukekov, T.N. Ignatova, D.A. Steindler, Neural stem cell heterogeneity demonstrated by molecular phenotyping of clonal neurospheres., Proc. Natl. Acad. Sci. U. S. A. 99 (2002) 14506–11. doi:10.1073/pnas.212525299.

[65] K.H. Narsinh, N. Sun, V. Sanchez-freire, A.S. Lee, P. Almeida, S. Hu, T. Jan, K.D. Wilson, D. Leong, J. Rosenberg, M. Yao, R.C. Robbins, J.C. Wu, Single cell transcriptional profiling reveals heterogeneity of human induced pluripotent stem cells, J. Clin. Invest. 121 (2011) 1217–1221. doi:10.1172/JCI44635DS1.

[66] L.H. Loo, H.J. Lin, D.K. Singh, K.M. Lyons, S.J. Altschuler, L.F. Wu, Heterogeneity in the physiological states and pharmacological responses of differentiating 3T3-L1 preadipocytes, J. Cell Biol. 187 (2009) 375–384. doi:10.1083/jcb.200904140.

[67] A. Ståhlberg, D. Andersson, J. Aurelius, M. Faiz, M. Pekna, M. Kubista, M. Pekny, Defining cell populations with single-cell gene expression profiling: correlations and identification of astrocyte subpopulations., Nucleic Acids Res. 39 (2011) e24. doi:10.1093/nar/gkq1182.

[68] D.G. Tang, Understanding cancer stem cell heterogeneity and plasticity, Cell Res. 22 (2012) 457–472. doi:10.1038/cr.2012.13.

[69] K. a Janes, C.-C. Wang, K.J. Holmberg, K. Cabral, J.S. Brugge, Identifying single-cell molecular programs by stochastic profiling., Nat. Methods. 7 (2010) 311–7. doi:10.1038/nmeth.1442.

[70] S.C. Bendall, G.P. Nolan, M. Roederer, P.K. Chattopadhyay, A deep profiler's guide to cytometry., Trends Immunol. 33 (2012) 323–32. doi:10.1016/j.it.2012.02.010.

[71] A.K. Shalek, R. Satija, X. Adiconis, R.S. Gertner, J.T. Gaublomme, R. Raychowdhury, S. Schwartz, N. Yosef, C. Malboeuf, D. Lu, J.J. Trombetta, D. Gennert, A. Gnirke, A. Goren, N. Hacohen, J.Z. Levin, H. Park, A. Regev, Single-cell transcriptomics reveals bimodality in expression and splicing in immune cells., Nature. 498 (2013) 236–40. doi:10.1038/nature12172.

[72] R. Satija, A.K. Shalek, Heterogeneity in immune responses: from populations to single cells, Trends Immunol. 35 (2014) 219–229. doi:10.1016/j.it.2014.03.004.

[73] R. Bahar, C.H. Hartmann, K. a Rodriguez, A.D. Denny, R. a Busuttil, M.E.T. Dollé, R.B. Calder, G.B. Chisholm, B.H. Pollock, C. a Klein, J. Vijg, Increased cell-to-cell variation in gene expression in ageing mouse heart., Nature. 441

(2006) 1011–1014. doi:10.1038/nature04844.

[74] S.J. Birren, E. Marder, Neuroscience. Plasticity in the neurotransmitter repertoire., Science. 340 (2013) 436–7. doi:10.1126/science.1238518.

[75] A. Ståhlberg, V. Rusnakova, A. Forootan, M. Anderova, M. Kubista, RT-qPCR work-flow for single-cell data analysis., Methods. 59 (2013) 80–8. doi:10.1016/j.ymeth.2012.09.007.

[76] A.K. White, M. VanInsberghe, O.I. Petriv, M. Hamidi, D. Sikorski, M.A. Marra, J. Piret, S. Aparicio, C.L. Hansen, High-throughput microfluidic single-cell RT-qPCR., Proc. Natl. Acad. Sci. U. S. A. 108 (2011) 13999–4004. doi:10.1073/pnas.1019446108.

[77] Q. Deng, D. Ramsköld, B. Reinius, R. Sandberg, Single-cell RNA-seq reveals dynamic, random monoallelic gene expression in mammalian cells., Science. 343 (2014) 193–6. doi:10.1126/science.1245316.

[78] L. Warren, D. Bryder, I.L. Weissman, S.R. Quake, Transcription factor profiling in individual hematopoietic progenitors by digital RT-PCR., Proc. Natl. Acad. Sci. U. S. A. 103 (2006) 17807–12. doi:10.1073/pnas.0608512103.

[79] R. Vadigepalli, P. Chakravarthula, D.E. Zak, J.S. Schwaber, G.E. Gonye, PAINT: a promoter analysis and interaction network generation tool for gene regulatory network identification., OMICS. 7 (2003) 235–52. doi:10.1089/153623103322452378.

[80] M. Ptashne, A. Gann, Genes and Signals, Cold Spring Harbor Press, Cold Spring Harbor, NY, 2002.

[81] W.P. Tansey, Transcriptional activation: risky business., Genes Dev. 15 (2001) 1045–50. doi:10.1101/gad.896501.

[82] T. Platt, and the Regulation of Gene Expression, 4310 (1986).

[83] H.H. McAdams, a Arkin, Stochastic mechanisms in gene expression., Proc. Natl. Acad. Sci. U. S. A. 94 (1997) 814–9.

[84] J.M. Raser, E.K. O'Shea, Noise in gene expression: origins, consequences, and control., Science. 309 (2005) 2010–3. doi:10.1126/science.1105891.

[85] E.M. Ozbudak, M. Thattai, I. Kurtser, A.D. Grossman, A. van Oudenaarden, Regulation of noise in the expression of a single gene., Nat. Genet. 31 (2002) 69–73. doi:10.1038/ng869.

[86] A. Raj, A. van Oudenaarden, Nature, nurture, or chance: stochastic gene expression and its consequences., Cell. 135 (2008) 216–26. doi:10.1016/j.cell.2008.09.050.

[87] D. Volfson, J. Marciniak, W.J. Blake, N. Ostroff, L.S. Tsimring, J. Hasty, Origins of extrinsic variability in eukaryotic gene expression., Nature. 439 (2006) 861–4. doi:10.1038/nature04281.

[88] N. Rosenfeld, J.W. Young, U. Alon, P.S. Swain, M.B. Elowitz, Gene regulation at the single-cell level, Sci. STKE. 307 (2005) 1962. doi:10.1126/science.1106914.

[89] A. Bar-Even, J. Paulsson, N. Maheshri, M. Carmi, E. O'Shea, Y. Pilpel, N. Barkai, Noise in protein expression scales with natural protein abundance., Nat. Genet. 38 (2006) 636–43. doi:10.1038/ng1807.

[90] U. Alon, An introduction to systems biology: design principles of biological circuits, CRC press, 2006.

[91] U. Alon, Network motifs: theory and experimental approaches., Nat. Rev. Genet. 8 (2007) 450–61. doi:10.1038/nrg2102.

[92] S. Hooshangi, R. Weiss, The effect of negative feedback on noise propagation in transcriptional gene networks, Chaos. 16 (2006). doi:10.1063/1.2208927.

[93] J. Eberwine, T. Bartfai, Single cell transcriptomics of hypothalamic warm sensitive neurons that control core body temperature and fever response Signaling asymmetry and an extension of chemical neuroanatomy., Pharmacol. Ther. 129 (2011) 241–59. doi:10.1016/j.pharmthera.2010.09.010.

[94] D. Usoskin, A. Furlan, S. Islam, H. Abdo, P. Lönnerberg, D. Lou, J. Hjerling-Leffler, J. Haeggström, O. Kharchenko, P. V Kharchenko, S. Linnarsson, P. Ernfors, Unbiased classification of sensory neuron types by large-scale single-cell RNA sequencing, Nat. Neurosci. 18 (2014) 145–153. doi:10.1038/nn.3881.

[95] I.M. Chiu, L.B. Barrett, E.K. Williams, D.E. Strochlic, S. Lee, A.D. Weyer, S. Lou, G.S. Bryman, D.P. Roberson, N. Ghasemlou, C. Piccoli, E. Ahat, V. Wang, E.J. Cobos, C.L. Stucky, Q. Ma, S.D. Liberles, C.J. Woolf, Transcriptional profiling at whole population and single cell levels reveals somatosensory neuron molecular diversity., Elife. 3 (2014) e04660. doi:10.7554/eLife.04660.

[96] D.J. Schulz, J.-M. Goaillard, E. Marder, Variable channel expression in identified single and electrically coupled neurons in different animals., Nat.

Neurosci. 9 (2006) 356–62. doi:10.1038/nn1639.

[97] S. Darmanis, S.A. Sloan, Y. Zhang, M. Enge, C. Caneda, L.M. Shuer, M.G. Hayden Gephart, B.A. Barres, S.R. Quake, A survey of human brain transcriptome diversity at the single cell level, Proc. Natl. Acad. Sci. 112 (2015) 201507125. doi:10.1073/pnas.1507125112.

[98] D.K. Welsh, D.E. Logothetis, M. Meister, S.M. Reppert, Individual neurons dissociated from rat suprachiasmatic nucleus express independently phased circadian firing rhythms., Neuron. 14 (1995) 697–706. doi:10.1016/0896-6273(95)90214-7.

[99] V. Rusnakova, P. Honsa, D. Dzamba, A. Ståhlberg, M. Kubista, M. Anderova, Heterogeneity of astrocytes: from development to injury - single cell gene expression., PLoS One. 8 (2013) e69734. doi:10.1371/journal.pone.0069734.

[100] E. Marder, A.L. Taylor, Multiple models to capture the variability in biological neurons and networks., Nat. Neurosci. 14 (2011) 133–8. doi:10.1038/nn.2735.

[101] C.I. Bargmann, E. Marder, From the connectome to brain function., Nat. Methods. 10 (2013) 483–90. doi:10.1038/nmeth.2451.

[102] H. Wichterle, D. Gifford, E. Mazzoni, Neuroscience. Mapping neuronal diversity one cell at a time., Science. 341 (2013) 726–7. doi:10.1126/science.1235884.

[103] D. Dulcis, P. Jamshidi, S. Leutgeb, N.C. Spitzer, Neurotransmitter switching in the adult brain regulates behavior., Science. 340 (2013) 449–53. doi:10.1126/science.1234152.

[104] A. De la Rossa, C. Bellone, B. Golding, I. Vitali, J. Moss, N. Toni, C. Lüscher, D. Jabaudon, In vivo reprogramming of circuit connectivity in postmitotic neocortical neurons., Nat. Neurosci. 16 (2013) 193–200. doi:10.1038/nn.3299.

[105] J. Park, A. Brureau, K. Kernan, A. Starks, S. Gulati, B. Ogunnaike, J. Schwaber, R. Vadigepalli, Inputs drive cell phenotype variability., Genome Res. (2014). doi:10.1101/gr.161802.113.

[106] J. Park, B. Ogunnaike, J. Schwaber, R. Vadigepalli, Identifying functional gene regulatory network phenotypes underlying single cell transcriptional variability, Prog. Biophys. Mol. Biol. 117 (2015) 87–98. doi:10.1016/j.pbiomolbio.2014.11.004.

[107] M.C. Andresen, D.L. Kunze, Nucleus tractus solitarius--gateway to neural

circulatory control., Annu. Rev. Physiol. 56 (1994) 93–116. doi:10.1146/annurev.ph.56.030194.000521.

[108] J.A. Mohawk, C.B. Green, J.S. Takahashi, Central and Peripheral Circadian Clocks in Mammals, Annu. Rev. Neurosci. 35 (2012) 445–462. doi:10.1146/annurev-neuro-060909-153128.

[109] L.C. Michelini, The NTS and integration of cardiovascular control during exercise in normotensive and hypertensive individuals., Curr. Hypertens. Rep. 9 (2007) 214–21.

[110] J.L. Seagard, C. Dean, F. a Hopp, Properties of NTS neurons receiving input from barosensitive receptors., Ann. N. Y. Acad. Sci. 940 (2001) 142–156.

[111] M. Takagishi, H. Waki, M. Bhuiyan, S. Gouraud, A. Kohsaka, H. Cui, T. Yamazaki, J.F.R. Paton, M. Maeda, IL-6 microinjected in the nucleus tractus solitarii attenuates cardiac baroreceptor reflex function in rats, Am. J. Physiol. Regul. Integr. Comp. Physiol. 298 (2010) R183–R190.

[112] M.J. McKinley, A.L. Albiston, A.M. Allen, M.L. Mathai, C.N. May, R.M. McAllen, B.J. Oldfield, F.A.O. Mendelsohn, S.Y. Chai, The brain renin-angiotensin system: location and physiological roles., Int. J. Biochem. Cell Biol. 35 (2003) 901–18.

[113] H. Waki, S.S. Gouraud, M.E.R. Bhuiyan, M. Takagishi, T. Yamazaki, A. Kohsaka, M. Maeda, Transcriptome of the NTS in exercise-trained spontaneously hypertensive rats: implications for NTS function and plasticity in regulating blood pressure., Physiol. Genomics. 45 (2013) 58–67. doi:10.1152/physiolgenomics.00074.2012.

[114] J.F. Paton, Y.W. Li, J.S. Schwaber, Response properties of baroreceptive NTS neurons., Ann. N. Y. Acad. Sci. 940 (2001) 157–68.

[115] R. Vadigepalli, G.E. Gonye, J.F.R. Paton, J.S. Schwaber, Adaptive transcriptional dynamics of A2 neurons and central cardiovascular control pathways., Exp. Physiol. 97 (2012) 462–8. doi:10.1113/expphysiol.2011.059790.

[116] L. Rinaman, Ascending projections from the caudal visceral nucleus of the solitary tract to brain regions involved in food intake and energy expenditure., Brain Res. 1350 (2010) 18–34. doi:10.1016/j.brainres.2010.03.059.

[117] V.S. Affleck, J.H. Coote, S. Pyner, The projection and synaptic organisation of NTS afferent connections with presympathetic neurons, GABA and nNOS

neurons in the paraventricular nucleus of the hypothalamus., Neuroscience. 219 (2012) 48–61. doi:10.1016/j.neuroscience.2012.05.070.

[118] S.K. Agarwal, F.R. Calaresu, Reciprocal connections between nucleus tractus solitarii and rostral ventrolateral medulla, Brain Res. 523 (1990) 305–308. doi:10.1016/0006-8993(90)91503-9.

[119] R.A. Dampney, J.W. Polson, Y. Hirooka, J. Horiuchi, Functional organization of brain pathways subserving the baroreceptor reflex: studies in conscious animals using immediate early gene expression., Cell Mol. Neurobilogy. 23 (2003) 597–616.

[120] C. Núñez, F. Martín, A. Földes, M. Luisa Laorden, K.J. Kovács, M. Victoria Milanés, Induction of FosB/ΔFosB in the brain stress system-related structures during morphine dependence and withdrawal, J. Neurochem. 114 (2010) 475–487. doi:10.1111/j.1471-4159.2010.06765.x.

[121] M. Miura, K. Takayama, J. Okada, Neuronal expression of Fos protein in the rat brain after baroreceptor stimulation., J. Auton. Nerv. Syst. 50 (1994) 31–43.

[122] Y.-W. Li, R.A.L. Dampney, Expression of fos-like protein in brain following sustained hypertension and hypotension in conscious rabbits, Neuroscience. 61 (1994) 613–634. doi:10.1016/0306-4522(94)90439-1.

[123] R.K. Chan, P.E. Sawchenko, Spatially and temporally differentiated patterns of c-fos expression in brainstem catecholaminergic cell groups induced by cardiovascular challenges in the rat., J. Comp. Neurol. 348 (1994) 433–60. doi:10.1002/cne.903480309.

[124] R.K.W. Chan, P.E. Sawchenko, Hemodynamic regulation of tyrosine hydroxylase messenger RNA in medullary catecholamine neurons: a c- fos-guided hybridization histochemical study, Neuroscience. 66 (1995) 377–390. doi:10.1016/0306-4522(94)00600-A.

[125] R.K. Chan, P.E. Sawchenko, Organization and transmitter specificity of medullary neurons activated by sustained hypertension: implications for understanding baroreceptor reflex circuitry., J. Neurosci. 18 (1998) 371–87.

[126] A. Machhada, N. Marina, A. Korsak, D.J. Stuckey, M.F. Lythgoe, A. V. Gourine, Origins of the vagal drive controlling left ventricular contractility, J. Physiol. 0 (2016) n/a-n/a. doi:10.1113/JP270984.

[127] D. Mendelowitz, Firing properties of identified parasympathetic cardiac neurons in nucleus ambiguus., Am. J. Physiol. 271 (1996) H2609–H2614.

[128] Z. Cheng, T.L. Powley, Nucleus ambiguus projections to cardiac ganglia of rat atria: an anterograde tracing study., J. Comp. Neurol. 424 (2000) 588–606.

[129] J.S. Schwaber, B.S. Kapp, G. Higgins, The origin and extent of direct amygdala projections to the region of the dorsal motor nucleus of the vagus and the nucleus of the solitary tract, Neurosci. Lett. 20 (1980) 15–20. doi:10.1016/0304-3940(80)90226-8.

[130] M.W. Chapleau, R. Sabharwal, Methods of assessing vagus nerve activity and reflexes, Heart Fail. Rev. 16 (2011) 109–127. doi:10.1007/s10741-010-9174-6.

[131] J.H. Coote, Myths and realities of the cardiac vagus., J. Physiol. 591 (2013) 4073–4085. doi:10.1113/jphysiol.2013.257758.

[132] J.F.X. Jones, Physiology : Vagal control of the rat heart Physiological Society Symposium – Vagal Control : From Axolotl to Man Vagal control of the rat heart, (2016) 797–801. doi:10.1113/eph8602269.

[133] M.A. Henson, B.A. Ogunnaike, J.S. Schwabert, F.J.D. I, The Baroreceptor Reflex: A Biological Control System with Applications in Chemical Process Control, Society. (1994) 2453–2466.

[134] T.N. Thrasher, Baroreceptors, baroreceptor unloading, and the long-term control of blood pressure., Am. J. Physiol. Regul. Integr. Comp. Physiol. 288 (2005) R819-27. doi:10.1152/ajpregu.00813.2004.

[135] B.S. Zanutto, M.E. Valentinuzzi, E.T. Segura, Neural set point for the control of arterial pressure: role of the nucleus tractus solitarius., Biomed. Eng. Online. 9 (2010) 4. doi:10.1186/1475-925X-9-4.

[136] D.J. Reis, The brain and hypertension: reflections on 35 years of inquiry into the neurobiology of the circulation., Circulation. 70 (1984) III31--45.

[137] J.W. Wright, J.W. Harding, The brain renin-angiotensin system: a diversity of functions and implications for CNS diseases., Pflugers Arch. 465 (2013) 133–51. doi:10.1007/s00424-012-1102-2.

[138] H. Waki, S.S. Gouraud, M. Maeda, M.K. Raizada, J.F.R. Paton, Contributions of vascular inflammation in the brainstem for neurogenic hypertension., Respir. Physiol. Neurobiol. (2011) 1–7. doi:10.1016/j.resp.2011.05.004.

[139] H. Waki, E.B. Hendy, C.C.T. Hindmarch, S. Gouraud, M. Toward, S. Kasparov, D. Murphy, J.F.R. Paton, Excessive leukotriene B4 in nucleus tractus solitarii is prohypertensive in spontaneously hypertensive rats., Hypertension.

61 (2013) 194–201. doi:10.1161/HYPERTENSIONAHA.112.192252.

[140] R.L. Khan, R. Vadigepalli, M.K. McDonald, R.F. Rogers, G.R. Gao, J.S. Schwaber, Dynamic transcriptomic response to acute hypertension in the nucleus tractus solitarius., Am. J. Physiol. Regul. Integr. Comp. Physiol. 295 (2008) R15-27. doi:10.1152/ajpregu.00152.2008.

[141] R.F. Rogers, J.F. Paton, J.S. Schwaber, NTS neuronal responses to arterial pressure and pressure changes in the rat NTS neuronal responses to arterial and pressure changes in the rat, Am J Physiol Regul Integr Comp Physiol. (1993) R1355–R1368.

[142] D.K. Welsh, J.S. Takahashi, S.A. Kay, Suprachiasmatic nucleus: cell autonomy and network properties., Annu. Rev. Physiol. 72 (2010) 551–77. doi:10.1146/annurev-physiol-021909-135919.

[143] J.M. Dragich, D.H. Loh, L.M. Wang, A.M. Vosko, T. Kudo, T.J. Nakamura, I.H. Odom, S. Tateyama, A. Hagopian, J. a. Waschek, C.S. Colwell, The role of the neuropeptides PACAP and VIP in the photic regulation of gene expression in the suprachiasmatic nucleus, Eur. J. Neurosci. 31 (2010) 864–875. doi:10.1111/j.1460-9568.2010.07119.x.

[144] C. Liu, S.M. Reppert, GABA synchronizes clock cells within the suprachiasmatic circadian clock., Neuron. 25 (2000) 123–128. doi:10.1016/S0896-6273(00)80876-4.

[145] M. Mieda, D. Ono, E. Hasegawa, H. Okamoto, K. Honma, S. Honma, T. Sakurai, Cellular Clocks in AVP Neurons of the SCN Are Critical for Interneuronal Coupling Regulating Circadian Behavior Rhythm, Neuron. 85 (2015) 1103–1116. doi:10.1016/j.neuron.2015.02.005.

[146] H.J. Romijn, A.A. Sluiter, C.W. Pool, J. Wortel, R.M. Buijs, Evidence from confocal fluorescence microscopy for a dense, reciprocal innervation between AVP-, somatostatin-, VIP/PHI-, GRP-, and VIP/PHI/GRP-immunoreactive neurons in the rat suprachiasmatic nucleus., Eur. J. Neurosci. 9 (1997) 2613–2623. doi:9517467.

[147] A.C. Liu, D.K. Welsh, C.H. Ko, H.G. Tran, E.E. Zhang, A. a. Priest, E.D. Buhr, O. Singer, K. Meeker, I.M. Verma, F.J. Doyle, J.S. Takahashi, S. a. Kay, Intercellular Coupling Confers Robustness against Mutations in the SCN Circadian Clock Network, Cell. 129 (2007) 605–616. doi:10.1016/j.cell.2007.02.047.

[148] E.E. Abrahamson, R.Y. Moore, Suprachiasmatic nucleus in the mouse: Retinal

innervation, intrinsic organization and efferent projections, Brain Res. 916 (2001) 172–191. doi:10.1016/S0006-8993(01)02890-6.

[149] H. Zhu, R. Vadigepalli, R. Rafferty, G.E. Gonye, D.R. Weaver, J.S. Schwaber, Integrative gene regulatory network analysis reveals light-induced regional gene expression phase shift programs in the mouse suprachiasmatic nucleus, PLoS One. 7 (2012). doi:10.1371/journal.pone.0037833.

[150] M.C. Antle, R. Silver, Orchestrating time: arrangements of the brain circadian clock, Trends Neurosci. 28 (2005) 145–151. doi:10.1016/j.tins.2005.01.003.

[151] M.U. Gillette, J.W. Mitchell, Signaling in the suprachiasmatic nucleus: selectively responsive and integrative, Cell Tissue Res. 309 (2002) 99–107. doi:10.1007/s00441-002-0576-1.

[152] R. Teclemariam-Mesbah, A. Kalsbeek, P. Pevet, R.M. Buijs, Direct vasoactive intestinal polypeptide-containing projection from the suprachiasmatic nucleus to spinal projecting hypothalamic paraventricular neurons, Brain Res. 748 (1997) 71–76. doi:10.1016/S0006-8993(96)01246-2.

[153] T.J. Bartness, C.K. Song, G.E. Demas, SCN efferents to peripheral tissues: implications for biological rhythms., J. Biol. Rhythms. 16 (2001) 196–204. doi:10.1177/074873040101600302.

[154] M. Sujino, K. Masumoto, S. Yamaguchi, G.T.J. van der Horst, H. Okamura, S.-I.T. Inouye, Suprachiasmatic nucleus grafts restore circadian behavioral rhythms of genetically arrhythmic mice, Curr. Biol. 13 (2003) 664–668.

[155] S.J. Kuhlman, R. Silver, J. Le Sauter, A. Bult-Ito, D.G. McMahon, Phase resetting light pulses induce Per1 and persistent spike activity in a subpopulation of biological clock neurons., J. Neurosci. 23 (2003) 1441–50. doi:23/4/1441 [pii].

[156] R. Araki, M. Nakahara, R. Fukumura, H. Takahashi, K. Mori, N. Umeda, M. Sujino, S.-I.T. Inouye, M. Abe, Identification of genes that express in response to light exposure and express rhythmically in a circadian manner in the mouse suprachiasmatic nucleus, Brain Res. 1098 (2006) 9–18. doi:10.1016/j.brainres.2006.04.096.

[157] M.H. Hastings, E.S. Maywood, A.B. Reddy, Two Decades of Circadian Time, J. Neuroendocrinol. 20 (2008) 812–819. doi:10.1111/j.1365-2826.2008.01715.x.

[158] V.M. Porterfield, H. Piontkivska, E.M. Mintz, Identification of novel light-

induced genes in the suprachiasmatic nucleus, BMC Neurosci. 8 (2007) 98. doi:10.1186/1471-2202-8-98.

[159] V.M. Porterfield, E.M. Mintz, Temporal patterns of light-induced immediate-early gene expression in the suprachiasmatic nucleus, Neurosci. Lett. 463 (2009) 70–73. doi:10.1016/j.neulet.2009.07.066.

[160] R.A.L. Dampney, Central mechanisms regulating coordinated cardiovascular and respiratory function during stress and arousal., Am. J. Physiol. Regul. Integr. Comp. Physiol. 309 (2015) R429-43. doi:10.1152/ajpregu.00051.2015.

[161] F.J. Doyle III, M. Henson, B.A. Ogunnaike, J.S. Schwaber, I. Rybak, Neuronal Modeling of the Baroreceptor Reflex with Applications in Process Modeling and Control, in: O. Omidvar, D.L. Elliot (Eds.), Neural Syst. Control, Academic Press, San Diego, 1997: pp. 87–122.

[162] G.A. Ordway, A. Szebeni, M.M. Duffourc, S. Dessus-Babus, K. Szebeni, Gene expression analyses of neurons, astrocytes, and oligodendrocytes isolated by laser capture microdissection from human brain: Detrimental effects of laboratory humidity, J. Neurosci. Res. 87 (2009) 2430–2438. doi:10.1002/jnr.22078.

[163] G.I. Murray, ed., Laser Capture Microdissection, Humana Press, Totowa, NJ, 2011. doi:10.1007/978-1-61779-163-5.

[164] J. Mojsilovic-Petrovic, M. Nesic, A. Pen, W. Zhang, D. Stanimirovic, Development of rapid staining protocols for laser-capture microdissection of brain vessels from human and rat coupled to gene expression analyses, J. Neurosci. Methods. 133 (2004) 39–48. doi:10.1016/j.jneumeth.2003.09.026.

[165] E. Kummari, S.X. Guo-Ross, J.B. Eells, Laser Capture Microdissection - A Demonstration of the Isolation of Individual Dopamine Neurons and the Entire Ventral Tegmental Area, J. Vis. Exp. (2015) 1–14. doi:10.3791/52336.

[166] N.L. Simone, R.F. Bonner, J.W. Gillespie, M.R. Emmert-Buck, L.A. Liotta, Laser-capture microdissection: Opening the microscopic frontier to molecular analysis, Trends Genet. 14 (1998) 272–276. doi:10.1016/S0168-9525(98)01489-9.

[167] B. Oktay, K. Sugino, S.B. Nelson, A quantitative Comparison of Cell-Type-Specific Microarray Gene Expression Profiling Methods in the Mouse Brain, PLoS One. (2011). http://www.plosone.org/article/fetchObject.action?uri=info%3Adoi%2F10.1371%2Fjournal.pone.0016493&representation=PDF.

[168] B. Tasic, V. Menon, T.N.T. Nguyen, T.T.K. Kim, T. Jarsky, Z. Yao, B.B. Levi, L.T. Gray, S.A. Sorensen, T. Dolbeare, D. Bertagnolli, J. Goldy, N. Shapovalova, S. Parry, C.C. Lee, K. Smith, A. Bernard, L. Madisen, S.M. Sunkin, M. Hawrylycz, C. Koch, H. Zeng, Z. Yao, C.C. Lee, N. Shapovalova, S. Parry, L. Madisen, S.M. Sunkin, M. Hawrylycz, C. Koch, H. Zeng, Adult mouse cortical cell taxonomy revealed by single cell transcriptomics, Nat. Neurosci. advance on (2016) 1–37. doi:10.1038/nn.4216.

[169] K. Freeman, M.M. Staehle, Z.H. Gümüş, R. Vadigepalli, G.E. Gonye, C.N. Nichols, B.A. Ogunnaike, J.B. Hoek, J.S. Schwaber, Rapid temporal changes in the expression of a set of neuromodulatory genes during alcohol withdrawal in the dorsal vagal complex: molecular evidence of homeostatic disturbance., Alcohol. Clin. Exp. Res. 36 (2012) 1688–700. doi:10.1111/j.1530-0277.2012.01791.x.

[170] K. Freeman, M.M. Staehle, R. Vadigepalli, G.E. Gonye, B.A. Ogunnaike, J.B. Hoek, J.S. Schwaber, Coordinated dynamic gene expression changes in the central nucleus of the amygdala during alcohol withdrawal., Alcohol. Clin. Exp. Res. 37 Suppl 1 (2013) E88-100. doi:10.1111/j.1530-0277.2012.01910.x.

[171] S.L. Spurgeon, R.C. Jones, R. Ramakrishnan, High throughput gene expression measurement with real time PCR in a microfluidic dynamic array., PLoS One. 3 (2008) e1662. doi:10.1371/journal.pone.0001662.

[172] S. Rozen, H. Skaletsky, Primer3 on the WWW for general users and for biologist programmers., Methods Mol. Biol. 132 (2000) 365–386. doi:10.1385/1-59259-192-2:365.

[173] J. Quackenbush, Microarray data normalization and transformation., Nat. Genet. 32 Suppl (2002) 496–501. doi:10.1038/ng1032.

[174] J. Vandesompele, K. De Preter, F. Pattyn, B. Poppe, N. Van Roy, A. De Paepe, F. Speleman, Accurate normalization of real-time quantitative RT-PCR data by geometric averaging of multiple internal control genes., Genome Biol. 3 (2002) RESEARCH0034.

[175] B.M. Bolstad, R. a Irizarry, M. Astrand, T.P. Speed, A comparison of normalization methods for high density oligonucleotide array data based on variance and bias., Bioinformatics. 19 (2003) 185–93.

[176] A. Bergkvist, V. Rusnakova, R. Sindelka, J.M.A. Garda, B. Sjögreen, D. Lindh, A. Forootan, M. Kubista, Gene expression profiling--Clusters of possibilities., Methods. 50 (2010) 323–35. doi:10.1016/j.ymeth.2010.01.009.

[177] K. Freeman, A. Brureau, R. Vadigepalli, M.M. Staehle, M.M. Brureau, G.E. Gonye, J.B. Hoek, D.C. Hooper, J.S. Schwaber, Temporal changes in innate immune signals in a rat model of alcohol withdrawal in emotional and cardiorespiratory homeostatic nuclei., J. Neuroinflammation. 9 (2012) 97. doi:10.1186/1742-2094-9-97.

[178] J.A. Warrington, A. Nair, M. Mahadevappa, M. Tsyganskaya, Comparison of human adult and fetal expression and identification of 535 housekeeping / maintenance genes Comparison of human adult and fetal expression and identification of 535 housekeeping / maintenance genes, Genomics, Physiol. 2 (2000) 143–147. doi:2/3/143 [pii].

[179] O. Thellin, W. Zorzi, B. Lakaye, B. De Borman, B. Coumans, G. Hennen, T. Grisar, A. Igout, E. Heinen, Housekeeping genes as internal standards: Use and limits, J. Biotechnol. 75 (1999) 291–295. doi:10.1016/S0168-1656(99)00163-7.

[180] C.L. Andersen, J.L. Jensen, T.F. Ørntoft, Normalization of real-time quantitative reverse transcription-PCR data: a model-based variance estimation approach to identify genes suited for normalization, applied to bladder and colon cancer data sets., Cancer Res. 64 (2004) 5245–50. doi:10.1158/0008-5472.CAN-04-0496.

[181] J. Gründemann, F. Schlaudraff, B. Liss, UV-laser microdissection and mRNA expression analysis of individual neurons from postmortem parkinson's disease brains, 2011. doi:10.1007/978-1-61779-163-5_30.

[182] J.K. Cleal, J.N. Shepherd, J.L. Shearer, K.D. Bruce, F.R. Cagampang, Sensitivity of housekeeping genes in the suprachiasmatic nucleus of the mouse brain to diet and the daily light-dark cycle, Brain Res. 1575 (2014) 72–77. doi:10.1016/j.brainres.2014.05.031.

[183] S. Westfall, A. Aguilar-Valles, V. Mongrain, G.N. Luheshi, N. Cermakian, Time-Dependent Effects of Localized Inflammation on Peripheral Clock Gene Expression in Rats, PLoS One. 8 (2013) 1–15. doi:10.1371/journal.pone.0059808.

[184] R. Santana, L.M. McGarry, C. Bielza, P. Larrañaga, R. Yuste, Classification of neocortical interneurons using affinity propagation., Front. Neural Circuits. 7 (2013) 185. doi:10.3389/fncir.2013.00185.

[185] M. Ringnér, What is principal component analysis ?, Nat. Biotechnol. 26 (2008) 303–304.

[186] C.E. Hart, L. Sharenbroich, B.J. Bornstein, D. Trout, B. King, E. Mjolsness,

B.J. Wold, A mathematical and computational framework for quantitative comparison and integration of large-scale gene expression data, Nucleic Acids Res. 33 (2005) 2580–2594. doi:10.1093/nar/gki536.

[187] A. Zeisel, A.B.M. Manchado, S. Codeluppi, P. Lönnerberg, G. La Manno, A. Juréus, S. Marques, Cell types in the mouse cortex and hippocampus revealed by single-cell RNA-seq, (2015) 1–8.

[188] M.E. Ross, X. Zhou, G. Song, S.A. Shurtleff, K. Girtman, W.K. Williams, H.-C. Liu, R. Mahfouz, S.C. Raimondi, N. Lenny, A. Patel, J.R. Downing, Classification of pediatric acute lymphoblastic leukemia by gene expression profiling., Blood. 102 (2003) 2951–9. doi:10.1182/blood-2003-01-0338.

[189] Y.-H. Taguchi, Y. Oono, Relational patterns of gene expression via non-metric multidimensional scaling analysis., Bioinformatics. 21 (2005) 730–40. doi:10.1093/bioinformatics/bti067.

[190] G.N. Fuller, K.R. Hess, C.H. Rhee, W.K.A. Yung, R.A. Sawaya, J.M. Bruner, W. Zhang, Molecular Classification of Human Diffuse Gliomas by Multidimensional Scaling Analysis of Gene Expression Profiles Parallels Morphology-Based Classification, Correlates with Survival, and Reveals Clinically-Relevant Novel Glioma Subsets, Brain Pathol. 12 (2006) 108–116. doi:10.1111/j.1750-3639.2002.tb00427.x.

[191] L. Van Der Maaten, G. Hinton, Visualizing Data using t-SNE, J. Mach. Learn. Res. 9 (2008) 2579–2605. doi:10.1007/s10479-011-0841-3.

[192] E.D. Amir, K.L. Davis, M.D. Tadmor, E.F. Simonds, J.H. Levine, S.C. Bendall, D.K. Shenfeld, S. Krishnaswamy, G.P. Nolan, D. Pe'er, viSNE enables visualization of high dimensional single-cell data and reveals phenotypic heterogeneity of leukemia., Nat. Biotechnol. 31 (2013) 545–52. doi:10.1038/nbt.2594.

[193] A. Mahfouz, M. van de Giessen, L. van der Maaten, S. Huisman, M. Reinders, M.J. Hawrylycz, B.P.F. Lelieveldt, Visualizing the spatial gene expression organization in the brain through non-linear similarity embeddings, Methods. 73 (2015) 79–89. doi:10.1016/j.ymeth.2014.10.004.

[194] P. Qiu, E.F. Simonds, S.C. Bendall, K.D. Gibbs, R. V Bruggner, M.D. Linderman, K. Sachs, G.P. Nolan, S.K. Plevritis, Extracting a cellular hierarchy from high-dimensional cytometry data with SPADE, Nat. Biotechnol. 29 (2011) 886–891. doi:10.1038/nbt.1991.

[195] R. Sánchez-Alvarez, S. Gayen, R. Vadigepalli, H. Anni, Ethanol diverts early

neuronal differentiation trajectory of embryonic stem cells by disrupting the balance of lineage specifiers., PLoS One. 8 (2013) e63794. doi:10.1371/journal.pone.0063794.

[196] P.M. Magwene, P. Lizardi, J. Kim, Reconstructing the temporal ordering of biological samples using microarray data, Bioinformatics. 19 (2003) 842–850. doi:10.1093/bioinformatics/btg081.

[197] C. Trapnell, D. Cacchiarelli, J. Grimsby, P. Pokharel, S. Li, M. Morse, N.J. Lennon, K.J. Livak, T.S. Mikkelsen, J.L. Rinn, The dynamics and regulators of cell fate decisions are revealed by pseudotemporal ordering of single cells., Nat. Biotechnol. 32 (2014) 381–6. doi:10.1038/nbt.2859.

[198] M.E.J. Newman, Finding community structure in networks using the eigenvectors of matrices, Phys. Rev. E. 74 (2006) 36104. doi:10.1103/PhysRevE.74.036104.

[199] J. Saez-Rodriguez, L.G. Alexopoulos, J. Epperlein, R. Samaga, D. a Lauffenburger, S. Klamt, P.K. Sorger, Discrete logic modelling as a means to link protein signalling networks with functional analysis of mammalian signal transduction., Mol. Syst. Biol. 5 (2009) 331. doi:10.1038/msb.2009.87.

[200] S. Bulashevska, R. Eils, Inferring genetic regulatory logic from expression data., Bioinformatics. 21 (2005) 2706–13. doi:10.1093/bioinformatics/bti388.

[201] N. Friedman, M. Linial, I. Nachman, D. Pe'er, Using Bayesian networks to analyze expression data., J. Comput. Biol. 7 (2000) 601–20. doi:10.1089/106652700750050961.

[202] B.W. Kunkle, C. Yoo, D. Roy, Reverse engineering of modified genes by Bayesian network analysis defines molecular determinants critical to the development of glioblastoma., PLoS One. 8 (2013) e64140. doi:10.1371/journal.pone.0064140.

[203] N. Friedman, Inferring cellular networks using probabilistic graphical models., Science. 303 (2004) 799–805. doi:10.1126/science.1094068.

[204] K. Basso, A.A. Margolin, G. Stolovitzky, U. Klein, R. Dalla-Favera, A. Califano, Reverse engineering of regulatory networks in human B cells., Nat. Genet. 37 (2005) 382–90. doi:10.1038/ng1532.

[205] A.A. Margolin, I. Nemenman, K. Basso, C. Wiggins, G. Stolovitzky, R. Dalla Favera, A. Califano, ARACNE: an algorithm for the reconstruction of gene regulatory networks in a mammalian cellular context., BMC Bioinformatics. 7

Suppl 1 (2006) S7. doi:10.1186/1471-2105-7-S1-S7.

[206] P.D. Potts, J.W. Polson, Y. Hirooka, R.A.L. Dampney, Effects of Sinoaortic Denervation on Fos Expression in the Brain Evoked by Hypertension and Hypotension in Conscious Rabbits, Neuroscience. 77 (1997) 503–520. doi:10.1016/S0306-4522(96)00459-9.

[207] R.K.W. Chan, E.V. Jarvina, P.E. Sawchenko, Effects of selective sinoaortic denervations on phenylephrine-induced activational responses in the nucleus of the solitary tract, Neuroscience. 101 (2000) 165–178. doi:10.1016/S0306-4522(00)00332-8.

[208] Y. Li, N. Zealand, W. Correspondence, Expression of c-fos protein in the medulla oblongata of conscious rabbits in response to baroreceptor activation, 144 (1992) 70–74.

[209] M.J. Glass, J. Chan, K.A. Frys, M. Oselkin, M.J. Tarsitano, C. Iadecola, V.M. Pickel, Changes in the subcellular distribution of NADPH oxidase subunit p47phox in dendrites of rat dorsomedial nucleus tractus solitarius neurons in response to chronic administration of hypertensive agents., Exp. Neurol. 205 (2007) 383–95. doi:10.1016/j.expneurol.2007.02.016.

[210] L. Rinaman, Hindbrain noradrenergic A2 neurons: diverse roles in autonomic, endocrine, cognitive, and behavioral functions., Am. J. Physiol. Regul. Integr. Comp. Physiol. 300 (2011) R222-35. doi:10.1152/ajpregu.00556.2010.

[211] J.Y.H. Chan, W.-C. Chen, H.-Y. Lee, S.H.H. Chan, Elevated Fos Expression in the Nucleus Tractus Solitarii Is Associated With Reduced Baroreflex Response in Spontaneously Hypertensive Rats, Hypertension. 32 (1998) 939–944. doi:10.1161/01.HYP.32.5.939.

[212] J.C. Graham, G.E. Hoffman, A.F. Sved, c-Fos expression in brain in response to hypotension and hypertension in conscious rats, J. Auton. Nerv. Syst. 55 (1995) 92–104. doi:10.1016/0165-1838(95)00032-S.

[213] C.-D. Shih, S.H.H. Chan, J.Y.H. Chan, Participation of Fos protein at the nucleus tractus solitarius in inhibitory modulation of baroreceptor reflex response in the rat, Brain Res. 738 (1996) 39–47.

[214] J. Wang, H. Zheng, X. Ou, L.M. Fink, M. Hauer-Jensen, Deficiency of Microvascular Thrombomodulin and Up-Regulation of Protease-Activated Receptor-1 in Irradiated Rat Intestine, Am. J. Pathol. 160 (2002) 2063–2072.

[215] P. Ye, R. Bagnell, A.J. D'Ercole, Mouse NG2+ Oligodendrocyte Precursors

Express mRNA for Proteolipid Protein But Not Its DM-20 Variant: A Study of Laser Microdissection-Captured NG2+ Cells, J. Neurosci. 23 (2003) 4401–4405.

[216] W. Zhang, J. Mojsilovic-Petrovic, M.F. Andrade, H. Zhang, M. Ball, D.B. Stanimirovic, The expression and functional characterization of ABCG2 in brain endothelial cells and vessels., FASEB J. 17 (2003) 2085–7. doi:10.1096/fj.02-1131fje.

[217] J.A. Macdonald, N. Murugesan, J.S. Pachter, Validation of immuno-laser capture microdissection coupled with quantitative RT-PCR to probe blood–brain barrier gene expression in situ, J. Neurosci. Methods. 174 (2008) 219–226.

[218] W. Stacklies, H. Redestig, M. Scholz, D. Walther, J. Selbig, pcaMethods -- a Bioconductor package providing PCA methods for incomplete data, Bioinformatics. 23 (2007) 1164–1167.

[219] R Core Team, R: A Language and Environment for Statistical Computing, (2013).

[220] W.N. Venables, B.D. Ripley, Modern Applied Statistics with S, Fourth, Springer, New York, 2002.

[221] J. Lemon, Plotrix: a package in the red light district of R, R-News. 6 (2006) 8–12.

[222] D. Adler, D. Murdoch, rgl: 3D visualization device system (OpenGL), (2013).

[223] M.E. Ross, X. Zhou, G. Song, S. a Shurtleff, K. Girtman, W.K. Williams, H.-C. Liu, R. Mahfouz, S.C. Raimondi, N. Lenny, A. Patel, J.R. Downing, Classification of pediatric acute lymphoblastic leukemia by gene expression profiling., Blood. 102 (2003) 2951–9. doi:10.1182/blood-2003-01-0338.

[224] G.N. Fuller, K.R. Hess, C.H. Rhee, W.K.A. Yung, R. a Sawaya, J.M. Bruner, W. Zhang, Molecular classification of human diffuse gliomas by multidimensional scaling analysis of gene expression profiles parallels morphology-based classification, correlates with survival, and reveals clinically-relevant novel glioma subsets., Brain Pathol. 12 (2002) 108–16.

[225] M.D. Dogan, C. Sumners, C.S. Broxson, N. Clark, N. Tümer, Central angiotensin II increases biosynthesis of tyrosine hydroxylase in the rat adrenal medulla, Biochem. Biophys. Res. Commun. 313 (2004) 623–626.

[226] E.M. Richards, M.K. Raizada, C.H. Gelband, C. Sumners, Angiotensin II type 1 receptor-modulated signaling pathways in neurons., Mol. Neurobiol. 19 (1999) 25–41. doi:10.1007/BF02741376.

[227] D. Lu, H. Yang, M.K. Raizada, Angiotensin II regulation of neuromodulation: downstream signaling mechanism from activation of mitogen-activated protein kinase., J. Cell Biol. 135 (1996) 1609–17.

[228] S. Gallinat, Gene Expression Profiling of Rat Brain Neurons Reveals Angiotensin II-Induced Regulation of Calmodulin and Synapsin I: Possible Role in Neuromodulation, Endocrinology. 142 (2001) 1009–1016. doi:10.1210/en.142.3.1009.

[229] T. Stadler, A. Veltmar, F. Qadri, T. Unger, Angiotensin II evokes noradrenaline release from the paraventricular nucleus in conscious rats, 1992.

[230] A. Blume, T. Herdegen, T. Unger, Angiotensin peptides and inducible transcription factors, J. Mol. Med. 77 (1999) 339–357. doi:10.1007/s001090050360.

[231] F. Qadri, E. Badoer, T. Stadler, T. Unger, Angiotensin II-induced noradrenaline release from anterior hypothalamus in conscious rats: a brain microdialysis study, Brain Res. 563 (1991) 137–141.

[232] S. Tay, J.J. Hughey, T.K. Lee, T. Lipniacki, S.R. Quake, M.W. Covert, Single-cell NF-kappaB dynamics reveal digital activation and analogue information processing., Nature. 466 (2010) 267–71. doi:10.1038/nature09145.

[233] C.-L. Chen, D.C. Broom, Y. Liu, J.C. de Nooij, Z. Li, C. Cen, O.A. Samad, T.M. Jessell, C.J. Woolf, Q. Ma, Runx1 determines nociceptive sensory neuron phenotype and is required for thermal and neuropathic pain., Neuron. 49 (2006) 365–77. doi:10.1016/j.neuron.2005.10.036.

[234] L. Luo, G. Fishell, S.A.D.T. di Sanguinetto, J.S. Dasen, S. Arber, Transcriptional mechanisms controlling motor neuron diversity and connectivity, Curr. Opin. Neurobiol. 18 (2008) 36–43.

[235] R.A.L. Dampney, J. Horiuchi, Functional organisation of central cardiovascular pathways: studies using c-fos gene expression, Prog. Neurobiol. 71 (2003) 359–384. doi:10.1016/j.pneurobio.2003.11.001.

[236] H. Grill, M. Hayes, Hindbrain neurons as an essential hub in the neuroanatomically distributed control of energy balance., Cell Metab. 16 (2012) 296–309.

[237] J.F. Paton, Convergence properties of solitary tract neurones driven synaptically by cardiac vagal afferents in the mouse., J. Physiol. 508 (Pt 1 (1998) 237–52.

[238] R.F. Rogers, W.C. Rose, J.S. Schwaber, R.F. Rogers, C. Rose, J.S. Schwaber, Simultaneous encoding of carotid sinus pressure and dP / dt by NTS target neurons of myelinated baroreceptors Simultaneous Encoding of Carotid Sinus Pressure and dP / dt by NTS Target Neurons of Myelinated aroreceptors, J Neurophysiol. 76 (1996) 2644–2660.

[239] B. Zhang, S. Horvath, A general framework for weighted gene co-expression network analysis., Stat. Appl. Genet. Mol. Biol. 4 (2005) Article17. doi:10.2202/1544-6115.1128.

[240] B. Schwanhäusser, D. Busse, N. Li, G. Dittmar, J. Schuchhardt, J. Wolf, W. Chen, M. Selbach, Global quantification of mammalian gene expression control., Nature. 473 (2011) 337–42. doi:10.1038/nature10098.

[241] Y. Buganim, D. a Faddah, A.W. Cheng, E. Itskovich, S. Markoulaki, K. Ganz, S.L. Klemm, A. van Oudenaarden, R. Jaenisch, Single-cell expression analyses during cellular reprogramming reveal an early stochastic and a late hierarchic phase., Cell. 150 (2012) 1209–22. doi:10.1016/j.cell.2012.08.023.

[242] A.J. Butte, P. Tamayo, D. Slonim, T.R. Golub, I.S. Kohane, Discovering functional relationships between RNA expression and chemotherapeutic susceptibility using relevance networks., Proc. Natl. Acad. Sci. U. S. A. 97 (2000) 12182–6. doi:10.1073/pnas.220392197.

[243] P.J. Woolf, Y. Wang, M.R. Aniba, S. Siguenza, A. Friedrich, F. Plewniak, A. Marchler-bauer, J.D. Thompson, A fuzzy logic approach to analyzing gene expression data A fuzzy logic approach to analyzing gene expression data, Physiol. Genomics. 3 (2000) 9–15.

[244] G.N. Brock, W.D. Beavis, L.S. Kubatko, Fuzzy logic and related methods as a screening tool for detecting gene regulatory networks, Inf. Fusion. 10 (2009) 250–259. doi:10.1016/j.inffus.2008.11.008.

[245] B.A. Sokhansanj, J.P. Fitch, J.N. Quong, A.A. Quong, Linear fuzzy gene network models obtained from microarray data by exhaustive search., BMC Bioinformatics. 5 (2004) 108. doi:10.1186/1471-2105-5-108.

[246] S. Zhang, G. Jin, X.-S. Zhang, L. Chen, Discovering functions and revealing mechanisms at molecular level from biological networks., Proteomics. 7 (2007) 2856–69. doi:10.1002/pmic.200700095.

[247] R.M. Tong, A Control Engineering Review of Fuzzy Systems*, Automatica. 13 (1977) 559–569.

[248] L.A. Zadeh, Fuzzy sets, Inf. Control. 8 (1965) 338–353.

[249] T.L. Seng, M. Bin Khalid, R. Yusof, Tuning of a neuro-fuzzy controller by genetic algorithm., IEEE Trans. Syst. Man. Cybern. B. Cybern. 29 (1999) 226–36. doi:10.1109/3477.752795.

[250] H. Ying, A general technique for deriving analytical structure of fuzzy controllers using arbitrary trapezoidal input fuzzy sets and Zadeh AND operator, Automatica. 39 (2003) 1171–1184. doi:10.1016/S0005-1098(03)00086-4.

[251] R. Linden, A. Bhaya, Evolving fuzzy rules to model gene expression., Biosystems. 88 (2007) 76–91. doi:10.1016/j.biosystems.2006.04.006.

[252] H. Ressom, D. Wang, R.S. Varghese, R. Reynolds, Fuzzy logic-based gene regulatory network, 12th IEEE Int. Conf. Fuzzy Syst. 2003. FUZZ '03. 2 (2003) 1210–1215. doi:10.1109/FUZZ.2003.1206604.

[253] H. Ressom, R. Reynolds, R.S. Varghese, Increasing the efficiency of fuzzy logic-based gene expression data analysis., Physiol. Genomics. 13 (2003) 107–17. doi:10.1152/physiolgenomics.00097.2002.

[254] Y. Jin, Fuzzy modeling of high-dimensional systems: complexity reduction and interpretability improvement, IEEE Trans. Fuzzy Syst. 8 (2000) 212–221. doi:10.1109/91.842154.

[255] Y. Jin, S. Member, B. Sendhoff, Evolving in silico Bistable and Oscillatory Dynamics for Gene Regulatory Network Motifs, (2008) 386–391.

[256] M. Martínez-Ballesteros, I.A. Nepomuceno-Chamorro, J.C. Riquelme, Discovering gene association networks by multi-objective evolutionary quantitative association rules, J. Comput. Syst. Sci. 80 (2014) 118–136. doi:10.1016/j.jcss.2013.03.010.

[257] A. Schatten, Genetic Algorithm Tutorial, (2002). http://www.cs.ucdavis.edu/~vemuri/classes/ecs271/Genetic Algorithms Short Tutorial.htm.

[258] M. Mitchell, An introduction to genetic algorithms, MIT press, 1998.

[259] M.K. Morris, J. Saez-Rodriguez, D.C. Clarke, P.K. Sorger, D. a Lauffenburger,

Training signaling pathway maps to biochemical data with constrained fuzzy logic: quantitative analysis of liver cell responses to inflammatory stimuli., PLoS Comput. Biol. 7 (2011) e1001099. doi:10.1371/journal.pcbi.1001099.

[260] C. Trapnell, B.A. Williams, G. Pertea, A. Mortazavi, G. Kwan, M.J. van Baren, S.L. Salzberg, B.J. Wold, L. Pachter, Transcript assembly and quantification by RNA-Seq reveals unannotated transcripts and isoform switching during cell differentiation., Nat. Biotechnol. 28 (2010) 511–5. doi:10.1038/nbt.1621.

[261] L. Zadeh, Fuzzy logic, Scholarpedia. 3 (2008) 1766. doi:10.4249/scholarpedia.1766.

[262] Y. Jin, L. Wang, eds., Fuzzy Systems in Bioinformatics and Computational Biology, Springer Berlin Heidelberg, Berlin, Heidelberg, 2009. doi:10.1007/978-3-540-89968-6.

[263] S.G. Johnson, The NLopt nonlinear-optimization package, (2008).

[264] D. Marbach, C. Mattiussi, D. Floreano, Combining multiple results of a reverse-engineering algorithm: application to the DREAM five-gene network challenge., Ann. N. Y. Acad. Sci. 1158 (2009) 102–13. doi:10.1111/j.1749-6632.2008.03945.x.

[265] S. Datta, B. a Sokhansanj, Accelerated search for biomolecular network models to interpret high-throughput experimental data., BMC Bioinformatics. 8 (2007) 258. doi:10.1186/1471-2105-8-258.

[266] P. Shannon, A. Markiel, O. Ozier, N.S. Baliga, J.T. Wang, D. Ramage, N. Amin, B. Schwikowski, T. Ideker, Cytoscape: a software environment for integrated models of biomolecular interaction networks., Genome Res. 13 (2003) 2498–504. doi:10.1101/gr.1239303.

[267] A.K. Mitra, L. Gao, I.H. Zucker, Angiotensin II-induced upregulation of AT 1 receptor expression : sequential activation of NF- B and Elk-1 in neurons, (2010) 561–569. doi:10.1152/ajpcell.00127.2010.

[268] C. Sumners, M.A. Fleegal, M. Zhu, Experimental Biology 2001 Symposium Neurotransmitters in Cardiovascular Regulation : Angiotensin ANGIOTENSIN AT 1 RECEPTOR SIGNALLING PATHWAYS IN NEURONS, (2002) 483–490.

[269] S.J. Veerasingham, M.K. Raizada, Brain renin-angiotensin system dysfunction in hypertension: recent advances and perspectives., Br. J. Pharmacol. 139 (2003) 191–202. doi:10.1038/sj.bjp.0705262.

[270] P.K. Mehta, K.K. Griendling, Angiotensin II cell signaling : physiological and pathological effects in the cardiovascular system, (2007) 82–97. doi:10.1152/ajpcell.00287.2006.

[271] R. Kvetnansky, E.L. Sabban, M. Palkovits, Catecholaminergic Systems in Stress : Structural and Molecular Genetic Approaches, (2009) 535–606. doi:10.1152/physrev.00042.2006.

[272] T. Herdegen, J.D. Leah, Inducible and constitutive transcription factors in the mammalian nervous system: control of gene expression by Jun, Fos and Krox, and CREB/ATF proteins, Brain Res. Rev. 28 (1998) 370–490. doi:10.1016/S0165-0173(98)00018-6.

[273] M. Karin, Z. Liu, E. Zandi, AP-1 function and regulation, Curr. Opin. Cell Biol. 9 (1997) 240–246. doi:10.1016/S0955-0674(97)80068-3.

[274] L.M. Luttrell, R.J. Lefkowitz, The role of beta-arrestins in the termination and transduction of G-protein-coupled receptor signals., J. Cell Sci. 115 (2002) 455–65.

[275] J.D. Violin, S.M. Dewire, W.G. Barnes, R.J. Lefkowitz, G protein-coupled receptor kinase and beta-arrestin-mediated desensitization of the angiotensin II type 1A receptor elucidated by diacylglycerol dynamics., J. Biol. Chem. 281 (2006) 36411–9. doi:10.1074/jbc.M607956200.

[276] H. Zhong, R.R. Neubig, Regulator of G protein signaling proteins: novel multifunctional drug targets., J. Pharmacol. Exp. Ther. 297 (2001) 837–45.

[277] B. Gasnier, The SLC32 transporter, a key protein for the synaptic release of inhibitory amino acids., Pflugers Arch. 447 (2004) 756–9. doi:10.1007/s00424-003-1091-2.

[278] T. Melander, A. Riikaeus, A.C. Cuello, W.H. Oertel, A. Verhofstad, Coexistence of Galanin-like lmmunoreactivity with Catecholamines , GABA and Neuropeptides in the Rat CNS, 6 (1986) 3640–3654.

[279] Y. Marc, C. Llorens-Cortes, The role of the brain renin-angiotensin system in hypertension: implications for new treatment., Prog. Neurobiol. 95 (2011) 89–103. doi:10.1016/j.pneurobio.2011.06.006.

[280] M.E. Hall, F.B. Miley, J.M. Stewart, Cardiovascular effects of substance P peptides in the nucleus of the solitary tract, Brain Res. 497 (1989) 280–290. doi:10.1016/0006-8993(89)90273-4.

[281] D.W. Lambert, N.E. Clarke, A.J. Turner, Not just angiotensinases: new roles for the angiotensin-converting enzymes., Cell. Mol. Life Sci. 67 (2010) 89–98. doi:10.1007/s00018-009-0152-x.

[282] D. Pe'er, N. Hacohen, Principles and strategies for developing network models in cancer., Cell. 144 (2011) 864–73. doi:10.1016/j.cell.2011.03.001.

[283] Y. Buganim, D. a Faddah, A.W. Cheng, E. Itskovich, S. Markoulaki, K. Ganz, S.L. Klemm, A. van Oudenaarden, R. Jaenisch, Single-cell expression analyses during cellular reprogramming reveal an early stochastic and a late hierarchic phase., Cell. 150 (2012) 1209–22. doi:10.1016/j.cell.2012.08.023.

[284] A.A. Cohen, N. Geva-Zatorsky, E. Eden, M. Frenkel-Morgenstern, I. Issaeva, A. Sigal, R. Milo, C. Cohen-Saidon, Y. Liron, Z. Kam, L. Cohen, T. Danon, N. Perzov, U. Alon, Dynamic proteomics of individual cancer cells in response to a drug., Science. 322 (2008) 1511–6. doi:10.1126/science.1160165.

[285] K.T. Flaherty, I. Puzanov, K.B. Kim, A. Ribas, G.A. McArthur, J. Sosman, P.J. O'Dwyer, R.J. Lee, J.F. Grippo, D. Ph, K. Nolop, P.B. Chapman, Inhibition of mutated, activated BRAF in metastatic melanoma, N. Engl. J. Med. 363 (2010) 809–819.

[286] P.I. Poulikakos, C. Zhang, G. Bollag, K.M. Shokat, N. Rosen, RAF inhibitors transactivate RAF dimers and ERK signalling in cells with wild-type BRAF., Nature. 464 (2010) 427–30. doi:10.1038/nature08902.

[287] S. Bandyopadhyay, M. Mehta, D. Kuo, M.-K. Sung, R. Chuang, E.J. Jaehnig, B. Bodenmiller, K. Licon, W. Copeland, M. Shales, D. Fiedler, J. Dutkowski, A. Guénolé, H. van Attikum, K.M. Shokat, R.D. Kolodner, W.-K. Huh, R. Aebersold, M.-C. Keogh, N.J. Krogan, T. Ideker, Rewiring of genetic networks in response to DNA damage., Science. 330 (2010) 1385–9. doi:10.1126/science.1195618.

[288] D. DeCicco, H. Zhu, A. Brureau, J.S. Schwaber, R. Vadigepalli, Dynamic regulation of microRNA networks in the brainstem underlie hypertension development, in: Exp. Biol., 2014.

[289] E. Magosso, S. Cavalcanti, M. Ursino, Theoretical analysis of rest and exercise hemodynamics in patients with total cavopulmonary connection., Am. J. Physiol. Heart Circ. Physiol. 282 (2002) H1018-34. doi:10.1152/ajpheart.00231.2001.

[290] M. Ursino, M. Antonucci, E. Belardinelli, Role of active changes in venous capacity by the carotid baroreflex: analysis with a mathematical model., Am. J.

Physiol. 267 (1994) H2531–H2546.

[291] M. Ursino, Interaction between carotid baroregulation and the pulsating heart: a mathematical model., Am. J. Physiol. 275 (1998) H1733–H1747.

[292] W.C. Rose, J.S. Schwaber, Analysis of heart rate-based control of arterial blood pressure., Am. J. Physiol. 271 (1996) H812-22.

[293] M.S. Olufsen, H.T. Tran, J.T. Ottesen, L. a Lipsitz, V. Novak, Modeling baroreflex regulation of heart rate during orthostatic stress., Am. J. Physiol. Regul. Integr. Comp. Physiol. 291 (2006) R1355–R1368. doi:10.1152/ajpregu.00205.2006.

[294] D.L. Eckberg, Nonlinearities of the human carotid baroreceptor-cardiac reflex, Circ. Res. 47 (1980) 208–216. doi:10.1161/01.RES.47.2.208.

[295] H. Degeest, M.N. Levy, H. Zieske, R.I. Lipman, Depression of Ventricular Contractility By Stimulation of the Vagus Nerves., Circ. Res. 17 (1965) 222–235. doi:10.1161/01.RES.17.3.222.

[296] R.J. Henning, I. Khalil, A u t o n o m i c nervous stimulation affects left ventricular relaxation more than left ventricular contraction, 28 (1989) 15–25.

[297] M. Frey, Cardiovascular response of women to lower body negative pressure, Aviat. Sp. Environ. Med. 57 (1986) 531–538.

[298] J.L. Ardell, P.S. Rajendran, H.A. Nier, B.H. KenKnight, J.A. Armour, Central-peripheral neural network interactions evoked by vagus nerve stimulation: functional consequences on control of cardiac function., Am. J. Physiol. Heart Circ. Physiol. 309 (2015) H1740-52. doi:10.1152/ajpheart.00557.2015.

[299] N. Levy, H. Zieske, Autonomic control and atrioventricular of cardiac pacemaker transmission activity, J. Appl. Physiol. 27 (1969) 465–470.

[300] M.E. Lewis, a H. Al-Khalidi, R.S. Bonser, T. Clutton-Brock, D. Morton, D. Paterson, J.N. Townend, J.H. Coote, Vagus nerve stimulation decreases left ventricular contractility in vivo in the human and pig heart., J. Physiol. 534 (2001) 547–52. doi:10.1111/j.1469-7793.2001.00547.x.

[301] B. Casadei, Physiological Society Symposium - Vagal Control: From Axolotl to Man. Vagal control of myocardial contractility in humans, Exp. Physiol. 86 (2001) 817–823. doi:10.1113/eph8602297.

[302] A.C. Fowler, M.J. McGuinnes, A delay recruitment model of the cardiovascular

control system, J. Math. Biol. (2005) 508–526.

[303] H. van de Vooren, M.G.J. Gademan, C. a Swenne, B.J. TenVoorde, M.J. Schalij, E.E. Van der Wall, Baroreflex sensitivity, blood pressure buffering, and resonance: what are the links? Computer simulation of healthy subjects and heart failure patients., J. Appl. Physiol. 102 (2007) 1348–1356. doi:10.1152/japplphysiol.00158.2006.

[304] S. Cavalcanti, Arterial baroreflex influence on heart rate variability: a mathematical model-based analysis., Med. Biol. Eng. Comput. 38 (2000) 189–197. doi:10.1007/BF02344775.

[305] H.U. Klein, G.M. De Ferrari, Vagus nerve stimulation: A new approach to reduce heart failure, Cardiol. J. 17 (2010) 638–643.

[306] S. Bibevski, M.E. Dunlap, Evidence for impaired vagus nerve activity in heart failure., Heart Fail. Rev. 16 (2011) 129–35. doi:10.1007/s10741-010-9190-6.

[307] A. Machhada, R. Ang, G.L. Ackland, N. Ninkina, V.L. Buchman, M.F. Lythgoe, S. Trapp, A. Tinker, N. Marina, A. V. Gourine, Control of ventricular excitability by neurons of the dorsal motor nucleus of the vagus nerve, Hear. Rhythm. 12 (2015) 2285–2293. doi:10.1016/j.hrthm.2015.06.005.

[308] V.J. Massari, L.W. Dickerson, A.L. Gray, J.M. Lauenstein, K.J. Blinder, J.T. Newsome, D.J. Rodak, T.J. Fleming, P.J. Gatti, R.A. Gillis, Neural control of left ventricular contractility in the dog heart: Synaptic interactions of negative inotropic vagal preganglionic neurons in the nucleus ambiguus with tyrosine hydroxylase immunoreactive terminals, Brain Res. 802 (1998) 205–220. doi:10.1016/S0006-8993(98)00613-1.

[309] E.S. Schelegle, J.F. Green, An overview of the anatomy and physiology of slowly adapting pulmonary stretch receptors, Respir. Physiol. 125 (2001) 17–31. doi:10.1016/S0034-5687(00)00202-4.

[310] L. Kubin, G.F. Alheid, E.J. Zuperku, D.R. McCrimmon, Central pathways of pulmonary and lower airway vagal afferents., J. Appl. Physiol. 101 (2006) 618–27. doi:10.1152/japplphysiol.00252.2006.

[311] H. Suga, K. Sagawa, D.P. Kostiuk, Controls of ventricular contractility assessed by pressure-volume ratio, Emax, Cardiovasc. Res. 10 (1976) 582–592.

[312] L.M. McDowall, R. a L. Dampney, Calculation of threshold and saturation points of sigmoidal baroreflex function curves., Am. J. Physiol. Heart Circ. Physiol. 291 (2006) H2003-7. doi:10.1152/ajpheart.00219.2006.

[313] P.V. Greenwood, R. Hainsworth, F. Karim, G.W. Morrison, O.A. Sofola, Reflex Inotropic Responses of the Heart from Lung Inflation in Anaesthetized Dogs, Eur. J. Physiol. 205 (1980) 199–205.

[314] R. Hainsworth, Circulatory inflation responses in anesthetized from lung dogs, Am. J. Physiol. 226 (1974).

[315] Boundless, Boundless Anatomy and Physiology, 2016.

[316] J.H. Coote, Myths and realities of the cardiac vagus., J. Physiol. 591 (2013) 4073–85. doi:10.1113/jphysiol.2013.257758.

[317] R.E. Klabunde, Ventricular Pressure-Volume Relationship, (2015). http://www.cvphysiology.com/Cardiac Function/CF024.htm.

[318] D.S. Warner, M. a Warner, a P. Story, Venous Function and Central Venous Pressure, Anesthesiology. 108 (2008) 735–48. doi:10.1097/ALN.0b013e3181672607.

[319] D.E. Burgess, J.C. Hundley, S.G. Li, D.C. Randall, D.R. Brown, First-order differential-delay equation for the baroreflex predicts the 0.4-Hz blood pressure rhythm in rats, Am J Physiol. 273 (1997) R1878-84.

[320] J. V Ringwood, S.C. Malpas, Slow oscillations in blood pressure via a nonlinear feedback model., Am. J. Physiol. Regul. Integr. Comp. Physiol. 280 (2001) R1105–R1115. doi:citeulike-article-id:2195425.

[321] J.T. Ottesen, Modelling of the baroreflex-feedback mechanism with time-delay., J. Math. Biol. 36 (1997) 41–63. doi:10.1007/s002850050089.

[322] J.T. Ottesen, M.S. Olufsen, Functionality of the baroreceptor nerves in heart rate regulation, Comput. Methods Programs Biomed. 101 (2011) 208–219. doi:10.1016/j.cmpb.2010.10.012.

[323] N. Westerhof, J.W. Lankhaar, B.E. Westerhof, The arterial windkessel, Med. Biol. Eng. Comput. 47 (2009) 131–141. doi:10.1007/s11517-008-0359-2.

[324] A. Ben-Tal, S.S. Shamailov, J.F.R. Paton, Central regulation of heart rate and the appearance of respiratory sinus arrhythmia: New insights from mathematical modeling, Math. Biosci. 255 (2014) 71–82. doi:10.1016/j.mbs.2014.06.015.

[325] E. Magosso, M. Ursino, Cardiovascular response to dynamic aerobic exercise: A methematical model, Med. Biol. Eng. Comput. 40 (2002) 660–674.

doi:10.1007/BF02345305.

[326] M. Ursino, E. Magosso, Acute cardiovascular response to isocapnic hypoxia. I. A mathematical model., Am. J. Physiol. Heart Circ. Physiol. 279 (2000) H149–H165.

[327] T. Kawada, M. Sugimachi, T. Shishido, H. Miyano, T. Sato, R. Yoshimura, H. Miyashita, T. Nakahara, J. Alexander, K. Sunagawa, Simultaneous identification of static and dynamic vagosympathetic interactions in regulating heart rate., Am. J. Physiol. 276 (1999) R782–R789.

[328] Z. Cheng, T.L. Powley, J.S. Schwaber, F.J. Doyle, Projections of the dorsal motor nucleus of the vagus to cardiac ganglia of rat atria: an anterograde tracing study., J. Comp. Neurol. 410 (1999) 320–41.

[329] S. Mastitskaya, N. Marina, A. Gourine, M.P. Gilbey, K.M. Spyer, A.G. Teschemacher, S. Kasparov, S. Trapp, G.L. Ackland, A. V Gourine, Cardioprotection evoked by remote ischaemic preconditioning is critically dependent on the activity of vagal pre-ganglionic neurones., Cardiovasc. Res. 95 (2012) 487–94. doi:10.1093/cvr/cvs212.

[330] R.A.L. Dampney, Functional organization of central pathways regulating the cardiovascular system., Physiol. Rev. 74 (1994) 323–364. doi:10.1017/CBO9781107415324.004.

[331] J.F. Jones, Y. Wang, D. Jordan, Activity of C fibre cardiac vagal efferents in anaesthetized cats and rats., J. Physiol. 507 (Pt 3 (1998) 869–80.

[332] J.A. Sala-Mercado, M. Moslehpour, R.L. Hammond, M. Ichinose, X. Chen, S. Evan, D.S. O'Leary, R. Mukkamala, Stimulation of the Cardiopulmonary Baroreflex Enhances Ventricular Contractility in Awake Dogs: A Mathematical Analysis Study., Am. J. Physiol. Regul. Integr. Comp. Physiol. (2014) ajpregu.00510.2013-. doi:10.1152/ajpregu.00510.2013.

[333] R.J. Henning, I.R. Khalil, M.N. Levy, Vagal stimulation attenuates sympathetic enhancement of left ventricular function., Am. J. Physiol. 258 (1990) H1470–H1475.

[334] P.A. Cain, R. Ahl, E. Hedstrom, M. Ugander, A. Allansdotter-Johnsson, P. Friberg, H. Arheden, Age and gender specific normal values of left ventricular mass, volume and function for gradient echo magnetic resonance imaging: a cross sectional study., BMC Med. Imaging. 9 (2009) 1–10. doi:10.1186/1471-2342-9-2.

[335] M. Homoud, Normal intracardiac pressures, Tufts Open Coursew. (2010). http://ocw.tufts.edu/Content/50/lecturenotes/634463/634530.

[336] S. Schwartzenberg, M.M. Redfield, A.M. From, P. Sorajja, R.A. Nishimura, B.A. Borlaug, Effects of vasodilation in heart failure with preserved or reduced ejection fraction: Implications of distinct pathophysiologies on response to therapy, J. Am. Coll. Cardiol. 59 (2012) 442–451. doi:10.1016/j.jacc.2011.09.062.

[337] W.J. Paulus, C. Tschope, J.E. Sanderson, C. Rusconi, F.A. Flachskampf, F.E. Rademakers, P. Marino, O.A. Smiseth, G. De Keulenaer, A.F. Leite-Moreira, A. Borbely, I. Edes, M.L. Handoko, S. Heymans, N. Pezzali, B. Pieske, K. Dickstein, A.G. Fraser, D.L. Brutsaert, How to diagnose diastolic heart failure: A consensus statement on the diagnosis of heart failure with normal left ventricular ejection fraction by the Heart Failure and Echocardiography Associations of the European Society of Cardiology, Eur. Heart J. 28 (2007) 2539–2550. doi:10.1093/eurheartj/ehm037.

[338] C.L. Hung, A. Verma, H. Uno, S.H. Shin, M. Bourgoun, A.H. Hassanein, J.J. McMurray, E.J. Velazquez, L. Kober, M.A. Pfeffer, S.D. Solomon, Longitudinal and circumferential strain rate, left ventricular remodeling, and prognosis after myocardial infarction, J. Am. Coll. Cardiol. 56 (2010) 1812–1822. doi:10.1016/j.jacc.2010.06.044.

[339] B.A. Borlaug, W.J. Paulus, Heart failure with preserved ejection fraction: Pathophysiology, diagnosis, and treatment, Eur. Heart J. 32 (2011) 670–679. doi:10.1093/eurheartj/ehq426.

[340] A.M. Katz, E.L. Rolett, Heart failure: When form fails to follow function, Eur. Heart J. 37 (2016) 449–454. doi:10.1093/eurheartj/ehv548.

[341] M.K. Lahiri, P.J. Kannankeril, J.J. Goldberger, Assessment of Autonomic Function in Cardiovascular Disease. Physiological Basis and Prognostic Implications, J. Am. Coll. Cardiol. 51 (2008) 1725–1733. doi:10.1016/j.jacc.2008.01.038.

[342] E. Glasscock, J.W. Yoo, T.T. Chen, T.L. Klassen, J.L. Noebels, Kv1.1 Potassium Channel Deficiency Reveals Brain-Driven Cardiac Dysfunction as a Candidate Mechanism for Sudden Unexplained Death in Epilepsy, J. Neurosci. 30 (2010) 5167–5175. doi:10.1523/JNEUROSCI.5591-09.2010.

[343] Y. Yamada, H. Kinoshita, K. Kuwahara, Y. Nakagawa, Y. Kuwabara, T. Minami, C. Yamada, J. Shibata, K. Nakao, K. Cho, Y. Arai, S. Yasuno, T. Nishikimi, K. Ueshima, S. Kamakura, M. Nishida, S. Kiyonaka, Y. Mori, T.

Kimura, K. Kangawa, K. Nakao, Inhibition of N-type Ca2+ channels ameliorates an imbalance in cardiac autonomic nerve activity and prevents lethal arrhythmias in mice with heart failure, Cardiovasc. Res. 104 (2014) 183–193. doi:10.1093/cvr/cvu185.

[344] R.K. Leak, J.P. Card, R.Y. Moore, Suprachiasmatic pacemaker organization analyzed by viral transynaptic transport., Brain Res. 819 (1999) 23–32. doi:10.1016/S0006-8993(98)01317-1.

[345] L.P. Morin, SCN Organization Reconsidered, J. Biol. Rhythms. 22 (2007) 3–13. doi:10.1177/0748730406296749.

[346] M.P. Gerkema, E. a Van der Zee, L.E. Feitsma, Expression of circadian rhythmicity correlates with the number of arginine-vasopressin-immunoreactive cells in the suprachiasmatic nucleus of common voles, Microtus arvalis, Brain Res. 639 (1994) 93–101. doi:0006-8993(94)91768-X [pii].

[347] T. Hamada, M.C. Antle, R. Silver, Temporal and spatial expression patterns of canonical clock genes and clock-controlled genes in the suprachiasmatic nucleus, Eur. J. Neurosci. 19 (2004) 1741–1748. doi:10.1111/j.1460-9568.2004.03275.x.

[348] X. Jin, L.P. Shearman, D.R. Weaver, M.J. Zylka, G.J. de Vries, S.M. Reppert, A molecular mechanism regulating rhythmic output from the suprachiasmatic circadian clock, Cell. 96 (1999) 57–68. doi:10.1016/S0092-8674(00)80959-9.

[349] E.A. Van der Zee, M. Oklejewicz, K. Jansen, S. Daan, M.P. Gerkema, Vasopressin immunoreactivity and release in the suprachiasmatic nucleus of wild-type and tau mutant Syrian hamsters., Brain Res. 936 (2002) 38–46. doi:S0006899302024976 [pii].

[350] J. Schaap, H. Albus, H.T. VanderLeest, P.H.C. Eilers, L. Détári, J.H. Meijer, Heterogeneity of rhythmic suprachiasmatic nucleus neurons: Implications for circadian waveform and photoperiodic encoding., Proc. Natl. Acad. Sci. U. S. A. 100 (2003) 15994–15999. doi:10.1073/pnas.2436298100.

[351] C.H. Ko, Y.R. Yamada, D.K. Welsh, E.D. Buhr, A.C. Liu, E.E. Zhang, M.R. Ralph, S. a. Kay, D.B. Forger, J.S. Takahashi, Emergence of Noise-Induced Oscillations in the Central Circadian Pacemaker, PLoS Biol. 8 (2010) e1000513. doi:10.1371/journal.pbio.1000513.

[352] A.B. Webb, N. Angelo, J.E. Huettner, E.D. Herzog, Intrinsic, nondeterministic circadian rhythm generation in identified mammalian neurons., Proc. Natl. Acad. Sci. U. S. A. 106 (2009) 16493–8. doi:10.1073/pnas.0902768106.

[353] J.A. Evans, T.L. Leise, O. Castanon-Cervantes, A.J. Davidson, Dynamic Interactions Mediated by Nonredundant Signaling Mechanisms Couple Circadian Clock Neurons, Neuron. 80 (2013) 973–983. doi:10.1016/j.neuron.2013.08.022.

[354] S.H. Chung, W. Shen, Laser capture microdissection: from its principle to applications in research on neurodegeneration., Neural Regen. Res. 10 (2015) 897–8. doi:10.4103/1673-5374.158346.

[355] S. Datta, L. Malhotra, R. Dickerson, S. Chaffee, C.K. Sen, S. Roy, Laser capture microdissection: Big data from small samples, Histol. Histopathol. 30 (2015) 1255–1269. doi:10.14670/HH-11-622.

[356] C. Doherty, S.A. Kay, Circadian Control of Global Gene Expression Patterns, Annu. Rev. Genet. 48 (2010) 1–6. doi:10.1097/MPG.0b013e3181a15ae8.Screening.

[357] T.K. Sato, S. Panda, S. a Kay, J.B. Hogenesch, DNA arrays: applications and implications for circadian biology., J. Biol. Rhythms. 18 (2003) 96–105. doi:10.1177/0748730403252245.

[358] J. Park, H. Zhu, S. O'Sullivan, B.A. Ogunnaike, D.R. Weaver, J.S. Schwaber, R. Vadigepalli, Single-cell Transcriptional Analysis Reveals Novel Neuronal Phenotypes and Interaction Networks involved In the Central Circadian Clock, Front. Neurosci. 10 (2016). doi:10.3389/fnins.2016.00481.

[359] A. Balsalobre, F. Damiola, U. Schibler, A serum shock induces circadian gene expression in mammalian tissue culture cells, Cell. 93 (1998) 929–937. doi:10.1016/S0092-8674(00)81199-X.

[360] N. Gossan, L. Zeef, J. Hensman, A. Hughes, J.F. Bateman, L. Rowley, C.B. Little, H.D. Piggins, M. Rattray, R.P. Boot-Handford, Q.J. Meng, The circadian clock in murine chondrocytes regulates genes controlling key aspects of cartilage homeostasis, Arthritis Rheum. 65 (2013) 2334–2345. doi:10.1002/art.38035.

[361] M. Maechler, P. Rousseeuw, A. Struyf, M. Hubert, K. Hornik, cluster: Cluster Analysis Basics and Extensions., (2015).

[362] R.Y. Moore, J.C. Speh, R.K. Leak, Suprachiasmatic nucleus organization, Cell Tissue Res. 309 (2002) 89–98. doi:10.1007/s00441-002-0575-2.

[363] H. Dardente, V.-J. Poirel, P. Klosen, P. Pévet, M. Masson-Pévet, Per and neuropeptide expression in the rat suprachiasmatic nuclei:

compartmentalization and differential cellular induction by light., Brain Res. 958 (2002) 261–71. doi:S0006899302035631 [pii].

[364] Y. Shigeyoshi, K. Taguchi, S. Yamamoto, S. Takekida, L. Yan, H. Tei, T. Moriya, S. Shibata, J.J. Loros, J.C. Dunlap, H. Okamura, Light-Induced Resetting of a Mammalian Circadian Clock Is Associated with Rapid Induction of the mPer1 Transcript, Cell. 91 (1997) 1043–1053. doi:10.1016/S0092-8674(00)80494-8.

[365] L. Yan, R. Silver, Differential induction and localization of mPer1 and mPer2 during advancing and delaying phase shifts, Eur. J. Neurosci. 16 (2002) 1531–1540. doi:10.1046/j.1460-9568.2002.02224.x.

[366] C.N. Allen, N.J. Klett, R.P. Irwin, M.G. Moldavan, Mechanisms of Circadian Systems in Animals and Their Clinical Relevance, in: R. Aguilar-Roblero, M. Diaz-Munoz, M.L. Fanjul-Moles (Eds.), Mech. Circadian Syst. Anim. Their Clin. Relev., Springer International Publishing, 2015: pp. 133–148. doi:10.1007/978-3-319-08945-4.

[367] E. Llorens-Bobadilla, S. Zhao, A. Baser, G. Saiz-Castro, K. Zwadlo, A. Martin-Villalba, Single-Cell Transcriptomics Reveals a Population of Dormant Neural Stem Cells that Become Activated upon Brain Injury, Cell Stem Cell. 17 (2015) 329–340. doi:10.1016/j.stem.2015.07.002.

[368] V. Moignard, S. Woodhouse, L. Haghverdi, A.J. Lilly, Y. Tanaka, A.C. Wilkinson, F. Buettner, I.C. Macaulay, W. Jawaid, E. Diamanti, S.-I. Nishikawa, N. Piterman, V. Kouskoff, F.J. Theis, J. Fisher, B. Göttgens, Decoding the regulatory network of early blood development from single-cell gene expression measurements, Nat. Biotechnol. advance on (2015). doi:10.1038/nbt.3154.

[369] J. Park, B.A. Ogunnaike, J.S. Schwaber, R. Vadigepalli, Identifying distinct gene regulatory networks subtending catecholaminergic neuronal subtypes contributing to hypertension development, in: AIChE Annu. Meet., 2013.

[370] O. Stegle, S.A. Teichmann, J.C. Marioni, Computational and analytical challenges in single-cell transcriptomics, Nat. Publ. Gr. 16 (2015) 133–145. doi:10.1038/nrg3833.

[371] A. Clauset, M.E.J. Newman, C. Moore, Finding community structure in very large networks, Phys. Rev. E. 70 (2004) 66111. doi:10.1103/PhysRevE.70.066111.

[372] U. Albrecht, Timing to Perfection: The Biology of Central and Peripheral

Circadian Clocks, Neuron. 74 (2012) 246–260. doi:10.1016/j.neuron.2012.04.006.

[373] U. Albrecht, Z.S. Sun, G. Eichele, C.C. Lee, A differential response of two putative mammalian circadian regulators, mper1 and mper2, to light., Cell. 91 (1997) 1055–64. doi:10.1016/S0092-8674(00)80495-X.

[374] R.Y. Moore, R. Silver, Suprachiasmatic Nucleus Organization, Chronobiol. Int. 15 (1998) 475–487. doi:10.3109/07420529808998703.

[375] N. Atkins, J.W. Mitchell, E. V. Romanova, D.J. Morgan, T.P. Cominski, J.L. Ecker, J.E. Pintar, J. V. Sweedler, M.U. Gillette, Circadian integration of glutamatergic signals by little SAAS in novel suprachiasmatic circuits, PLoS One. 5 (2010) 1–13. doi:10.1371/journal.pone.0012612.

[376] P. Paszek, S. Ryan, L. Ashall, K. Sillitoe, C. V Harper, D.G. Spiller, D. a Rand, M.R.H. White, Population robustness arising from cellular heterogeneity., Proc. Natl. Acad. Sci. U. S. A. 107 (2010) 11644–11649. doi:10.1073/pnas.0913798107.

[377] E.S. Maywood, J.E. Chesham, J.A. O'Brien, M.H. Hastings, A diversity of paracrine signals sustains molecular circadian cycling in suprachiasmatic nucleus circuits., Proc. Natl. Acad. Sci. U. S. A. 108 (2011) 14306–14311. doi:10.1073/pnas.1101767108.

[378] M.Y. Cheng, C.M. Bullock, C. Li, A.G. Lee, J.C. Bermak, J. Belluzzi, D.R. Weaver, F.M. Leslie, Q.-Y. Zhou, Prokineticin 2 transmits the behavioural circadian rhythm of the suprachiasmatic nucleus., Nature. 417 (2002) 405–10. doi:10.1038/417405a.

[379] H.M. Prosser, A. Bradley, J.E. Chesham, F.J.P. Ebling, M.H. Hastings, E.S. Maywood, Prokineticin receptor 2 (Prokr2) is essential for the regulation of circadian behavior by the suprachiasmatic nuclei., Proc. Natl. Acad. Sci. U. S. A. 104 (2007) 648–653. doi:10.1073/pnas.0606884104.

[380] H. Dziema, K. Obrietan, PACAP potentiates L-type calcium channel conductance in suprachiasmatic nucleus neurons by activating the MAPK pathway., J. Neurophysiol. 88 (2002) 1374–86.

[381] K. Kume, M.J. Zylka, S. Sriram, L.P. Shearman, D.R. Weaver, X. Jin, E.S. Maywood, M.H. Hastings, S.M. Reppert, mCRY1 and mCRY2 Are Essential Components of the Negative Limb of the Circadian Clock Feedback Loop, Cell. 98 (1999) 193–205. doi:10.1016/S0092-8674(00)81014-4.

[382] H.J. Romijn, J.F.M. Van Uum, J. Emmering, V. Goncharuk, R.M. Buijs, Colocalization of VIP with AVP in neurons of the human paraventricular, supraoptic and suprachiasmatic nucleus, Brain Res. 832 (1999) 47–53. doi:10.1016/S0006-8993(99)01468-7.

[383] S.M. Abbott, J.M. Arnold, Q. Chang, H. Miao, N. Ota, C. Cecala, P.E. Gold, J. V. Sweedler, M.U. Gillette, Signals from the Brainstem Sleep/Wake Centers Regulate Behavioral Timing via the Circadian Clock, PLoS One. 8 (2013) e70481. doi:10.1371/journal.pone.0070481.

[384] R. Iyer, T.A. Wang, M.U. Gillette, Circadian gating of neuronal functionality: a basis for iterative metaplasticity1, Front. Syst. Neurosci. 8 (2014) 1–14. doi:10.3389/fnsys.2014.00164.

[385] T.-L. To, M. a Henson, E.D. Herzog, F.J. Doyle, A molecular model for intercellular synchronization in the mammalian circadian clock., Biophys. J. 92 (2007) 3792–3803. doi:10.1529/biophysj.106.094086.

[386] M.A. Henson, Multicellular model for intercellular synchronization in circadian neural networks, Biophys. J. 101 (2011) 12–20. doi:10.1016/j.bpj.2011.04.051.

[387] D.E. Zak, H. Hao, R. Vadigepalli, G.M. Miller, B.A. Ogunnaike, J.S. Schwaber, Systems analysis of circadian time-dependent neuronal epidermal growth factor receptor signaling., Genome Biol. 7 (2006) R48. doi:10.1186/gb-2006-7-6-r48.

[388] J.H. Abel, K. Meeker, D. Granados-Fuentes, P.C. St. John, T.J. Wang, B.B. Bales, F.J. Doyle, E.D. Herzog, L.R. Petzold, Functional network inference of the suprachiasmatic nucleus, Proc. Natl. Acad. Sci. (2016) 201521178. doi:10.1073/pnas.1521178113.

[389] J.H. Newman, Lectures on the present position of Catholics in England . Second edition, Burns & Lambert, 1851.

[390] P.J. Marvar, E.B. Hendy, T. Cruise, D. Walas, D. DeCicco, R. Vadigepalli, J.S. Schwaber, H. Waki, D. Murphy, J.F.R. Paton, Systemic leukotriene b4 receptor antagonism lowers arterial blood pressure and improves autonomic function in the spontaneously hypertensive rat., J. Physiol. 0 (2016) 1–15. doi:10.1113/JP272065.

[391] C. Vasalou, E.D. Herzog, M.A. Henson, Multicellular model for intercellular synchronization in circadian neural networks, Biophys. J. 101 (2011) 12–20. doi:10.1016/j.bpj.2011.04.051.

[392] R. Bailón, G. Laouini, C. Grao, M. Orini, P. Laguna, O. Meste, The integral pulse frequency modulation model with time-varying threshold: Application to heart rate variability analysis during exercise stress testing, IEEE Trans. Biomed. Eng. 58 (2011) 642–652. doi:10.1109/TBME.2010.2095011.

[393] A.H. Moreno, A.I. Katz, L.D. Gold, An integrated approach to the study of the venous system with steps toward a detailed model of the dynamics of venous return to the right heart., IEEE Trans. Biomed. Eng. 16 (1969) 308–324. doi:10.1109/TBME.1969.4502662.

Appendix A

ANALYSIS OF SINGLE NEURONS FROM THE NUCLEUS TRACTUS SOLITARIUS

A.1 Nucleus tractus solitarius gene assay set and functional annotation for analysis

Table A.1 Gene categorization, primer sequences, and entrez ID

Entrez ID	Gene	Primer Design Forward	Primer Design Reverse	UPL#	Gene Functional Categorization
24310	Ace	gacaactatccagagggaattga	cacaacaccttggctgtcc	25	Angiotensin System
81822	Actb	ctggctcctagcaccatga	tagagccaccaatccacaca	63	housekeeping
25238	Adrbk1	aagaagatcctgctgccaga	ccggaaaagcaggtatccta	89	Signaling feedback
24179	Agt	cacctacgttcacttccaagg	agaactcatggagcccagtc	7	Angiotensin System
24180	Agtr1a	ggctagccaaaggaagagtca	ctgccagcgaactgttttc	42	Angiotensin System
24182	Agtr2	gaacagaattacccgtgacca	atgaatgccaacacaacagc	121	Angiotensin System
298646	Agtrap	ccatcttcagcttgctgct	cctgagaaggtccgaagaaa	2	Angiotensin System
24185	Akt1	aacgacgtagccattgtgaa	ccatcattcttgaggaggaagt	71	Intracellular Signaling
64363	Araf	gaagacaagcccaagatgga	gactgggcaggtgccata	77	Intracellular Signaling
25387	Arrb1	gggagaccttgcatccagt	ggagtctcgctctctggaac	76	Signaling feedback
25388	Arrb2	gatcctgtcgatggtgtggt	ggaaagacaggcccagtaca	98	Signaling feedback
81647	Atf2	ctggtggctgaaaggaacat	tcccaagttgccatctagtgt	85	transcriptional regulators
29716	Cacna1d	ggcagaagacatagatcctgaga	actggtgggcatgctagtgt	55	Ion Channel
24241	Calca	cagatgaaagtcagggagctg	caggatctcttctgggcagt	63	neuromodulatory regulator
314322	Fos	cagcctttcctactaccattcc	acagatctgcgcaaaagtcc	67	transcriptional regulators
81646	Creb1	ctagtgcccagcaaccaagt	ggaggacgccataacaactc	9	transcriptional regulators

81648	Crh	caacctcagccgattctgat	gcgggacttctgttgaggt	69	neuromodulatory regulator
25699	Dbh	actactgtcgccacgtgct	accggcttcttctgggtagt	81	neuromodulatory regulator
116663	Dusp6	tctctgatcactggagccaaa	gtttttgcctcgggcttc	123	Intracellular Signaling
24330	Egr1	cgaacaaccctacgagcac	gcgccttctcgttattcaga	114	transcriptional regulators
114090	Egr2	ctacccggtggaagacctc	tcaatgttgatcatgccatctc	60	transcriptional regulators
25148	Egr3	caatctgtaccccgaggaga	ccgatgtccatcacattctct	7	transcriptional regulators
314436	Elk1	caccagtccaaaccccttag	tcaactcttcagatttctggtttg	16	transcriptional regulators
25445	Fosl1	gcagaaaccgaagaaaggaa	tcctccaacttgtcggtctc	4	transcriptional regulators
29705	Gabra1	cgatcctctctcccacactt	tcttcatcacgggcttgtc	50	neuromodulatory targets – Ion channel
289606	Gabra2	ggtttccgctgcttgttct	ttcttggatgttagccagcac	20	neuromodulatory targets – Ion channel
140675	Gabra4	gtacctgcgatcgtgctgt	ctgtcctggggattcgttta	98	neuromodulatory targets – Ion channel
24922	Gabrb3	tcatgggtgtccttctggat	atggtgagcacggtggtaat	84	neuromodulatory targets – Ion channel
65187	Gabrq	gcggagaatcgtgtatttcaa	gctgctgttgtggtaagtcg	123	neuromodulatory targets – Ion channel
24379	Gad1	tacaacctttggctgcatgt	tgagtttgtggcgatgctt	77	neuromodulatory regulator
29141	Gal	tggagtttctcagtttcttgcac	ggtgtggtctcaggactgct	10	neuromodulatory regulator
29627	Gria2	gccaaggactcgggaagta	cccccgacaaggatgtaga	67	neuromodulatory targets – Ion channel
29628	Gria3	ttcaacaaaagaatttttcagacg	ccgtcagctgttgttttgg	21	neuromodulatory targets – Ion channel
24409	Grin2a	cgtcatggtctccaggagtaa	gaggcactgaagggttcg	94	neuromodulatory targets – Ion channel
24408	Grin1	gcttttgcagccgtgaac	gggctctgctctaccactctt	69	neuromodulatory targets – Ion channel
24410	Grin2b	tcctgcagctgtttggagat	gctgctcatcacctcattctt	106	neuromodulatory targets – Ion channel
24411	Grin2c	ggcactcctgcaacttctg	gttctggcagatccctgaga	78	neuromodulatory targets – Ion channel
24412	Grin2d	gccctgctgcgagactat	cggttatcccaggtgatgtt	67	neuromodulatory targets – Ion channel
59075	Grk5	ccaccaaagaaagggctgt	tcttggaattgttttgatgctg	124	Signaling feedback
59076	Grk6	atgtctttgggctggatgg	cagttcccacagcaatcctt	85	Signaling feedback
114244	Hcn2	cacccctacagcgacttcag	tttcccaccatgaacaacag	95	neuromodulatory targets – Ion channel
24465	Hprt1	gaccggttctgtcatgtcg	acctggttcatcatcactaatcac	95	housekeeping
293621	Hras	tcacagtaaattatttgatggtcttga	ccacaggcactacacctcct	20	Intracellular Signaling

25262	Itpr1	catcacagccctcatccttaac	ggagtagctttgaagcattgttct	60	Intracellular Signaling
25679	Itpr3	gtgatggagaccaagctgaag	tagtctaggcgcacgttgag	80	Intracellular Signaling
24516	Jun	ttctgaccaactgcctggat	gaagggactctccaagtgctc	17	transcriptional regulators
24517	Junb	gggagctgagagaagagacg	tggtagctgtgcgtaaaagc	50	transcriptional regulators
24518	jund	caagctggagcgtatctcg	cggtgttctggcttttgag	25	transcriptional regulators
29712	Kcnj2	gctgccttcctcttctccat	tcgggcactcgtctgtaac	115	neuromodulatory targets – Ion channel
170851	Map2k1	ggcctggttatggctagga	gatgatctggttccggattg	80	Intracellular Signaling
287398	Map2k4	aacaaaatggtccacaaacca	tttttcatccacaagttgatcgt	118	Intracellular Signaling
363855	Map2k7	tcaggggacttccagtcatt	gatgaagctgtgttcaagtagtttg	114	Intracellular Signaling
309168	Map3k11	cgggaagagacacgtgga	ccaggagcagagcgtgata	22	Intracellular Signaling
25579	Map3k12	cctctcacctccattcctga	agccaggtgtgctgagtagc	3	Intracellular Signaling
116596	Map3k8	acctccggggaacagaga	gcctgtctgcatgtgaatga	125	Intracellular Signaling
116590	Mapk1	tgaagttgaacaggctctgg	tgaatggtgcttcagcaatg	1	Intracellular Signaling
50689	Mapk3	ggaggtggaggtggtgaa	gcacgtggtcatatgctgag	46	Intracellular Signaling
114509	Mapk7	acccagcaactgtccaagtc	ggtcaaagccaacaccgtag	16	Intracellular Signaling
116554	Mapk8	gcagccgtctcctttaggt	cattgacagacggcgaaga	89	Intracellular Signaling
24604	Npy	atccctgctcgtgtgtttg	ctggccatgtcctctgct	129	neuromodulatory regulator
29358	Npy1r	ctgcaaccacaatctgctgt	tgacgcaggtggagatcat	53	neuromodulatory regulator
29431	Pak1	tcgagaagattggacaaggtg	gccctgtggctacatccat	98	Intracellular Signaling
81745	Pdpk1	aaaactttcttcgtccacacg	ggactgctctggtactgttgc	79	Intracellular Signaling
29542	Pebp1	cggacctcccaaagacac	agaggctgctcctgctcata	20	Intracellular Signaling
364152	Phox2b	gagagtccaggtgtggttcc	ggcttctttgctctcgtcat	70	transcriptional regulators
60664	Pik3r3	atcccaaacttgatgtgaagc	ttatcttcttttaccaactgatcctg	130	Intracellular Signaling
24680	Prkca	tacggcgtgctcctgtatg	cttggcagggtgtttggt	44	Intracellular Signaling
24654	Plcb1	cgccaaaaaggatagcaaga	gcggatgagccatgatct	3	Intracellular Signaling
29322	Plcb3	cttcacacaatacctatctcactgc	cggtacatctccactgacga	20	Intracellular Signaling
25594	Ppp1cb	tgaacgtggacagcctcat	acaatttttcccggacgac	67	Intracellular Signaling

24669	Ppp1cc	ggcggatatcgataaactcaa	tggcttggaccctctcact	66	Intracellular Signaling
117281	Ppp2r1a	gctacatggtggcagacaaa	tagtgatctcaggcccaactg	50	Intracellular Signaling
65179	Ppp5c	ccgaaggcactctgaagc	tgatagcgttctcgtagtccttg	82	Intracellular Signaling
29340	Prkce	tctaccctgtctggcttagca	cgggttcttggtcatgaaag	89	Intracellular Signaling
50646	Ptk2b	caatctgctggctcctaagc	taggagagctggcacacaga	85	Intracellular Signaling
24697	Ptpn1	ggaacaggtaccgagatgtca	agtcattatcttcctgatgcaatttt	114	Intracellular Signaling
117063	Ptpn2	aggctacaaccgctcagaag	catttaggtgtctgtcaatcttgg	84	Intracellular Signaling
24703	Raf1	tttcttgccgaataagcaaag	cagtcgtgcaagctcatcc	114	Intracellular Signaling
25676	Rasa1	catctaataaacgccttcgtca	tggtagtttatgagcttcttcaata tg	66	Intracellular Signaling
192213	Rasgrf1	ggctggtctcaaacttaggatg	tcatgcctgtaatcccagcta	49	Intracellular Signaling
114513	Rasgrf2	aggagcaagcagggaaaga	tctcaatcaaaatgtctgcgtaa	58	Intracellular Signaling
29434	Rasgrp1	gttcatccatgtggctcaga	acagccattagcgtgttgaa	22	Intracellular Signaling
54289	Rgs1	gcaagaagaacagggtgagg	cactgtatttcatgacagtaccaca	12	Signaling feedback
84583	Rgs2	aacttttatcaagccttctcctga	acgctctgaatgcagcaag	113	Signaling feedback
54293	Rgs3	ccggaagagaaagagcaaaaa	ggccccaggagattcatt	124	Signaling feedback
29480	Rgs4	caagatgtgcaaaggactcg	ccagccgatgtttcatatcc	4	Signaling feedback
54294	Rgs5	ccagagaagcctgccaag	gaagtttgtccagggattgg	25	Signaling feedback
81767	Rpl19	tgccggaagaacaccttg	gcaggatcctcatccttcg	85	housekeeping
157074	Sdha	tgccatccattacatgacaga	aaatcctcccatcttcagtcc	16	housekeeping
83612	Slc32a1	aggctcggaaacttgacctt	gacgcagtagattccaagcac	76	neuromodulatory targets – Ion channel
83511	Slc6a2	agtgaagacatcgggaaagg	aaccaggagcacaaagagga	76	neuromodulatory targets – Ion channel
59114	Slc9a3r1	caggaccggattgtggag	agcagcttggcttcatcac	121	neuromodulatory targets – Ion channel
24797	Sst	agcccaaccagacagagaac	cctcatctcgtcctgctca	1	neuromodulatory regulator
24949	Syn1	ggacggaagggatcacatta	tggtgatccccaatgagtg	25	neuromodulatory targets – Ion channel
24806	Tac1	cagaaaggctgctgtgagg	gaagcgcaagacacacagg	13	neuromodulatory regulator
25085	Th	gggagctgaaggcttatggt	cctctgacagggagtgcag	66	neuromodulatory regulator

A.2 Selection of genes contributing to expression variability

Table A.2 PCA loadings for genes across PC 1-5

No.	Gene Symbol	PC 1 loadings	PC 2 loadings	PC 3 loadings	PC 4 loadings	PC 5 loadings
1	Th	**0.444**	**-0.137**	**0.208**	-0.218	0.051
2	Dbh	**0.317**	**-0.068**	0.107	**-0.258**	0.005
3	Gabrq	**0.228**	**-0.006**	0.101	0.040	0.081
4	Gal	**0.212**	0.016	0.095	-0.117	**0.144**
5	Rgs4	**0.202**	0.002	0.102	0.069	0.024
6	Slc6a2	0.186	**-0.053**	0.121	-0.165	-0.055
7	Phox2b	0.162	0.089	0.057	0.040	**-0.105**
8	Rasgrp2	0.148	0.004	0.034	0.035	0.116
9	Gria3	0.141	**0.215**	-0.173	-0.090	0.015
10	Gria2	0.133	0.160	-0.105	-0.017	-0.009
11	Rgs2	0.132	0.049	0.106	0.048	-0.067
12	Rasgrf2	0.131	0.055	0.052	0.008	0.139
13	Cacna1d	0.128	0.074	0.080	0.059	0.077
14	Grin 2a	0.128	0.098	-0.048	0.062	0.106
15	Dusp6	0.115	0.047	0.072	-0.058	-0.009
16	Prkca	0.101	**0.227**	**-0.435**	-0.192	-0.082
17	Ppp5c	0.099	0.113	-0.139	-0.017	-0.025
18	Hprt1	0.097	0.081	0.016	**0.115**	0.019
19	Grin1	0.088	0.094	0.146	**0.166**	-0.007
20	Atf2	0.088	0.096	-0.007	0.069	0.052
21	Fosl1	0.086	**0.068**	0.113	-0.098	-0.218
22	Araf	0.085	0.062	-0.011	0.083	0.016
23	Ptpn1	0.085	0.050	0.093	-0.049	0.071
24	Map2k1	0.085	0.064	0.009	**0.116**	0.017
25	Grin2b	0.084	0.112	0.021	0.012	0.048
26	Mapk1	0.083	0.096	-0.041	0.100	0.042
27	Ace	0.082	0.038	0.103	0.001	0.084
28	Rgs3	0.079	0.059	**-0.172**	-0.194	0.069
29	Gabra2	0.070	0.120	-0.003	0.113	0.102
30	Gabra4	0.069	0.066	0.018	0.145	0.089
31	Pak1	0.064	0.065	0.032	0.093	0.050
32	Syn1	0.050	0.119	0.045	0.076	0.052
33	Ppp2r1a	0.048	0.062	0.039	0.102	0.050
34	Adrbk1	0.044	0.106	-0.019	0.038	0.030
35	Raf1	0.043	0.196	**-0.275**	-0.166	0.035
36	Pdpk1	0.041	0.130	-0.027	0.001	0.066

37	Elk1	0.039	0.192	-0.060	-0.088	0.083
38	Akt1	0.039	0.065	-0.003	0.043	0.082
39	Prkce	0.037	0.103	0.111	0.082	0.067
40	Jund	0.036	0.033	0.099	0.051	0.002
41	Map2k7	0.032	0.062	-0.064	0.047	0.044
42	Rasa1	0.028	0.100	-0.063	0.016	0.092
43	Ppp1cc	0.024	0.083	0.072	0.024	0.059
44	Map3k12	0.022	0.107	0.085	0.038	0.117
45	Grin2c	0.021	0.061	0.000	-0.122	-0.019
46	Ppp1cb	0.020	0.071	0.013	0.024	0.023
47	Arrb1	0.017	0.100	0.022	0.041	0.077
48	Gabra1	0.016	0.196	-0.099	**0.315**	**0.144**
49	Pik3r3	0.014	0.088	-0.020	0.006	0.123
50	Hcn2	0.014	0.075	-0.112	-0.071	0.037
51	Rpl19	0.004	0.012	-0.034	-0.032	-0.008
52	Ptpn2	0.002	0.047	0.092	-0.032	0.021
53	Creb1	0.000	0.079	0.076	-0.061	0.070
54	Itpr1	-0.001	0.058	0.091	-0.073	0.123
55	Mapk7	-0.003	0.055	0.047	-0.083	0.058
56	Actb	-0.004	-0.012	0.034	0.032	0.008
57	Mapk3	-0.005	0.042	-0.085	-0.014	0.037
58	Jun	-0.005	0.126	0.117	0.018	-0.066
59	Egr1	-0.006	**0.284**	0.113	0.013	**-0.369**
60	Plcb1	-0.011	**0.231**	**-0.165**	-0.049	0.122
61	Agt	-0.015	0.021	0.127	0.050	0.061
62	Arrb2	-0.017	0.109	-0.001	0.098	0.010
63	Agtrap	-0.017	0.063	-0.011	-0.045	0.076
64	Pebp1	-0.019	0.051	0.002	0.087	0.014
65	Agtr1a	-0.021	0.029	0.136	-0.182	0.096
66	Fos	-0.034	0.341	**0.192**	-0.036	**-0.556**
67	Map3k11	-0.041	0.054	0.006	-0.114	0.091
68	Grk5	-0.063	0.077	0.002	-0.062	0.100
69	Rasgrf1	-0.075	0.105	0.126	-0.140	0.050
70	Gad1	-0.077	0.157	**0.165**	0.104	0.141
71	Slc9a3r1	-0.081	0.035	0.057	-0.104	0.077
72	Hras	-0.083	0.061	0.079	**-0.228**	0.104
73	Npy1r	-0.092	0.054	0.143	-0.120	**0.149**
74	Junb	-0.092	0.209	0.100	-0.035	**-0.186**
75	Kcnj2	-0.105	0.116	0.037	**-0.277**	0.057
76	Rgs1	-0.105	0.026	0.113	**-0.221**	0.066
77	Crh	**-0.119**	0.068	0.056	**-0.248**	0.045
78	Npy	**-0.129**	0.088	**0.231**	0.114	0.030
79	Slc32a1	**-0.141**	0.118	**0.222**	0.046	**0.168**
80	Tac1	**-0.145**	0.115	0.139	-0.109	0.092

81	Sst	**-0.289**	0.159	0.029	-0.043	**0.168**	

A.3 Rank order of PCA loadings (PC 3-5)

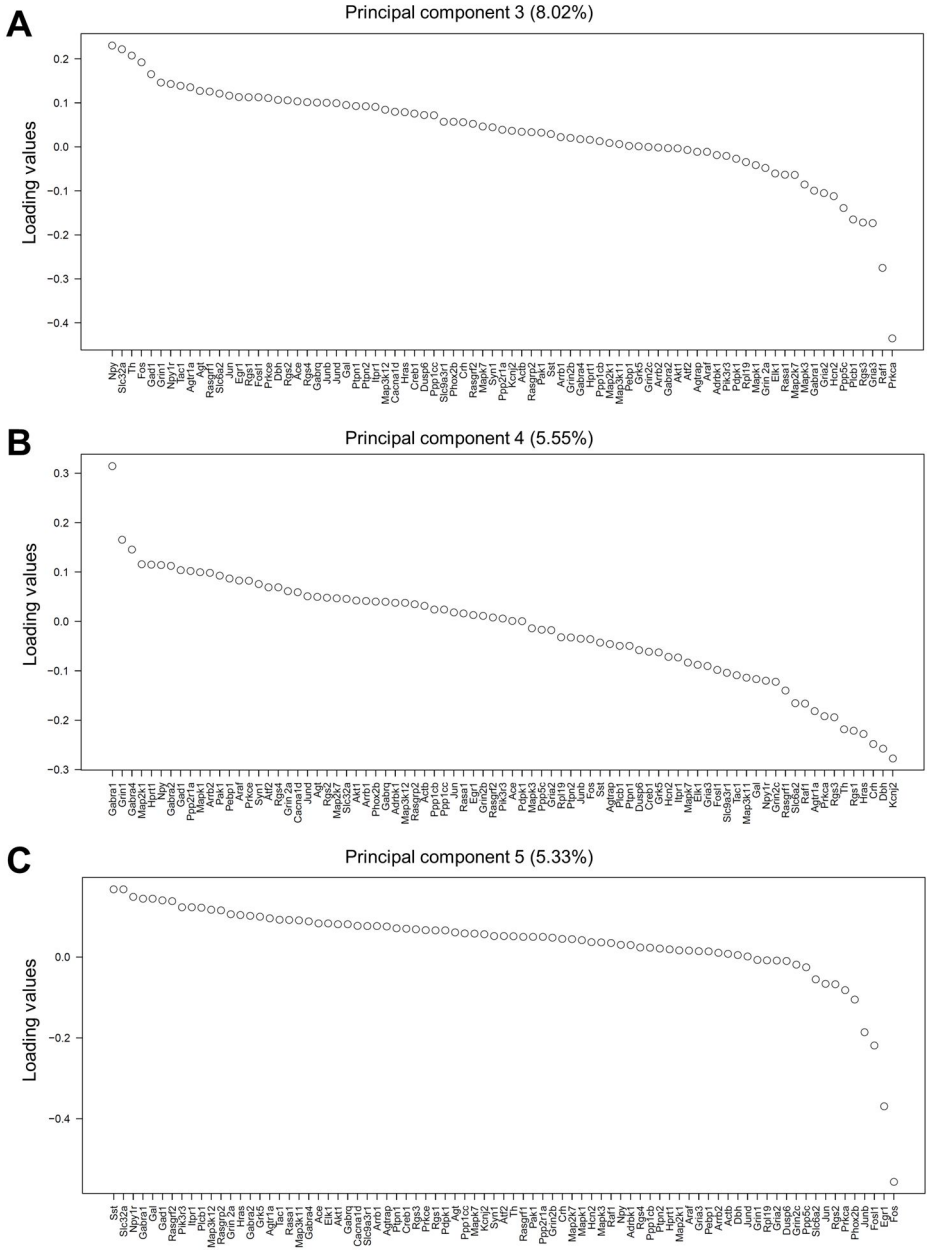

Figure A.1 Contribution of genes to variability. Ranked loading values for all 81 genes analyzed across multiple principal components (PCs). (A) PC 3, (B) PC 4, and (C) PC 5 are included. Different genes have greater (or lower) contributions to the variation in data along each principal component.

Appendix B

HEMODYNAMIC MODEL OF SHORT-TERM BAROREFLEX REGULATION OF CARDIOVASCULAR SYSTEM

B.1 Model description of base hemodynamic model

The model described in Chapter 5 is based on a quantitative model originally developed by M. Ursino, who used the model to examine the interaction between carotid baroregulation and the pulsating heart [291]. Subsequent revisions to this model has been made by Ursino, et al. to explore various aspects of carotid baroregulation, respiration, and how this physiological control system responds to various stressors. A combination of various versions of this model [289,291,325,326] are used in order to capture hemodynamic characteristics necessary to incorporate neuronal components driven by afferent input types. Conservation of mass and force balance equations used to characterize hemodynamics throughout the cardiovascular system are reproduced here. The following equations use the following variables to characterize hemodynamic behavior. Note that the subscript j represents the j^{th} compartment.

Table B.1 Hemodynamic variables

Model parameters	**Corresponding physiological parameter**
P_j	Intravascular pressure
$V_{u,j}$	Unstressed volume
F_j	Blood flow
C_j	Compliance
L_j	Inertance
R_j	Resistances
$F_{o,r}$	Flow out of right ventricle
$F_{o,l}$	Flow out of left ventricle

Vascular system

Conservation of mass at pulmonary arteries *(pa)*

$$\frac{dP_{pa}}{dt} = \frac{1}{C_{pa}}\left(F_{o,r} - F_{pa}\right) \qquad \text{B.1}$$

Balance of forces at pulmonary arteries *(pa)*

$$\frac{dF_{pa}}{dt} = \frac{1}{L_{pa}}\left(P_{pa} - P_{pp} - R_{pa} * F_{pa}\right) \qquad \text{B.2}$$

The inertance represents the change in pressure required to cause a change in flow-rate of a fluid. Due to the large diameter of the arteries, inertances affect hemodynamic behavior more noticeably in these blood vessels than in the smaller diameter veins.

Conservation of mass at pulmonary peripheral circulation *(pp)*

$$\frac{dP_{pp}}{dt} = \frac{1}{C_{pa}}\left(F_{pa} - \frac{P_{pp} - P_{pv}}{R_{pp}}\right) \quad \text{B.3}$$

Conservation of mass at pulmonary veins *(pv)*

$$\frac{dP_{pv}}{dt} = \frac{1}{C_{pv}}\left(\frac{P_{pp} - P_{pv}}{R_{pp}} - \frac{P_{pv} - P_{la}}{R_{pv}}\right) \quad \text{B.4}$$

Conservation of mass at systemic arteries *(sa)*

$$\frac{dP_{sa}}{dt} = \frac{1}{C_{sa}}\left(F_{o,l} - F_{sa}\right) \quad \text{B.5}$$

Force balance at systemic arteries

$$\frac{dF_{sa}}{dt} = \frac{1}{L_{sa}}\left(P_{sa} - P_{sp} - R_{sa} * F_{sa}\right) \quad \text{B.6}$$

Conservation of mass at peripheral systemic circulation – splanchnic, extrasplanchnic, and lower body compartments *(sp, ep, mp)*

$$\frac{dP_{sp}}{dt} = \frac{1}{C_{sp} + C_{ep} + C_{mp}} * \left(F_{sa} - \frac{P_{sp} - P_{sv}}{R_{sp}} - \frac{P_{sp} - P_{ev}}{R_{ep}} - \frac{P_{sp} - P_{mv}}{R_{lb}} \right) \quad \text{B.7}$$

Where

$$\left(R_{lb} = \frac{1}{R_{mp}} + \frac{1}{R_d} \right) \quad \text{B.7.1}$$

NOTE: To incorporate the effects of varying abdominal pressure P_{abd} due to respiration, transmural pressure is calculated by subtracting P_{abd} from P_{sp}. Equations for P_{abd} are provided in later equations.

$$P_{sp-trans} = P_{sp} - P_{abd} \quad \text{B.7.2}$$

This transmural pressure is subsequently used to determine downstream pressures.

Conservation of mass at extrasplanchnic venous circulation *(ev)*

$$\frac{dP_{ev}}{dt} = \frac{1}{C_{ev}} \left(\frac{P_{sp} - P_{ev}}{R_{ep}} - \frac{P_{ev} - P_{tv}}{R_{ev}} - \frac{dV_{u,ev}}{dt} \right) \quad \text{B.8}$$

Conservation of mass at skeletal muscle, part of the lower body *(mv)*

$$\frac{dP_{mv}}{dt} = \frac{1}{C_{mv}} \left(\frac{P_{sp} - P_{mv}}{R_{lb}} - \frac{P_{mv} - P_{tv}}{R_{mv}} - \frac{dV_{u,mv}}{dt} \right) \quad \text{B.9}$$

Conservation of mass at thoracic vein *(tv)*

$$\frac{dP_{tv}}{dt} = \frac{1}{C_{tv}} \left(\frac{P_{mv} - P_{tv}}{R_{mv}} + \frac{P_{ev} - P_{tv}}{R_{ev}} + \frac{P_{sv} - P_{tv}}{R_{ev}} - \frac{P_{tv} - P_{ra}}{R_{tv}} \right) \quad \text{B.10}$$

NOTE: To incorporate the effects of varying thoracic pressure P_{thor} due to respiration, transmural pressure is calculated by subtracting P_{thor} from P_{tv}. Equations for P_{thor} are provided in later equations.

$$P_{tv-trans} = P_{tv} - P_{thor} \qquad \text{B.10.1}$$

Conservation of mass to determine splanchnic venous circulation, which assumes total blood volume *(V_t)* is known.

$$\begin{aligned} P_{sv} = \frac{1}{C_{sv}}\big(V_t - C_{sa} * P_{sa} - \big(C_{sp} + C_{ep} + C_{mp}\big) * P_{sp} - C_{ev} \\ * P_{ev} - C_{mv} * P_{mv} - C_{tv} * P_{tv} - C_{ra} * P_{ra} \\ - V_{ra} - C_{pa} * P_{pa} - C_{pp} * P_{pp} - C_{pv} * P_{pv} \\ - C_{la} * P_{la} - V_{lv} - V_u\big) \end{aligned} \qquad \text{B.11}$$

Here, V_{rv} and V_{lv} are the volumes of the right and left ventricles. V_u is the total unstressed volume, defined by:

Pulsatile (left) heart

Conservation of mass at left atrium (la)

$$\frac{dP_{la}}{dt} = \frac{1}{C_{la}}\left(\frac{P_{pv} - P_{la}}{R_{pv}} - F_{i,l}\right) \qquad \text{B.12}$$

$F_{i,l}$ refers to the flow into the left ventricle, determined by the following mass balance:

$$F_{i,l} = \begin{cases} 0, & P_{la} < P_{lv} \\ \dfrac{P_{la} - P_{lv}}{R_{la}}, & P_{la} \geq P_{lv} \end{cases} \qquad \text{B.13}$$

Ventricular volume is calculated using the following equation:

$$\frac{dV_{lv}}{dt} = F_{i,l} - F_{o,l} \qquad \text{B.14}$$

And flow out of the left ventricle *($F_{o,l}$)* is determined by:

$$F_{o,l} = \begin{cases} 0, & P_{max,lv} < P_{sa} \\ \dfrac{P_{max,lv} - P_{sa}}{R_{lv}}, & P_{max,lv} \geq P_{sa} \end{cases} \qquad \text{B.15}$$

$P_{max,lv}$ represents the isometric pressure of the left ventricle. This value is used to determine ventricular pressure over the course of the cardiac cycle. R_{lv} represents the viscous resistance of the left ventricle and is assumed to be proportional to $P_{max,lv}$, where:

$$R_{lv} = k_{R,lv} * P_{max,lv} \qquad \text{B.16}$$

$k_{R,lv}$ is a constant parameter.

Instantaneous pressure in the left ventricle represents the difference between the isometric pressure ($P_{max,lv}$) and viscous losses, therefore:

$$P_{lv} = P_{max,lv} - R_{lv} * F_{o,l} \qquad \text{B.17}$$

Isometric pressure is time-dependent and varies throughout the cardiac cycle. The base model by Ursino assumes that isometric pressure/volume can be characterized by an exponential function during diastole, when the ventricle is relaxed, and by a linear

function at the end of systole, when the ventricle is contracted maximally. Thus isometric pressure transitions between an exponential and linear function over the course of the cardia cycle.

$$P_{max,lv}(t) - \varphi(t) * E_{max,lv} * \left(V_{lv} - V_{u,lv}\right) + [1 - \varphi(t)] * P_{0lv} * \left(\exp\left(k_{E,lv} * V_{lv}\right) - 1\right) \quad \text{B.18}$$

Where $0 \leq \varphi(t) \leq 1$

$E_{max,lv}$ is the ventricular elastance at the maximal contraction of the ventricle. $V_{u,lv}$ is the corresponding unstressed volume of the ventricle and is the x-axis intercept of the end-systolic pressure/volume function. $P_{0,lv}$ and $k_{E,lv}$ are constant parameters that describe the monoexponential pressure/volume function at diastole.

The term $\varphi(t)$ represents the "activation function" of the ventricle. When $\varphi(t) = 1$, the ventricle is at maximum contraction, when $\varphi(t) = 0$, it is at complete relaxation. This activation function is defined as:

$$\varphi(t) = \begin{cases} \sin^2\left[\dfrac{\pi * T(t)}{T_{sys}(t)} * u\right], & 0 \leq u \leq \dfrac{T_{sys}}{T} \\ 0, & \dfrac{T_{sys}}{T} \leq u \leq 1 \end{cases} \quad \text{B.19}$$

T represents the heart period (i.e. inverse of heart rate). T_{sys} is the duration of systole and u is a dimensionless variable ranging between 0 and 1 and represents the fraction

of the cardiac cycle. A value of $u = 0$ corresponds to the beginning of systole. This variable has been modeled as an integral pulse frequency modulation function [392].

$$u(t) = frac\left[\int_{t_0}^{t} \frac{1}{T(t)} d\tau + u(t_0)\right] \quad \text{B.20}$$

The fractional part of this equation [frac()] indicates that the variable *u(t)* is reset to zero as soon as the value reaches a value of 1.

The duration of systole is determined by the following equation:

$$T_{sys} = T_{sys,0} - k_{sys} * \frac{1}{T} \quad \text{B.21}$$

Where k_{sys} and $T_{sys,0}$ are constant parameters. A similar set of equations (B.13-B.22) are used to describe the right heart as well.

Pulsatile (right) heart

Conservation of mass at right atrium (ra)

$$\frac{dP_{ra}}{dt} = \frac{1}{C_{ra}}\left(\frac{P_{tv} - P_{ra}}{R_{tv}} - F_{i,l}\right) \quad \text{B.22}$$

Flow into right ventricle:

$$F_{i,r} = \begin{cases} 0, & P_{ra} < P_{rv} \\ \dfrac{P_{ra} - P_{rv}}{R_{ra}}, & P_{ra} \geq P_{rv} \end{cases} \quad \text{B.23}$$

Volume of right ventricle:

$$\frac{dV_{rv}}{dt} = F_{i,r} - F_{o,r} \tag{B.24}$$

Flow out of right ventricle:

$$F_{o,r} = \begin{cases} 0, & P_{max,rv} < P_{pa} \\ \dfrac{P_{max,rv} - P_{pa}}{R_{rv}}, & P_{max,rv} \geq P_{pa} \end{cases} \tag{B.25}$$

Viscous resistance of right ventricle:

$$R_{rv} = k_{R,rv} * P_{max,rv} \tag{B.26}$$

Instantaneous pressure in right ventricle:

$$P_{rv} = P_{max,rv} - R_{rv} * F_{o,r} \tag{B.27}$$

Isometric pressure in right ventricle:

$$\begin{aligned} P_{max,rv}(t) - \varphi(t) * E_{max,rv} * \left(V_{rv} - V_{u,rv}\right) + [1 - \varphi(t)] \\ * P_{0rv} * (\exp\left(k_{E,rv} * V_{rv}\right) - 1 \end{aligned} \tag{B.28}$$

Where $\varphi(t)$ is determined from equations B.20-B.22.

Afferent input types

Baroreceptors are modeled using a linear derivative first-order dynamic function and a sigmoidal static characteristic function in series, described by the following equations:

$$\tau_p \frac{d\acute{P}}{dt} = P_{br} + \tau_z * \frac{dP_{br}}{dt} - \acute{P} \tag{B.29}$$

$$f_{br} = \left[f_{min} + f_{max} * exp\left(\frac{\acute{P} - P_n}{k_a}\right)\right] \Big/ \left[1 + exp\left(\frac{\acute{P} - P_n}{k_a}\right)\right] \qquad \text{B.30}$$

Here, $\tau_p$and $\tau_z$are time constants for the real pole and real zero in the linear dynamic block. P_{br} is the arterial pressure measured by the baroreceptors. $\acute{P}$ is the output variable of the dynamic block (with dimensions of pressure). f_{br} is the frequency of spikes in the afferent fibers. f_{min} and $f_{max}$are the lower and upper saturation limits of the frequency discharge of the baroreceptors. P_n is the intrasinus pressure at the central point of the sigmoidal curve and $k_a$is a constant parameter (with dimensions of pressure).

<u>*Cardiopulmonary receptors*</u> are modeled using a first-order low-pass filter in series with the same sigmoidal static characteristic function type used to model the baroreceptors. Because cardiopulmonary receptors depend on transmural pressure at the pulmonary veins, this pressure difference is used as an input to first-order low-pass filter:

$$\tau_{cp} \frac{dP_l}{dt} = -P_l + \left(P_{pv} - P_{thor}\right) \qquad \text{B.31}$$

$$f_{cp} = \frac{f_{max,l}}{1 + exp\left(\frac{P_{tn} - P_l}{k_l}\right)} \qquad \text{B.32}$$

Here $P_{pv} - P_{thor}$ is the transmural pressure at the pulmonary vein or input value to the low-pass filter function. $P_l$is the output variable of the low-pass filter. f_{cp} is the spike

frequency of the afferent fibers from the cardiopulmonary receptors and $f_{max,l}$ is the upper saturation limit of the frequency discharge of these receptors, the lower limit being zero. P_{tn} represents the pulmonary venous pressure at the central point of the sigmoid curve. k_l is another constant that determines the slope of the sigmoid curve, or sensitivity of the cardiopulmonary receptors.

Lung stretch receptors are modeled using a first-order low-pass filter:

$$\frac{df_{lr}}{dt} = \tau_{lung} * \left(-f_{lr} + G_{al} * V_{lung}\right) \qquad \text{B.33}$$

Here f_{lr} is the firing discharge rate of the slowly adapting lung stretch receptors (SARs). τ_{lung} is the time constant of the receptor response to lung inflation. G_{al} is a constant gain factor and V_{lung} is the lung volume.

Efferent sympathetic outflow

Sympathetic efferent outflow is modeled to be dependent on the afferent input signals sent by the baroreceptor, cardiopulmonary, and lung stretch receptors. Moreover, the combined effects of these input signals affect sympathetic efferent outflow to different effector functions differently. Therefore a series of calculations are included to determine *i)* the afferent firing frequency input that is then used to determine *ii)* the

distinct sympathetic efferent outflow signals to the respective effector functions associated with the heart (h), peripheral circulation (p), and unstressed volumes (v)

$$f_{as,h} = G_{ab,h} * f_{br} - G_{alh} * f_{lr} + G_{ac,h} * f_{cp} \quad \text{B.34}$$

$$f_{as,p} = G_{ab,p} * f_{br} + G_{al,p} * f_{lr} + G_{ac,p} * f_{cp} \quad \text{B.35}$$

$$f_{as,v} = G_{ab,v} * f_{br} + G_{al,v} * f_{lr} + G_{ac,v} * f_{cp} \quad \text{B.36}$$

$G_{ab,j}$, where j is a general index for the heart, peripheral circulation, or unstressed volume, represents a constant gain factor indicating how much influence each afferent input has on determining sympathetic efferent outflow. A factor of -1 is used for $G_{al,h}$as this provided the best fits for the model. The resulting $f_{as,j}$ values are then used to determine sympathetic efferent outflow to the respective effector functions using a negative monotonic function to relate afferent activity to efferent neural pathways,

$$f_{es,h} = f_{es,\infty} + \left(f_{es,0} - f_{es,\infty}\right) * exp\left(-k_{es} * f_{as,h}\right) \quad \text{B.37}$$

$$f_{es,p} = f_{es,\infty} + \left(f_{es,0} - f_{es,\infty}\right) * exp\left(-k_{es} * f_{as,p}\right) \quad \text{B.38}$$

$$f_{es,v} = f_{es,\infty} + \left(f_{es,0} - f_{es,\infty}\right) * exp\left(-k_{es} * f_{as,v}\right) \quad \text{B.39}$$

Parasympathetic (vagal) efferent output is described in detail § 5.4.1.

Effector function regulation

Physiological parameters affected by sympathetic and parasympathetic outflow include resistances, unstressed volumes, and cardiac elastances. Sympathetic outflow regulates resistances and unstressed volumes via a monotonic logarithmic static function, a low-pass first-order dynamics, and a time delay specific to each effector function.

$$\sigma_\theta(t) = \begin{cases} G_\theta * ln\left[f_{es,j}(t - D_\theta) - f_{es,min} + 1\right], & f_{es,j} \geq f_{es,min} \\ 0 & , \quad f_{es,j} < f_{es,min} \end{cases} \qquad \text{B.40}$$

$$\frac{d\Delta\theta}{dt}(t) = \frac{1}{\tau_\theta} * \left(-\Delta\theta(t) + \sigma_\theta(t)\right) \qquad \text{B.41}$$

$$\theta(t) = \Delta\theta(t) + \theta_0 \qquad \text{B.42}$$

Where θ represents a generic controlled parameters (i.e. resistance or unstressed volume). τ_θ and D_θ are the time constants and time delays associated with sympathetic regulatory mechanisms on these effector functions. G_θ is a constant gain factor for the various effector functions and θ_0 represents constant values for respective effector functions. Note that $f_{es,j}$ is used to represent the different sympathetic tones specific to a particular effector function.

Heart period

In the original model developed by Ursino [291], heart period, as opposed to heart rate, is modeled. By modeling heart period, Ursino was able to reproduce the nonlinear effect that sympathetic and vagal tone have on heart rate. Thus a linear interaction between sympathetic and parasympathetic effect on heart period is used. Heart period (not heart rate) has been shown to be linearly dependent on vagal drive, while the same monotonic logarithmic static function and low-pass first-order dynamics characterize sympathetic effects on heart period.

$$\sigma_{T,s}(t) = \begin{cases} G_{T,s} * ln\left[f_{es,h}(t - D_\theta) - f_{es,min} + 1\right], & f_{es,h} \geq f_{es,min} \\ 0 & , \quad f_{es,h} < f_{es,min} \end{cases} \quad \text{B.43}$$

$$\frac{d\Delta T_s}{dt}(t) = \frac{1}{\tau_{T,s}} * \left(-\Delta T_s(t) + \sigma_{T,s}(t)\right) \quad \text{B.44}$$

$$\sigma_{T,v} = G_{T,v} * f_{ev,h}\left(t - D_{T,v}\right) \quad \text{B.45}$$

$$\frac{d\Delta T_v}{dt}(t) = \frac{1}{\tau_{T,v}} * \left(-\Delta T_v(t) + \sigma_{T,v}(t)\right) \quad \text{B.46}$$

$$T = \Delta T_s + \Delta T_v + T_0 \quad \text{B.47}$$

Ventricular Contractility

Because ventricular contractility is dependent on the balance of sympathetic and parasympathetic drive, similar to heart period, a similar approach is used to determine

contractility. Thus a linear interaction between sympathetic and parasympathetic effects on the inverse of E_{max} is used

$$\sigma_{E,s}(t) = \begin{cases} -G_{s,Emax} * ln\left[f_{es,h}\left(t - D_{E,s}\right) - f_{es,min} + 1\right], & f_{es,h} \geq f_{es,min} \\ 0 & , \ f_{es,h} < f_{es,min} \end{cases} \quad \text{B.48}$$

$$\frac{d\Delta\left(1/E_{max,lv}\right)_s}{dt}(t) = \frac{1}{\tau_{E,s}} * \left(-\Delta\left(1/E_{max,lv}\right)_s(t) + \sigma_{E,s}(t)\right) \quad \text{B.49}$$

$$\sigma_{E,v} = G_{E,v} * f_{ev,h}\left(t - D_{E,v}\right) \quad \text{B.50}$$

$$\frac{d\Delta\left(1/E_{max,lv}\right)_v}{dt}(t) = \frac{1}{\tau_{E,v}} * \left(-\Delta\left(1/E_{max,lv}\right)_v(t) + \sigma_{E,v}(t)\right) \quad \text{B.51}$$

$$\left(1/E'_{max,lv}\right) = \Delta\left(1/E_{max,lv}\right)_s + \Delta\left(1/E_{max,lv}\right)_v \quad \text{B.52}$$

$$E_{max,lv} = E'_{max,lv} + E_{max,lv,0} \quad \text{B.53}$$

Here,$\tau_{E,s}$, and $\tau_{E,v}$,represent the time constants associated with the sympathetic and parasympathetic regulatory mechanisms on contractility. $D_{E,s}$ and $D_{E,v}$ correspond to the time delays associated the sympathetic and parasympathetic mechanisms. Once $1/E'_{max,lv}$ is determined, $E_{max,lv}$ can easily be calculated using equation B.53. $E_{max,lv,0}$ represents a constant, baseline elasticity value determined from experimental

data collected from a dog whose stellate ganglion and vagal nerve fibers were denervated, effectively removing any autonomic influence [311].

Similar equations (B.48-B.53) are used to determine $^1/_{E_{max,rv}}$ (right ventricle). However, all gains were adjusted by a factor of (1/0.59), based on the ratio value used to relate contractility between the right and left ventricle used by Ursino originally.

Lung volume, thoracic, and abdominal pressures

A linear relationship between lung volume and thoracic pressure is used to model lung volume measured by the lung stretch receptors:

$$V_{lung} = V_{lung,0} - 0.1 * P_{thor} \qquad \text{B.54}$$

Thoracic pressure varies with time due to the effects of the respiratory cycle, which is modeled independently from any autonomic regulation. Parameters were chosen based on experimental work by Moreno, et al. [393]. Thoracic pressure varies linearly during respiration between a minimum of –9 mmHg and a maximum of –4 mmHg, which represents steady-state thoracic pressure during the respiratory pause.

$$P_{abd} = \begin{cases} -2.5 * s * \frac{T_{resp}}{T_{insp}/2} - 4 & 0 < s < \frac{T_{insp}/2}{T_{resp}} \\ -2.5 & \frac{T_{insp}/2}{T_{resp}} < s < \frac{T_{insp}}{T_{resp}} \\ -2.5 * \frac{T_{insp}+T_{exp}-s*T_{resp}}{T_{exp}} & \frac{T_{insp}}{T_{resp}} < s < \frac{T_{insp}+T_{exp}}{T_{resp}} \\ -5 * \frac{T_{insp}+T_{exp}-s*T_{resp}}{T_{exp}} - 4 & \frac{T_{insp}+T_{exp}}{T_{resp}} < s < 1 \end{cases} \quad \text{B.55}$$

Where T_{resp} represents the respiratory period, T_{insp} represents the duration of inspiration and T_{exp} represents the duration of expiration. s is a dimensionless variable, similar to the variable $u(t)$, used to represent the fraction of the cardiac cycle that has completed. Here, s is calculated by solving for an additional state variable, ε

$$\frac{d\varepsilon}{dt} = \frac{1}{T_{resp}} \quad \text{B.56}$$

$$s(t) = frac(\varepsilon) \quad \text{B.57}$$

Where the fractional portion $frac(\varepsilon)$ resets the variable $s(t)$ to zero once it reaches a value of 1.

B.2 Full model parameter values

Table B.2 Hemodynamic parameter values (vascular system)

Parameter	Value	Reference
Compliances (mL/mmHg)		
C_{sa}	0.28	[291]
C_{sp}	2.05	[291]
C_{ep}	1.36	[289]
C_{mp}	0.31	[289]
C_{sv}	43.11	[289]
C_{ev}	28.40	[289]
C_{mv}	6.60	[289]
C_{tv}	33	[289]
C_{pa}	0.76	[291]
C_{pp}	5.80	[291]
C_{pv}	25.37	[291]
Unstressed Volumes (mL)		
$V_{u,sa}$	0	[291]
$V_{u,sp}$	274.40	[291]
$V_{u,ep}$	274.1	[289]
$V_{u,mp}$	62.50	[289]
$V_{u,sv}$	1121	[291]
$V_{u,ev}$	1120	[289]
$V_{u,mv}$	255	[289]
$V_{u,tv}$	0	[325]
$V_{u,pa}$	0	[291]
$V_{u,pp}$	123	[291]
$V_{u,pv}$	120	[291]
Hydraulic Resistances (mmHg*s*mL^{-1})		
R_{sa}	0.06	[291]
R_{sp}	3.307	[291]
R_{ep}	1.725	[289]
R_{mp}	4.130	[289]
R_{sv}	0.038	[291]
R_{ev}	0.0197	[289]
R_{mv}	0.0848	[289]

R_{tv}	0.0054	[289]
R_{pa}	0.0230	[291]
R_{pp}	0.0894	[291]
R_{pv}	0.0056	[291]
Inertance (mmHg*ml*s^{-2})		
L_{sa}	2.2e-4	[291]
L_{pa}	1.8e-4	[291]

Table B.3 Hemodynamic parameters (left heart)

Parameter	**Value**	**Units**	**Reference**
C_{la}	19.23	mL/mmHg	[291]
$V_{u,la}$	25	mL	[291]
R_{la}	2.5e-3	mmHg*s*mL^{-1}	[291]
$P_{0,lv}$	1.5	mmHg	[291]
$k_{E,lv}$	0.014	mL^{-1}	[291]
$V_{u,lv}$	16.77	mL	[291]
$E_{max,lv,0}$	1.283	mmHg/mL	estimated
$k_{R,lv}$	3.75e-4	s/mL	[291]

Table B.4 Activation function parameters

Parameter	**Value**	**Units**	**Reference**
k_{sys}	0.075	sec^2	[291]
$T_{sys,0}$	0.40	sec	[291]

Table B.5 Hemodynamic parameters (left heart)

Parameter	Value	Units	Reference
C_{ra}	31.25	mL/mmHg	[291]
$V_{u,ra}$	25	mL	[291]
R_{ra}	2.5e-3	mmHg*s*mL^{-1}	[291]
$P_{0,rv}$	1.5	mmHg	[291]
$k_{E,rv}$	0.0110	mL^{-1}	[291]
$V_{u,rv}$	40.8	mL	[291]
$E_{max,rv,0}$	0.7570	mmHg/mL	estimated
$k_{R,rv}$	1.4e-3	s/mL	[291]

Table B.6 Afferent input parameters (baroreceptors)

Parameter	Value	Units	Reference
P_n	92	mmHg	[291]
f_{min}	2.52	Hz	[291]
f_{max}	47.78	Hz	[291]
k_a	11.758	mmHg	[289]
τ_z	6.37	sec	[291]
τ_p	2.076	Sec	[291]

Table B.7 Afferent input parameters (cardiopulmonary receptors)

Parameter	Value	Units	Reference
P_{tn}	10.80	mmHg	[289]
$f_{max.l}$	20	Hz	[291]
k_l	11.758	mmHg	[289]
τ_{cp}	10	sec	[289]

Table B.8 Afferent firing frequency gains (to heart)

Parameter	Value	Units	Reference
$G_{ab,h}$	1	--	[291]
$G_{al,h}$	-1.541	--	Estimated
$G_{ac,h}$	2	--	[289]

Table B.9 Afferent firing frequency gains (to peripheral circulation)

Parameter	Value	Units	Reference
$G_{ab,p}$	1	--	[291]
$G_{al,p}$	0.33	--	[326]
$G_{ac,p}$	2.5	--	[289]

Table B.10 Afferent firing frequency gains (to unstressed volumes)

Parameter	Value	Units	Reference
$G_{ab,v}$	1	--	[291]
$G_{al,v}$	0	--	[289]
$G_{ac,v}$	0	--	[289]

Table B.11 Efferent sympathetic outflow parameters

Parameter	Value	Units	Reference
$f_{es,0}$	16.11	Hz	[291]
$f_{es,\infty}$	2.1	Hz	[291]
$f_{es,min}$	2.66	Hz	[291]
k_{es}	0.0675	Sec	[291]

Table B.12 Effector function regulation (gains)

Parameter	Value	Units	Reference
$G_{R,sp}$	0.695	mmHg*mL^{-1}*ν^{-1}	[291]
$G_{R,ep}$	0.653	mmHg*mL^{-1}*ν^{-1}	[291]
$G_{R,mp}$	2.81	mmHg*mL^{-1}*ν^{-1}	[289]
$G_{Vu,sv}$	-265.4	mL/ν	[291]
$G_{Vu,ev}$	-107.5	mL/ν	[289]
$G_{Vu,mv}$	-25	mL/ν	[289]
$G_{T,s}$	-0.13	ν	[291]
$G_{T,v}$	0.09	ν	[291]
$G_{s,Emax,lv}$	0.103	mmHg*mL^{-1}*ν^{-1}	estimated
$G_{v,Emax,lv}$	0.205	mmHg*mL^{-1}*ν^{-1}	estimated

Where ν = spikes/s (i.e. Hz)

Table B.13 Effector function (time constants)

Parameter	Value	Units	Reference
$D_{R,sp}$	2	sec	[291]
$D_{R,ep}$	2	sec	[291]
$D_{R,mp}$	2	sec	[289]
$D_{Vu,sv}$	5	sec	[291]
$D_{Vu,sv}$	5	sec	[289]
$D_{Vu,mv}$	5	sec	[289]
$D_{T,s}$	2	sec	[291]
$D_{T,v}$	0.2	sec	[291]
$D_{E,s}$	2	sec	estimated
$D_{E,v}$	0.2	sec	estimated

Table B.14 Effector function (constants)

Parameter	Value	Units	Reference
$R_{sp,0}$	2.49	mmHg*s*mL^{-1}	[291]
$R_{ep,0}$	0.78	mmHg*s*mL^{-1}	[291]
$R_{mp,0}$	4.13	mmHg*s*mL^{-1}	[289]
$V_{u,sv,0}$	1435.4	mL	[291]
$V_{u,ev,0}$	1247	mL	[289]
$V_{u,mv,0}$	290	mL	[325]
T_0	0.58	sec	[291]
$D_{T,v}$	0.2	sec	[291]
$E_{max,lv.0}$	1.283	mmHg/mL	estimated
$E_{max,rv.0}$	0.757	mmHg/mL	estimated

Table B.15 Respiration

Parameter	Value	Units	Reference
T_{insp}	1.6	sec	[325]
T_{resp}	4.0	sec	[325]
T_{exp}	1.4	sec	[325]

Parasympathetic (vagal) outflow

Table B.16 Neuronal subtype parameters (baroreceptor-input subtype)

Parameter	Value	Units	Reference
$f_{min,BR}$	0.30	Hz	estimated
$f_{max,BR}$	21.50	Hz	estimated
$f_{midpt,BR}$	1.76	Hz	estimated
k_{BR}	2.14	Hz	estimated

Table B.17 Neuronal subtype parameters (cardiopulmonary receptor-input subtype)

Parameter	Value	Units	Reference
$f_{min,BR}$	0.30	Hz	estimated
$f_{max,BR}$	21.50	Hz	estimated
$f_{midpt,BR}$	1.76	Hz	estimated
k_{BR}	2.14	Hz	estimated

Table B.18 Neuronal subtype parameters (lung-stretch receptor input subtype)

Parameter	Value	Units	Reference
$f_{min,LS}$	2.75	Hz	estimated
$f_{max,LS}$	31.57	Hz	estimated
$f_{midpt,LS}$	0.96	Hz	estimated
k_{LS}	7.52	Hz	estimated

Table B.19 Nucleus ambiguus neuronal population parameters (heart rate)

Parameter	Value	Units	Reference
$f_{min,NA}$	4.88	Hz	estimated
$f_{max,NA}$	15.78	Hz	estimated
$f_{midpt,NA}$	0.74	Hz	estimated
k_{NA}	2.55	Hz	estimated

Table B.20 Nucleus ambiguus neuronal population parameters (contractility)

Parameter	Value	Units	Reference
$f_{min,NActr}$	0.61	Hz	estimated
$f_{max,NActr}$	11.00	Hz	estimated

$f_{midpt,NActr}$	0.62	Hz	estimated
k_{NActr}	1.20	Hz	estimated

Table B.21 Dorsal motor nucleus neuronal population (contractility)

Parameter	**Value**	**Units**	**Reference**
$f_{min,DMV}$	2.59	Hz	estimated
$f_{max,DMV}$	6.66	Hz	estimated
$f_{midpt,DMV}$	0.53	Hz	estimated
k_{DMV}	1.24	Hz	estimated

Appendix C

SUPRACHIASMATIC NUCLEUS GENE ASSAY SET AND FUNCTIONAL ANNOTATION

Table C.1 Gene categorization, primer sequences, and accession number

Gene Symbol	Accession No.	Forward Design	Reverse Design	Function
Actb	NM_007393.3	aaggccaaccgtgaaaagat	gtggtacgaccagaggcatac	housekeeping
Adcyap1	NM_009625.2	gagaatctgggggcaagtct	caccagcacctgatctgtca	neuropeptide
Adcyap1r1	NM_007407.3, NM_001025372.1	ggctgtgctgaggctctact	ccacagagctgtgctgtcat	receptor
Arih1	NM_019927.2	gccacttcaattgggataaaga	ggattaattacatgacactcagcaa	light induced
Arntl	NM_007489.3	accttcccgcagctaacag	tcctctttgggccacctt	circadian clock
Atp5b	NM_016774.3	ctgaggtcttcacgggtca	gcttgttctgggagatggtc	housekeeping
Avp	NM_009732.1	ctacgctctccgcttgtttc	gggcagttctggaagtagca	neuropeptide
Avpr1a	NM_016847.2	gccaaggatgactcggatag	tgggcttcggttgttagaat	receptor
Avpr1b	NM_011924.2	tcctcggtgtcacctctca	gggaggtgggtgttaatatgg	receptor
Avpr2	NM_019404.1	tgggtcctcaagatgagtcc	aggagggtgtatccttcatcag	receptor
Bhlhe40	NM_011498.4	cagcttcatgaacccagaca	gtgccaaaggagaagggagt	circadian clock
Bhlhe41	NM_001271768.1, NM-024469.2	cctgcccttctatctgctgt	tcttgtctagccagggctgt	circadian clock
Brs3	NM_009766.3	gtgagcagtgccctctttct	atgacacgtgaacagccaga	receptor
Calb1	NM_009788.4	tctgtgtgagaagaacaaacagg	taagagcaaggtctgttcggta	signal transduction
Calb2	NM_007586.1	gatggcaaattgggtctctc	tctgaggtcagcttcataccc	signal transduction
Camk2a	NM_009792.3, NM_177407.4	cagatcgtccacttccacag	tccagcaaaatccaaaggag	signal transduction
Camk2b	NM_007595.4	cagccccaaaggatctctc	ttccttaatcccgtccactg	signal transduction
Cebpb	NM_009883.3	aagatgcgcaacctggag	cagggtgctgagctctcg	light induced
Clk	NM_001289826.1, NM_001305222.1, NM_007715.6	tgacaaggacaaagcaaaaaga	cgcgttaccaggaagcata	circadian clock
Creb1	NM_001037726.1, NM_009952.2, NM_133828.2	ccactgatggacagcagattc	ggtatgtttgtacatcgcctga	signal transduction
Crebbp	NM_001025432.1	gatgaggactctcaatgcccta	ggctgttgatctgttgttattcc	signal transduction
Cry1	NM_007771.3	ctatatcctcgacccctggtt	caagacactgaagcaaaaatcg	circadian clock
Cry2	NM_009963.4, NM_001113333.1	gccatcatgacccaactga	ctcccagctgacccagag	circadian clock

Csnk1d	NM_139059.2, NM_027874.2	catcctcagctccacattga	acattgtagtccccctcagc	circadian clock
Csnk1e	NM_013767.6	tgagcatgagactccacagag	tcaaatggcacgcttgtct	circadian clock
Csnk2a1	NM_007788.3	gtttggatatgtggagcttgg	tgttcccagaaccttggcta	circadian clock
Cul5	NM_001161618.1, NM_027807.3	gcatattataagtgcgggccta	gctccacatacttctcagagtcag	receptor
Dbp	NM_016974.3	cttttgaccctcggagacac	ccggctccagtacttctcat	circadian clock
Drd1a	NM_001291801.1, NM_010076.3	tgtgcatcgaggtgaatgag	cagcgatgagcccaactatc	receptor
Dusp1	NM_013642.3	ccactcaagtcttctttctccaa	gactgtttgctgcacagctc	light induced
Dusp4	NM_176933.4	acggacatctgcctgctta	ggtgctgggaggtacagg	light induced
Egr1	NM_007913.5	cctatgagcacctgaccaca	tcgtttggctgggataactc	light induced
Egr2	NM_010118.3	cccttccagtgtcggatct	tgtgggttcggatgtgagta	light induced
Fos	NM_010234.2	gggacagcctttcctactacc	gatctgcgcaaaagtcctgt	light induced
Gabbr2	NM_001081141.1	ctgcggaggacagtggag	gtgttttcgcagtgttccag	receptor
Gabra1	NM_010250.4	gctccggctaaacaacctta	cacagacttctttccattgtgg	receptor
Gadd45b	NM_008655.1	ctgcctcctggtcacgaa	ttgcctctgctctcttcaca	light induced
Gapdh	NM_008084.2	tgtccgtcgtggatctgac	cctgcttcaccaccttcttg	housekeeping
Gria1	NM_001113325.1, NM_008165.3	tttgctttgtcacaactcacg	tttggagaactgggaacagaa	receptor
Gria2	NM_001039195.1, NM_001083806.1, NM_013540.2	gatggtcaacactcgaagagaa	tcataagtcagggccgaagt	receptor
Gria4	NM_001113180.1, NM_001113181.1, NM_019691.4	cttcagctaagaccttcattgaga	cctgctttttccattatagcttg	receptor
Grin1	NM_008169.1	tacaagcgacacaaggatgc	ggctctgctctaccactctttc	receptor
Grin2c	NM_010350.2	gaagcgggccatagacct	tggcagatccctgagagc	receptor
Grm1	NM_001114333.1, NM_016976.2	gatgagaagggggatgcac	caggttcccacatggacata	receptor
Grm5	NM_001081414.2, NM_001143834.1	gcagtgaaccgtgtgagaaa	gtgtgcaggtccaacaacag	receptor
Grp	NM_175012.2	acgacgttcaaaccgctaag	tggcagttcctccctttttc	neuropeptide
Grpr	NM_008177.2	ctccatgctccactttgtca	aggggttcacacaggagttg	receptor
Gsk3b	NM_019827.6	ttctacaggacaagcgatttaaga	cggactatgttacagtggtctagc	circadian clock
Hprt	NM_013556.2	tcctcctcagaccgctttt	cctggttcatcatcgctaatc	housekeeping
Id2	NM_010496.3	actatcgtcagcctgcatca	agctcagaagggaattcagatg	circadian clock
Jun	NM_010591.2	tggagtgggaaggacgtg	aaagtctgccggccaatag	light induced
Junb	NM_008416.2	cgtctacaccaacctcagca	cgggtatgagctcccagtc	light induced
Mapk1	NM_001038663.1, NM_011949.3	accgtgacctcaagccttc	tgatctggatctgcaacacg	signal transduction
Mapk3	NM_011952.2	acacccctgtccttttggat	tctgggttgagcaaagttca	signal transduction
Nfil3	XM_006516877.1, XM_011244379.1, XM_006516878.1, XM_006516875.1, XM_006516876.2	gaccagggagcagaaccac	ccccagtcttctttcaggtct	circadian clock
Nmbr	NM_008703.2	gctgggctgcaaactcat	catggggttcacgatagctc	receptor
Npas2	NM_008719.2	ggcacctcaggctacgact	ctttgccaaactgcatcaga	circadian clock
npy1r	NM_010934.4	catcatgctgctctccattg	tggttccagtcgaacacagt	receptor
npy2r	NM_001205099.1, NM_008731.3	gcggatcttttggtgaaca	ttccactctcccatcaaggt	receptor
npy5r	NM_016708.3	cgcagtgttttctacagactgac	cacgtggaagacgtggagt	receptor

Nr1d1	NM_145434.3	aggagctgggcctattcac	cggttcttcagcaccagag	circadian clock
Nr1d2	NM_011584.4	cagcactaccagctcaggaa	ccaatcacttcctcctttgc	circadian clock
Nr4a1	NM_010444.2	gctgcaagggcttcttca	tctggaagcggcagaact	light induced
Nr4a2	NM_001139509.1, NM_013613.2	tcagagcccacgtcgatt	tagtcagggtttgcctggaa	light induced
Nras	NM_010937.2	agtacatgaggacaggcgaag	ctttcacacgcttaatttgctc	signal transduction
Pcsk1n	NM_013892.3	gatcctcaccggaagttcg	aaatcctggtccacagatcg	neuropeptide
Per1	NM_011065.4, NM_001159367.1	gcttcgtggacttgacacct	tgctttagatcggcagtggt	circadian clock
Per2	NM_011066.3	acccacacaccaaactgctt	ggcgtctcgatcagatcct	circadian clock
Per3	NM_011067.2	cactgcacctctggtgagc	actgctggcactgcttcc	circadian clock
Pou2f2	NM_001163554.1, NM_001163555.1, NM_011138.2	ggcccaactcatgctgac	actgagcaggtggctgga	light induced
Ppp1ca	NM_031868.2	cagccattgtggatgagaag	ctaatctgctccatggattgc	signal transduction
Ppp2ca	NM_019411.4	gctgaacgagtgcaagcag	cgttggattcttttgtcagga	signal transduction
Prkaca	NM_008854.4	aaaaatgggagaccccttctc	gtgccaagggtcttgattcta	signal transduction
Prkacb	NM_011100.4, NM_001164198.1	gcaggacatggacattgtgt	tccaccgccttattgtaacc	signal transduction
Prkca	NM_011101.3	ggaatgagtccttcacgttca	cccatgaagtcattccgagt	signal transduction
Prkcb	NM_008855.2	accaagacattctgtggcact	agacttcccgtagggctgat	signal transduction
Prkg1	NM_001013833.2, NM_011160.2	cacctcccataattccaagtg	atgtcccagcctgagttgtc	signal transduction
Prkg2	NM_008926.4	cgatggctaccttaagttggtt	ccacagaatgtccacgttttc	signal transduction
Prok2	NM_015768.2, NM_001037539.2, NM_001170419.1	tcatttggggcagacgtt	aaagccagtgggccagat	neuropeptide
prokr2	NM_144944.3	gggcatcctcacagcctac	ggggaagaagtctcgcacta	receptor
Pvalb	NM_013645.3	ggcaagattggggttgaag	agcagtcagcgccacttag	signal transduction
Rasa1	NM_145452.3	tccttagtcagacaaatgttgtcaat	aaacaagaaacgtgactgtaataacc	signal transduction
Rasa2	NM_053268.2	gctaaagtcaccagatgttcagc	gcagcaacagtcgtacaagg	signal transduction
Rasd1	NM_009026.4	tgcacagcgacctcatgta	acacagcgctccttgtcc	signal transduction
Rgs16	NM_011267.3	ctctccacgacgtgctgtc	ccgcgtcttgaactctttg	signal transduction
Rora	NM_013646.1	cctactgttccttcaccaacg	atgttctgggcaaggtgttc	circadian clock
Rorb	NM_001043354.1, NM_146095.3	cacgtgtgaaggctgcaa	ggcaggagtaagaggcattg	circadian clock
Rrad	NM_019662.2	gggttgtgcgccagatac	ttcttgccaaggctctcc	light induced
Slc12a4	NM_009195.2	cccctacttcctgctcaaca	ccaggtaagcgctccaga	receptor
Slc12a5	NM_020333.2	tttctggacaaccatccaca	ttcaccttctcagcctccat	receptor
Slc12a6	NM_133648.2, NM_133649.2	ggtgccatcaagtcttcctt	ttgatgacagggtacggttg	receptor
Slc12a7	NM_011390.2	gtaccacctcaggatcagtgc	ctcataggtgaatgcggaaat	receptor
Slc32a1	NM_009508.2	acgtgacaaatgccattcag	tgaggaacaaccccaggtag	receptor
Tbp	NM_013684.3	gggagaatcatggaccagaa	gatgggaattccaggagtca	housekeeping
Vip	NM_011702.2	gcctctctttggaccacctt	ctccttcaaacggcatcct	neuropeptide
Vipr2	NM_009511.2	cttcctggcctaccttctga	gtcccagcaacctgtgtctt	receptor

Appendix D

PERMISSION LETTERS

Licensed Content Title	Identifying functional gene regulatory network phenotypes underlying single cell transcriptional variability
Licensed Content Author	James Park, Babatunde Ogunnaike, James Schwaber, Rajanikanth Vadigepalli
Licensed Content Date	January 2015
Licensed Content Volume	117
Licensed Content Issue	1
Licensed Content Pages	12
Type of Use	reuse in a thesis/dissertation
Portion	full article
Format	electronic
Are you the author of this Elsevier article?	Yes
Will you be translating?	No
Order reference number	20161021
Title of your thesis/dissertation	A single-cell analysis approach to understanding molecular organization and plasticity in the brain
Expected completion date	Oct 2016
Estimated size (number of pages)	405
Elsevier VAT number	GB 494 6272 12
Requestor Location	James H Park 79 Ray Street NEWARK, DE 19711 United States Attn: James H Park